PSFC/RR-09-14 **DOE/ET-54512-368**

Behavior of Lower Hybrid Waves in the Scrape Off Layer of a Diverted Tokamak

Gregory M. Wallace

Plasma Science and Fusion Center
Massachusetts Institute of Technology
Cambridge MA 02139 USA

November 2009

This work was supported by the U.S. Department of Energy, Grant No. DE-FC02-99ER54512.

Behavior of Lower Hybrid Waves in the Scrape Off Layer of a Diverted Tokamak

by

Gregory M. Wallace

Submitted to the Department of Nuclear Science and Engineering
in partial fulfillment of the requirements for the degree of

Doctor of Philosophy in Applied Plasma Physics

at the

MASSACHUSETTS INSTITUTE OF TECHNOLOGY

February 2010

Author .....
Department of Nuclear Science and Engineering
November 12, 2009

Certified by .....
Ronald R. Parker
Professor, Department of Nuclear Science and Engineering
Thesis Supervisor

Certified by .....
Dennis G. Whyte
Professor, Department of Nuclear Science and Engineering
Thesis Reader

Certified by .....
Paul T. Bonoli
Senior Research Scientist, MIT Plasma Science and Fusion Center
Thesis Reader

Accepted by .....
Jacquelyn C. Yanch
Chair, Department Committee on Graduate Theses

Behavior of Lower Hybrid Waves in the Scrape Off Layer of a Diverted Tokamak

by

Gregory M. Wallace

Submitted to the Department of Nuclear Science and Engineering
on November 12, 2009, in partial fulfillment of the
requirements for the degree of
Doctor of Philosophy in Applied Plasma Physics

Abstract

The goal of the Lower Hybrid Current Drive (LHCD) system on the Alcator C-Mod tokamak is to investigate current profile control under plasma conditions relevant to future devices such as ITER and DEMO. This thesis addresses the behavior of Lower Hybrid (LH) waves in the edge and Scrape Off Layer (SOL) of Alcator C-Mod, a compact, high field, high density, diverted tokamak.

The results of coupling experiments over a range of plasma parameters in both L- and H-mode plasmas are presented. Experimental observations suggest that power absorption in the SOL (from both Ion Cyclotron Heating and LHCD sources) modifies the density profile in the vicinity of the LH launcher, thereby affecting the coupling of LH waves.

An analysis of the damage sustained by the LH launcher also shows absorption of the LH waves in the SOL near the antenna. Estimates of the heat flux sustained by the antenna during high power LHCD are in agreement with measurements of the density and temperature increase on flux tubes intersecting the antenna. Power absorption due to high parallel refractive index modes and collisional absorption are not sufficient to explain the increase in density and temperature of the plasma in front of the antenna.

Experimental observations of the LHCD "density limit" for C-Mod are presented. Bremsstrahlung emission and relativistic electron cyclotron emission from fast electrons in the core plasma drop suddenly above line averaged densities of 10^{20} m^{-3}, well below the previously observed density limit. These experimental data are compared to both conventional modeling, which gives poor agreement with experiment above the density limit, and a model including edge collisional absorption, which dramatically improves agreement with experiment above the density limit.

Combined together, these results show that strong absorption of LH waves in the SOL is possible on a high density tokamak. The paradigm of computationally

treating the plasma core and edge as two separate regions with no or weak interaction fails when compared with the C-Mod results. These observations have spurred a shift towards simulating the core and SOL plasma together in predictive simulations of LHCD.

Thesis Supervisor: Ronald R. Parker
Title: Professor, Department of Nuclear Science and Engineering

Thesis Reader: Dennis G. Whyte
Title: Professor, Department of Nuclear Science and Engineering

Thesis Reader: Paul T. Bonoli
Title: Senior Research Scientist, MIT Plasma Science and Fusion Center

Acknowledgments

"Nothing is trivial if it's on fire."

I would first like to thank all the members of the C-Mod LHCD team for their efforts. Dave Terry, Dave Johnson, Dave Gwinn, Pat MacGibbon, Atma Kanojia, and George MacKay have committed themselves to keeping the system running despite numerous difficulties. I'd also like to thank the rest of the engineering and technical staff of C-Mod, in particular Peter Koert and Rui Viera, for their support in moving from design sketches to a functional system. My fellow graduate students are great friends and the best colleagues imaginable. Their assistance was invaluable while I struggled to understand plasma physics and pass my qualifying exams. My "editor," Aaron Bader, has kindly removed all extraneous and erroneous which's from this document. Andréa Schmidt deserves special recognition for being a constant resource in the control room. John Wright has been an immense help with learning the ins and outs of high performance computing, and I am indebted to Bob Harvey and Sascha Smirnov for implementing the SOL model in GENRAY at my request. My thesis adviser, Ron Parker, and my readers, Paul Bonoli and Dennis Whyte, have given me guidance when necessary while allowing me to pursue my own path. I'm lucky to have a great group of friends and family who have supported me through twenty years in the educational system. Finally, I need to thank Kristina for being a constant source of encouragement since I arrived at MIT.

Contents

List of Figures

List of Tables

Chapter 1

Introduction

For much of human history, energy needs have been met in a largely sustainable manner with locally available resources. Heating, cooking, and lighting were provided largely by burning biomass, while transportation needs were met by beasts of burden or wind power. Still, examples exist of resource exhaustion and subsequent societal collapse, such as the *Rapanui* of Easter Island and the Norse settlements on Greenland. With the start of the Industrial Revolution, however, demand for energy to run new machinery rose dramatically. The energy needs of industrialized regions quickly outpaced the rate at which traditional renewable fuels could be replenished, at which point coal and oil were extracted from the earth in ever increasing quantities. Two centuries after the start of the Industrial Revolution, the world's appetite for fossil fuels continues to surge. Estimates for the remaining reserves of oil, natural gas, and coal range from 20-200 years at current rates of consumption (see Table 1.1). In addition to the imminent exhaustion of fossil fuels, the mass release of carbon dioxide and other greenhouse gases into the atmosphere is pushing the earth towards a tipping point beyond which global climate change will be inevitable. As a result of these trends, there has been great interest in using non-fossil fuels for the generation of electricity as it can be easily transported over long distances converted into other forms of useful energy such as heat, light, and mechanical movement.

Table 1.1: World energy reserves [1]. Time remaining is the number of years until the resource is exhausted assuming assuming a usage rate of 500 Quads/y (the estimated 2010 world energy use rate [2]). The time remaining is extended if a combination of multiple fuel sources is utilized.

Resource	Reserves [Quads]	Time remaining [y]
Coal	10^5	200
Oil	10^4	20
Natural Gas	10^4	20
Fission (U^{235})	10^4	20
Fission (U^{238}-Th^{232})	10^7	2×10^4
Fusion (D-T)	10^7	2×10^4
Fusion (D-D)	10^{12}	2×10^9

1.1 Fusion Basics

Many "renewable" sources of energy have found proponents in recent years as the end of fossil fuel reserves looms on the horizon. Wind and solar power are intermittent resources that cannot provide the consistent base load generation necessary to maintain a reliable electric grid. Consequently, intermittent resources cannot exceed approximately 20% of the installed generating capacity without destabilizing the electric grid. Hydroelectric dams can provide steady state electric production with no emissions, however most major rivers in the industrialized world have already been fully tapped for hydroelectric projects. Although hydroelectric electricity production is renewable and does not release any pollutants, it has a substantial negative impact on the river ecosystem by disrupting the natural flow of sediment and interfering with the migration of anadromous fish.

Although not strictly speaking a "renewable" resource, nuclear energy can fill the gap left when fossil fuel sources run out without contributing to climate change. The source of nuclear energy is the strong force inside the nucleus, which is 10^2 times more powerful than the electromagnetic forces which form chemical bonds, and 10^{38} times more powerful than the gravitational forces which generate potential energy. This

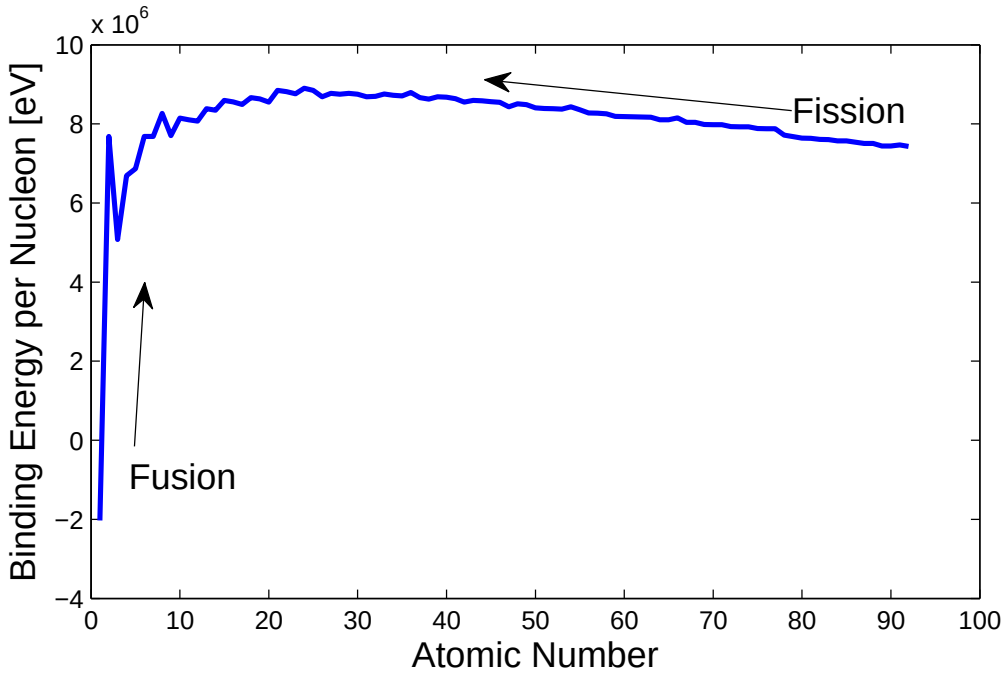

Figure 1-1: Nuclear binding energy per nucleon as a function of atomic number peaks for Fe. The most abundant isotope for each element is plotted [3].

force binds the protons and neutrons in the nucleus together, and is strongest for Fe^{56}. Heavier and lighter elements are less tightly bound, and consequently energy is released when lighter elements combine together (fusion) or heavier elements split apart (fission). Figure 1-1 shows the binding energy per nucleon as a function of atomic number. Fusion is achieved by moving up from the left side of the peak, while fission is achieved by moving up from the right side of the peak.

Nuclear fission, which has for decades been a workhorse of electric utilities, is attractive as a near-term source of energy. Uranium fuel is for the time being still plentiful, and many of the difficult engineering challenges in designing a safe, reliable fission power plant have been solved. Both fission and fusion reactors can in principle provide a steady base load which is not dependent on the weather unlike solar and wind power.

Nuclear fission is not without its downsides, though. Fission byproducts are highly

radioactive with long half-lives, and a suitable long-term storage facility for this waste has not been selected in the United States at this time. In addition, public concern regarding the safety of fission power plants has been a major obstacle to the construction of new facilities, and the proliferation of weapons-grade fissile materials limits the attractiveness of fission power production in less stable regions of the world. As compared to fission, nuclear fusion is very attractive as a long-term energy solution. The byproducts of a fusion reaction have short half lives, mostly on the order of minutes to months, as compared to thousands or millions of years for fission byproducts.

The fuel considered for most fusion reactor studies is comprised of deuterium and tritium. Deuterium is a naturally occurring isotope with a relative abundance of 0.015% of hydrogen on earth. Even though deuterium accounts for a very small fraction of the hydrogen supply, the vast oceans contain enough deuterium to power the world for approximately 10^{12} years. Tritium is not a naturally occurring isotope, however it can be "bred" by bombarding lithium with neutrons to produce helium and tritium.

1.2 Fusion Reactions and Ignition

The positive slope of the curve in Figure 1-1 between H and Fe suggests that several fusion reactions of light elements are possible, however the greatest change in binding energy, and therefore energy release, occurs for the fusing of hydrogen isotopes on the far left end of the curve. Among these are the D-D reaction and the D-T reaction. Other more exotic fusion reactions, such as D-^{3}He and H-^{11}B, exist although the rarity of fuel for these reactions makes them less interesting than the hydrogenic reactions.

The power released in a fusing plasma is

$$P_{fus} = n_a n_b \langle \sigma v \rangle Q_{fus} \tag{1.1}$$

where P_{fus} is the fusion power density, n_a and n_b are the number density of the two

fusing species (for like particle reactions, $n_a n_b = n^2/2$), σ is the cross section of the reaction, v is the relative velocity of the two particles, and Q_{fus} is the energy released per fusion reaction. Here, $\langle \ldots \rangle$ represents an average over a Maxwellian distribution function at a temperature T.

To achieve a self-sustaining chain reaction (a "burning plasma"), it is necessary that the fusion power released to the plasma from the fusion reaction exceed the power lost from the plasma through radiation and conduction. The conditions necessary for thermonuclear fusion were first addressed by Lawson in an initially classified report [4] and later in a published journal [5]. Assuming a D-T fusion reaction, this results in the inequality

$$\begin{aligned} P_{fus} - P_{loss} &\geq 0 \\ n_D n_T \langle \sigma v \rangle Q_\alpha - W/\tau_E &\geq 0 \end{aligned} \tag{1.2}$$

where $Q_\alpha = 3.5$ MeV is the energy of the helium nucleus coming from the D-T fusion reaction. Here we have taken that the energy loss rate from the plasma is equal to the thermal energy stored in the plasma, W, divided by the energy confinement time, τ_E of the plasma. For a thermal plasma

$$W = 3nkT \tag{1.3}$$

which leads to the "Lawson Criterion" [3]

$$n_e \tau_E \geq \frac{12kT}{Q_\alpha \langle \sigma v \rangle} \tag{1.4}$$

where we have assumed $n_D = n_T = n_e/2$. The right hand side of Equation 1.4 has a minimum at 25 keV of approximately 1.5×10^{20} m^{-3}s. The top panel of Figure 1-2 shows $\langle \sigma v \rangle$ as a function of temperature for the D-D, D-T, and D-^{3}He reactions. The bottom panel shows the minimum value of $n\tau$ necessary for ignition as a function of temperature for the D-T reaction. This simple analysis does not include the power

radiated by the plasma through bremsstrahlung which sets a minimum temperature of ~ 4.4 keV for ignition.

There are two primary approaches used to simultaneously achieve the n, τ and T required for ignition. The first approach, inertial confinement, uses a shock-wave to compress a small volume of plasma to extremely high densities and temperatures. This results in a miniature explosion as the plasma burns. Inertial confinement does not lend itself readily to large scale electricity production since it is by its nature a pulsed power source.

As suggested by its name, magnetic confinement fusion uses magnetic fields to confine the fusing plasma. To first order, the Lorentz force on a charged particle moving perpendicular to a magnetic field causes that the particle to gyrate around the field rather than transit across the field. If the magnetic field forms a closed path without intersecting any physical objects, a magnetic surface is created in which the plasma can be confined.

1.3 Tokamaks

To date, the highest performance magnetic confinement concept is the tokamak. The tokamak uses a combination of toroidal, poloidal, and vertical magnetic fields to confine the plasma inside a toroidal vacuum vessel. The toroidal and vertical fields are imposed by external electromagnets, while the poloidal field is generated by a current flowing toroidally through the plasma itself. In the absence of any of these three key magnetic fields, instability will quickly thrust the plasma into the vacuum vessel wall, thereby quenching the plasma and possibly damaging the tokamak.

The combination of a toroidal and poloidal magnetic fields result in a total magnetic field such that any given line of magnetic field will wrap in a helical manner around the torus, and will eventually map out a surface known as a flux surface. If the flux surface intersects a solid structure such as the vacuum vessel, it is called an

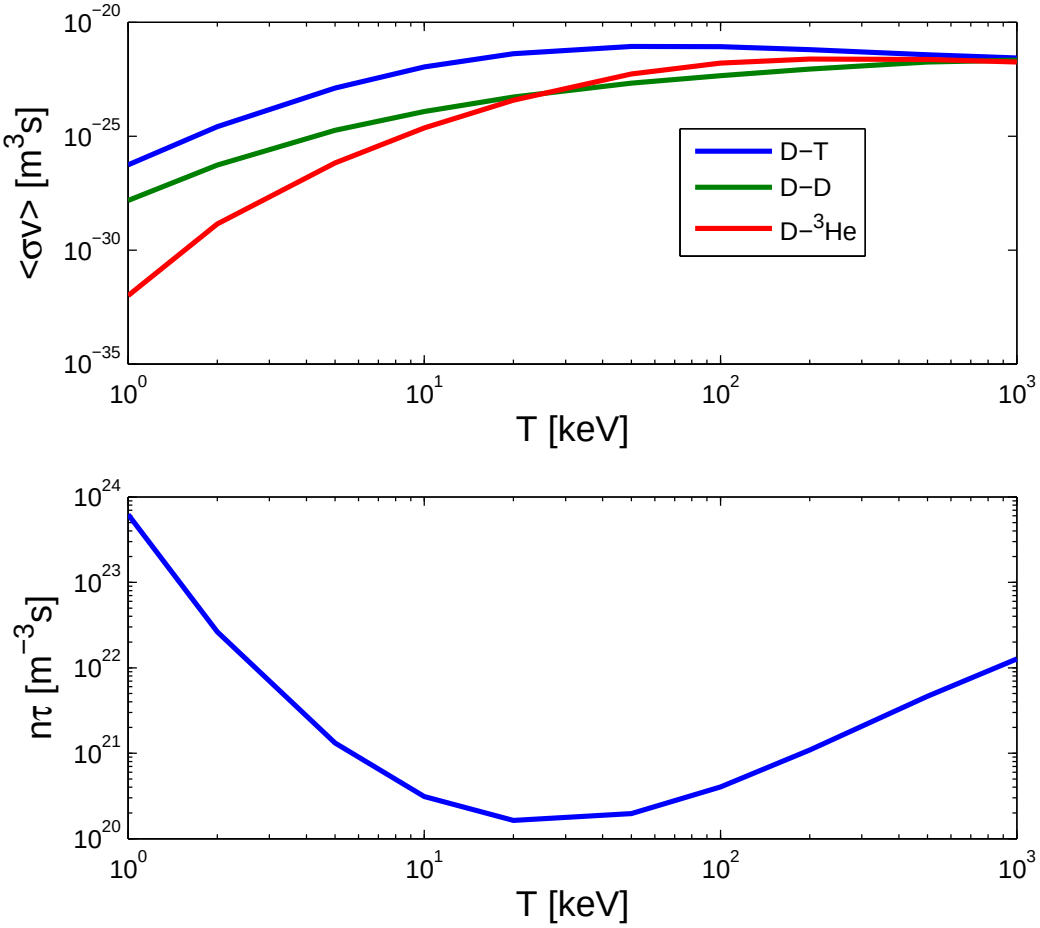

Figure 1-2: Fusion cross sections $\langle \sigma v \rangle$ as a function of temperature for the D-D, D-T, and D-^{3}He reactions [6]. (top) Minimum value of $n\tau$ necessary for ignition as a function of temperature for the D-T reaction. The effect of bremsstrahlung emission is ignored in this calculation. (bottom)

open flux surface, while flux surfaces not contacting a solid structure are closed flux surfaces. The boundary between these two regions is known as the separatrix or last closed flux surface (LCFS). The region of open flux surfaces is commonly referred to as the scrape-off-layer (SOL).

1.4 Current Drive and Steady State Operation

For reliable electricity generation, it is desirable to have a steady-state reactor which can fulfill the base load generation requirements, however the conventional tokamak is an inherently pulsed device. A toroidal current is required to maintain plasma stability, and this toroidal current is typically provided through mutual induction with an electromagnet as the primary coil and the plasma itself as the secondary coil of the transformer. By using the integral form of Faraday's Law, the voltage induced around a closed toroidal contour in the plasma is

$$V_{loop} = \oint_C \vec{E} \cdot d\vec{l} = -\frac{\partial}{\partial t} \iint_S \vec{B} \cdot d\vec{A} = -\frac{\partial \psi}{\partial t} \tag{1.5}$$

To create a steady state toroidal current in the plasma through inductive current drive V_{loop} must be held constant, however it is not possible to maintain a constant $\partial\psi/\partial t$ indefinitely. For a solenoidal electromagnet, $\psi \propto I_{OH}$ where I_{OH} is the current flowing through the transformer magnet and ψ is the magnetic flux through the coils of the magnet. It would therefore require a power supply with no current limit, as well as a magnet which can withstand an infinite current, to sustain a steady state tokamak plasma. In practice, the transformer is run in a "double swing" configuration where the starting current in the magnet is at the negative limit, and the current is then ramped through zero to the positive limit or vice-versa, but this can only increase the maximum pulse length by a factor of 2.

The limitations of a pulsed tokamak can be overcome by the addition of non-inductive current drive mechanisms. Current can be driven non-inductively through

the application of high power neutral beams and microwaves, and even by the plasma itself under the correct conditions.

1.4.1 Neutral Beam Current Drive

Neutral beams can be used as both a source of auxiliary heating and non-inductive current drive in a tokamak. A charged particle beam cannot be used for current drive since the gyromotion of the charged particle will prevent penetration across the magnetic field into the core plasma. Although the physics of beam current drive are relatively simple and robust, the biggest detriment of neutral beams are the size, cost, and complexity of the beams. High energy, high current neutral beams require large structures to accelerate an ionized beam followed by a neutralization process. This neutralization process is not highly efficient and many of the high energy ions are not converted into high energy neutrals.

1.4.2 Microwave Current Drive

Non-inductive current drive can also be achieved with high power microwaves under certain conditions [7]. Electron Cyclotron Current Drive (ECCD) relies on preferentially heating electrons moving in one toroidal direction to create an asymmetry in the resistivity of the plasma.

Lower Hybrid Current Drive (LHCD) utilizes a more direct current drive mechanism. Lower Hybrid (LH) waves are launched in one toroidal direction and directly deposit the wave momentum and energy on electrons traveling roughly in phase with the waves. These electrons, which move at relativistic velocities and are relatively collisionless, can drive a significant current even if they are few in number. The current drive mechanism for LH waves will be discussed in detail later in this chapter.

As compared to ECCD, LHCD has a much higher current drive efficiency as measured in driven current per unit power. This makes LHCD a very desirable means for driving current, however LHCD is not without its drawbacks. Unresolved physics

and engineering issues such as poor edge coupling during ion cyclotron resonance heating (ICRH), loss of current drive efficiency at high density, and survivability of the LHCD antenna still exist. An analysis of these issues comprises the bulk of this thesis.

1.4.3 Bootstrap Current

The "bootstrap current" is a self driven plasma current which requires no external input under the appropriate conditions. The reader may consult a review by Peeters [8] for a complete treatment of the physical process leading to the bootstrap current as only a simple description will be included here. The bootstrap current arises due to the effects of trapped electrons in the presence of pressure gradients in the plasma. As the trapped electrons traverse toroidally, they follow banana-shaped orbits as viewed in the poloidal plane. The electrons travel one direction toroidally on the inside of the banana, and the opposite direction on the outside of the banana. If a density gradient exists in the plasma, there will be a difference in the number of trapped electrons traveling one direction toroidally versus the other at a given point in space, which will generate a net current. By a similar argument, a temperature gradient in the plasma will generate electrons moving faster in one toroidal direction as compared to the opposite, thereby generating a net current. The direction of the current created by these trapped electrons is fortuitously in the same direction as the main plasma current.

Although the bootstrap current is not directly driven by external means, as is the case with NBCD, ECCD, and LHCD, it must be noted that generating the steep pressure gradients necessary to sustain the bootstrap current generally requires the application of external heating, and in practice it is impossible to create a plasma with 100% bootstrap current. Most proposed non-inductive tokamaks rely on bootstrap current for at most 70% of the total current with RF or neutral beams supplying the balance.

1.5 LH Background Physics

The propagation of electomagnetic waves in a plasma can be studied by first considering Maxwell's Equations

$$\nabla \times \vec{E} = -\frac{\partial \vec{B}}{\partial t} \tag{1.6a}$$

$$\nabla \times \vec{B} = \mu_0 \vec{J} + \frac{1}{c^2}\frac{\partial \vec{E}}{\partial t} \tag{1.6b}$$

as well as Ohm's Law

$$\vec{J} = \overline{\overline{\sigma}} \cdot \vec{E} \tag{1.7}$$

where $\overline{\overline{\sigma}}$ is the anisotropic conductivity of the plasma. Equations 1.6a, 1.6b, and 1.7 can be combined to form

$$\nabla \times \nabla \times \vec{E} = -\frac{1}{c^2}\frac{\partial^2 \vec{E}}{\partial t^2} - \frac{\partial}{\partial t}(\mu_0 \overline{\overline{\sigma}} \cdot \vec{E}) \tag{1.8}$$

Assuming variations of the wave field of the form $e^{i(\vec{k}\cdot\vec{x}-\omega t)}$, we can Fourier analyze this equation, taking $\nabla = i\vec{k}$ and $\frac{\partial}{\partial t} = -i\omega$. The equation can thus be simplified to

$$\vec{k} \times \vec{k} \times \vec{E} + i\omega\mu_0 \overline{\overline{\sigma}} \cdot \vec{E} + \frac{\omega^2}{c^2}\vec{E} = 0 \tag{1.9}$$

Substituting

$$\vec{n} = \frac{c\vec{k}}{\omega}$$

into Equation 1.9 results in

$$\vec{n} \times \vec{n} \times \vec{E} + \overline{\overline{\epsilon}} \cdot \vec{E} = 0 \tag{1.10}$$

where

$$\overline{\overline{\epsilon}} \equiv \overline{\overline{I}} + \frac{ic^2\mu_0}{\omega}\overline{\overline{\sigma}} \tag{1.11}$$

which then simplifies to

$$(\vec{n}\vec{n} - n^2\overline{\overline{I}}) \cdot \vec{E} + \overline{\overline{\epsilon}} \cdot \vec{E} = 0 \tag{1.12}$$

By taking $\vec{n} = n_\perp \hat{x} + n_{||}\hat{z}$, Equation 1.10 can be written in matrix form as

$$\begin{pmatrix} \epsilon_\perp - n_{||}^2 & -i\epsilon_\times & n_\perp n_{||} \\ i\epsilon_\times & \epsilon_\perp - n_{||}^2 - n_\perp^2 & 0 \\ n_{||}n_\perp & 0 & \epsilon_{||} - n_\perp^2 \end{pmatrix} \cdot \vec{E} = 0 \tag{1.13}$$

where $\epsilon_\perp$, $\epsilon_\times$, and $\epsilon_{||}$ are the elements of $\overline{\overline{\epsilon}}$

$$\overline{\overline{\epsilon}} = \begin{pmatrix} \epsilon_\perp & -i\epsilon_\times & 0 \\ i\epsilon_\times & \epsilon_\perp & 0 \\ 0 & 0 & \epsilon_{||} \end{pmatrix} \tag{1.14}$$

At this point, it is convenient to derive the elements of the conductivity tensor, $\overline{\overline{\sigma}}$. We begin with momentum conservation for a charged particle in the presence of a magnetic field

$$q(\vec{E} + \vec{v} \times \vec{B}) = m\frac{\partial \vec{v}}{\partial t} \tag{1.15}$$

where q is the (signed) charge of the particle, m, is the mass of the particle, $\vec{v}$ is the velocity of the particle, and $\vec{E}$ and $\vec{B}$ are the electric and magnetic fields. Here we will assume $\vec{E} = \vec{E}_1$, $\vec{B} = \vec{B}_0 + \vec{B}_1$, and $\vec{v} = \vec{v}_1$ where the subscript zero indicates background quantities and the subscript one indicates perturbed quantities. The zeroth order components of the velocity and the electric field are taken to be zero. Again, we can replace $\frac{\partial}{\partial t}$ with $-i\omega$, which leads to

$$q(\vec{E}_1 + \vec{v}_1 \times \vec{B}_0) = -i\omega m \vec{v}_1 \tag{1.16}$$

if we only retain first order quantities. It should be noted that this equation is valid for both ions and electrons. Each must be solved for independently and their

contributions added together. We assume $\vec{B_0} = B_0\hat{z}$ without any loss of generality. Solving for the components of $\vec{v_1}$ results in

$$\begin{aligned} v_{1x} &= \frac{iq}{m\omega}(E_{1x} + v_{1y}B_0) \\ v_{1y} &= \frac{iq}{m\omega}(E_{1y} - v_{1x}B_0) \\ v_{1z} &= \frac{iq}{m\omega}E_{1z} \end{aligned} \tag{1.17}$$

Solving this system of equations results in

$$\begin{aligned} v_{1x} &= \frac{1}{1-\omega_c^2/\omega^2}\left(\frac{iq}{m\omega}E_{1x} - \frac{q^2B_0}{m^2\omega^2}E_{1y}\right) \\ v_{1y} &= \frac{1}{1-\omega_c^2/\omega^2}\left(\frac{iq}{m\omega}E_{1y} + \frac{q^2B_0}{m^2\omega^2}E_{1x}\right) \\ v_{1z} &= \frac{iq}{m\omega}E_{1z} \end{aligned} \tag{1.18}$$

From Equation 1.18 we can form the matrix $\overline{\overline{\sigma}}$ by using the relation that $\vec{J} = \sum nq\vec{v}$

$$\overline{\overline{\sigma}} = \sum \frac{q^2n}{m}\begin{pmatrix} \frac{i\omega}{\omega^2-\omega_c^2} & \frac{-\omega_c}{\omega^2-\omega_c^2} & 0 \\ \frac{\omega_c}{\omega^2-\omega_c^2} & \frac{i\omega}{\omega^2-\omega_c^2} & 0 \\ 0 & 0 & \frac{i}{\omega} \end{pmatrix} \tag{1.19}$$

where the sum is performed over the electrons and all ion species. We can now express the elements of Equation 1.11 as

$$\overline{\overline{\epsilon}} = \begin{pmatrix} 1-\sum\frac{\omega_p^2}{\omega^2-\omega_c^2} & -\sum\frac{i\omega_c\omega_p^2}{\omega(\omega^2-\omega_c^2)} & 0 \\ \sum\frac{i\omega_c\omega_p^2}{\omega(\omega^2-\omega_c^2)} & 1-\sum\frac{\omega_p^2}{\omega^2-\omega_c^2} & 0 \\ 0 & 0 & 1-\sum\frac{\omega_p^2}{\omega^2} \end{pmatrix} \tag{1.20}$$

where $\omega_c = qB/m$ and $\omega_p = \sqrt{nq^2/m\epsilon_0}$.

To find the non-trivial solutions to Equation 1.13, we take the determinant of the

matrix and set it equal to zero. The result is the wave dispersion relation, denoted as

$$D(\omega, \vec{k}) = \begin{vmatrix} \epsilon_\perp - n_{||}^2 & -i\epsilon_\times & n_\perp n_{||} \\ i\epsilon_\times & \epsilon_\perp - n_{||}^2 - n_\perp^2 & 0 \\ n_{||} n_\perp & 0 & \epsilon_{||} - n_\perp^2 \end{vmatrix} = 0 \tag{1.21}$$

If we take $n_{||}$ as a fixed value set at the edge by the antenna structure, we can solve Equation 1.21 for $n_\perp$. This leads to a fourth order bi-quadratic equation for $n_\perp$

$$0 = C_4 n_\perp^4 + C_2 n_\perp^2 + C_0 \tag{1.22}$$

where

$$C_4 = \epsilon_\perp \tag{1.23a}$$

$$C_2 = (n_{||}^2 - \epsilon_\perp)(\epsilon_{||} + \epsilon_\perp) + \epsilon_\times^2 \tag{1.23b}$$

$$C_0 = \epsilon_{||}((n_{||}^2 - \epsilon_\perp)^2 - \epsilon_\times^2) \tag{1.23c}$$

Equation 1.22 can be solved for $n_\perp^2$ using the quadratic equation

$$n_\perp^2 = \frac{-C_2 \pm \sqrt{C_2^2 - 4C_4 C_0}}{2C_4} \tag{1.24}$$

The first (+) root of Equation 1.24 is known as the slow wave, while the second (-) root is the fast wave. These names come from the perpendicular phase velocities of the two waves, $v_{ph\perp} = \omega/k_\perp = c/n_\perp$, which is larger for the fast wave and smaller for the slow wave.

1.5.1 Accessibility

Equation 1.24 shows that distinct slow and fast wave modes can propagate for a single value of $n_{||}$ provided that the discriminant is locally greater than zero. When the two modes are separated and propagating, the accessibility criterion is said to be met.

Figure 1-3 shows the two roots of the cold plasma dispersion relation for typical C-Mod parameters. The $n_{||} = 1.55$ case exhibits a violation of the accessibility criterion when the local electron density reaches 5×10^{19} m^{-3} with a local magnetic field of 5.0 T. At this density, the discriminant approaches zero and the fast and slow wave branches of the dispersion relation coalesce. In this case, a slow wave launched from a lower density region near the edge of the plasma will reflect back as a fast wave, and vice versa. The point at which the discriminant goes to zero is known as the mode conversion layer. Higher values of $n_{||}$ are accessible to higher densities for a given value of magnetic field. Since the slow wave is the desirable branch for current drive (the reason for which will be discussed in Section 1.5.4), it is necessary to prevent the launched waves from reaching any point in the plasma where the accessibility criterion is violated.

The inequality

$$C_2^2 - 4C_4C_0 > 0 \tag{1.25}$$

can be simplified for LH waves with some ordering of the terms in C_4, C_2, and C_0. First, we consider how the launched LH wave frequency, ω, compares to the cyclotron and plasma frequencies for electrons and ions in a tokamak. For ions, $\omega \gg \omega_{ci}$ and $\omega > \omega_{pi}$, while for electrons $\omega \ll \omega_{ce}$ and $\omega < \omega_{pe}$. This allows us to approximate the elements of $\bar{\bar{\epsilon}}$ as $\epsilon_\perp \approx 1 - \omega_{pi}^2/\omega^2 + \omega_{pe}^2/\omega_{ce}^2$, $\epsilon_\times \approx \omega_{pe}^2/\omega\omega_{ce}$, and $\epsilon_{||} \approx -\omega_{pe}^2/\omega^2$, which leads to an ordering $\epsilon_\perp \sim 1$, $\epsilon_\times > 1$, and $|\epsilon_{||}| \gg 1$. We can therefore simplify Equation 1.23 as

$$C_4 = \epsilon_\perp \tag{1.26a}$$

$$C_2 = (n_{||}^2 - \epsilon_\perp)(\epsilon_{||}) + \epsilon_\times^2 \tag{1.26b}$$

$$C_0 = -\epsilon_{||}\epsilon_\times^2 \tag{1.26c}$$

Plugging these values into Equation 1.25 results in

$$\left((n_{||}^2 - \epsilon_\perp)\epsilon_{||} + \epsilon_\times^2\right)^2 > -4\epsilon_\perp\epsilon_{||}\epsilon_\times^2 \tag{1.27}$$

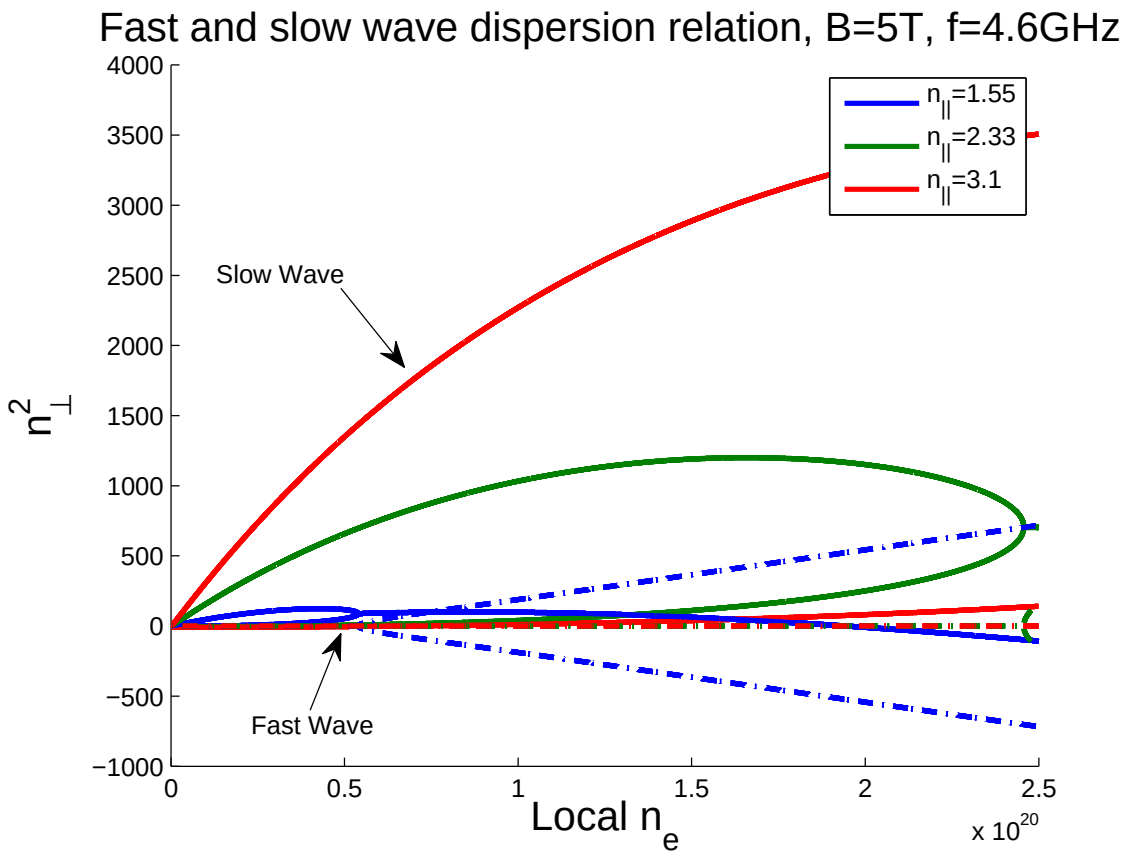

Figure 1-3: LH dispersion relation for $B = 5.0$ T, $f = 4.6$ GHz. Solid lines represent the real part of $n_\perp^2$ while dashed lines represent the imaginary part of $n_\perp^2$.

Solving this equation for $n_{||}^2$ and factoring yields

$$n_{||}^2 > \left(\sqrt{\epsilon_\perp} + \sqrt{-\frac{\epsilon_\times^2}{\epsilon_{||}}} \right)^2 \tag{1.28}$$

Finally, substituting the simplified elements of $\overline{\overline{\epsilon}}$ gives the accessibility criterion as

$$|n_{||}| > \sqrt{1 - \frac{\omega_{pi}^2}{\omega^2} + \frac{\omega_{pe}^2}{\omega_{ce}^2}} + \frac{\omega_{pe}}{|\omega_{ce}|} \tag{1.29}$$

The condition for the accessibility of LH waves was first correctly identified by Golant [9]. Troyon and Perkins [10] derived the approximate accessibility criterion of Equation 1.29. The accessibility profile along the midplane of a hypothetical C-Mod plasma with a parabolic density profile is shown in Figure 1-4.

1.5.2 Wave Launching

Lower Hybrid waves in the low GHz frequency range are often launched from phased arrays of waveguides operating in the fundamental TE_{10} mode. The waveguides are oriented such that the wave electric field in the waveguide is nearly parallel to the background magnetic field in the plasma. For the TE_{10} mode, the wave electric field is directed across the narrow dimension of the waveguide. This orientation of the electric field assures that the slow wave branch of the dispersion relation, for which the wave electric field is also parallel to the background magnetic field, is excited. Multiple waveguides are located in a row with adjacent waveguides separated by a thin septum. The interference of waves launched from each of the waveguides results in an electric field pattern with a characteristic spectrum in $k_{||}$. The $k_{||}$ spectrum can be determined by performing a Fourier transform in real space along the direction of the magnetic field

$$E_z(k_z) = \mathfrak{F}(E_z(z)) \equiv \int_{-\infty}^{\infty} e^{-ik_z z} E_z(z) dz \tag{1.30}$$

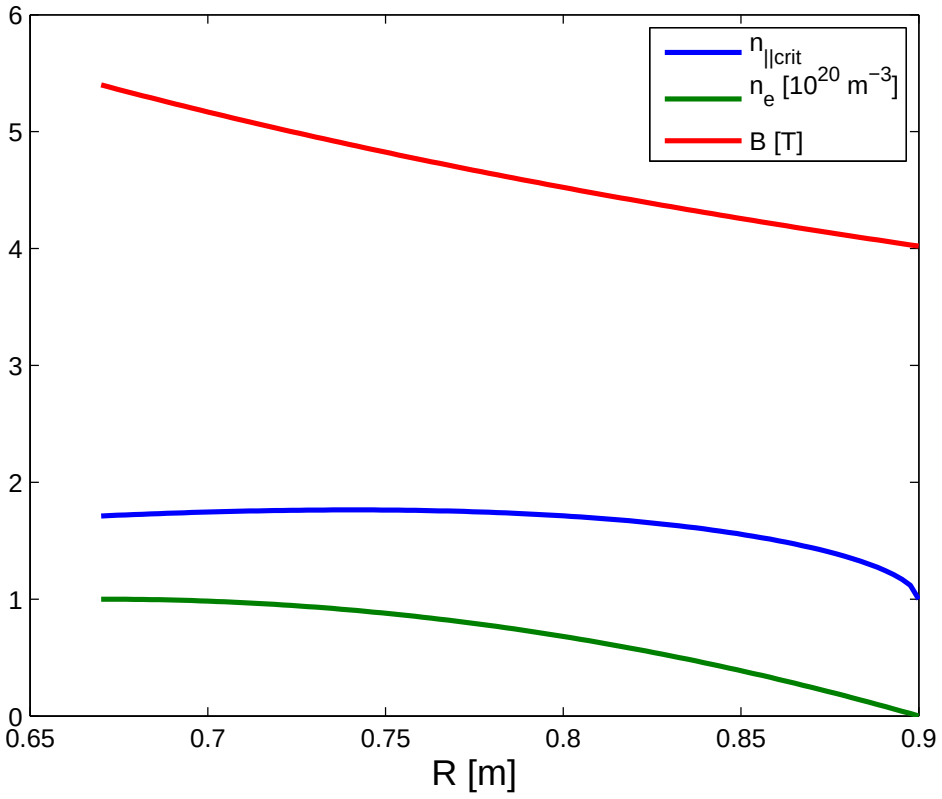

Figure 1-4: Critical $n_{||}$ for LH wave accessibility on the mid-plane of a tokamak as a function of major radius for a parabolic density profile. The magnetic axis is at 0.67 m and the plasma edge is at 0.9 m.

where the magnetic field is in the $\hat{z}$ direction and $f(z)$ is the complex electric field at the waveguide mouth. Taking $n_{||} \equiv ck_z/\omega$, the Fourier spectrum is

$$F(n_{||}) = \int_{-\infty}^{\infty} e^{-in_{||}\frac{\omega}{c}z} f(z)dz \tag{1.31}$$

The electric field at the waveguide mouth can be expressed as a sum of rectangle functions. The rectangle function is a single square pulse of width 1 centered about the origin

$$\text{rect}(x) = u(x + 1/2) - u(x - 1/2) \tag{1.32}$$

where $u(x)$ is the Heaviside function. The electric field is thus

$$E_z(z) = \sum_{j=0}^{N-1} E_j \text{rect}([z - (j(w + \delta) + w/2)]/w)e^{-i\phi_j} \tag{1.33}$$

where E_j is the magnitude of the electric field, w is the waveguide width, δ is the septum width, and ϕ_j is the phase of the electric field. The subscript j refers to the value of the quantity for the j^{th} waveguide. The top panel of Figure 1-5 shows the magnitude and phase of the electric field for a 10 waveguide array with a phase difference between adjacent waveguides of $\pi/2$.

The Fourier transform for a single rectangular pulse of width w centered at $z = 0$ is given by the sinc function

$$\mathfrak{F}(\text{rect(z/w)}) = \frac{\sin(kw/2)}{\sqrt{2\pi}k/2} \tag{1.34}$$

Making use of the property of Fourier transforms that

$$\mathfrak{F}(g(t - a)) = e^{-ia\omega}\mathfrak{F}(g(t)) \tag{1.35}$$

the Fourier transform of Equation 1.33 is

$$E_z(n_{||}) = \sum_{j=0}^{N-1} E_j \frac{\sin(n_{||}\frac{w\omega}{2c})}{\sqrt{2\pi} n_{||}\frac{\omega}{2c}} e^{-i(\beta+\phi_j)} \tag{1.36}$$

where

$$\beta = n_{||}\frac{\omega}{c}(j(w+\delta) + w/2) \tag{1.37}$$

The power spectrum as a function of $n_{||}$ is proportional to $E_z E_z^*$. This gives

$$P(n_{||}) \propto \frac{\sin^2(n_{||}\frac{w\omega}{2c})}{n_{||}^2} \sum_{j=0}^{N-1} E_j e^{-i(\beta+\phi_j)} \sum_{j=0}^{N-1} E_j e^{i(\beta+\phi_j)} \tag{1.38}$$

If the value of E_j is the same for each waveguide, then this term can be moved outside the sum. If we take $\phi_j = j\Delta\phi$, where $\Delta\phi$ is the phase difference between adjacent waveguides in radians, and neglect the $w/2$ term in β (which comes only from an initial shift of position in real space and does not effect the power spectrum), we can rewrite the sum

$$\sum_{j=0}^{N-1} e^{-i(\beta+\phi_j)} = \sum_{j=0}^{N-1} e^{-i(n_{||}\frac{\omega}{c}(w+\delta)+\Delta\phi)j} = \sum_{j=0}^{N-1} e^{-i\alpha j} \tag{1.39}$$

Making use of the identity

$$\sum_{j=1}^{N} x^j = x\frac{1-x^N}{1-x} \tag{1.40}$$

the sum can be eliminated. This results in a power spectrum

$$P(n_{||}) = P_0 \frac{\sin^2(n_{||}\frac{w\omega}{2c})}{n_{||}^2} \frac{\sin^2(N\alpha/2)}{\sin^2(\alpha/2)} \tag{1.41}$$

where

$$\alpha = \left(\Delta\phi + n_{||}\frac{\omega}{c}(w+\delta)\right) \tag{1.42}$$

and P_0 is a normalization constant. The power spectrum for a 10 waveguide array is

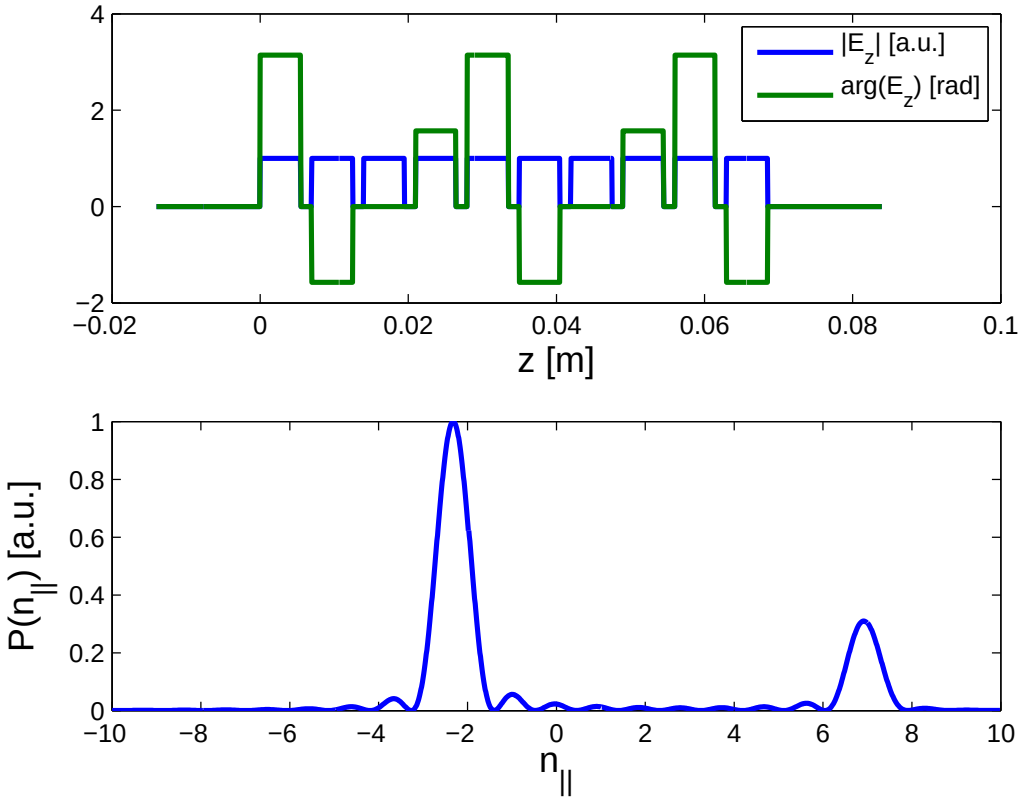

Figure 1-5: Amplitude and phase of electric field for the forward wave in an LH launcher with 10 waveguides. Waveguide width is 0.0055 m and septum width is 0.0015 m. The phase difference between adjacent waveguides is $\pi/2$. (top) Fourier transform of the top panel showing the $n_{||}$ spectrum. (bottom)

shown in the bottom panel of Figure 1-5. A convenient formula for the peak of the $n_{||}$ spectrum is

$$n_{||} = \frac{c\Delta\phi}{2\pi f(w+\delta)} \tag{1.43}$$

By adjusting the phase difference between adjacent waveguides, the peak of the spectrum can be tuned to a desired value. It should be noted that this treatment is valid only for the ideal case where there is no variation in amplitude nor errors in phasing among the waveguides. Slight differences in the low amplitude sidebands of the spectrum can result from these imperfections.

1.5.3 Wave Damping

The cold plasma treatment of Lower Hybrid waves treats propagation without introducing any losses. However, a hot plasma treatment of the plasma including the effects of finite electron temperature results in both propagation and damping of the waves. This hot plasma description includes the effects of wave-particle resonances, which lead to imaginary components of the dispersion relation and therefore wave damping. For the purposes of current drive with LH waves, Landau damping is the dominant absorption mechanism. Landau damping is a collisionless damping process by which charged particles and waves traveling with nearly the same phase velocity parallel to the magnetic field exchange energy and momentum. In principle, Landau damping is possible for both electrons and ions, however the ion absorption rate is typically negligible due to their lower thermal velocity.

To derive the hot plasma dispersion relation, we follow a similar procedure as for the cold plasma case, however we take the current to be the moment of the distribution function

$$\vec{J} = n_0 \iiint \left(q_e \vec{v} f_i(\vec{v}) + q_e \vec{v} f_e \vec{v}\right) d^3\vec{v} \tag{1.44}$$

where $f_i(\vec{v})$ and $f_e(\vec{v})$ are the normalized distribution functions for ions and electrons, and q_m is the charge of species m. We now will examine how these distribution functions are perturbed by the waves, beginning with a Maxwellian distribution function

$$f_0 = \frac{1}{(2\pi)^{3/2} v_t^3} e^{-\frac{v_\perp^2 + v_{||}^2}{2v_t^2}} \tag{1.45}$$

where $v_t = \sqrt{T/m}$ is the thermal velocity. This distribution function is valid for both electrons and ions. We then consider a linearized Vlasov equation

$$\frac{\partial}{\partial t} f_1 + \vec{v} \cdot \nabla f_1 + \frac{q}{m} \vec{v} \times \vec{B}_0 \cdot \nabla_v f_1 = \frac{q}{m} \left(E_1 + \vec{v} \times \vec{B}_1\right) \cdot \nabla_v f_0 \tag{1.46}$$

where $f = f_0 + f_1$ is the distribution function including the unperturbed and perturbed

components. Again, this is valid for both ions and electrons. This equation can be solved by integrating particle orbits along $\vec{B}_0$. The result is used in the derivation of the dispersion relation, which separates into real and imaginary parts $D(\omega, \vec{k}) = D_r(\omega, \vec{k}) + iD_i(\omega, \vec{k})$ [11]. The real part of D is identical to the cold plasma dispersion relation except for the addition of a $n_\perp^6$ term. The imaginary part of D contains two terms, the first of which is due to electrons and the second of which is due to ions

$$D_i = 2\sqrt{\pi}\left(\frac{\omega_{pe}^2}{\omega^2} n_\perp^2 n_{||}^2 x_e^3 e^{-x_e^2} + \frac{\omega_{pi}^2}{\omega^2} n_\perp^4 x_i^3 e^{-x_i^2}\right) \tag{1.47}$$

where $x_e = \omega/(\sqrt{2}k_{||}v_{te})$ and $x_i = \omega/(\sqrt{2}k_{||}v_{ti})$. It is this imaginary part of D which gives rise to the damping of the LH waves. It can be seen that, except for very slow waves or very hot ions, $x_i \ll 1$ and therefore the ions will not contribute substantially to the damping process. To solve for the imaginary part of $k_\perp$, we make a Taylor expansion of D around $k_{\perp r}$

$$D(\omega, \vec{k}) = D(\omega, k_{\perp r}) + (k_\perp - k_{\perp r})\frac{\partial D}{\partial k_{\perp r}} + \ldots = 0 \tag{1.48}$$

Since both $k_\perp$ and D are both complex quantities, we can rewrite this expansion as

$$D_r + iD_i + ik_{\perp i}\frac{\partial D_r}{\partial k_{\perp r}} - k_{\perp i}\frac{\partial D_i}{\partial k_{\perp r}} + \ldots = 0 \tag{1.49}$$

The real and imaginary parts of this equation can be set to zero and be solved for $k_{\perp r}$ and $k_{\perp i}$. The fourth term in Equation 1.49 is second order and is therefore negligible. Assuming we have a normal mode of the system $D_r(k_{\perp r}, \omega) = 0$, the expression for $k_{\perp i}$ is

$$k_{\perp i} = -\frac{D_i}{\partial D_r/\partial k_{\perp r}} \tag{1.50}$$

Substituting the cold plasma dispersion relation for D_r into the denominator and

making use of $\epsilon_\perp \sim 1$ and $\epsilon_{||} \sim -\omega_{pe}^2/\omega^2$ results in

$$k_{\perp i} = \sqrt{\pi}\frac{\omega_{pe}}{c} n_{||} x_e^3 e^{-x_e^2} \tag{1.51}$$

The maximum of $k_{\perp i}$, and thus the strongest damping, is located at $x_e = \sqrt[3]{2}$, or approximately $\omega/k_{||} = v_{te}$. For an electric field which varies as $E_0 \exp(i\vec{k} \cdot \vec{x})$, the power carried by the wave will decay exponentially as $\exp(-2k_{\perp i}x)$, we can set the condition for strong absorption in a tokamak, $k_{\perp i}a > 1$, where a is the minor radius of the plasma. Figure 1-6 shows the imaginary part of $k_\perp^{-1}$ due to Landau damping as a function of $n_{||}$ and T_e. A value for $k_{\perp i}$ of 10^{-2} m corresponds to 86% of the wave power absorbed in 1 cm of propagation perpendicular to the magnetic field, which would be strong single-pass absorption for C-Mod where $a \sim 20$ cm. For a temperature of 2 keV, this requires $n_{||} \geq 4$. This condition can also be expressed as a general rule of thumb that the temperature in keV must be greater than $30/n_{||}^2$ for strong single pass damping.

1.5.4 Current Drive Efficiency

The total current driven in the plasma is the first moment of the distribution functions for ions and electrons, however we will neglect the contribution from ions. Ions have a much lower velocity as compared to electrons which makes their contribution small. We then have

$$J_{||} = q \int_{-\infty}^{\infty} v_{||} f_{||}(v_{||}) dv_{||} \tag{1.52}$$

where $J_{||}$ is the current density parallel to the magnetic field, and $f_{||}(v_{||})$ is the electron distribution as a function of $v_{||}$. For a distribution function symmetric about $v_{||} = 0$, there is obviously no net current. We have already indicated in the preceding section that the distribution function is modified in the region near $\omega/k_{||} \sim v_{||}$, which leads to an asymmetric distribution function with a net $J_{||}$ if the waves are launched preferentially in one direction with respect to the magnetic field.

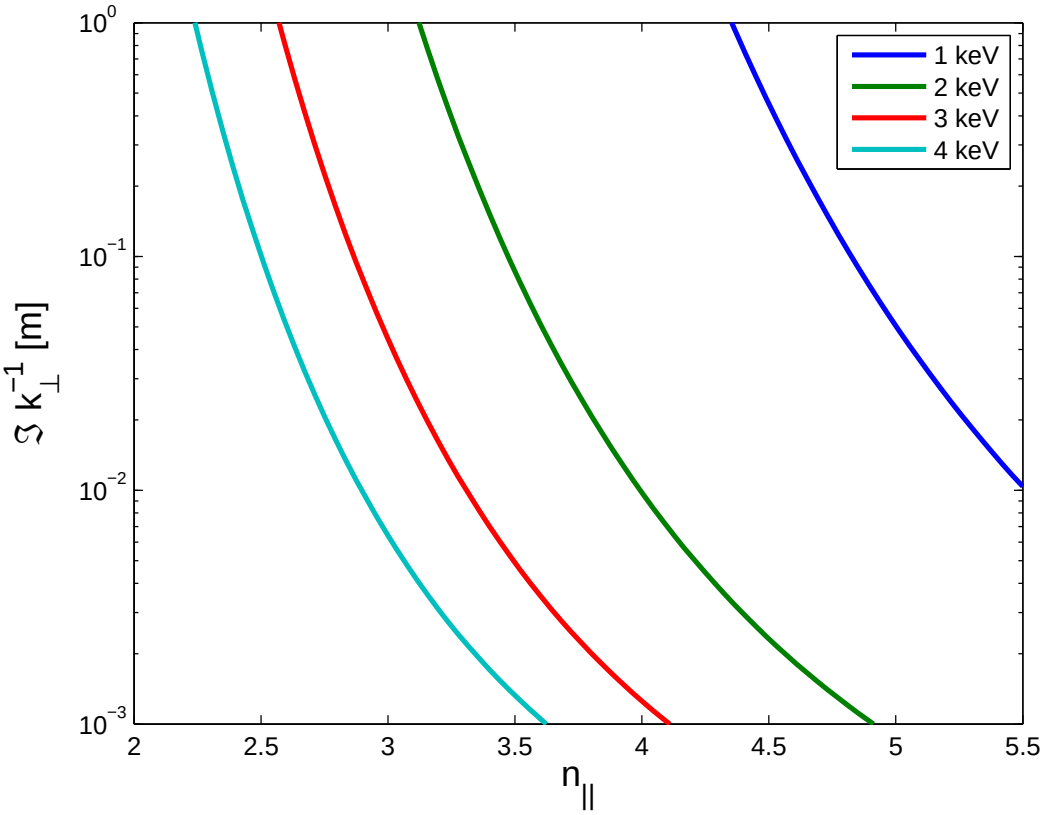

Figure 1-6: Landau damping e-folding length for LH waves as a function of T_e and $n_{||}$. A value for $k_{\perp i}$ of 1×10^{-2} m corresponds to 86.4% of the wave power absorbed in 1 cm of propagation perpendicular to the magnetic field.

As discussed in Section 1.4.2, LHCD is highly very efficient as compared with other non-inductive current drive mechanisms. The following estimate of current drive efficiency is based on the argument of Fisch in *Reviews of Modern Physics* [7]. Current drive efficiency can be quantified as the ratio of the current driven to the power dissipated. This ratio can be expressed locally as $J_{||}/P_d$. In a simple model, the current driven by the lower hybrid waves is carried by a small population of electrons, δf, which is displaced in velocity space from $v_{||}$ to $v_{||} + \delta v_{||}$. Assuming that the remainder of the distribution function is symmetric about $v_{||} = 0$, the net driven parallel current is

$$J_{||} = q\delta v_{||}\delta f \tag{1.53}$$

Moving these electrons in velocity space requires an amount of energy, δE, equal to

$$\delta E = \frac{m_e \delta f}{2}(v_{||} + \delta v_{||})^2 - \frac{m_e \delta f}{2} v_{||}^2 \approx m_e \delta f v_{||} \delta v_{||} \tag{1.54}$$

for $\delta v_{||} \ll v_{||}$. These fast electrons have a finite lifespan prior to slowing down due to collisions with the background plasma. The power necessary to sustain a steady state population of fast electrons can be estimated as the energy input per electron multiplied by the collision frequency of the electrons

$$P_d = \nu(v)\delta E = m_e \nu(v) v_{||} \delta f \delta v_{||} \tag{1.55}$$

where $\nu(v)$ is the electron collision frequency and P_d is the local power deposition per unit volume. We can now show that the efficiency is

$$\frac{J_{||}}{P_d} = \frac{q}{m_e v_{||} \nu(v)} \tag{1.56}$$

This would suggest that more current can be driven with low $v_{||}$ electrons, however we have not considered the contribution of $\nu(v)$. Most of the electrons in the population δf have $v_{||} \gg v_{\perp}$, and we can approximate $\nu(v) \sim \nu(v_{||})$. Since $\nu \propto n_e v^{-3}$, Equation

1.56 can be rewritten as

$$\frac{J_{||}}{P_d} \propto \frac{v_{||}^2}{n_e} \tag{1.57}$$

If these electrons are resonant with the parallel phase velocity of the lower hybrid wave, $v_{||} = c/n_{||}$, we get a scaling that

$$\frac{J_{||}}{P_d} \propto \frac{1}{n_e n_{||}^2} \tag{1.58}$$

A more rigorous analysis of LHCD efficiency includes the effect of both direct momentum input and energy input [12]. The end result is

$$\frac{J_{||}}{P_d} = \frac{4}{5 + Z_{eff}} \frac{\hat{s} \cdot \nabla_v (w u^3)}{\hat{s} \cdot \nabla_v u^2} \tag{1.59}$$

where $\hat{s}$ is the direction of velocity space displacement of the electrons, ∇_v is the gradient in velocity space, $w = v_{||}/v_{te}$, and $u = v/v_{te}$. The surprising consequence of Equation 1.59 is that the current arising from energy input is three times the size of the term arising from momentum input.

Efficiency is typically compared between different tokamaks and current drive schemes using the figure of merit nIR/PT. Here, n is the line averaged density, I is the total plasma current, R is the major radius of the torus, and P is the net power used for current drive. This figure of merit comes from approximating that the driven current, and the power deposited, are distributed uniformly throughout an incremental area ΔA. This leads to

$$I_p = \Delta A J_{||} \tag{1.60a}$$

and

$$P = \Delta V P_d = 2\pi R \Delta A P_d \tag{1.60b}$$

where ΔV is the toroidal volume associated with ΔA. If we solve these expressions

for $J_{||}$ and P_d, we can show that

$$\frac{J_{||}}{P_d} = \frac{2\pi IR}{P} \tag{1.61}$$

If we renormalize $J_{||}$ and P_d to their thermal values

$$\tilde{J} = \frac{J_{||}}{n_e e v_{te}} \tag{1.62a}$$

$$\tilde{P}_d = \frac{P_d}{n_e m_e v_{te}^2 \nu_0} \tag{1.62b}$$

we get

$$\frac{\tilde{J}}{\tilde{P}_d} = \frac{m_e v_{te} \nu_0}{e} \frac{J_{||}}{P_d} \tag{1.63}$$

Using

$$\nu_0 = \frac{\omega_{pe}^4 \ln \Lambda}{2\pi n_e v_{te}^3} \tag{1.64}$$

and combining Equations 1.61 and 1.63 results in

$$\eta = \frac{nIR}{PT_e} \tag{1.65}$$

where η is the normalized current drive efficiency, frequently expressed in units of 10^{20}A/(W m^2 keV). Values of $\eta \sim 0.1$ are typical for LHCD on tokamaks.

1.6 Ray Tracing, Full Wave, and Fokker-Planck Simulation Codes

Self-consistent modeling of LH waves in a tokamak plasma is a difficult undertaking requiring the iterative use of two simulation codes. The first code determines the location of the waves in the plasma, either by ray tracing or through a full-wave approach. The wave code is used to evaluate the RF diffusion coefficient which is

then used in the Fokker-Planck solver to calculate the perturbed electron distribution function. Since the absorption of the waves, and consequently the wave electric field strength, is a function of the electron distribution, the perturbed distribution function is then passed back to the wave code, which recalculates the quasi-linear diffusion coefficient with the new distribution function. The process is repeated until the result converges.

Two methods are used to determine the propagation and damping of the waves in the plasma. The ray tracing approach makes use of WKB and geometrical optics approximations to represent waves as packets of photon energy traversing through the plasma. A series of "rays" are launched to approximate the wave-number spectrum produced by a three-dimensional antenna structure. These rays are independently followed through the plasma until they reach a damping threshold, at which point the ray is terminated. This approach is computationally simple but is fundamentally limited by the WKB approximation, which requires changes in wave characteristics to occur on scales long compared to the wavelength.

Another approach is to solve Maxwell's Equations numerically. This correctly treats physical phenomena not addressed by ray tracing such as partial reflections, interference, and scattering, but at a substantial computational cost. To properly resolve the waves, the grid size and/or mode resolution used in the numerical method must be adequate to resolve the shortest wavelength in the system.

1.6.1 GENRAY

The GENRAY ray tracing package allows for the simulation of electromagnetic and electrostatic waves in a plasma medium through the use of the geometrical optics approximation [13]. The following outline of ray tracing derives from discussion in Landau and Lifshitz [14] and Weinberg [15].

First, we must introduce the concept of a "wave surface." A wave surface is a two dimensional surface on which the amplitude and phase of a propagating electromag-

netic wave remain nearly constant over the distance of a wavelength. This allows for a plane wave approximation. On a wave surface, we can represent the electric and magnetic fields as follows

$$\vec{E} = \vec{E}_0 e^{iS(\vec{x},t)} \tag{1.66a}$$

$$\vec{B} = \vec{B}_0 e^{iS(\vec{x},t)} \tag{1.66b}$$

where

$$S(\vec{x}, t) \tag{1.67}$$

is the eikonal, or phase, of the wave. On each wave surface, the normal vector to the surface represents the direction of propagation of the wave. A series of wave surface normals on successive wave surfaces forms a "ray" which defines the path of the wave.

For geometricical optics to be a valid approximation, the following relations must be satisfied

$$\left| \lambda \frac{1}{\vec{E}_0} \frac{\partial}{\partial \vec{x}} \vec{E}_0 \right| \ll 1 \tag{1.68a}$$

and

$$\left| \lambda \frac{1}{\vec{B}_0} \frac{\partial}{\partial \vec{x}} \vec{B}_0 \right| \ll 1 \tag{1.68b}$$

which are the requirements for a WKB approximation.

The eikonal S can be expanded in a Taylor Series as

$$S \simeq S_0 + \vec{x} \cdot \frac{\partial S}{\partial \vec{x}} + t \frac{\partial S}{\partial t} + \ldots \tag{1.69}$$

Then by analogy with plane waves we can write

$$S = S_0 + \vec{k} \cdot \vec{x} - \omega t \tag{1.70}$$

where

$$\vec{k} = \frac{\partial S}{\partial \vec{x}} \tag{1.71a}$$

$$\omega = -\frac{\partial S}{\partial t} \tag{1.71b}$$

Next consider an electromagnetic wave that satisfies the local dispersion relation

$$|\bar{\bar{D}}| \equiv D_0(\vec{x}, \vec{k}, \omega) = 0 \tag{1.72}$$

We can construct ray paths $\vec{x}(\tau)$, $\vec{k}(\tau)$, $\omega(\tau)$, and $t(\tau)$, where τ is a parameter representing the distance traveled along a ray path. These paths must satisfy the initial conditions

$$\begin{aligned} \vec{x}_0 &= \vec{x}(\tau_0) \\ \vec{k}_0 &= \vec{k}(\tau_0) \\ \omega_0 &= \omega(\tau_0) \\ t_0 &= t(\tau_0) \\ \nabla \times \vec{k}(\tau_0) &= 0 \\ D_0(\vec{x}_0, \vec{k}_0, \omega_0, t_0) &= 0 \end{aligned} \tag{1.73}$$

Using the theory of characteristics it was shown by Weinberg [15] that the phase space solution of a wave that simultaneously satisfies Equation 1.73 is given by the ray equations

$$\frac{d\vec{x}}{d\tau} = \frac{\partial D_0}{\partial \vec{k}} \tag{1.74a}$$

$$\frac{d\omega}{d\tau} = \frac{\partial D_0}{\partial t} \tag{1.74b}$$

$$\frac{d\vec{k}}{d\tau} = -\frac{\partial D_0}{\partial \vec{x}} \tag{1.74c}$$

$$\frac{dt}{d\tau} = -\frac{\partial D_0}{\partial \omega} \tag{1.74d}$$

If we take $\partial D_0/\partial t = 0$, we can use the chain rule to change from the step parameter τ to time t

$$\frac{d}{d\tau} = \frac{d}{dt}\frac{dt}{d\tau} = -\frac{\partial D_0}{\partial \omega}\frac{d}{dt} \tag{1.75}$$

This leads to

$$\frac{d\vec{x}}{dt} = -\frac{\frac{\partial D_0}{\partial \vec{k}}}{\frac{\partial D_0}{\partial \omega}} \tag{1.76a}$$

$$\frac{d\vec{k}}{dt} = \frac{\frac{\partial D_0}{\partial \vec{x}}}{\frac{\partial D_0}{\partial \omega}} \tag{1.76b}$$

GENRAY utilizes this framework to follow the ray trajectories for lower hybrid waves in an axisymmetric toroidal system. When calculated in the traditional manner, rays are launched from inside the edge of the plasma, and are allowed to propagate until they have damped beyond a user defined threshold. If the rays traverse to the edge of the plasma prior to fully damping, then they are reflected either off of a cutoff layer (if the density profile is such that a cutoff exists inside the plasma) or an artificial perfect conductor located at the plasma edge. The edge of the plasma is defined by the last closed flux surface from the EQDSK equilibrium file generated by EFIT.

GENRAY was recently modified to extend ray trajectories into the SOL, which was motivated in large part by the experimental observations detailed in Chapter 5. This new version of GENRAY allows the rays to propagate outside the separatrix provided that the local plasma density exceeds the cutoff density and includes a two dimensional SOL profile for plasma density and a one dimensional SOL profile for plasma temperature. The temperature and density profiles consist of exponentially decaying profiles based on the distance from a point in the SOL to the separatrix, with the e-folding length chosen by the user. The e-folding length for density may be defined as a function of poloidal angle.

1.6.2 Full Wave Solvers

As opposed to the geometrical optics approach used in ray tracing, the full wave computational approach directly solves for the solutions to Maxwell's Equations using a carefully chosen basis set. Frequently spectral decomposition is used to simplify the

problem along periodic dimensions such as the poloidal and toroidal directions in a torus, while finite elements are used in the non-periodic directions, such as the minor radius in a torus. The full wave approach attempts to solve a boundary value problem as opposed to the initial value problem of ray tracing. Boundary conditions on the wave electric field are specified on a surface surrounding the computational domain, and then the wave fields are computed everywhere inside that domain. The boundary can be arbitrarily defined to contain part or all of the plasma, even including the SOL and regions of zero density. Unlike the ray tracing approach, which does not treat evanescent waves, the full wave approach allows for finite, though exponentially decaying, fields in regions where the plasma density is below cutoff. Also, the full wave approach properly treats wave behavior in regions where the WKB approximation is not satisfied such as a dielectric mismatch or the pedestal of an H-mode.

1.6.3 CQL3D

To self-consistently calculate the damping profile with ray tracing or a full wave code, it is necessary to solve the Fokker-Planck equation, which determines the quasi-linear electron distribution function in the presence of RF wave fields.

As the name suggests, CQL3D (Collisional Quasi-Linear 3D) [16, 17] solves the Fokker-Planck equation for a quasi-linear distribution function in 3 dimensions. To reduce the problem from seven dimensions ($f(\vec{x}, \vec{v}, t)$ to four dimensions ($f(\rho, \vec{v})$), the distribution is "bounce averaged" over the toroidal motion of the electrons, which leads to toroidal and flux surface symmetry. This assumption can be justified when the bounce time, τ_b, is short compared to the collision time, τ_c, as is the case in the "banana regime." The problem can be further reduced as $\tau_c \gg \omega_c^{-1}$, which leads to particle velocities that are isotropic in $v_\perp$. The simplified distribution function is then $f(\rho, v_\perp, v_{||})$.

The basis for CQL3D is the Fokker-Planck Equation

$$\frac{df}{dt} = RF + C \tag{1.77}$$

where RF is the term relating to the modification of f by the radio frequency (RF) wave and C is the term relating to the collisional relaxation of the distribution function. The solution to this equation is a distribution function where the effects of the RF waves and of collisions are balanced, resulting in a steady state. The RF term in one dimension is

$$RF = \frac{\partial}{\partial v_z} D(v_z) \frac{\partial}{\partial v_z} f_{e0} \tag{1.78}$$

where we have assumed $\hat{b} = \hat{z}$ for simplicity. The term $D(v_z)$ is the RF quasilinear diffusion coefficient [18]. The one-dimensional quasilinear diffusion coefficient is determined by solving the Vlasov equation in one dimension while neglecting collisions

$$\frac{\partial f_e}{\partial t} + v_z \frac{\partial f_e}{\partial z} - \frac{e}{m_e} E_z \frac{\partial f_e}{\partial v_z} = 0 \tag{1.79}$$

The distribution function f_e is assumed to be

$$f_e(v_z, z, t) = f_{e0}(v_z, t) + f_{e1}(v_z, z, t) \tag{1.80}$$

where

$$f_{e0}(v_z, t) = \lim_{L \to \infty} \frac{1}{L} \int_{-L}^{L} f_e(v_z, z, t) dz \equiv \langle f_e \rangle \tag{1.81}$$

We also assume that the electric field, E_z, is a first order quantity, $E_1(z, t)$. Taking the spatial average of Equation 1.79 results in

$$\frac{\partial f_{e0}}{\partial t} = \frac{e}{m_e} \frac{\partial}{\partial v_z} \langle E_1 f_{e1} \rangle \tag{1.82}$$

Using $f_e = f_{e0} + f_{e1}$ in Equation 1.79 yields

$$\frac{\partial f_{e1}}{\partial t} + v_z \frac{\partial f_{e1}}{\partial z} - \frac{e}{m_e} E_1 \frac{\partial f_{e0}}{\partial v_z} = \frac{e}{m_e} \frac{\partial}{\partial v_z} \left(E_1 f_{e1} - \langle E_1 f_{e1} \rangle \right) \tag{1.83}$$

At this point, we can solve for f_{e1} by eliminating second order terms and assuming that f_{e1} varies in time and space proportional to $\exp(i(k_z z - \omega t))$. This results in

$$f_{e1} = \frac{(ie/m_e)E_1}{\omega - k_z v_z} \frac{\partial f_{e0}}{\partial v_z} \tag{1.84}$$

Inserting this into Equation 1.82 yields

$$\frac{\partial f_{e0}}{\partial t} = \frac{\partial}{\partial v_z} \left\langle \frac{ie^2}{m_e^2} \frac{E_1^2(z,t)}{\omega - k_z v_z} \right\rangle \frac{\partial f_{e0}}{\partial v_z} \tag{1.85}$$

with

$$D(v_z) = \left\langle \frac{ie^2}{m_e^2} \frac{E_1^2(z,t)}{\omega - k_z v_z} \right\rangle \tag{1.86}$$

The collisional term, C, of Equation 1.77 can be determined by examining the scattering of fast test electrons from a fixed background of thermal electrons and ions [19, 20]. This results in

$$C = \frac{\partial f_{e0}}{\partial t} = \frac{2 + Z_{eff}}{2} \frac{\partial \nu(v_z)}{\partial v_z} \left(v_e^2 \frac{\partial}{\partial v_z} + v_z \right) f_{e0} \tag{1.87}$$

where

$$\nu(v_z) = \nu_0 \left(\frac{v_e}{v_z} \right)^3 \tag{1.88}$$

and

$$\nu_0 = \frac{\omega_{pe}^4 \log(\Lambda)}{2\pi n_e v_e^3} \tag{1.89}$$

CQL3D uses the ray data from GENRAY to evaluate Equation 1.86. A perturbed distribution function is then numerically determined on each flux surface. The non-Maxwellian distribution function from CQL3D is then used to recalculate

the damping of the rays and the process is repeated until the damping profile and distribution function converge. The perturbed distribution function is used to determine the driven current profile, fast electron bremsstrahlung and electron cyclotron emission emissivity, and other quantities of interest to compare with experimental measurements.

Although the GENRAY code has been extended to include the SOL in the model, the assumption of flux surface symmetry in CQL3D prevents its application to the SOL. As a consequence, changes in the distribution function (and therefore current drive and fast electron bremsstrahlung) of the SOL are not calculated.

1.7 A Note on the International System of Units

Unless otherwise noted, the units used in this thesis conform to the International System of Units (SI). Frequent exceptions to the use of SI units are in the measurement of temperature and power, which are often expressed in eV and kW, respectively.

1.8 Thesis Outline and Summary of Results

This thesis addresses the behavior of Lower Hybrid waves in the edge and scrape off layer of a diverted tokamak. Chapter 2 gives an overview of the Alcator C-Mod tokamak on which the experimental results were obtained. A detailed description of the C-Mod Lower Hybrid Current Drive system is also included.

Chapter 3 gives an overview of the theory of LH wave coupling and describes experiments conducted to maximize the coupling efficiency of the C-Mod LHCD system. The results of coupling experiments over a range of plasma parameters in both L- and H-mode plasmas are presented. Experimental observations suggest that power absorption in the SOL (from both ICRF and LHCD) modifies the density profile in the vicinity of the LH launcher, thereby affecting the coupling of LH waves.

Chapter 4 contains an analysis of modifications to the edge plasma by high power LH waves and the damage sustained by the LH launcher as a result. Estimates of the heat flux sustained by the antenna during high power LHCD are in agreement with measurements of the density and temperature increase on flux tubes intersecting the antenna. Calculations of power absorption due to high $n_{||}$ modes and collisional absorption are not sufficient to explain the increase in density and temperature of the plasma in front of the antenna.

Experimental observations of the LHCD "density limit" for C-Mod are presented in Chapter 5. The density limit observed on C-Mod is not associated with a violation of the accessibility criterion nor parametric decay instabilities, which have been identified on prior experiments as causes of the LHCD density limit. Bremsstrahlung emission and relativistic electron cyclotron emission from fast electrons in the core plasma drop suddenly above line averaged densities of 10^{20} m^{-3}. Electric currents measured in the Scrape Off Layer increase simultaneously with the drop in X-ray emissivity. These currents are associated with a large increase in plasma density at the ion collecting end of the open field lines. These experimental data are compared to both conventional modeling, which gives poor agreement with experiment above the density limit, and a model including edge collisional absorption, which dramatically improves agreement with experiment above the density limit.

Combined together, the results of Chapters 3 through 5 show evidence that strong absorption of LH waves in the SOL is possible on a high density tokamak. The paradigm of computationally treating the plasma core and edge as two separate regions with no interaction fails when compared with the C-Mod results. These observations have spurred a shift towards simulating the entire plasma, including regions of open and closed flux surfaces, in predictive analysis of LHCD.

Chapter 2

Alcator C-Mod

Alcator C-Mod [21] is the third experiment in the Alcator series of tokamaks at the MIT Plasma Science and Fusion Center (PSFC). C-Mod is a compact, high field, high density device with properties similar to that of ITER, but on a smaller scale. Although designed as a diverted tokamak, limited discharges are also possible. C-Mod normally operates in upper single null, lower single null, or double null configuration. A cryopump in the upper divertor in conjunction with feedback controlled gas capillaries provide density control. Auxiliary heating is provided by ICRF antennas on D-, E-, and J-ports for a total of 6 MW at 50-80 MHz [22]. A diagnostic neutral beam (DNB) with a beamline nearly perpendicular to the magnetic field provides a source of fast neutral particles for use with other diagnostic techniques. Due to its low power level, the DNB provides negligible amounts of heating and torque to the plasma. Figure 2-1 shows a top-down schematic of the tokamak with the locations of key heating and diagnostic systems on the horizontal ports.

Typical C-Mod discharge lengths are $\sim$ 2 seconds. Pulsed power for the magnet coils is provided by a dedicated dipole alternator attached to a 60 ton flywheel spinning at 1800 rotations per minute (60 Hz). The alternator/flywheel system is used to minimize the pulsed load on the electric grid during discharges. A delay of 10-15 minutes between discharges is necessary to cool the copper magnet coils back to their

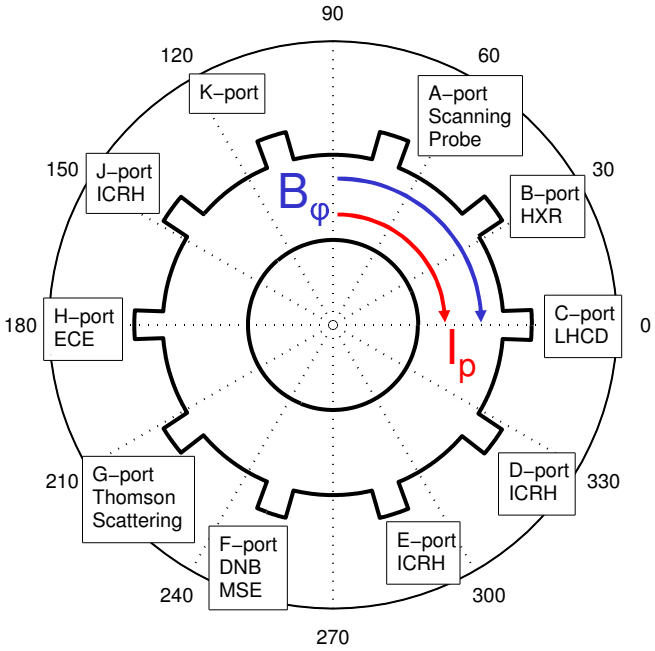

Figure 2-1: Top-down view of the location of C-Mod horizontal ports. Key heating and diagnostic systems are labeled at their respective ports. The direction of the toroidal magnetic field and plasma current are clockwise in normal operation.

Table 2.1: Alcator C-Mod Device Parameters

R_0	0.67 m
a	0.2 m
B_T	3-8 T
Wall Material	Mo, W
Net P_{ICRF}	6 MW
Net P_{LH}	1.2 MW
I_p	0.3-1.5 MA
$\bar{n}_e$	$0.1 - 5 \times 10^{20}$ m^{-3}
t_{pulse}	1-3 s

starting temperatures and for the vacuum pumps to reduce the torus pressure to the pre-shot level of $10^{-4} - 10^{-5}$ Pa. The cooling delay also allows for the alternator to recoup energy dissipated in the magnet coils during the discharge. A summary of device parameters for C-Mod is found in Table 2.1.

2.1 Lower Hybrid Current Drive System

The LHCD system on C-Mod was designed to provide 3.0 MW of source power with precise control of the launched $n_{||}$ spectrum at a frequency of 4.6 GHz [22, 23]. Design and manufacture of the system was conducted as a joint effort between the MIT PSFC and the Princeton Plasma Physics Laboratory (PPPL), with engineers and scientists from both organizations involved at all levels of the process. The LH antenna consists of 4 rows of 24 active waveguides located on C-port. Each of the 12 klystrons, capable of providing 250 kW for 5 seconds, is split between two adjacent columns of 4 waveguides. The $n_{||}$ spectrum can be shifted from 1.5-3.1 on a timescale of 1 millisecond, although changing from current-drive to counter-current or heating phasing requires a cell access to adjust mechanical phase shifters. The LHCD system can be divided into three subsystems: power generation, power delivery, and vacuum components. The power generation subsystem consists of the 12 klystron amplifiers and the power supplies and control systems related to their operation. The power

delivery subsystem is a series of waveguide components which delivers the power from the 12 klystrons to the 96 waveguides at the plasma edge. The vacuum components consist of the parts of the LHCD system which interface directly with the plasma and the interior of the vacuum vessel.

2.1.1 Klystrons and Control System

The LHCD power on C-Mod is provided by 12 Varian Associates (now Communications and Power Industries) klystron amplifiers, originally manufactured in 1979-1980 for the Alcator C LHCD experiment [24]. Each klystron is capable of producing a nominal 250 kW under CW operation, however the pulse length for the C-Mod system is limited to 5 seconds by the high voltage power supply (HVPS) manufactured by Thales Broadcast and Multimedia AG [25]. The klystrons are mounted on "carts" in groups of 4 for a total of 3 carts. Each cart shares a connection to the HVPS, and the high voltage input to the different klystrons on each cart is regulated as a group. Each klystron is individually protected by an optical arc detector with a line of sight to the klystron output window. A circulator for each klystron protects the tube from reflected power. The circulators consist of both new, water cooled units made specifically for the C-Mod LHCD system by Advanced Ferrite Technologies and several surplus air cooled Raytheon units from the Alcator C system. Directional couplers monitoring forward and reflected power at the output of each klystron provide voltage standing wave ratio (VSWR) protection of the klystrons in the event that the circulator does not provide proper isolation.

The dominant factor in determining the $n_{||}$ spectrum launched by the LHCD antenna is the relative phasing between waveguide columns. To make accurate changes in launched $n_{||}$ possible on a fast timescale electronic control of both the amplitude and the relative phase of each klystron is required. A master oscillator provides an input signal to twelve vector modulators (VM), each of which provides the low power RF drive for an individual klystron. The VMs can change the amplitude and phase

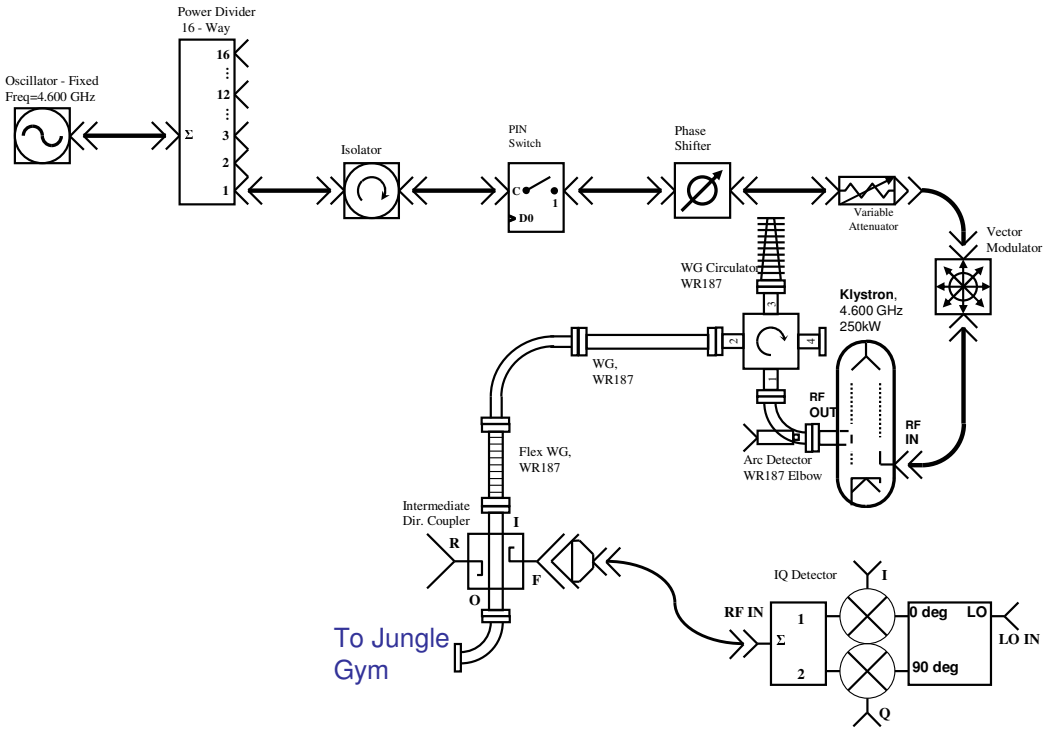

Figure 2-2: Schematic of LH system drive leg.

of the input drive for each transmitter on a sub-millisecond timescale. The phase and amplitude of each klystron output is monitored by an I/Q detector, which measures the in-phase (I) and quadrature-phase (Q) components of the forward wave. The forward wave is measured by the Intermediate Directional Couplers (IDCs) at the input to the "Jungle Gym" structure described below. Figure 2-2 shows a schematic diagram for a single klystron channel of the LHCD control system.

Arc protection for the klystrons is handled by the Transmitter Protection System (TPS), while arc protection for the splitting network and vacuum windows is handled by the Coupler Protection System (CPS). While the two-stage protection system has some advantages, such as protection of the transmitters during test shots without the

need to override features of the CPS, the main disadvantage is a limitation on the maximum safe pulse length. When the TPS encounters a fault condition, the HVPS is tripped in order to protect the klystrons from damage. Although this is obviously the best way to protect the klystrons, re-energizing the HVPS after a trip requires several seconds, by which time the discharge is complete. Since the CPS detects faults that are physically far removed from the klystrons, the klystrons are in no immediate danger. To make fast restrikes possible, the CPS is not designed to trip the HVPS. When the CPS detects a fault, the RF drive to the klystrons is cut via the VMs and the PIN switches, however the klystron remains energized and the full beam energy is deposited in the collector in the absence of RF drive. If the RF drive remains off for more than 500 ms, there is substantial risk that water in the cooling channels will boil and internal components will be damaged by overheating. Since there is no provision in the CPS to trip the HVPS, pulse lengths must be limited to 500 ms to prevent damage to the klystrons.

2.1.2 Waveguide Splitting Network

The antenna design chosen for C-Mod is a fully active system with a high degree of isolation between both the rows and the columns of the antenna. As compared with a "multi-junction" type antenna, used on experiments at Tore Supra [26], JET [27, 28], and JT-60U [29], the $n_{||}$ spectrum of this antenna is highly flexible and is not adversely effected by waves making multiple bounces through the power splitting network. In the C-Mod LHCD system, each pair of columns is driven by a single klystron. Although there is real-time control of the phase difference between klystrons, the phase difference between adjacent columns fed by the same klystron is set by a manually adjustable mechanical phase shifter. The antenna can be switched from current-drive phasing to either heating or counter-current phasing by adjusting the mechanical phase shifters.

Power is transmitted from the klystrons to the splitting network with conventional

Table 2.2: Waveguide Properties [30].

Type	TE_{10} Cutoff [GHz]	Inner Dimensions [m]	Loss [dB/m]
WR187 Rigid Copper	3.152	0.04755×0.02215	0.04
WR187 Flex Copper	3.152	0.04755×0.02215	0.4
WR187 Rigid Aluminum	3.152	0.04755×0.02215	0.04
Reduced Height Aluminum	3.152	0.04755×0.0055	0.4
Reduced Height Copper Plated Steel	2.49	0.060×0.0055	0.4

WR187 copper waveguide. Since the klystrons and circulators are located in a fixed position while the launcher and splitting network move radially in and out, short flexible "accordion" waveguides are needed to prevent stressing the rigid waveguide where it interfaces with the moving launcher assembly. Table 2.2 summarizes the properties of the waveguide used for transmission from the waveguides.

Figure 2-3 shows a view of the assembled waveguide splitting network known as the "Jungle Gym." The Jungle Gym is comprised of WR187 waveguide components including directional couplers, "Magic-T" splitters, "Pant Leg" splitters, DC breaks, and gas pressure breaks. Figure 2-4 shows a schematic of the splitting network of the Jungle Gym. Also included in the Jungle Gym are the mechanical phase shifter assemblies. The LHCD launcher was originally assembled with commercially available phase shifters that relied upon a screw mechanism to move a plunger in a waveguide stub, thereby adjusting the phase through the component. During the FY2008 campaign these components were identified as a source of arcing and were replaced by custom phase shims designed and manufactured in house. The custom phase shims require several hours to adjust from current-drive phasing to counter-current or heating phasing as compared to only a few minutes to adjust the original phase shifters. However, the breakdown limit increased from 900 kW to 1200 kW with the new phase

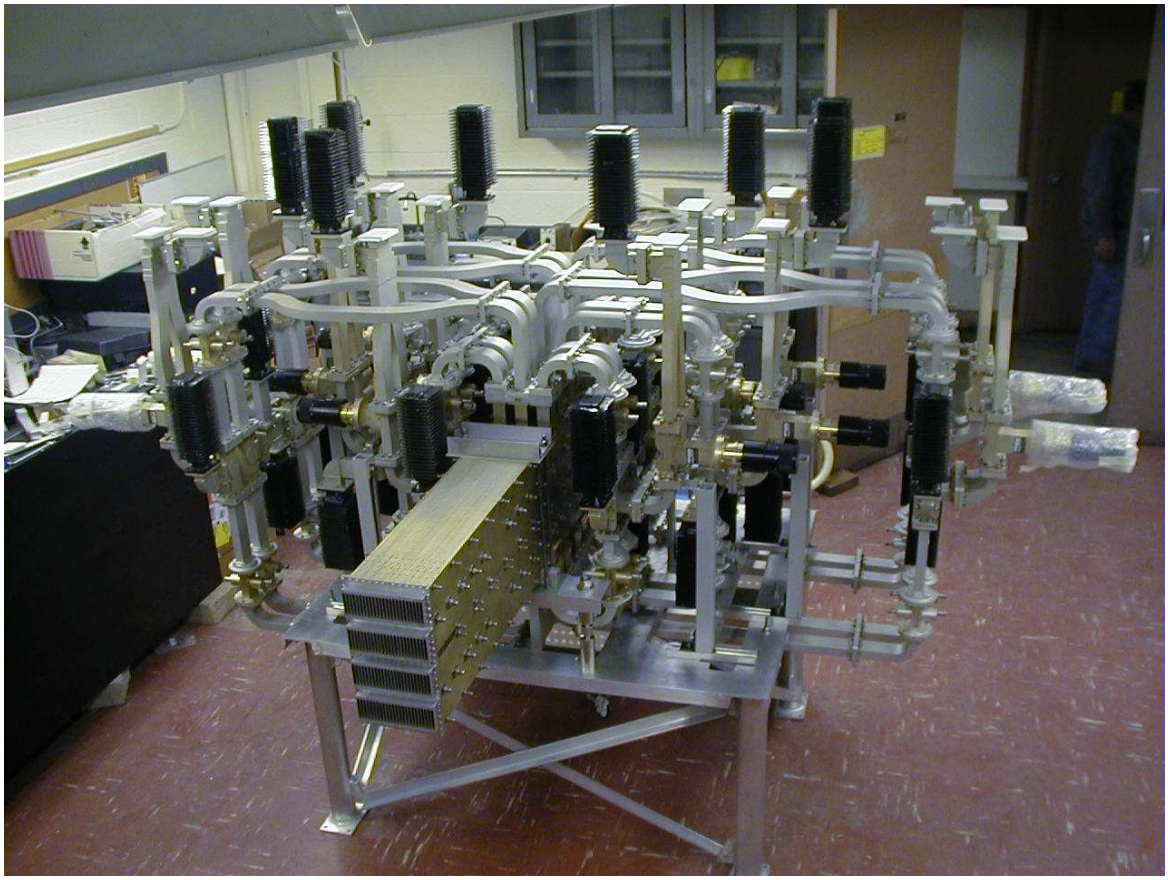

Figure 2-3: C-Mod LHCD "Jungle Gym" and RWA. Power from 12 klystrons is fed into the "Pant Leg" splitters at the top of the Jungle Gym and split eight ways into the 96 waveguides seen at the RWA/FWA interface in the foreground of the picture.

shifters. Since operation with counter-current or heating phasing is rare, the extra time required to adjust the phase shifters had no detrimental impact on the operation of the LHCD system.

The first two 3-dB splitters are located in the Jungle Gym assembly and consist of commercially available WR187 components. The Pant Leg splitters first divide the power between adjacent columns, then the Magic-T's divide the power between the top half and bottom half of the launcher. After this, the waveguides feeding the top and bottom halves of each column transition through a transformer into the reduced height waveguide of the rear waveguide assembly (RWA). As was shown in

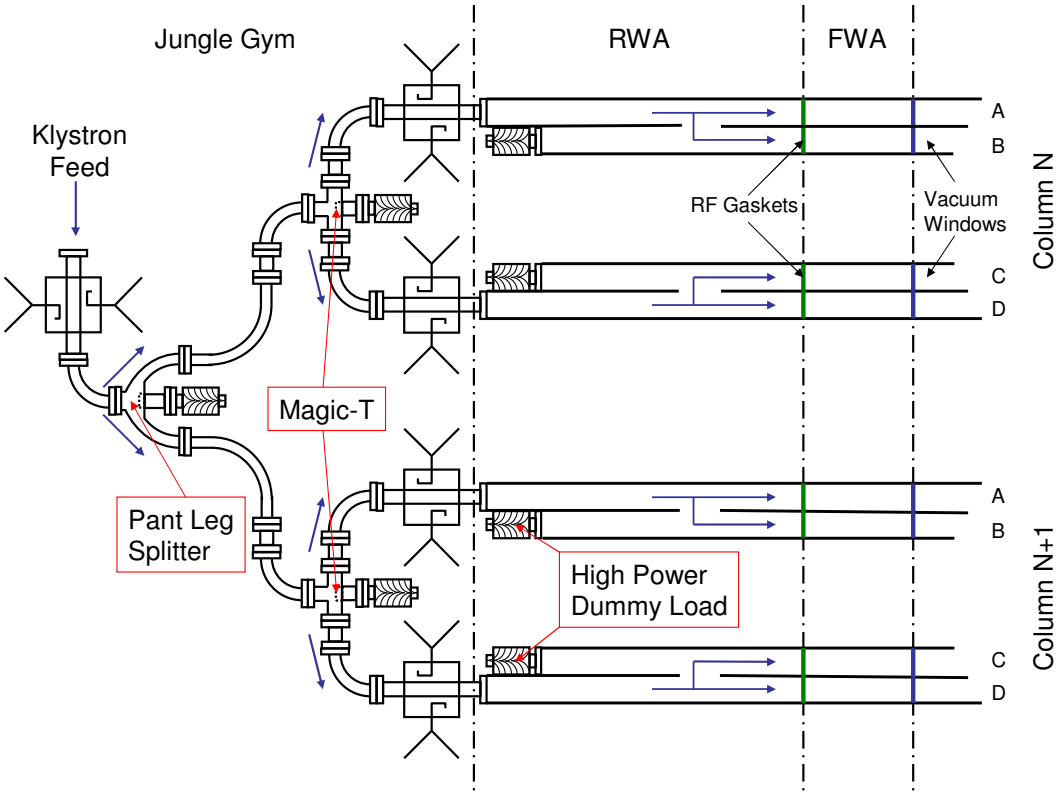

Figure 2-4: Schematic diagram of the Jungle Gym, rear waveguide assembly, and forward waveguide assembly. The power from each klystron is split between 4 rows and 2 columns.

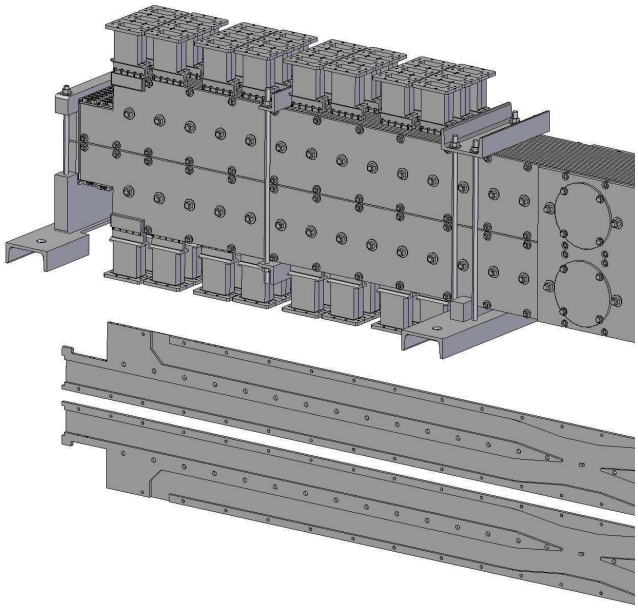

Figure 2-5: Computer model of the rear waveguide assembly. The completed assembly (top) consists of individual plates (bottom) stacked together to create the waveguides. A 3-dB splitter is machined into each of the plates.

Section 1.5, the height of the waveguides in a LHCD grill must be reduced in order to provide the desired $n_{||}$ spectrum. In the case of the C-Mod LHCD system, the height is reduced from the standard 0.02215 m of the WR187 to 0.0055 m. The RWA is comprised of a set of stacked aluminum plates, with each plate having a set of channels machined into the surface such that, when the plates are secured together, waveguides are formed by the "C" shaped channel pressing against the flat surface of the adjacent plate. A final 3-dB splitter is machined into the RWA plates for a final 8-way split of the power from each klystron. Figure 2-5 shows the waveguide channels and 3-dB splitter machined into the stacked plates of the RWA.

The RWA is in turn connected to the Forward Waveguide Assembly (FWA). The FWA serves as a transmission link between the RWA and the Grills. The Grills are the short section of waveguide on the vacuum side of the window that directly interface with the plasma. To increase the strength of the FWA and to reduce the eddy current forces during disruptions, the FWA is manufactured from copper plated stainless steel because steel is both stronger and more resistive than copper or aluminum, thereby reducing the risk of damage due to disruption forces. The FWA includes a taper in the broad dimension of the waveguide from 0.04755 m to 0.0600 m, which is the final dimension at the plasma interface. The location of the taper is adjusted on the top and bottom rows to achieve zero poloidal phasing. The FWA is constructed with the same stacked-plate method as the RWA. Considerable difficulty was experienced in aligning the FWA and RWA where the two meet end-to-end. Because the tolerances in the thickness of each plate add up when stacking 25 plates together, the final dimensions of the FWA and RWA mating surfaces are not exactly equal. With the center waveguides aligned, waveguides on the extremes of the assembly show a misalignment of $\sim$0.001 m out of a waveguide width of only 0.0055 m. An aluminum RF gasket with a "V" shaped knife edge along the center of each waveguide wall is sandwiched between the FWA and RWA, however exact alignment of the gasket with the two waveguides, each of which is slightly different in overall dimension, is not possible. Inevitably the gasket protrudes into the waveguides due to the dimensional mismatch between the FWA and RWA. Figure 2-6 shows a boroscope picture of arc damage to the RF gasket caused by this misalignment.

2.1.3 Grill and Limiters

The pressurized FWA couples with the vacuum vessel via the shroud and "grills." The shroud provides a vacuum seal around the pressurized FWA, and also serves as additional support and shielding to protect the FWA from damage due to eddy current forces. A bellows system at the connection between the port extension and

Figure 2-6: Arc damage at the RWA/FWA interface due to misalignment of the gasket. The copper shaded region in the upper left is the FWA, and the silver region in the lower right is the RWA. The gasket runs diagonally through the picture. This view is from the bottom of column 23, row C looking up along the broad wall of the waveguide. Splatter from melting of the gasket can be seen on the RWA.

the shroud allows the shroud to move radially in and out of the vacuum vessel with the other launcher components. The launcher is pulled back to its maximum extent of 0.03 m behind the LH limiters when not in use to avoid damage during disruptions and to prevent coating of the windows during boronization. The four waveguide grills were manufactured out of 304L stainless steel blocks using an electron discharge machining (EDM) process. 24 individual waveguides were EDM-ed into each grill, and a half wavelength aluminum oxide (Al_2O_3) vacuum window was brazed into each waveguide. Each waveguide is machined to a size of 0.0055 m by 0.060 m with a 0.0015 m septum between adjacent guides. The front face of each grill is machined with the appropriate poloidal and toroidal curvature to match the LH limiter shape including the effects of the toroidal field ripple.

Due to the nonuniform expansion of the windows and grill during the brazing process, the windows in the first and last waveguides of each of the four grills developed cracks in the outer corners. Consequently, these waveguides were cut short and fitted with stainless steel plugs, reducing the size of the coupler array to 4×22 waveguides. The grills are joined to the FWA with the same RF gasket system as for the connection of the FWA to the RWA. Consequently, the grill to FWA connection suffers from the same tolerance stacking issues as the RWA to FWA connection. Despite the issues associated with window brazing and aligning the grill to FWA interface, operation of the stainless steel couplers has been relatively trouble free.

The original grill design used a titanium block in which the waveguides were EDM-ed. Titanium was chosen as a material both for its low secondary electron emission coefficient (to reduce the risk of multipactoring) and also because the thermal expansion coefficient of titanium closely matches that of the alumina windows. These titanium grills suffered from catastrophic damage following a reaction of the titanium surface with deuterium gas during an atmospheric pressure backfill, which created a brittle titanium deuteride compound. The titanium grills disintegrated into titanium deuteride dust and the LH launcher was removed from the tokamak. Except for

melting to the septa at the plasma interface, which will be discussed in detail in Chapter 4, the stainless steel grills showed no damage after 3 run campaigns.

The LH launcher on C-Mod is protected by dedicated limiters on either side of the launcher. The limiter tiles are made of molybdenum and shaped to provide protection to the launcher for a wide range of plasma shapes. The LH limiters are fixed in position inside the vacuum vessel, and consequently, the amount by which the limiters protrude beyond the launcher can be varied. It is also possible to insert the launcher proud of the limiters, thereby eliminating the effect of the limiters. Figure 2-7 shows the LH launcher in its fully retracted position.

2.2 Diagnostics

Alcator C-Mod is a well diagnosed tokamak with multiple independent measurements of critical plasma parameters such as temperature and density. The line integrated plasma density, $\bar{n}_e$, is measured by the two color interferometer (TCI) system at a rate of 5 kHz. The line integrated current measurement from TCI is used in the feedback control of the plasma density. The Thomson Scattering diagnostic provides profiles of the electron density and temperature in the core and pedestal regions at a rate of 30 Hz. Other quantities of interest, such as plasma current, rotation velocity, and radiation are directly measured as well. Magnetics measurements allow for real-time reconstruction of the magnetic equilibrium with EFIT, which is complimented by a Motional Stark Effect diagnostic for determining the pitch angle of the magnetic field line in the plasma. Descriptions of several key diagnostics for the analysis presented in this thesis are included in the following sections. A complete overview of the C-Mod diagnostic systems can be found in a review by Basse [31].

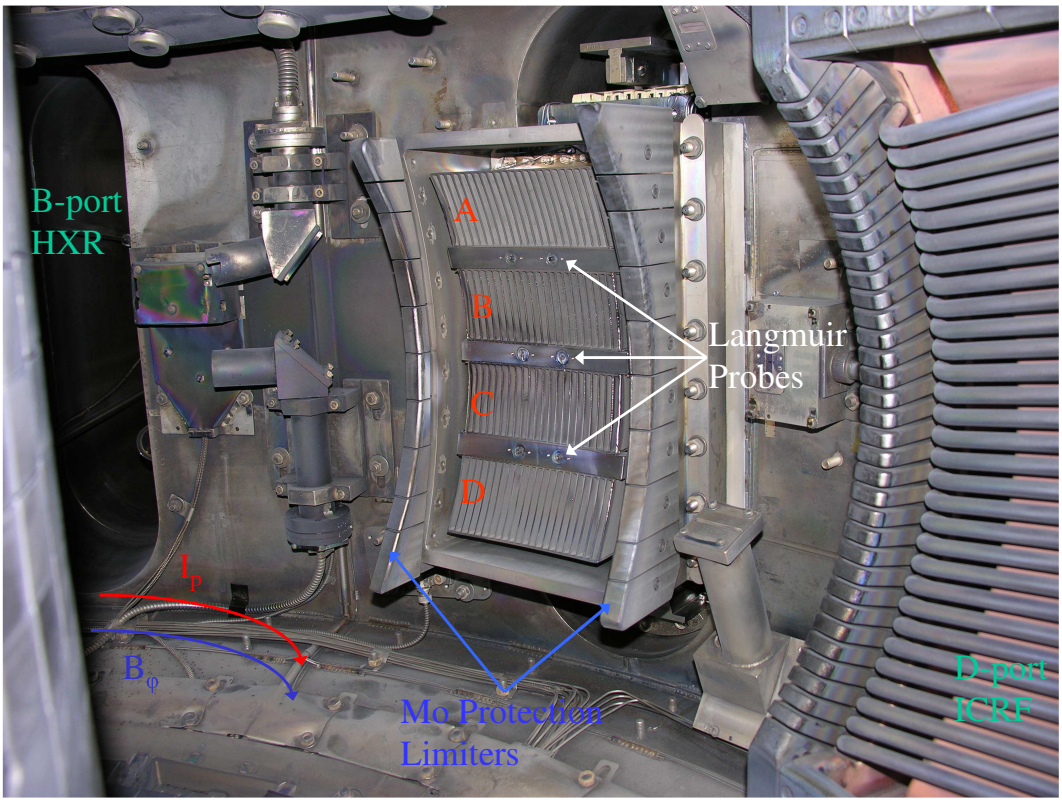

Figure 2-7: View of the LH launcher as installed on C-port. The launcher is in its fully retracted position in this photo. Waveguide rows A through D are labeled in red. Column number descends from 23 to 2 counting from left to right from this perspective.

2.2.1 Hard X-ray Camera

The Hard X-Ray camera (HXR) measures bremsstrahlung x-rays emitted by non-thermal electrons as they decelerate due to collisions with other charged particles [32, 33]. The HXR camera uses 32 detectors arranged in a fan configuration around a pinhole on the B-port horizontal flange. The viewing chords for all 32 chords are shown in Figure 2-8. Each channel consists of a cadmium zinc telluride (CZT) detector, preamp, shaper, and digitizer. The current created by an X-ray photon hitting the detector is amplified by the preamp, then shaped into a Gaussian waveform by the shaper, and then digitized at 10 MHz. The raw pulse data is then analyzed to determine the energy and time of each incident photon. This system allows the raw pulse information to be re-binned after each discharge allowing for photon counting statistics to be balanced against time and energy resolution.

2.2.2 Electron Cyclotron Emission

The Electron Cyclotron Emission (ECE) diagnostic measures second harmonic cyclotron emission from electrons gyrating in a magnetic field. For thermal electrons in an optically thick plasma, the frequency of the emitted radiation is proportional to the local magnetic field through the cyclotron relationship $\omega_{ce} = \frac{qB_0}{m_e}$, while the intensity of the emission is proportional to the temperature. The $1/R$ dependence of the magnetic field allows localization of the measurement for thermal electron populations. The radiation is downshifted by a factor of $\sqrt{1 - v_e^2/c^2}$ for relativistic electrons due to the increase in electron mass as $v_e \rightarrow c$. A qualitative measure of the non-thermal electron population can be made by looking at frequencies for which $2\omega_{ce}$ would correspond to large radii near or outside the plasma edge. At these frequencies there is negligible contribution from the thermal electrons and the measured emission is due to the radiation from non-thermal electrons at indeterminate locations. Figure 2-9 shows the cyclotron frequencies for a 5.4 T C-Mod discharge. The dashed lines indicate downshifted radiation from relativistic electrons in the plasma core.

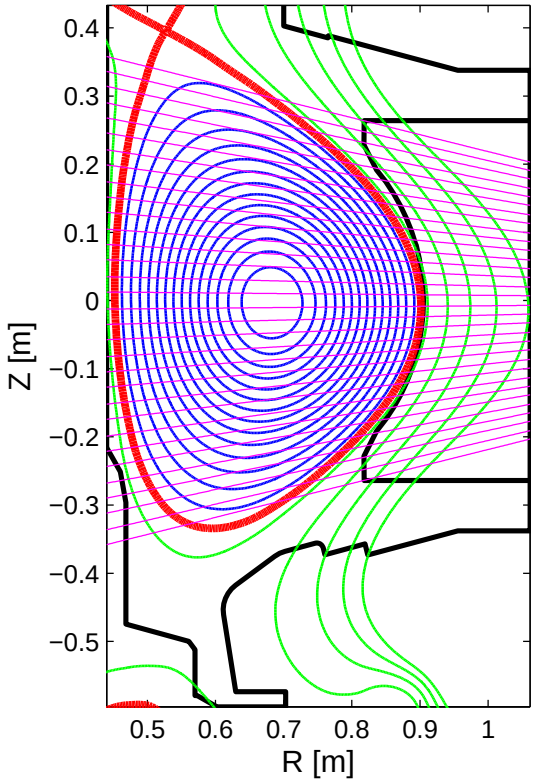

Figure 2-8: Viewing chords for the C-Mod HXR system (magenta) are superimposed on the flux surfaces for an USN discharge. Limiter and vacuum vessel surfaces are shown in black. Chord 32 intersects the top of the plasma while chord 1 intersects the bottom of the plasma.

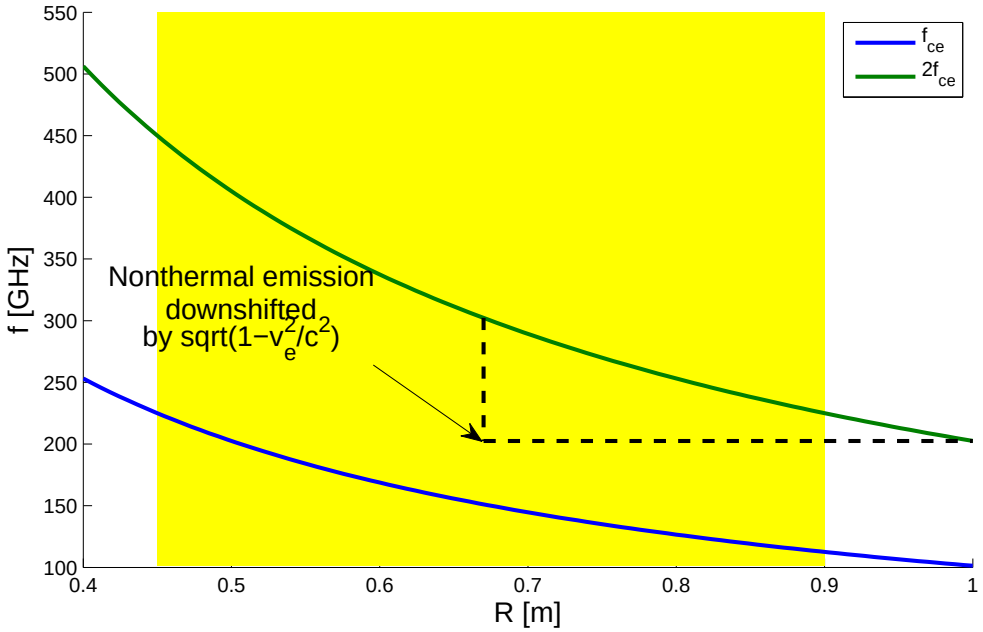

Figure 2-9: Fundamental and second harmonic electron cyclotron frequencies for a 5.4 T C-Mod discharge. The plasma region is shaded yellow. Relativistic electrons exhibit a downshift in cyclotron emission frequency by a factor of $\sqrt{1 - v_e^2/c^2}$. For some electrons this downshifted frequency corresponds to a nominal location outside the plasma.

2.2.3 Langmuir Probes

Alcator C-Mod has a compliment of Langmuir and Gundestrup probes mounted in a variety of locations around the torus. Fixed position probes are located in the upper and lower divertor surfaces on both the high and low field sides. These probes are mounted nearly flush with the surface of the tiles in which they are embedded. In addition, the LHCD launcher has 6 probes mounted in the 3 spacer bars between the waveguide rows. These probes are fixed to the LH launcher and consequently move radially in and out with the antenna. The probes are normally operated in a voltage sweep configuration which allows for measurement of the plasma density and temperature at a rate of 100 Hz.

Two scanning Gundestrup probes are located at A-port and F-Port on the low field side. The A-port probe plunges radially into the plasma while the F-port probe plunges vertically from the bottom of the plasma. Two scanning Gundestrup probes are also mounted on the inner wall. The four Gundestrup probes measure not only temperature and density profiles but also plasma flows parallel and perpendicular to the magnetic field.

2.3 Comparison with Other Tokamaks

Alcator C-Mod occupies a unique position for the study of LHCD. The densities and temperatures on C-Mod, along with its compact size, make the current relaxation time less than the LH pulse length. This allows the study of "quasi steady-state" operation despite the 0.5 s limit on LH pulse length. As compared to the larger experiments, the compact size of C-Mod gives a higher power density in the plasma despite having lower source power. In addition, the ratio of ω_{pe} to ω_{ce} is similar to that of ITER. This is important because LH wave propagation and accessibility are determined by this parameter. The proximity of the C-Mod LHCD frequency to that proposed for ITER (5 GHz) also makes C-Mod an ideal test bed for future LHCD

Table 2.3: Comparison of C-Mod LHCD System with Other Recent and Current Experiments

Exp.	f [GHz]	P_{source} [MW]	$n_{\|\|}$ Range	t_{pulse} [s]	Antenna Type	Notes
C-Mod [22]	4.6	3	±(1.0-4.7)	0.5	Fully Active	Maximum power to plasma 1.2 MW.
Tore Supra [26, 34]	3.7	4	1.6-2.3	210-1000	Multi-junction	Increase in source power Fall 2009 [35]
JET [36]	3.7	12	1.4-2.3	20	Multi-junction	
FTU [37, 38]	8.0	6	1.0-3.8	1	Fully Active & Multi-junction	
JT-60U [39, 40]	1.72, 2.23	5-10	1.3-3.75	10	Multi-junction	No longer in operation.

experiments. The fully active (relative phase of each column controlled individually) design of the C-Mod LHCD system allows considerably more flexibility in the launched $n_{||}$ spectrum as compared with multijunction type launchers. Not only is the range of $n_{||}$ greater, but the fully active system is able to operate in co- and counter-current drive mode for both normal and reversed current operation. Table 2.3 summarizes the key parameters of current and recent LHCD experiments in the world tokamak program.

Chapter 3

Slow Wave Launching and Coupling

As discussed in Section 1.5, Lower Hybrid Current Drive requires the excitation of the Slow Wave branch of the dispersion relation. This wave is polarized such that E_1 is nearly parallel to B_0 at the edge of the plasma, and the wave is evanescent when the local electron plasma frequency, ω_{pe}, is less than the wave frequency, ω_0. A review by Knowlton and Porkolab [41] details several slow wave antenna types. The type of antenna implemented on Alcator C-Mod, detailed in Section 2.1.3, is a 22×4 phased waveguide array, known as a Grill [42]. The transmission of power from the waveguides to the plasma was first treated by Brambilla [43] for linear density profiles.

Although there is a well developed basis for the linear physics of the coupling problem, experimentally there are still several outstanding issues to resolve. Predictions from linear models agree favorably with experimental measurements at low power levels, although agreement is not as good at higher power levels. Experiments have also shown that it is difficult to couple LH waves to the plasma in the presence of high power from nearby ICRF antennas. Attempts have been made to improve coupling during high power LH operation combined with ICRF by locally increasing

the plasma density at the launcher through the use of gas puffing. However, there have been mixed results from this approach. Coupling over large distances between the separatrix and the plasma is another unsolved issue. This will be of particular importance for LHCD on ITER and beyond. The antenna-plasma distance must be sufficiently large that the launcher is not immediately destroyed by the high heat flux at the edge of a burning plasma. On the other hand, the plasma must be close enough that the LH waves are able to couple from the antenna into the plasma. Again, gas puffing has been proposed as a solution to this issue.

3.1 Linear Coupling Physics

For lower hybrid waves, slow wave structures couple to the electrostatic branch of the cold plasma dispersion relation. By combining Faraday's Law and Ampere's Law we get

$$\nabla \times \nabla \times \vec{E} - \frac{\omega^2}{c^2}\bar{\bar{\epsilon}} \cdot \vec{E} = 0 \tag{3.1}$$

where $\bar{\bar{\epsilon}}$ is the plasma dielectric tensor from Equation 1.20.

We choose a slab geometry such that the background magnetic field is in the $\hat{z}$ direction, and the density gradient is in the $\hat{x}$ direction. Figure 3-1 shows the geometry used in the following derivation. The $x = 0$ plane is the interface between the waveguide and vacuum regions. Since there is no variation in the $\hat{y}$ direction we can eliminate all y derivatives. The $\hat{x}$, $\hat{y}$, and $\hat{z}$ components of Equation 3.1 can be written in partial differential form as

$$\hat{x} : \frac{\partial}{\partial x}\left[\frac{\partial}{\partial x}E_x + \frac{\partial}{\partial z}E_z\right] - \left[\frac{\partial^2}{\partial x^2} + \frac{\partial^2}{\partial z^2}\right]E_x - \frac{\omega^2}{c^2}(\epsilon_\perp E_x - i\epsilon_\times E_y) = 0 \tag{3.2a}$$

$$\hat{y} : -\left[\frac{\partial^2}{\partial x^2} + \frac{\partial^2}{\partial z^2}\right]E_y - \frac{\omega^2}{c^2}(i\epsilon_\times E_x + \epsilon_\perp E_y) = 0 \tag{3.2b}$$

$$\hat{z} : \frac{\partial}{\partial z}\left[\frac{\partial}{\partial x}E_x + \frac{\partial}{\partial z}E_z\right] - \left[\frac{\partial^2}{\partial x^2} + \frac{\partial^2}{\partial z^2}\right]E_z - \frac{\omega^2}{c^2}\epsilon_{||}E_z = 0 \tag{3.2c}$$

If we compare the launched LH wave frequency, ω, to the cyclotron and plasma frequencies in the coupling region near the edge, we find that, for ions, $\omega \gg \omega_{ci}$ and $\omega \gg \omega_{pi}$, while for electrons $\omega \ll \omega_{ce}$ and $\omega \sim \omega_{pe}$. We can simplify $\epsilon_\perp \approx 1 - \omega_{pe}^2/\omega_{ce}^2 + \omega_{pi}^2/\omega^2 \sim 1$, $\epsilon_\times \approx -\omega_{pe}^2/\omega\omega_{ce} \sim 0$, and $\epsilon_{||} \approx 1 - \omega_{pe}^2/\omega^2$. Assuming that $\vec{E}(x,z,t) = \vec{E}(x) \times e^{i(k_{||}z - \omega t)}$ and $\epsilon_\times \sim 0$, Equation 3.2a can be solved for E_x

$$E_x = \frac{ik_{||}E_z'}{\frac{\omega^2\epsilon_\perp}{c^2} - k_{||}^2} \tag{3.3}$$

where the prime denotes a derivative with respect to x. Combining Equations 3.2c and 3.3 results in

$$E_z'' - \frac{\omega^2}{c^2}\epsilon_{||}\frac{(n_{||}^2 - \epsilon_\perp)}{\epsilon_\perp}E_z = 0 \tag{3.4}$$

The quantity $\epsilon_{||}$ can be rewritten in the form

$$\epsilon_{||} = 1 - \frac{\omega_p^2}{\omega^2} = 1 - \frac{n_e}{n_{cut}} \tag{3.5}$$

and taking $\epsilon_\perp \sim 1$ results in

$$E_z'' + \frac{\omega^2}{c^2}(1 - n_{||}^2)\left(1 - \frac{n(x)}{n_{cut}}\right)E_z = 0 \tag{3.6}$$

where n_{cut} is the cutoff density defined by $\omega = \omega_{pe}$. It is interesting to note that the coupling behavior is independent of the magnetic field strength in this approximation. By taking

$$f(x) = \frac{\omega^2}{c^2}(1 - n_{||}^2)\left(1 - \frac{n(x)}{n_{cut}}\right) \tag{3.7}$$

we can rewrite Equation 3.6 as

$$E_z'' + f(x)E_z = 0 \tag{3.8}$$

The solutions to this differential equation for a linear $f(x)$ are linear combinations

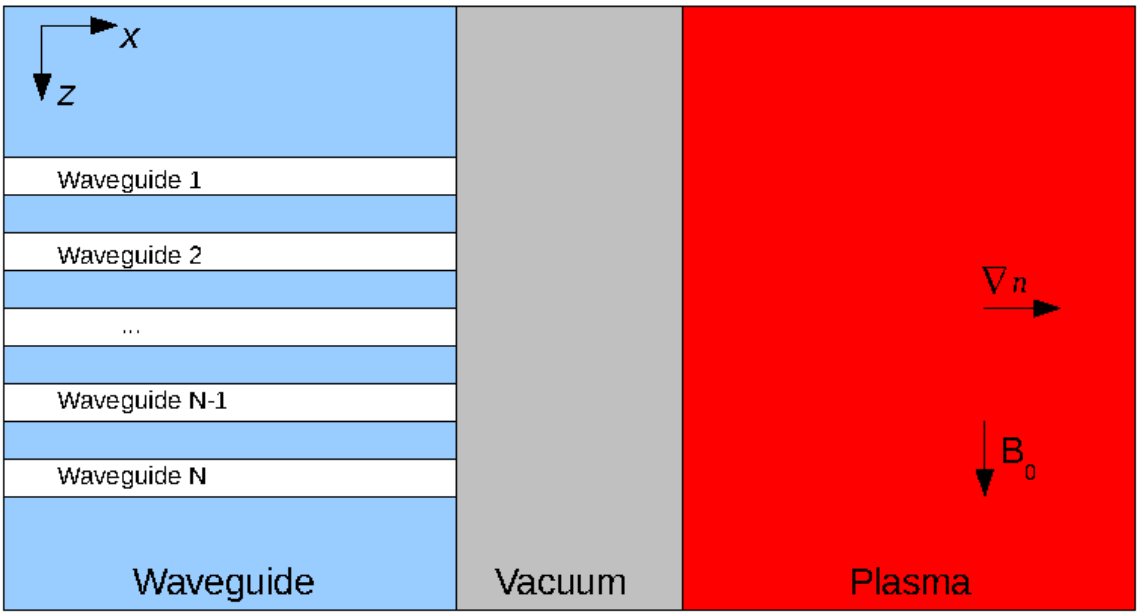

Figure 3-1: The slab geometry used for the coupling problem. There are no variations in the $\hat{y}$ direction.

of the Airy functions Ai and Bi [44], however we are interested in a more general solution to the coupling problem for arbitrary density profiles.

If we take a solution with both forward and reflected waves of the form

$$E_z(x) = E_z^+(x)e^{i\int k_\perp dx} + E_z^-(x)e^{-i\int k_\perp dx} \tag{3.9}$$

where the + and - superscripts represent the forward and reflected waves, with boundary conditions

$$E_z(0) = 1 \tag{3.10a}$$

$$E_z^-(\infty) = 0 \tag{3.10b}$$

we can solve the coupling problem for a single value of $n_{||}$ by numerically integrating Equation 3.8. First, we form a system of first order differential equations equivalent

to Equation 3.8

$$y_1' = y_2 \tag{3.11a}$$

$$y_2' = -f(x)y_1 \tag{3.11b}$$

and modify the boundary condition at $x = \infty$ to reflect the finite computational domain. The boundary condition from Equation 3.10b can be transformed to conditions on E_z and E_z' by differentiating Equation 3.9

$$\begin{aligned} E_z' &= ik_\perp E^+ e^{i\int k_\perp dx} + E^{+\prime} e^{i\int k_\perp dx} - ik_\perp E^- e^{-i\int k_\perp dx} + E^{-\prime} e^{-i\int k_\perp dx} \\ &\approx ik_\perp E^+ e^{i\int k_\perp dx} - ik_\perp E^- e^{-i\int k_\perp dx} \end{aligned} \tag{3.12}$$

Here we have neglected terms containing $E^{\pm\prime}$ by assuming that $E(x)^\pm$ is a slowly varying function of x compared to the eikonal variation. We choose the distance x_{max} such that the density at this point is much greater than cutoff. Since $k_\perp \propto \sqrt{n_e/n_{cut} - 1}$, $k_\perp'/k_\perp^2 \ll 1$ for $n_e \gg n_{cut}$. The WKB approximation is therefore satisfied in the vicinity of the boundary at x_{max}. Solving the linear system formed by Equations 3.9 and 3.12 for E_z^+ and E_z^- and substituting into Equation 3.10b yields a boundary condition at x_{max} in terms of E_z and E_z'

$$E_z'(x_{max}) = ik_\perp E_z(x_{max}) \tag{3.13}$$

Figure 3-2 shows the numerical solution to Equation 3.8 for a single value of $n_{||}$ and a linear density profile. The density profile in these cases is

$$n_e(x) = n_0 + x\frac{dn}{dx} \tag{3.14}$$

where n_0 is the density at the plasma edge and dn/dx is the constant density gradient in the plasma. The top panel shows a case where the density at the edge is above the cutoff density and the waves propagate freely across the entire domain. In the bottom panel, the waves are evanescent at the plasma edge and do not propagate

until the local density exceeds the cutoff density at $x = 0.0026$ m. Figure 3-3 shows the reconstructed two dimensional electric field pattern formed by superimposing the solution for each value of $n_{||}$ in the spectrum for the $n_0 > n_{cut}$ case. The $n_{||}$ spectrum used is shown in Figure 1-5. The so-called "resonance cones" formed by the waves leaving the antenna are clearly visible in the figure. The positive $n_{||}$ (extending upward) and negative $n_{||}$ (extending downward) components of the spectrum propagate in opposite directions along the magnetic field. The location of the waveguide grill is on the left side of the figure between z = -0.09 and 0.09 m. The x and z axes are not scaled equally in this figure, giving the impression that the wave group velocity is nearly perpendicular to the magnetic field, when in fact the group velocity is nearly parallel to the magnetic field.

After numerically solving for E_z and E_z' between $x = 0$ and $x = x_{max}$, we can construct an input impedance of the plasma

$$Z_p(n_{||}) = \frac{E_z(0)}{H_y(0)} = -i\omega\mu_0 \frac{E_z}{E_z'\left(1 + \frac{n_{||}^2}{\epsilon_\perp - n_{||}^2}\right)} \tag{3.15}$$

The reflection coefficient of the waveguide to plasma matching for an infinite grill is thus

$$\Gamma = \frac{Z_p - Z_{wg}}{Z_p + Z_{wg}} \tag{3.16}$$

where Γ is the ratio of reflected to forward field amplitude and Z_{wg} is the waveguide impedance. This method gives a qualitative answer to the coupling problem. However, it does not address the case of a spectrum of values for $n_{||}$, nor does it take into account the cross-coupling of adjacent waveguides.

A more detailed analysis must also include the finite width of the $n_{||}$ spectrum and cross-coupling of the waveguides. This is accomplished by matching the fields in the plasma to those of a grill-type antenna with a finite number of waveguides. The

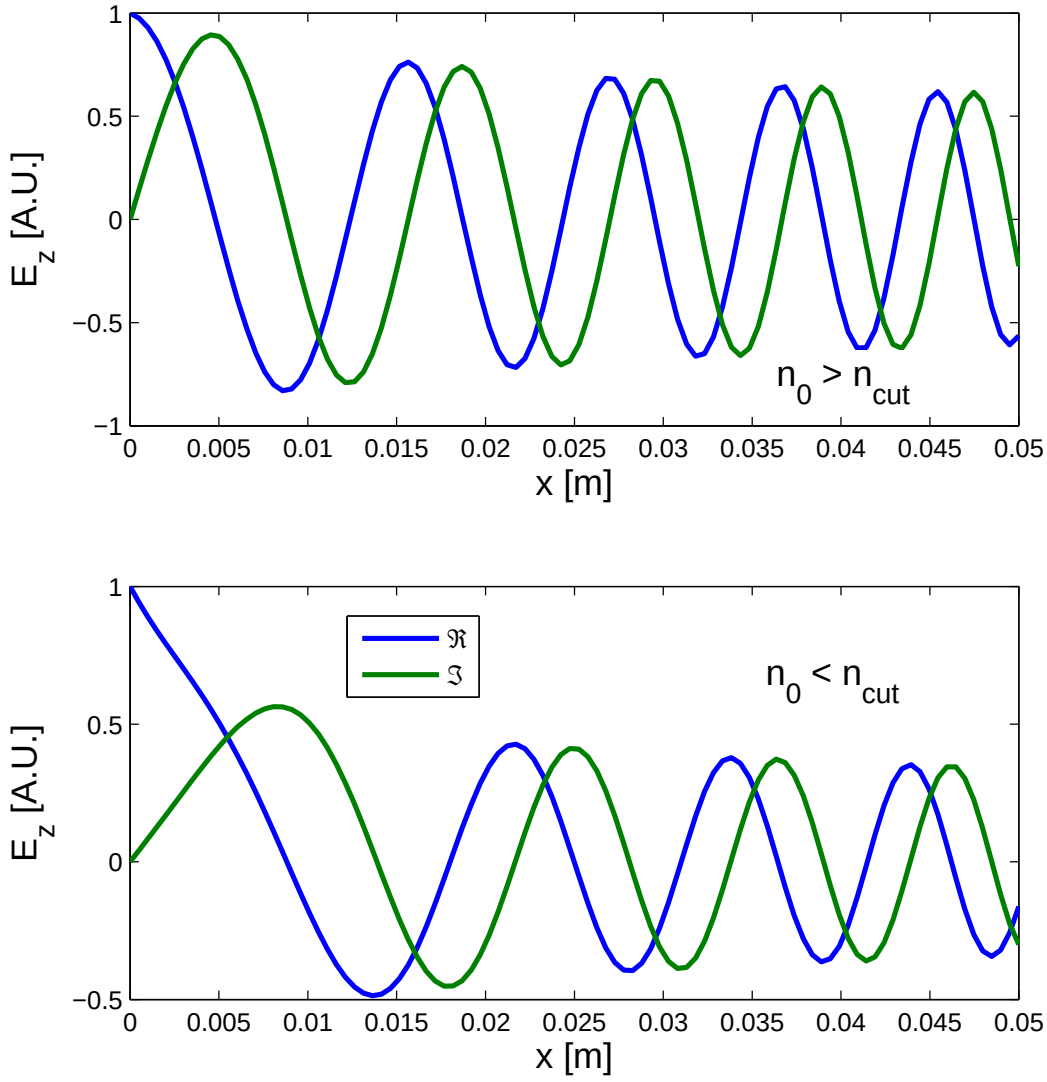

Figure 3-2: The one-dimensional solution to Equation 3.8 is plotted in the plasma edge region for $n_0 > n_{cut}$ (top) and $n_0 < n_{cut}$ (bottom), where $n(x) = n_0 + x(dn/dx)$. The blue and green curves represent the real and imaginary components of E_z. Parameters for the top panel are $n_{||} = 2.0$, $n_0 = 1 \times 10^{18}$ m^{-3}, and $\frac{dn}{dx} = 1 \times 10^{20}$ m^{-4}. Parameters for the bottom panel are $n_{||} = 2.0$, $n_0 = 0$, and $\frac{dn}{dx} = 1 \times 10^{20}$ m^{-4}.

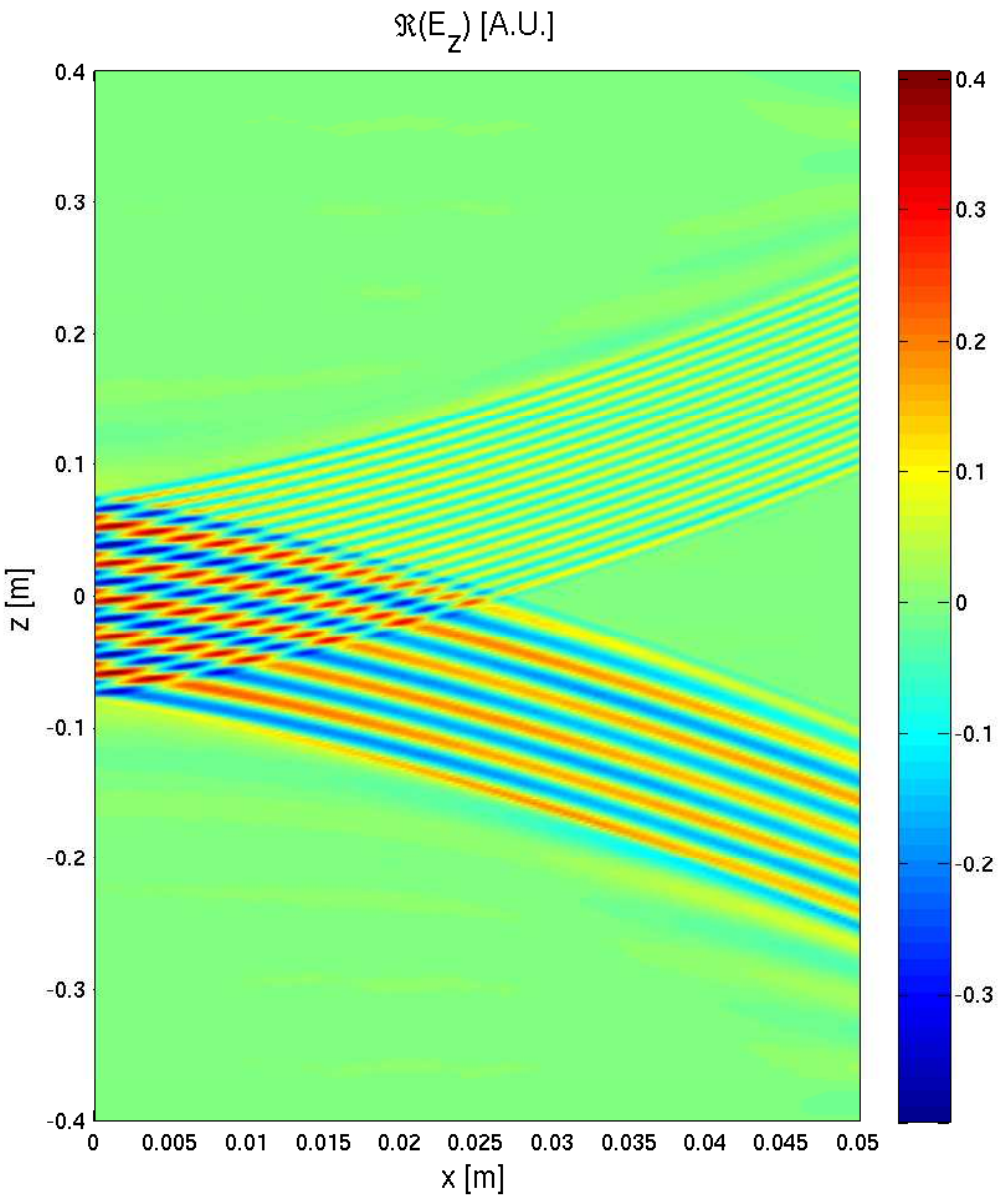

Figure 3-3: Electric fields near the waveguide grill computed by solving Equation 3.8 numerically for a spectrum of $n_{||}$ modes and superimposing those solutions. Resonance cones are observed to propagate away from the launcher located at $-0.8 < z < 0.8$. Simulation parameters are $n_{||} = 2.3$, $n_0 = 1 \times 10^{18}$ m^{-3} and $\frac{dn}{dx} = 1 \times 10^{20}$ m^{-4}. The z axis has been compressed to fit on the page.

fields in the waveguides can be represented as [43]

$$E_z^{wg}(x,z) = \sum_{p=1}^{N} e^{i\phi_p}\theta_p(z)\left[\sum_{n=0}^{\infty}(\alpha_{np}e^{ik_n x} + \beta_{np}e^{-ik_n x})\cos\frac{n\pi(z-z_p)}{b}\right] \tag{3.17a}$$

$$B_y^{wg}(x,z) = \sum_{p=1}^{N} e^{i\phi_p}\theta_p(z)\left[\sum_{n=0}^{\infty} -\frac{\omega}{ck_n}(\alpha_{np}e^{ik_n x} - \beta_{np}e^{-ik_n x})\cos\frac{n\pi(z-z_p)}{b}\right] \tag{3.17b}$$

$$E_x^{wg}(x,z) = -i\frac{c^2}{\omega}\frac{\partial B_y^{wg}}{\partial z} \tag{3.17c}$$

where there are N waveguides, each of which has a phase ϕ_p relative to waveguide 1, and

$$\theta_p(z) = \begin{cases} 1, & z_p \le z \le z_p + b \\ 0, & \text{otherwise} \end{cases} \tag{3.18}$$

is a square wave pulse representing the spatial width of the p^{th} waveguide, which extends from z_p to $z_p + b$. Here, $z_p = z_{p-1} + b + \delta$ where b is the waveguide width and δ is the septum thickness between waveguides. The wavenumber of the n^{th} mode is

$$k_n = \sqrt{k_0^2 - \left(\frac{n\pi}{b}\right)^2}$$

where $k_0 = \omega/c$. Only the TE_0 transverse electric mode is included, while the sum over n modes includes all possible TM_{1n} transverse magnetic modes. The coefficient α_{np} represents the wave traveling towards the plasma through the waveguide, while β_{np} is the wave reflected back by the plasma. The value of α_{0p} is proportional to the electric field of the incident wave for the TE_0 mode, and $\alpha_{np} = 0$ for $n \neq 0$ assuming that only the TE_0 mode is launched. For frequencies such that the waveguide is operating in the fundamental mode (as is usually the case), all higher order modes are cutoff in the waveguide, and therefore, k_n is purely imaginary for $n > 0$.

To match the antenna fields to the plasma fields, we introduce a vacuum region between the antenna and the plasma. This is merely a mathematical convenience, and

the vacuum region is usually assumed to be of width zero. However, a finite width vacuum region between the antenna and the plasma is sometimes used to explain experimental results [45]. We can define another quantity, Y, which is the ratio of reflected to forward fields for plane waves transitioning from a vacuum into the plasma

$$Y(n_{||}) = \frac{Z_p(n_{||}) - Z_0}{Z_p(n_{||}) + Z_0} \tag{3.19}$$

where Z_0 is the vacuum wave impedance equal to 377 Ω, and Z_p is the plasma input impedance from Equation 3.15. Without assuming a vacuum region, the impedance for the calculation of the reflection coefficient in Equation 3.19 is not defined. We can represent the vacuum electric and magnetic fields in front of the antenna as

$$E_z(x,z) = \int_{-\infty}^{\infty} \frac{\omega}{c}[\sigma(n_{||}) + \rho(n_{||})]e^{i(\omega/c)n_{||}z}dn_{||} \tag{3.20a}$$

$$B_y(x,z) = \int_{-\infty}^{\infty} \frac{i\omega}{c(n_{||}^2 - 1)^{1/2}}[\sigma(n_{||}) - \rho(n_{||})]e^{i(\omega/c)n_{||}z}dn_{||} \tag{3.20b}$$

where $\sigma(n_{||})$ is the incident field amplitude, and $\rho(n_{||})$ is the reflected field amplitude. The ratio of these two quantities for a single value of $n_{||}$ is given by Equation 3.19. Since the ratio of $\rho(n_{||})$ to $\sigma(n_{||})$ is known, we can solve for the remaining unknown, β_{np}, by matching Equations 3.17 and 3.20 at $x = 0$. The reflection coefficient in the p_{th} waveguide is then

$$\Gamma_p = \frac{\beta_{0p}}{\alpha_{0p}} \tag{3.21}$$

The launched $n_{||}$ spectrum is given by the function $\sigma(n_{||})$. This spectrum varies slightly from the ideal spectrum described in Section 1.5.2.

3.1.1 GRILL Code

The GRILL code [43, 46], written by Marco Brambilla, uses the plasma model described in Section 3.1, but assumes a constant density gradient, which leads to Airy

function solutions for Equation 3.8. The input parameters to the code are shown in Table 3.1.1. The code can be run with a range of values for several of the input parameters, which allows many plasma conditions to be simulated with a single run of the code. For example, the density at the plasma edge is equal to

$$n_{edge} = \text{DNEDGE} + \text{DNEDGE} \times \text{FDNEDG} \times \text{n}$$

where $n = (0, 1, ..., \text{NDNEDG} - 1)$. The density gradient and vacuum gap can be varied in the same manner using the variables in the namelist. The code was modified by the author of this thesis to include the LAMBDA variable which allows the density gradient to be linked to the edge density by a density scale length via the following relation

$$\frac{dn}{dx} = n_{edge} \times \text{LAMBDA}$$

Figure 3-4 shows a comparison of the GRILL code with a numerical solution to the model developed in Section 3.1. A broad minimum of the reflection coefficient is observed near $n_{edge} = n_{cut} n_{||}^2$ [45], above which the reflection coefficient begins to rise again. The results of the two codes agree very closely across a range of density and launched $n_{||}$. Due to the close agreement of the results and the significantly faster run time of the GRILL code, the experimental results in the subsequent sections will be compared with the GRILL code.

3.2 Experimental Results

The coupling of LH waves is sensitive to the density at the plasma edge, particularly when the edge density is in the vicinity of the cutoff density. Figure 3-2 shows the sensitivity of wave propagation (and thus the power reflection coefficient) to the density at the plasma edge. For even a small region of evanescence at the plasma edge the power coupled to the plasma is significantly reduced. The density at the plasma

Table 3.1: GRILL Code Namelist Variables

Variable Name	Description
FREQCY	Wave frequency
NWGUID	Number of waveguides in each row
WIDTH	Small internal dimension of waveguide
DWALL	Thickness of septum between waveguides
HEIGTH	Large internal dimension of waveguide[a]
NMOD	Number of TM modes to include in analysis
DNEDGE	Electron density at the plasma edge
NDNEDG	Number of edge density iterations
FDNEDG	Multiplier for each edge density iteration
DNDX	Density gradient
NDNDX	Number of density gradient iterations. If NDNDX = -1, then DNDX is set equal to LAMBDA×DNEDGE
FDNDX	Multiplier for each density gradient iteration
LAMBDA	Density scale length
DXPL	Vacuum gap width between antenna and plasma
NDXPL	Number of vacuum gap iterations
FDXPL	Multiplier for each vacuum gap iteration
JOUTRF	Output control for reflection coefficients. Set = 1 for magnitude only, set = 2 for complex coefficients
ISPEC	$n_{\|\|}$ spectrum included in output file if set = 1
NPHASE	Number of waveguide phasings

[a]Although the plasma treatment of the GRILL code assumes no variation in the $\hat{y}$ direction, the code namelist does include the long dimension of the waveguide, HEIGTH. This parameter is used to properly normalize the $n_{||}$ spectrum.

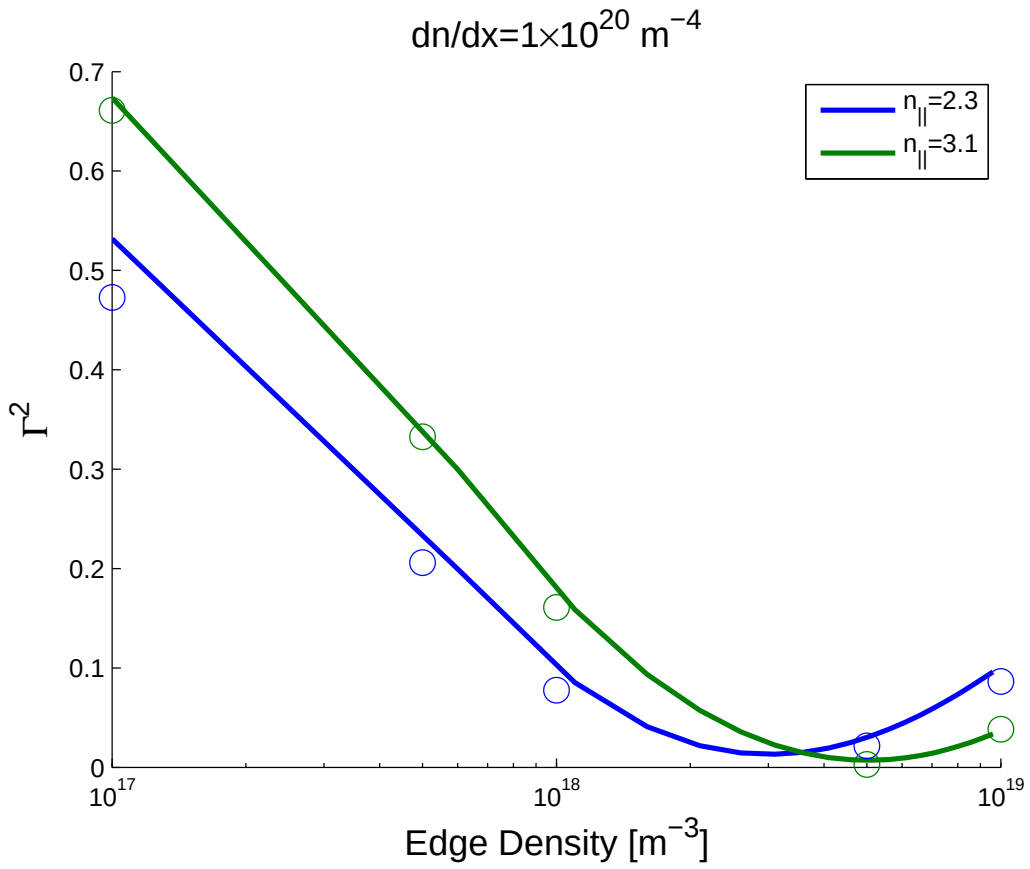

Figure 3-4: LH wave coupling as a function of edge density for the GRILL code (lines) and for a numerical solution to the model developed in Section 3.1 (circles).

edge is monitored with the six Langmuir probes described in Section 2.2.3. These probes measure the plasma density between the rows of the grill and do not respond to changes in the density profile that are localized only in front of the waveguide grill.

The C-Mod LHCD Launcher measures forward and reflected power via directional couplers at multiple points in the launcher structure. Figure 3-5 shows the location of the directional couplers in the launcher. Because access to the forward waveguide (FWG) is difficult, there are no direct measurements of the forward or reflected power on the B or C rows of the antenna, and special directional couplers [47, 48] were designed to fit in the small space available for monitoring the A and D rows. All forward and reflected power is accounted for, including waveguide losses between the measurement locations and the waveguide apertures. Appendix A describes the calibration technique used to determine the corrected reflection coefficients.

The directional couplers used for calculating reflection coefficients are also part of the launcher arc protection system. High reflection coefficients usually indicate the presence of an arc in the waveguide system under normal operating conditions. If the ratio of reflected to forward power measured by a directional coupler exceeds a preset threshold, then the arc protection system trips, thereby shutting off power from the klystrons.

3.2.1 Non-Perturbing L-mode Coupling

Since high reflection coefficients caused by poor coupling can create similar ratios of reflected to forward power as an arc, it is necessary to bypass the arc protection system to obtain reliable operation under poor coupling conditions. Poor coupling is characterized by a global power reflection coefficient, Γ^2, of greater than $\sim$40%. In order to minimize the likelihood of catastrophic damage to the launcher from an undetected arc, pulse length and power level were limited to 10 ms and $\sim$150 kW during experiments with the arc protection bypassed. Figure 3-6 shows a typical waveform for the low power coupling experiments.

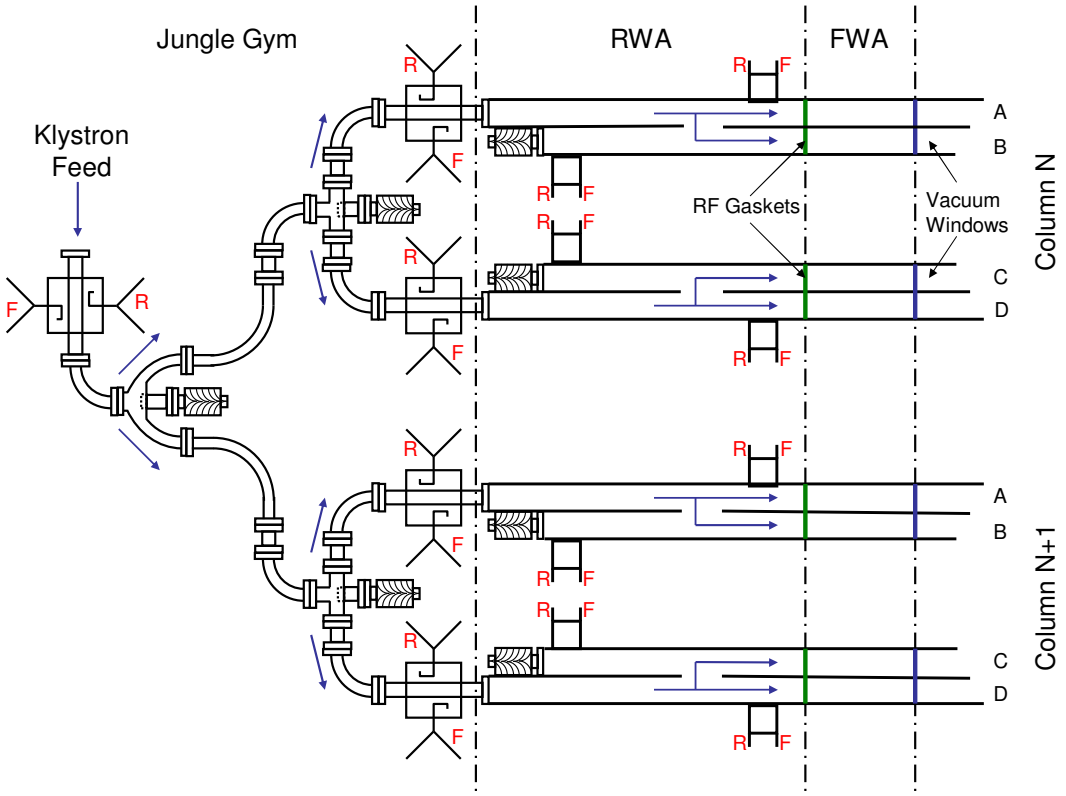

Figure 3-5: Directional couplers used for measuring forward and reflected power in the LH launcher. This schematic shows the instrumentation for one klystron channel. Measurement locations for forward and reflected power are indicated by red "F" and "R" letters, respectively.

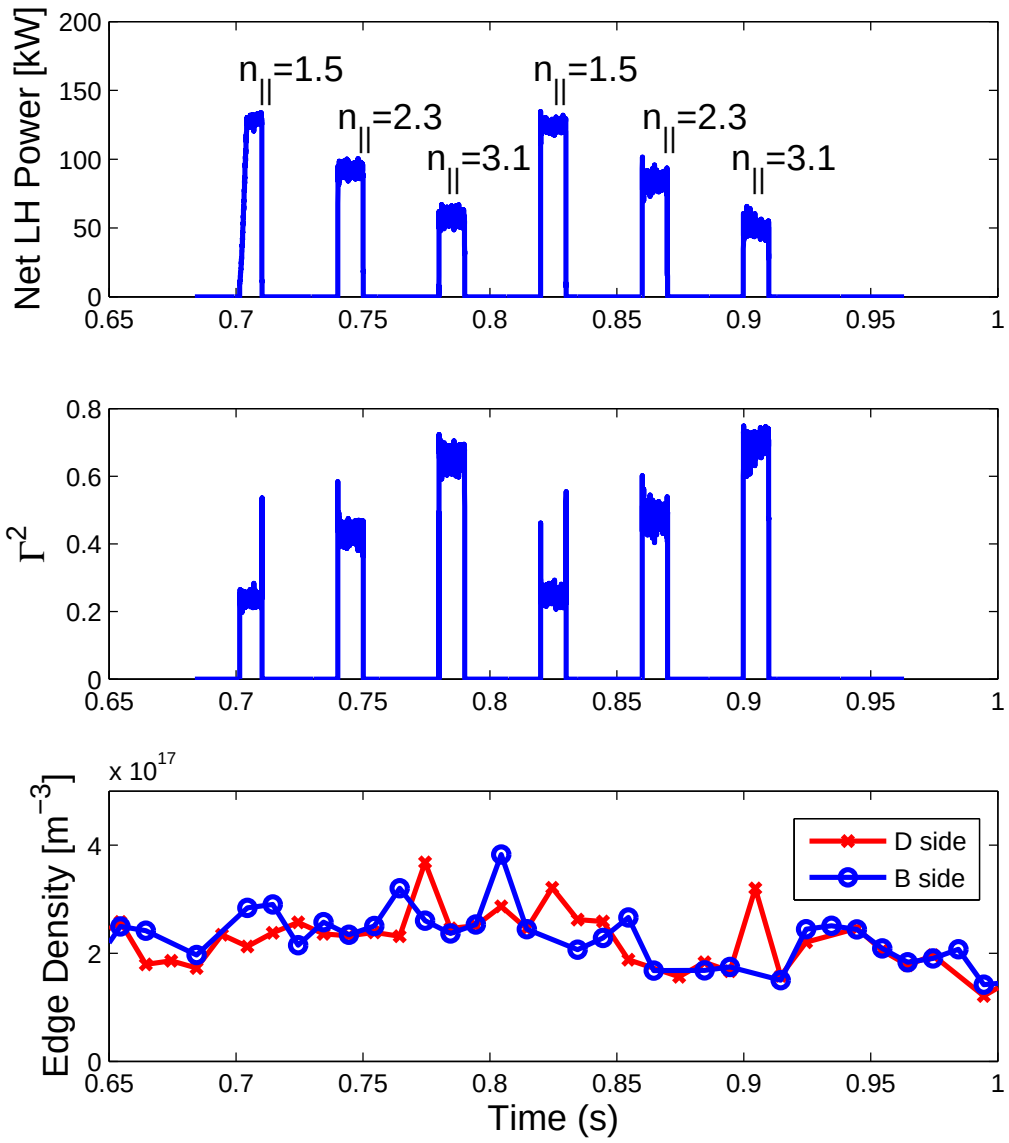

Figure 3-6: Typical waveform for low power coupling experiments. The waveguide phasing progression repeats twice in this discharge. The edge density shown is measured on the D side and B side Langmuir probes mounted between the B and C rows of the LH antenna. Shot number = 1070329012.

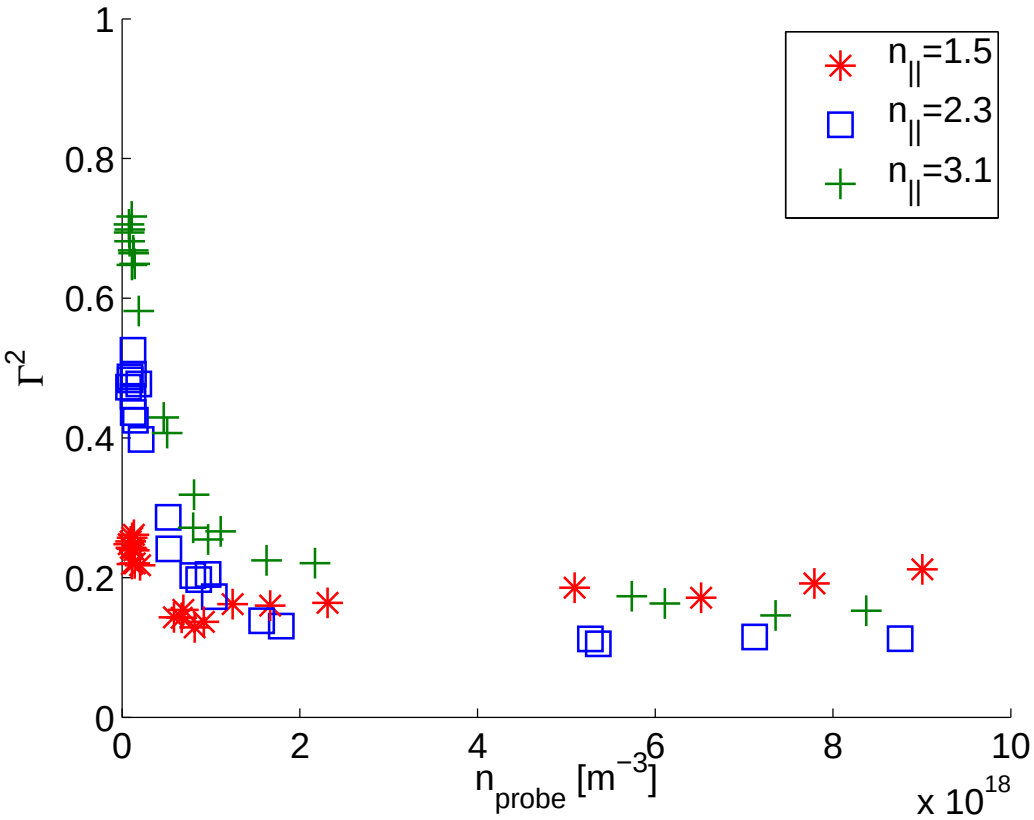

Figure 3-7: Non-perturbing L-mode coupling results. Pulse length is 10 ms and power level is ∼150 kW.

At these power levels and pulse lengths, plasma conditions are observed to be nearly constant for the duration of a single LH pulse. As shown in Figure 3-7, the short pulse, low power data points form smooth curves with little scatter as plasma density is scanned. The abscissa of Figure 3-7 is the density at the grill as measured by a cylindrical Langmuir probe extending 1.5 mm beyond the edge of the antenna. This probe averages the electron density over the 1.5 mm thick region in front of the grill. The small changes in magnitude of Γ^2 during each pulse in Figure 3-6 indicates that the coupling conditions are not varying significantly during the course of the 10 ms of LH operation.

3.2.2 Comparison of the GRILL Code with Low Power Experimental Results

Coupling data at power levels near 150 kW with three values of $n_{||}$ [49, 50] are compared with the results of the GRILL coupling code. The abscissa of Figure 3-8 is the density at the grill as measured by a cylindrical Langmuir probe extending 1.5 mm beyond the edge of the antenna. This probe averages the electron density over the 1.5 mm thick region in front of the grill. Figures 3-8, 3-9, and 3-10 show the results of simulations with the GRILL code using three models for the edge density profile.

In Figure 3-8, a density profile of the form

$$n(x) = n_0 + x\frac{dn}{dx} \tag{3.22}$$

is assumed for the model. The density at the aperture of the waveguide, n_0, is held constant, and the density gradient is varied to match the model density profile to the spatially averaged density as measured by the Langmuir probes. The relationship between n_{probe}, n_0, and $\frac{dn}{dx}$ is

$$n_{probe} = n_0 + \frac{x_{probe}}{2}\frac{dn}{dx} \tag{3.23}$$

where the waveguide aperture is at $x = 0$ and the probe tip is at $x = x_{probe}$. The measured probe density, n_{probe}, can be compared with the code results by using a fixed aperture density, n_0, and varying the density gradient, dn/dx, to agree with the measured value of n_{probe}. An aperture density of 4×10^{17} m^{-3} gives the best fit to the experimental data, although a non-physical negative density gradient is required to match the model to measured probe densities of less than 4×10^{17} m^{-3}.

Figure 3-9 shows the observed reflection coefficient and that predicted by simulation with a vacuum gap model for the edge electron density profile [45]. The vacuum

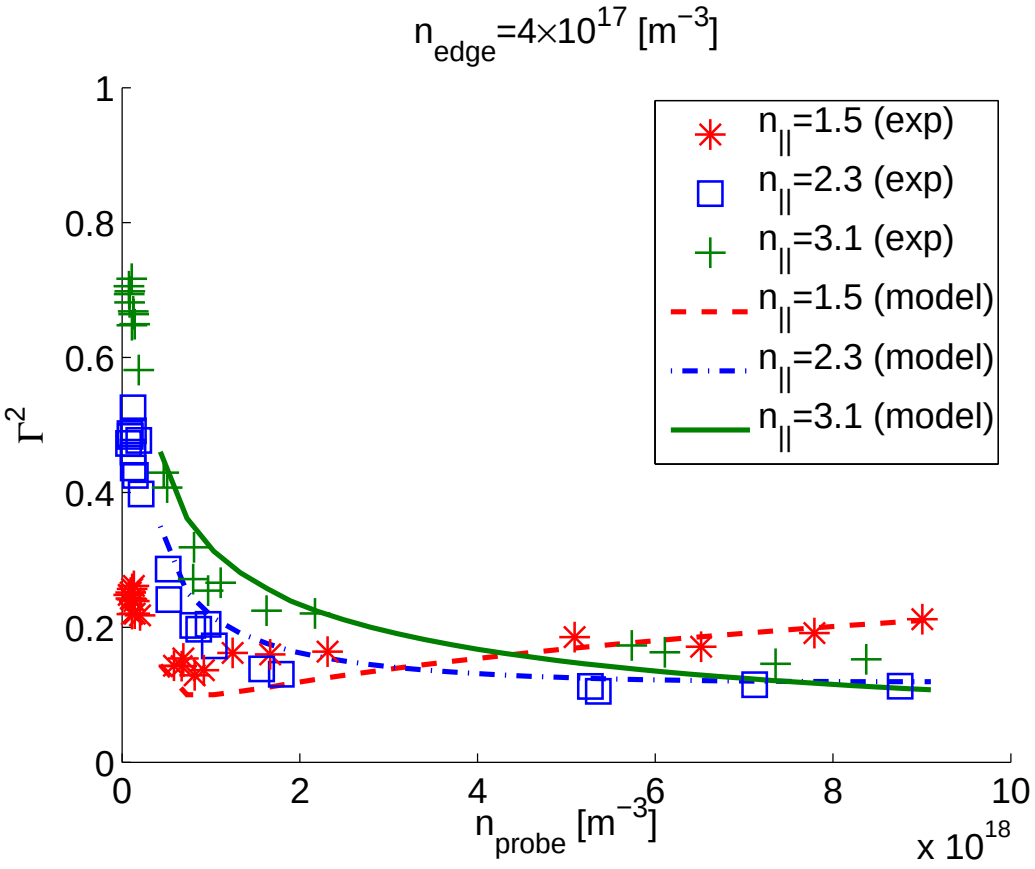

Figure 3-8: Reflection coefficient vs. probe density with variable gradient model. Dashed curves show simulation for 60° phasing, dotted for 90° phasing, and solid for 120° phasing.

gap model density profile is

$$n\left(x\right)=\begin{cases} 0, & \text{if } x < x_{gap} \\ n_0 + (x - x_{gap})\frac{dn}{dx}, & \text{if } x \geq x_{gap} \end{cases} \tag{3.24}$$

where x_{gap} is the width of the vacuum gap and n_0 is the density at the end of the vacuum gap. The measured probe density is

$$n_{probe} = \frac{x_{probe} - x_{gap}}{x_{probe}}(n_0 + \frac{x_{probe} - x_{gap}}{2}\frac{dn}{dx}) \tag{3.25}$$

The vacuum gap model agrees well with experimental data for densities below 1×10^{18} m^{-3}. A vacuum gap, x_{gap}, of 0.5 mm and a density gradient of 1×10^{20} m^{-4} give the best fit for $n_{||}$ of 1.55, 2.32, and 3.11 (60°, 90°, and 120° phasing).

A third density profile of the type

$$n(x) = n_0 + \lambda n_0 x \tag{3.26}$$

where

$$\lambda = \frac{(\frac{dn}{dx})}{n_0}$$

is used to create the coupling curves in Figure 3-10. This profile gives similar results to the vacuum gap model for $\lambda = 4 \times 10^4$ m^{-1}. This value of λ produces a very short e-folding length of 0.025 mm.

In the absence of an accurate measurement of the density profile, there is insufficient information to determine which of these density profile types best represents the experiment. Each density profile type has at least one free parameter which can be used to account for inaccuracies in the physical model used to predict the coupling results, and as such any comparison between the model and the experiment cannot confirm the accuracy of the model. This ambiguity should be resolved with the installation of an X-mode reflectometer system adjacent to the LH2 launcher in the

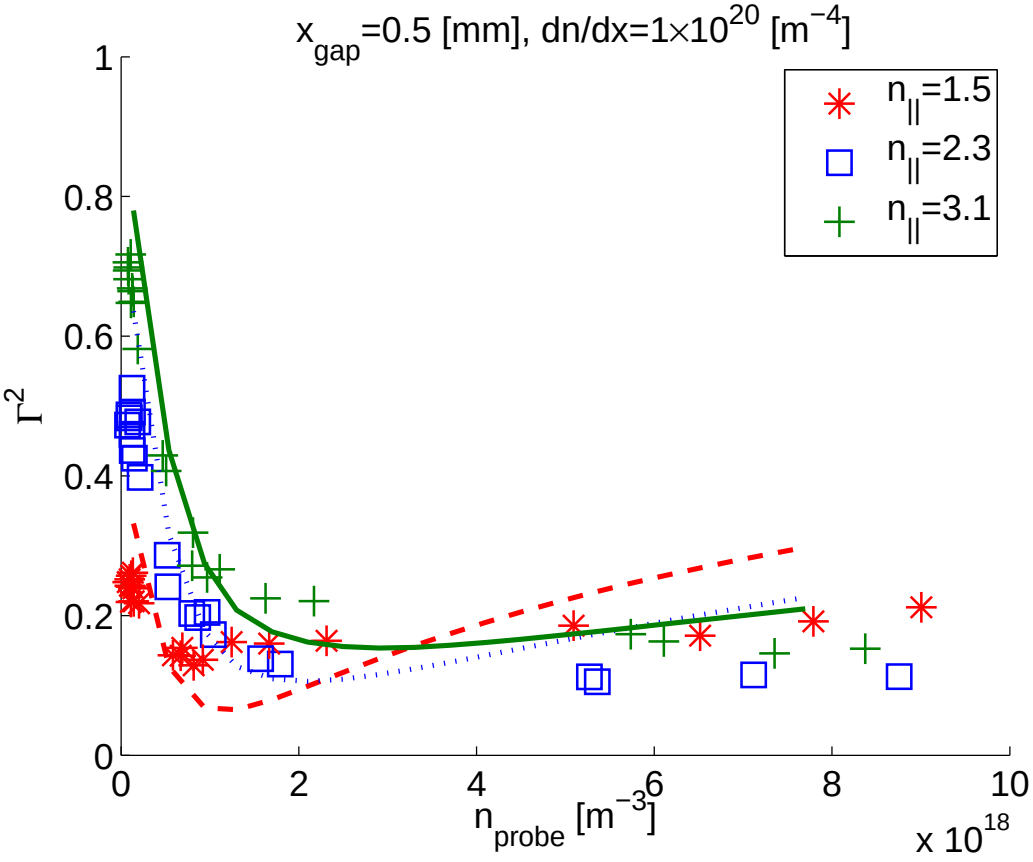

Figure 3-9: Reflection coefficient vs. probe density with vacuum gap model. Dashed curves show simulation for 60° phasing, dotted for 90° phasing, and solid for 120° phasing.

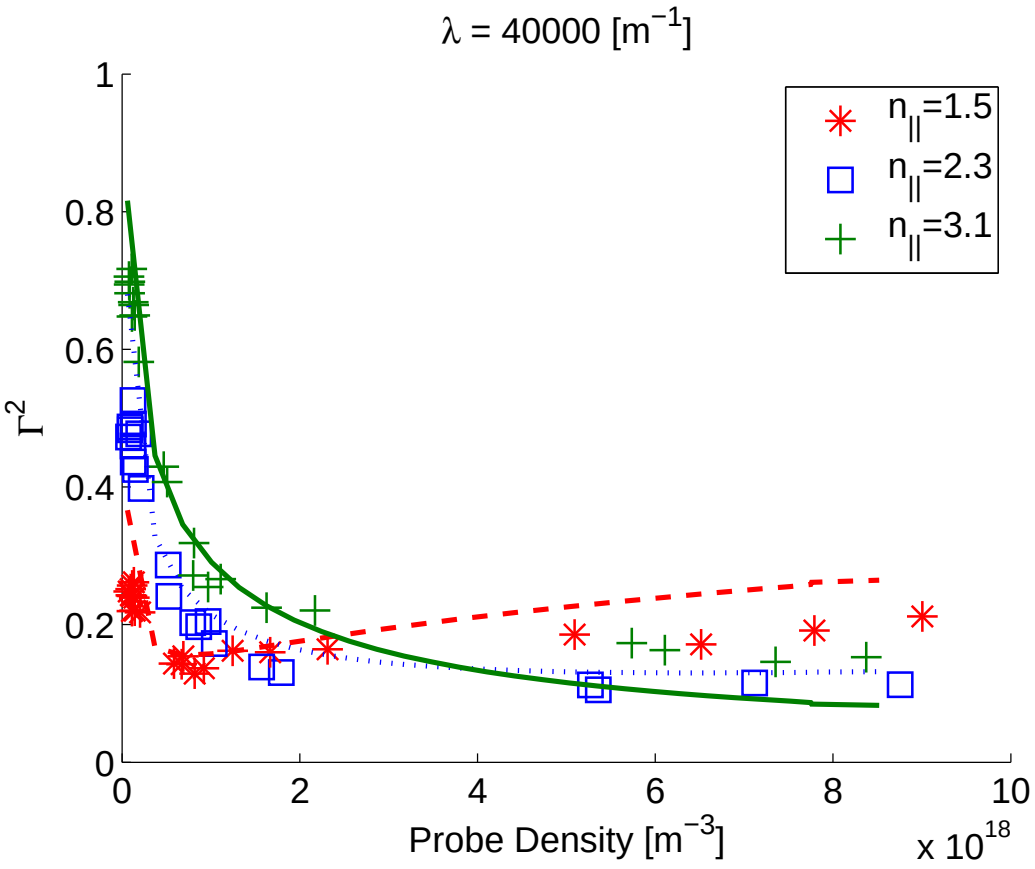

Figure 3-10: Reflection coefficient vs. probe density with density scale length model. Dashed curves show simulation for 60° phasing, dotted for 90° phasing, and solid for 120° phasing.

FY2010 run campaign [51, 52]. With the edge density profiles in hand (as opposed to the edge density averaged over the probe width) a comparison between experimental and modeling results can be made without the use of free parameters.

3.2.3 High Power Coupling

During high power operation, the density measured by the LH Langmuir probes is frequently observed to vary from the pre-LH value. Furthermore, since the probes average the plasma density in the 1.5 mm thick region in front of the coupler, simultaneous changes to both the edge density and the density gradient may occur without a corresponding change in the density measured by the probe. Figure 3-11 shows two possible density profiles with the same measured probe density.

Figure 3-12 shows a typical 1 MW LHCD discharge. Although in this discharge the line averaged density drops during the application of LHCD, the density measured by the LH Langmuir probes is observed to rise slightly. This differs from the usual relationship between line averaged density and edge density, in which $n_{edge} \propto \overline{n}_e^{\gamma}$, where $\gamma \sim 3$ [53], for a given plasma configuration. Figure 3-13 shows the power reflection coefficient as a function of net LH power for three values of $n_{||}$. Although no trend is apparent in the range from 400-1000 kW, the high power reflection coefficients are substantially higher than the low power ($\sim$ 150 kW) data. The increase of the high power reflection coefficients in Figure 3-13 as compared to the low power measurements, combined with the observations in Figure 3-12, indicate a change in not only the edge density, but also the edge density gradient during the presence of high power, long pulse LHCD.

Results from the ASDEX LHCD experiment [54] also show an increase in reflection coefficients as the incident LH power rises. The poor coupling at high power in ASDEX was attributed to the ponderomotive force of the LH waves pushing the plasma away from the coupler, thus creating a thin region of plasma near the waveguide apertures below the cutoff density. Since the coupling of LH waves to the plasma

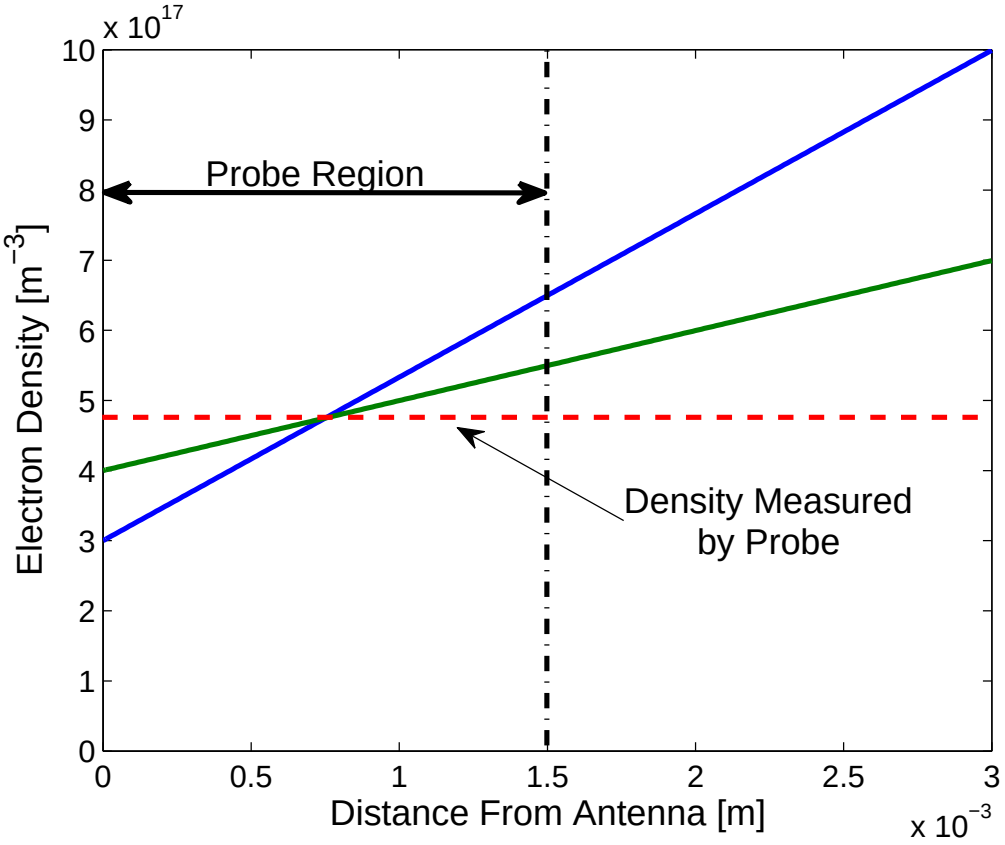

Figure 3-11: Two possible edge density profiles which agree with the LH Langmuir probe measurement.

is very sensitive to the density profile in the first few millimeters, a narrow region below the cutoff density can have a substantial negative effect on coupling. Another possible explanation is that the density in front of the LH launcher is increasing such that the edge density is above the optimum value of n_{edge}. The increase of Γ^2 above the optimum value of n_{edge} can be seen in Figure 3-4. With the density increase observed on the LH Langmuir probes, this explanation must be considered. The changes in density in front of the LH launcher will be discussed in additional detail in Chapter 4.

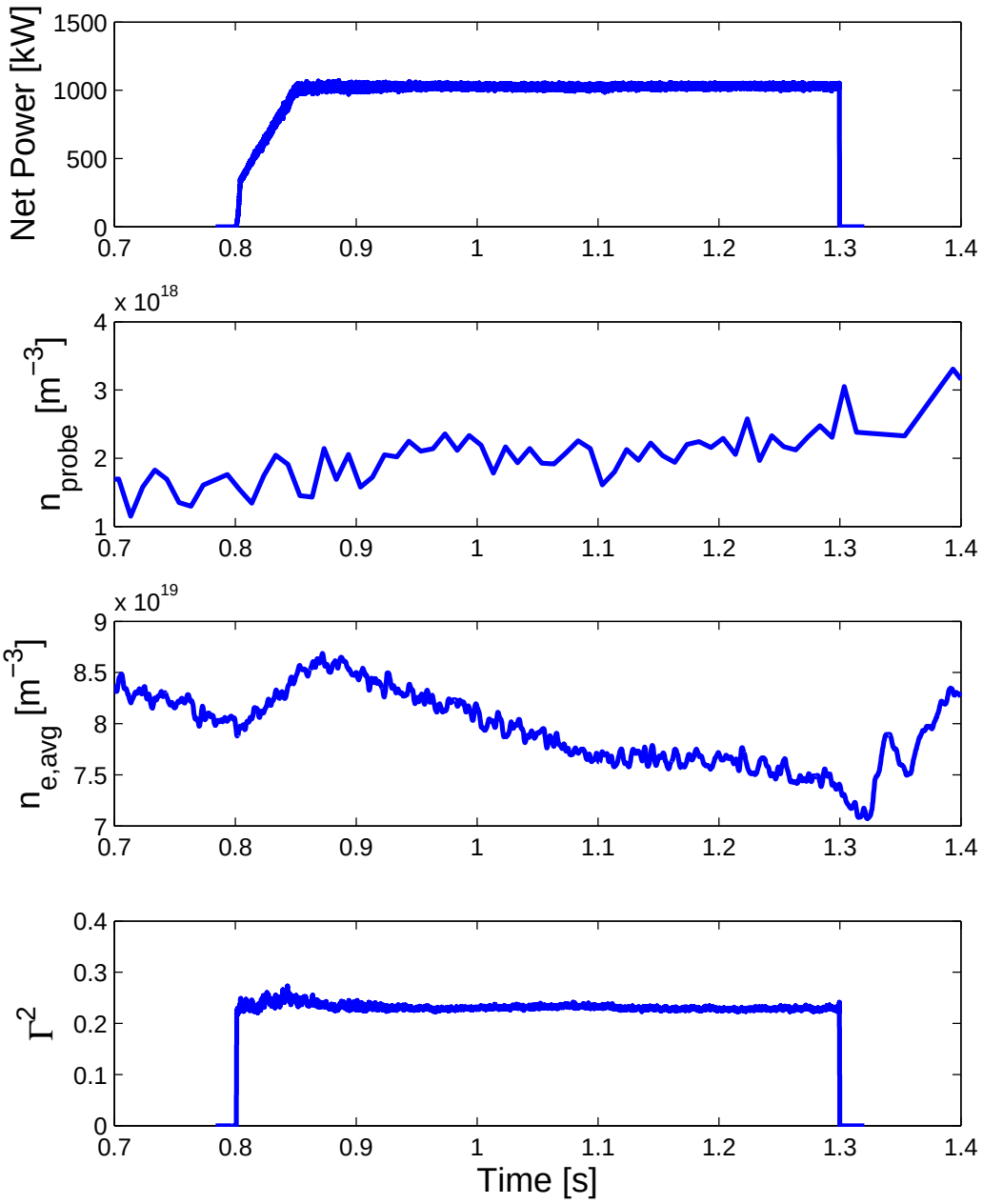

Figure 3-12: Edge density is observed to change during long pulse, high power operation. Density measured by the LH Langmuir probe rises slightly during LHCD and is not well correlated with changes in line averaged density. Shot number = 1080226006.

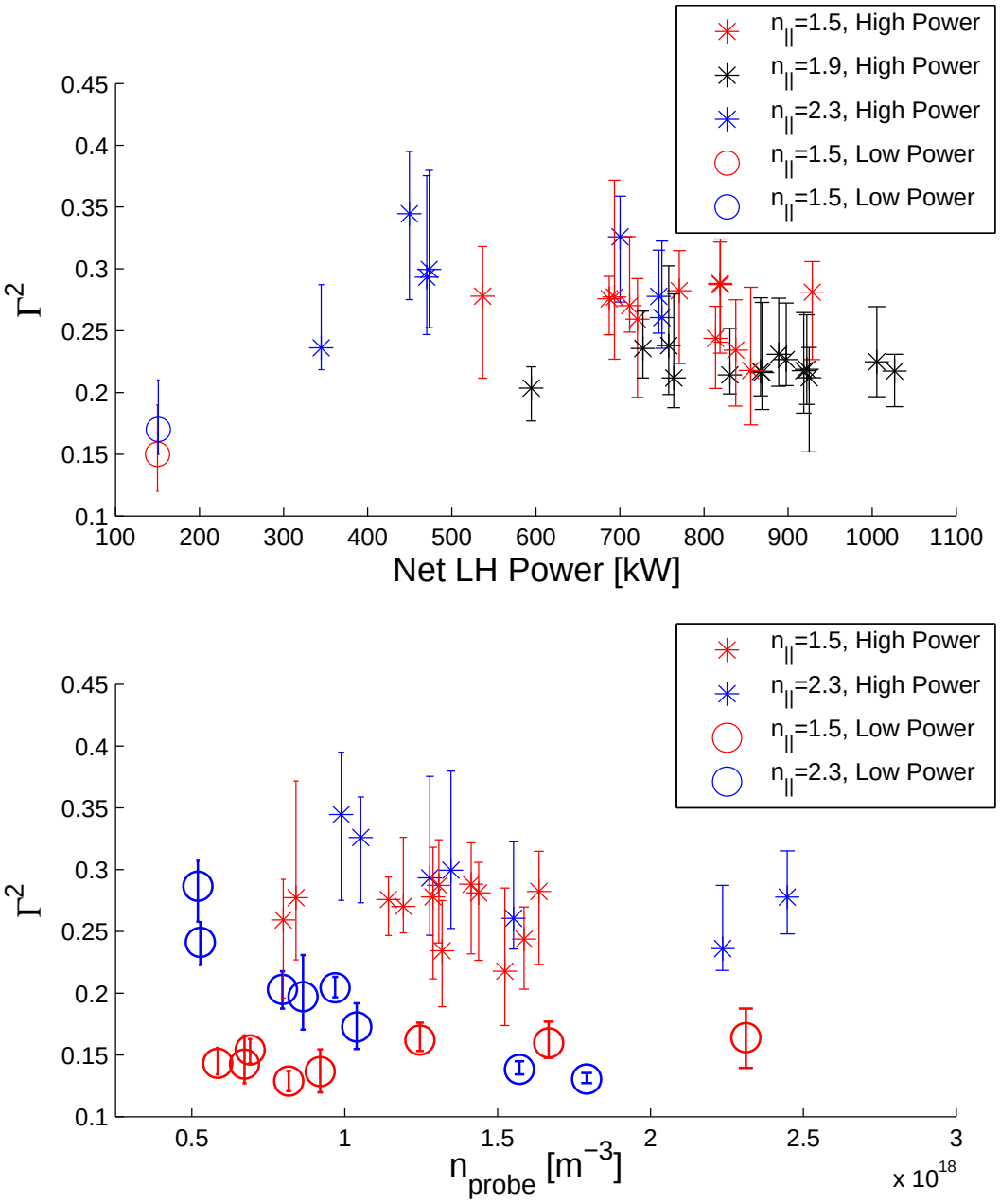

Figure 3-13: Power reflection coefficient, Γ^2, as a function of net LH power for three values of $n_{||}$. The average edge density measured during LHCD by the LH Langmuir probes varied from $8 \times 10^{17} - 2.5 \times 10^{18}$ m^{-3} in these discharges. (top) Comparison between high power (asterisks, 400-1000 kW) and low power (circles, $\sim$ 150 kW) coupling results. (bottom)

3.2.4 Coupling with ICRF

Other tokamaks with both ICRF and LHCD systems, such as Tore Supra [55] and JET [36], have experienced difficulties operating the two RF systems simultaneously. These effects have been shown to be most pronounced when the ICRF antenna is connected along a flux tube to the LH antenna. Figure 3-14 shows two similar C-Mod shots, one with 1.0 MW from the D-port ICRF antenna, and one with 2.0 MW from the J-port ICRF antenna. The J-port antenna does not substantially change the magnitude of Γ^2, while the D-port antenna causes a considerable increase in Γ^2 resulting in a trip of the LH system shortly after the ICRF turns on. The D-port ICRF antenna is located immediately next to the LH launcher at C-port and is well connected magnetically, while the J-port ICRF antenna is significantly farther away toroidally, and is not magnetically connected to the LH launcher. The E-port ICRF antenna is located at an intermediate distance from the LH launcher and also causes an increase in Γ^2, although not as pronounced as the D-port antenna. Figure 3-15 shows the position of the antennas and a magnetic field line for a 5.4 T, 750 kA shot.

The interference caused by the D-port ICRF antenna is severe enough to preclude any routine simultaneous operation with the C-port LHCD launcher. For this reason, a long term plan has been made to remove both the D- and E-port antennas (two current straps each) and replace them with a four strap antenna located at E-port.

3.2.5 H-mode Coupling

Reliable coupling during H-modes has been obtained. The steep density gradients in the pedestal do not seem to be a major problem for wave coupling, although other effects of the pedestal are discussed in Chapter 5. Figure 3-16 shows LHCD operation during an ICRF heated H-mode, while Figure 3-17 is an example of an LHCD triggered H-mode with no ICRF. As with high power LH operation in L-mode, the measured edge density does not scale predictably as a function of line averaged density. The shot shown in Figure 3-16 exhibits a considerable increase in

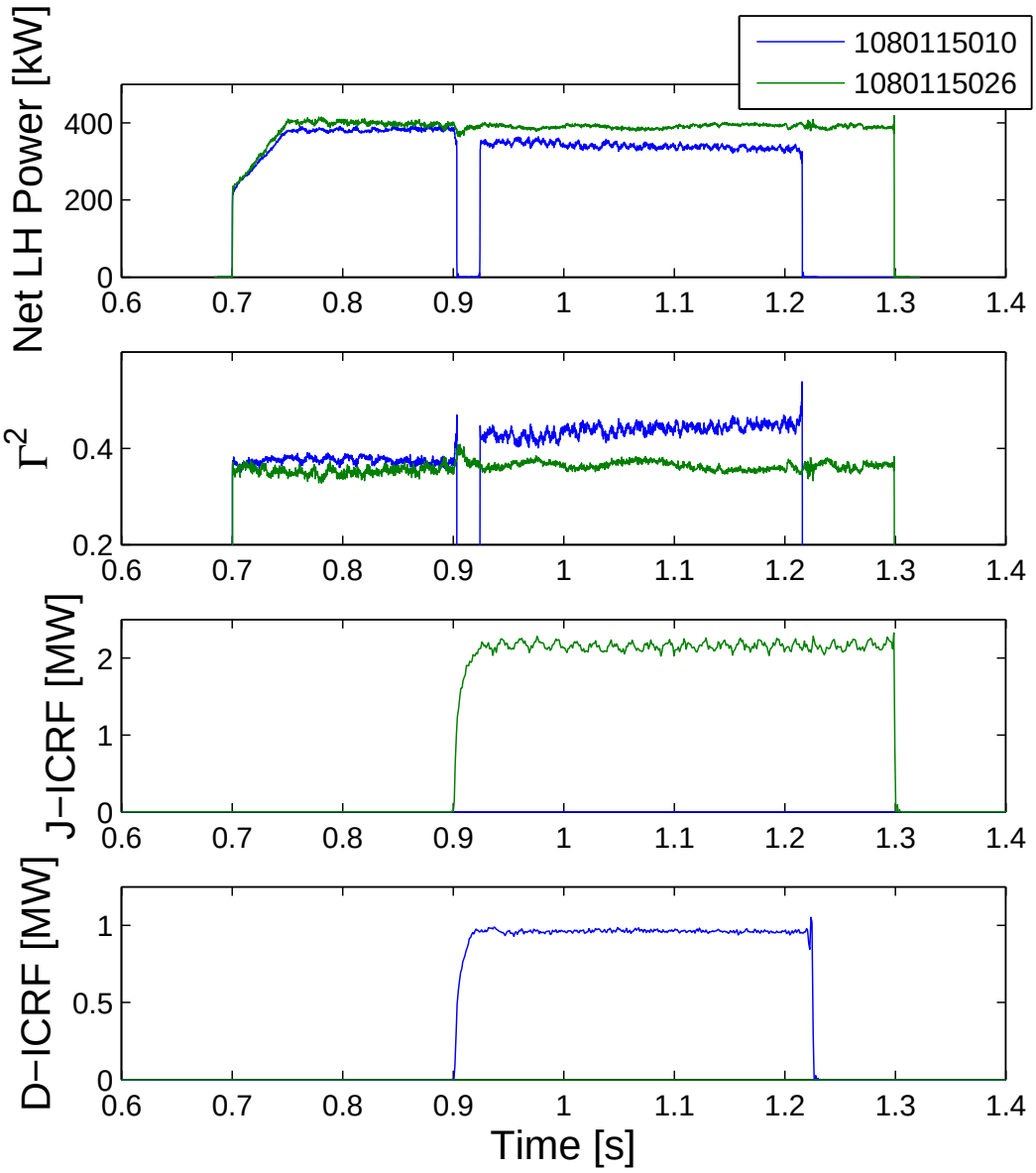

Figure 3-14: LH wave coupling in the presence of ICRF during matched L-mode discharges. 2 MW of ICRF power from the J-port antenna (green traces) does not noticably change the magnitude of Γ^2, while 1 MW of ICRF power from the D-port antenna (blue traces) causes a trip and a significant increase in Γ^2.

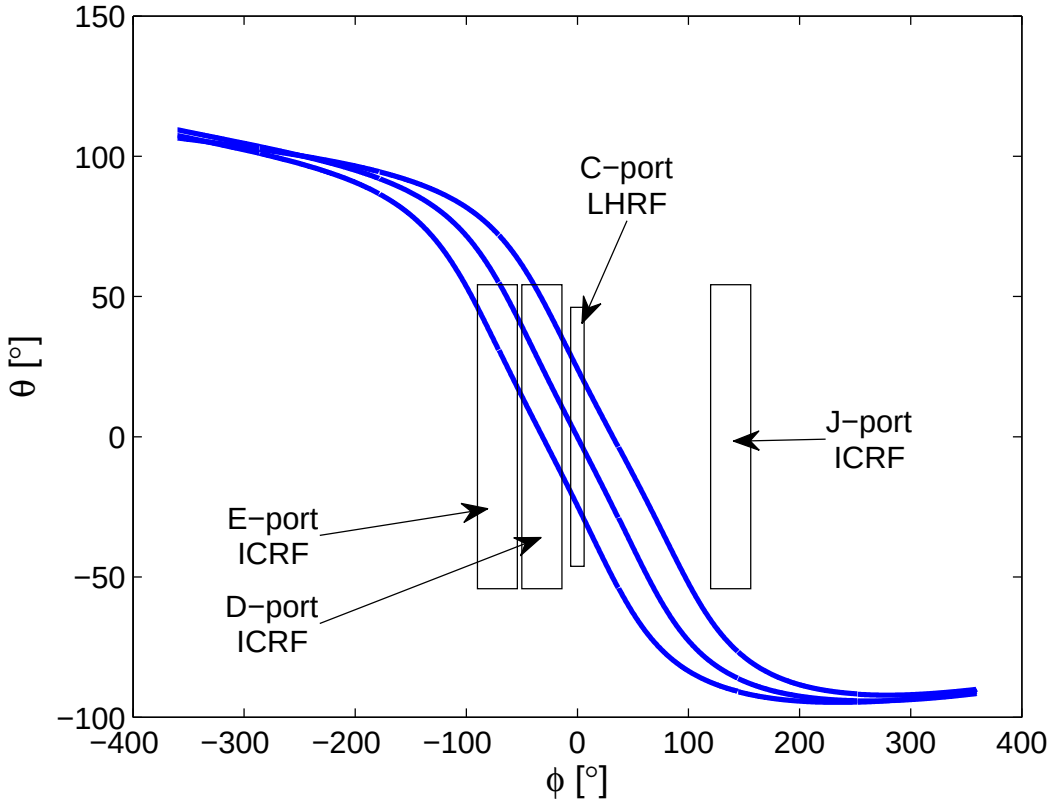

Figure 3-15: Magnetic field line map showing connection between the LH and ICRF antennas. The plot is generated by calculating the poloidal angle with respect to the magnetic axis, θ, as a function of the toroidal angle, ϕ, along a field line. The midplane of the LH antenna is located at (0,0). The D-port ICRF antenna has the closest connection to the LH coupler at C-port, whereas the J-port ICRF antenna is not connected to the LH coupler.

edge density measured on the LH Mid Langmuir probe while the line averaged density decreases. Figure 3-18 shows that Γ^2 is slightly lower for LSN H-mode discharges as compared to similar USN L-mode discharges. The data shown are for 2.4 MW of ICRF from the J-port antenna.

3.2.6 Localized Gas Puffing

Two gas capillary tubes were installed adjacent to the LH coupler prior to the FY2008 run campaign. The purpose of these capillaries is to locally increase the plasma density in front of the launcher to improve coupling without increasing the core density. It is desirable to keep the core density low since the current drive efficiency is inversely proportional to plasma density. JET [36] and ASDEX [56] have improved LH wave coupling to the plasma in low density ($n_{edge} < n_{cut}$) conditions by puffing gas from a manifold near the LH antenna. Figure 3-19 shows the location of the capillaries as seen from inside the tokamak. The two capillaries are located near the top D-side and bottom B-side corners of the LH antenna. This choice of location allows the flux tubes connected to the capillaries to intersect as many waveguides as possible. The capillaries were tack welded to the inner surface of the limiter "box" approximately 6 cm radially from the edge of the limiter, with the tube openings pointing radially at the plasma. The capillaries are driven by the Neutral Gas Injection Array (NINJA) system [57], which allows for independent control of the two capillaries.

Figure 3-20 shows the LH camera view before and during puffing from the launcher capillaries. When the gas is injected through the capillaries, a diffuse glow is visible in the upper D-side and lower B-side of the antenna. The glowing indicates that the injected gas diffuses both radially and poloidally prior to ionization. The glow does not spread toroidally, however, which indicates that the neutral gas does not diffuse toroidally beyond the LH limiters prior to ionization. The ionization must therefore occur before the gas diffuses beyond the edge of the limiter shadow.

At a given value of line averaged density, the local density measured by the LH

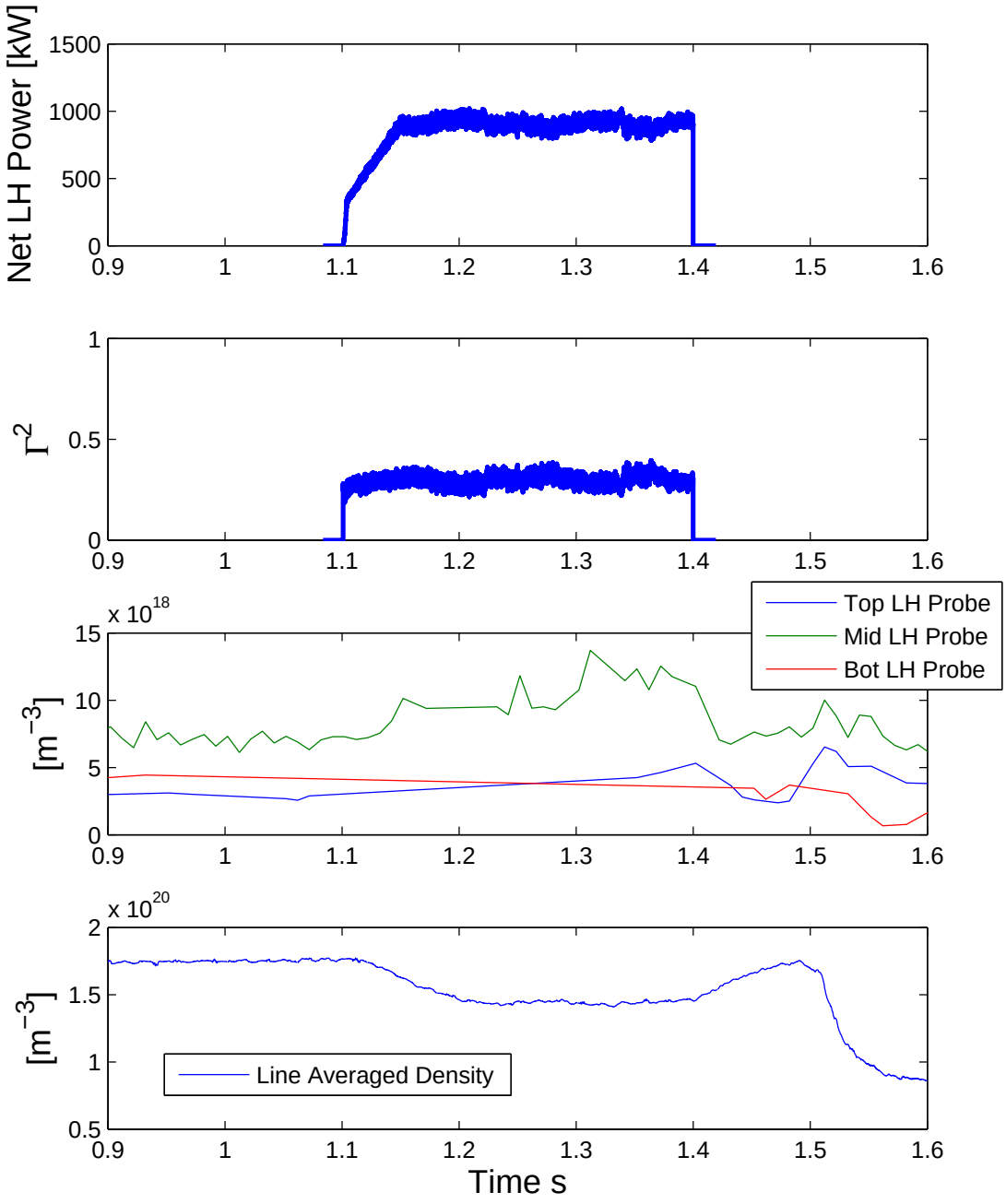

Figure 3-16: LH wave coupling during an ICRF heated H-mode. Although the line averaged density decreases during the LH pulse, the edge density stays constant or rises during the application of LHCD. Shot number = 1080306013.

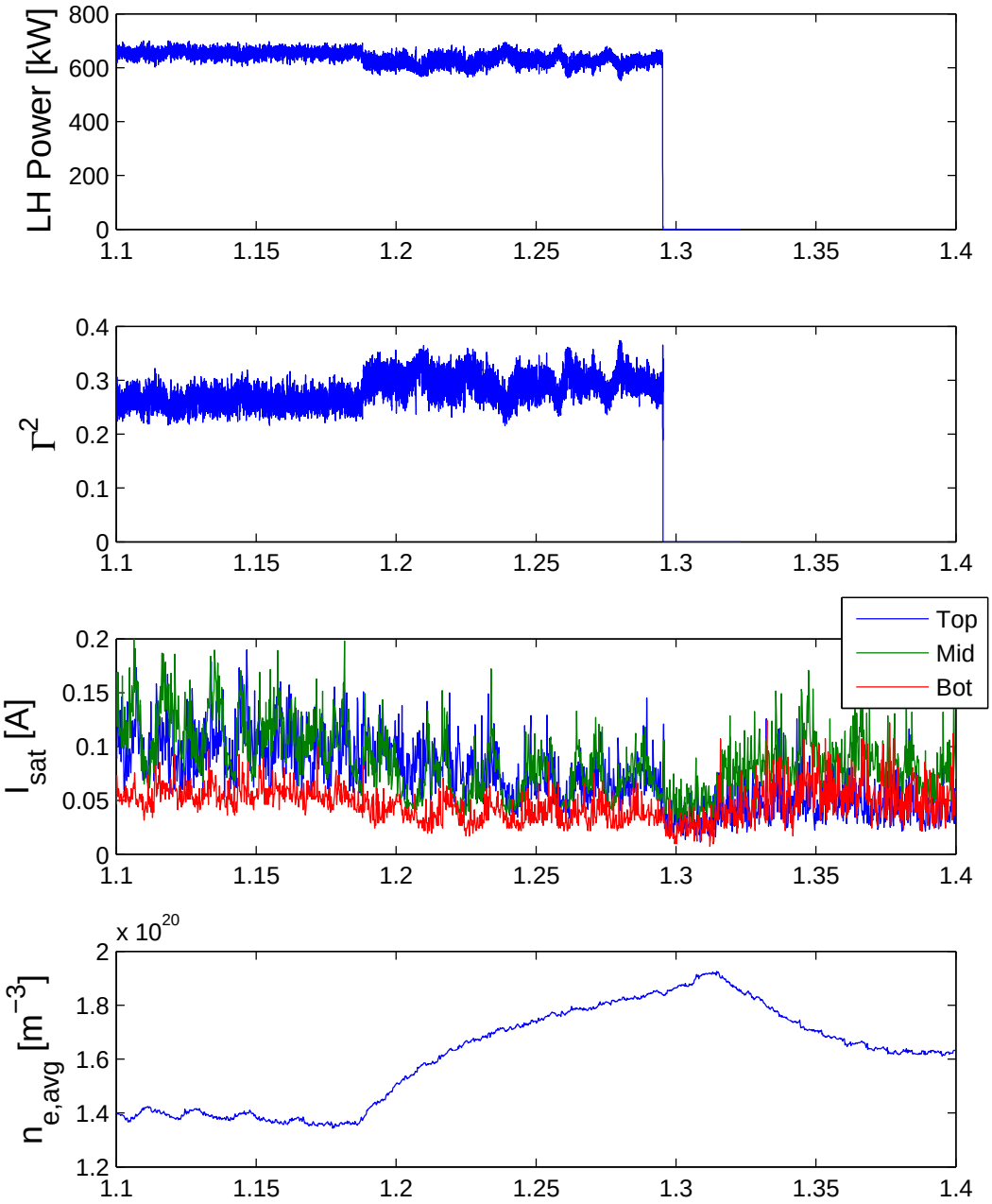

Figure 3-17: LH wave coupling during an LHCD triggered H-mode. The H-mode transition occurs at 1.19 seconds. Shot number = 1070523016.

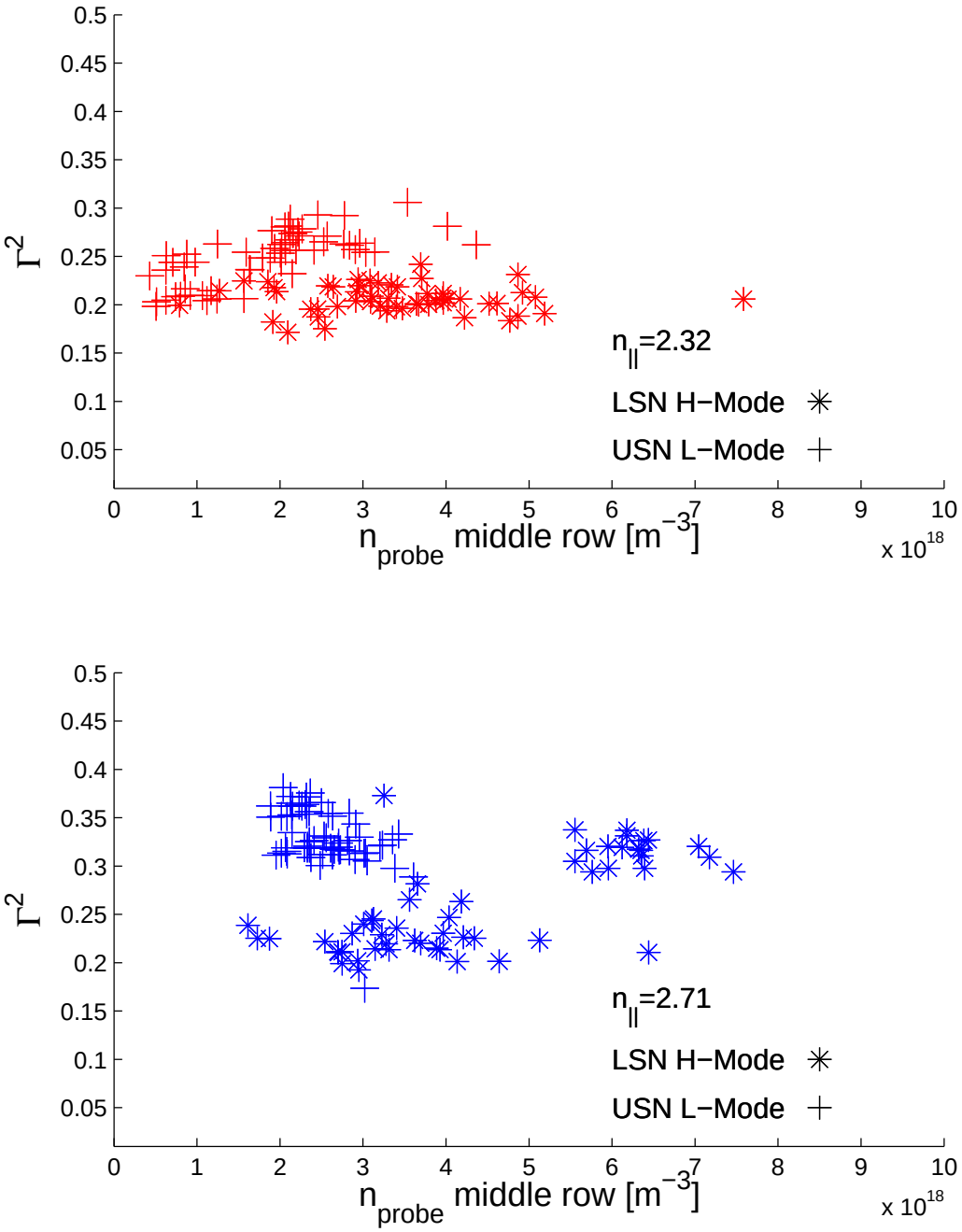

Figure 3-18: LH wave coupling in the presence of ICRF for H- and L-mode discharges. 2.4 MW of ICRF from J-port antenna in all shots. Data in red is for $n_{||}$=2.32, while data in blue is for $n_{||}$=2.71.

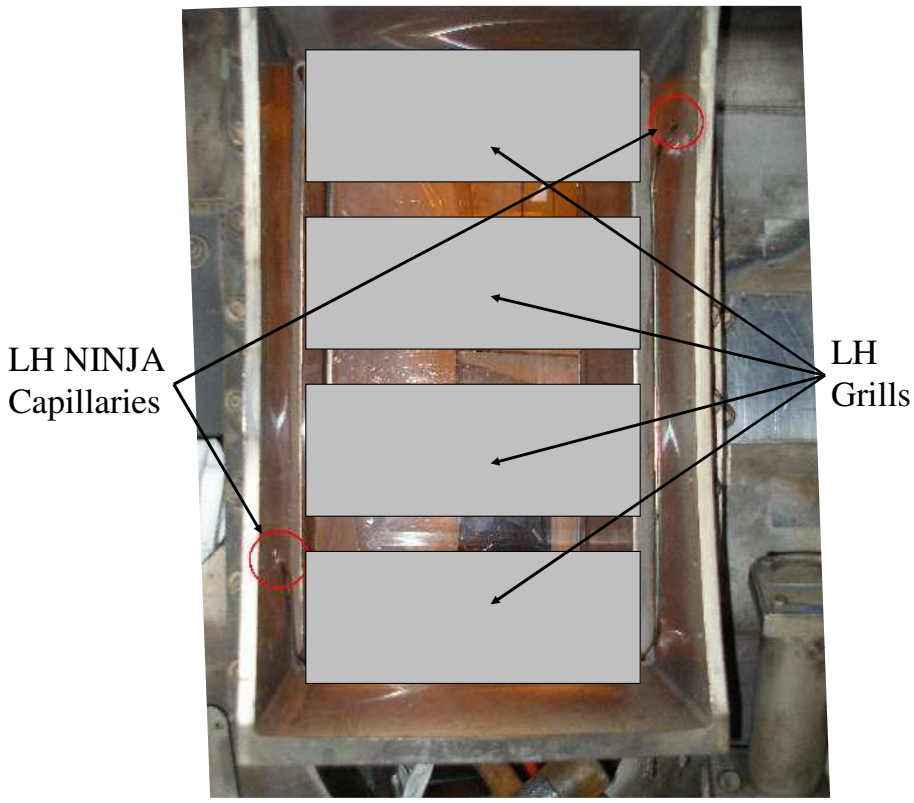

Figure 3-19: Image of the location of the gas puffing capillaries as seen from inside the tokamak. The two capillaries are circled in red in the image. Approximate locations of the four LH waveguide rows are shown in gray.

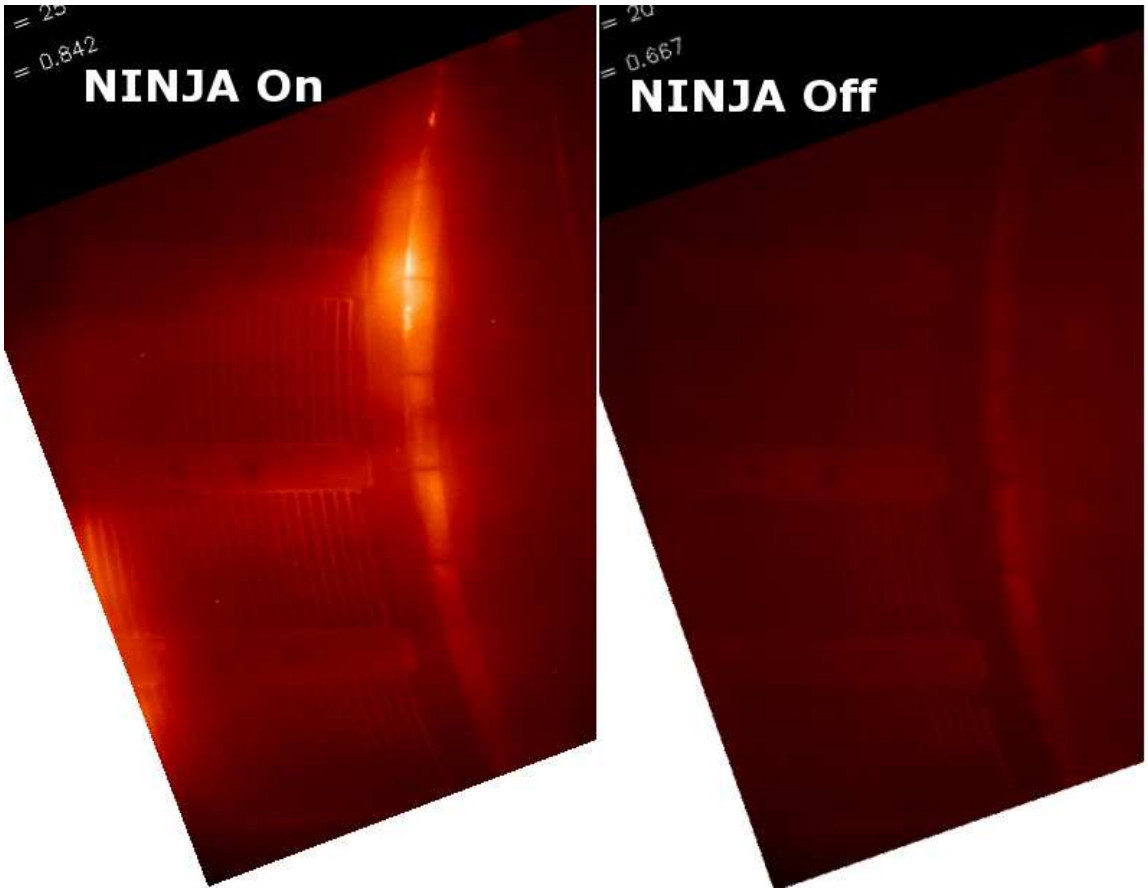

Figure 3-20: Image of LH launcher with gas puffing on (left) and off (right). The emission visible in the upper right and lower left of the image indicates a local increase in recycling in the vicinity of the gas injection capillaries.

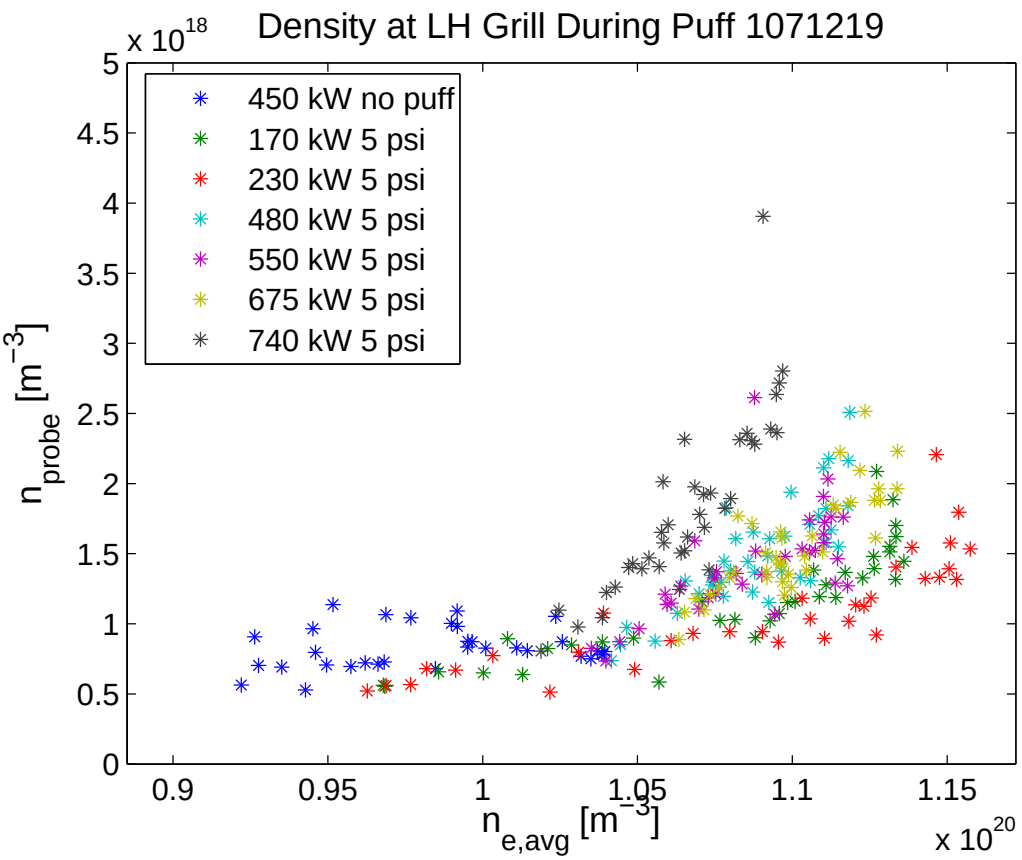

Figure 3-21: LH probe density vs line averaged density during gas puffing. Plasma density in front of the launcher rises much more sharply as a function of line averaged density in the presence of high power LHRF.

Langmuir probes is higher with gas puffing than without puffing. A gas plenum pressure of 5psi, corresponding to an injection rate of $\sim$ 7 torrL/sec, was found to augment the local density without drastically increasing line averaged density. Figure 3-21 shows that the density measured by the LH Langmuir probes is higher at a given value of line averaged density in the presence of high power LHRF with auxiliary gas puffing. This is consistent with the physical picture that the LH wave fields are partly responsible for the ionization of the injected gas [36].

Despite locally increasing the edge density in front of the LH antenna, the gas puffing system was not found to substantially improve the coupling of LH power to

the plasma. A series of coupling experiments were conducted with the launcher pulled back 5 mm from the LH limiter. Although the density measured by the Langmuir probes was raised well above cutoff, the reflection coefficient did not drop, and the arc protection system tripped continually. This may be due to a non-monotonic density profile within the local limiter box. If the plasma density drops below cutoff somewhere between the LH launcher and the edge of the limiter, this will have a detrimental effect on wave coupling. The LH Langmuir probes are not capable of detecting the cutoff region if it is located more than 1.5 mm from the launcher.

3.3 Conclusions

A variety of edge density profile types have been used in conjunction with the GRILL coupling code and compared to low power experimental coupling results. For each type of density profile, there exists a free parameter which can be varied to obtain good agreement between the theory and experiment. In the absence of accurate density profile measurements which would eliminate these free parameters, it is not possible to determine which profile type is most similar to the experimental profile, and therefore the model itself cannot be fully tested. The "fixed edge density-variable density gradient" model, which has only one free parameter versus multiple free parameters for the other models, gives the best agreement with experimental results above $n_{probe} = 4 \times 10^{17}$ m^{-3}. This model requires a negative density gradient for measured edge densities below 4×10^{17} m^{-3}, and consequently its validity in that regime is questionable.

Similarly, deleterious effects on wave coupling at high power and in the presence of high power ICRH are observed, although without density profile measurements it is not possible to determine if the effects are due to a modification of the edge conditions or an as yet undetermined physical mechanism. It is necessary to make a localized measurement of the density profile on field lines which pass directly in front

of the LH launcher grills to improve the understanding of coupling physics under these conditions.

Chapter 4

Plasma Edge Modification and Launcher Damage

The conditions necessary for good coupling described in Chapter 3 require the LH antenna to be located in a region where the electron density is a factor of 5-10 above cutoff ($n_{cut} = 2.7 \times 10^{17}$ m^{-3}). Although the density and temperature near the launcher are several orders of magnitude lower than the density and temperature inside the separatrix, there can still be substantial heat flux on the antenna. The long term survivability of an LH antenna is a major concern for the proposed LHCD systems on future tokamaks such as ITER and DEMO. LH launchers on large tokamaks such as JET have sustained considerable damage due to fast electrons excited at the edge by the LHRF wave fields [58]. Increases in the plasma density and temperature observed on the LH Langmuir probes during high power LHCD will increase the parallel heat flux from the plasma to the launcher. In addition to the coupling issues associated with combined operation of magnetically linked ICRF and LHCD antennas, damage to the LHCD launcher on C-Mod has been caused by the D-port ICRF antenna.

4.1 Modification of the Plasma Edge with LHCD

The following sections describe observations of modification to the plasma edge and SOL caused by the application of high power LHCD. Some of these effects, such as an increase in visible line radiation, are localized to the launcher and the field lines which pass in front of it, while there are global changes to the pedestal and SOL as well. This chapter will focus on the changes to the SOL which are localized to the region near the LH launcher. The changes to the SOL far away from the launcher will be discussed in Chapter 5.

4.1.1 Visible Emission During High Power Discharges

During high power (>500 kW) operation of the LH antenna, bands of visible light are frequently observed across the face of the LH launcher. These bands can be seen both on the LH and WIDE2 digital video cameras, as shown in Figure 4-1. The bright bands are tilted at an angle approximately the same as the pitch of the magnetic field on the low field side of C-Mod, which is $\sim 7 - 10°$. Figure 4-2 shows the LH camera before and during a high power LHCD discharge. These bright bands are well modulated with the incident LH power, appearing on the video frame following the LH turn on, and disappearing on the frame following the LH turn off. Figure 4-3 shows the time history of the brightness on the mid-B Langmuir probe and the stripe across the C waveguide row for a 1.0 MW LH pulse. The brightest band is located across the C row, with less intense bands on the B and D rows. Banding is not frequently observed on the A row. This may be due to shape of the separatrix, which is typically closer to the middle and bottom rows of the launcher.

The visible light emitted in these bright stripes is due to electron impact line emission. The dominant visible spectral line for a deuterium plasma is known as D_α, and is emitted by electrons transitioning from the $n = 3$ to $n = 2$ quantum state of neutral deuterium. The brightness of this line is proportional to the ionization rate

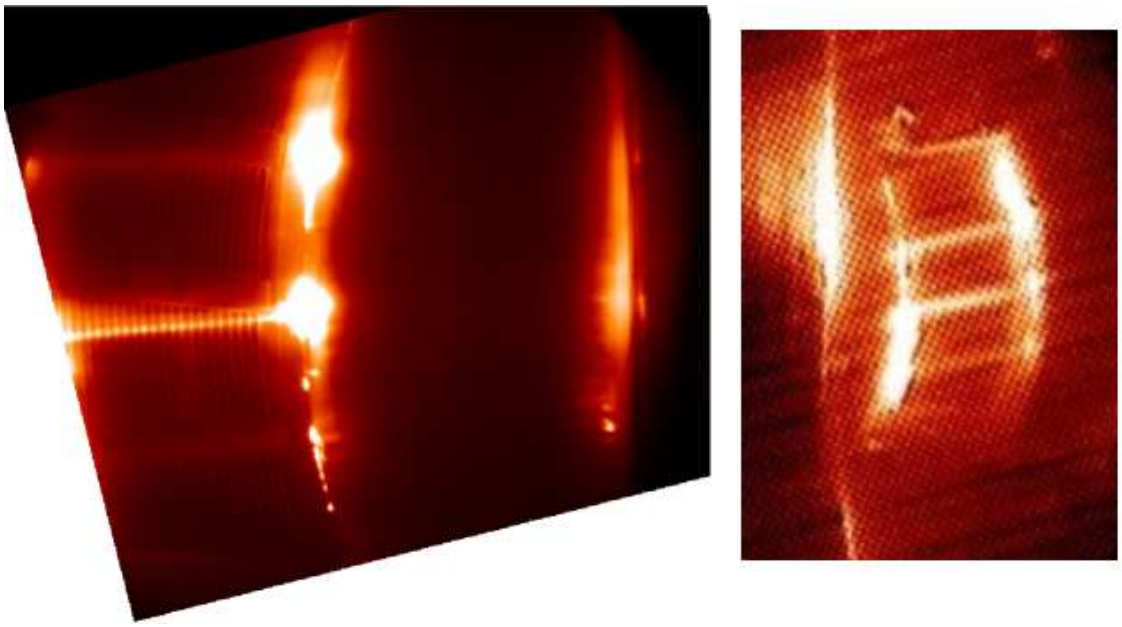

Figure 4-1: Visible plasma emission during high power LH as captured by the LH video camera (left) and the WIDE2 video camera (right). Bright stripes of light, tilted at the magnetic field pitch angle, can be seen across the face of the launcher. The image has been rotated and cropped to show the LH antenna in the correct orientation. The central column is visible to the right of the launcher in the LH camera image and to the left of the launcher in the WIDE2 camera image. The apparent difference in curvature between the two images is due to the sight lines of the cameras. The left image is taken from the B-port side of the launcher while the right image is taken from the D-port side of the launcher. Shot number = 1080109030.

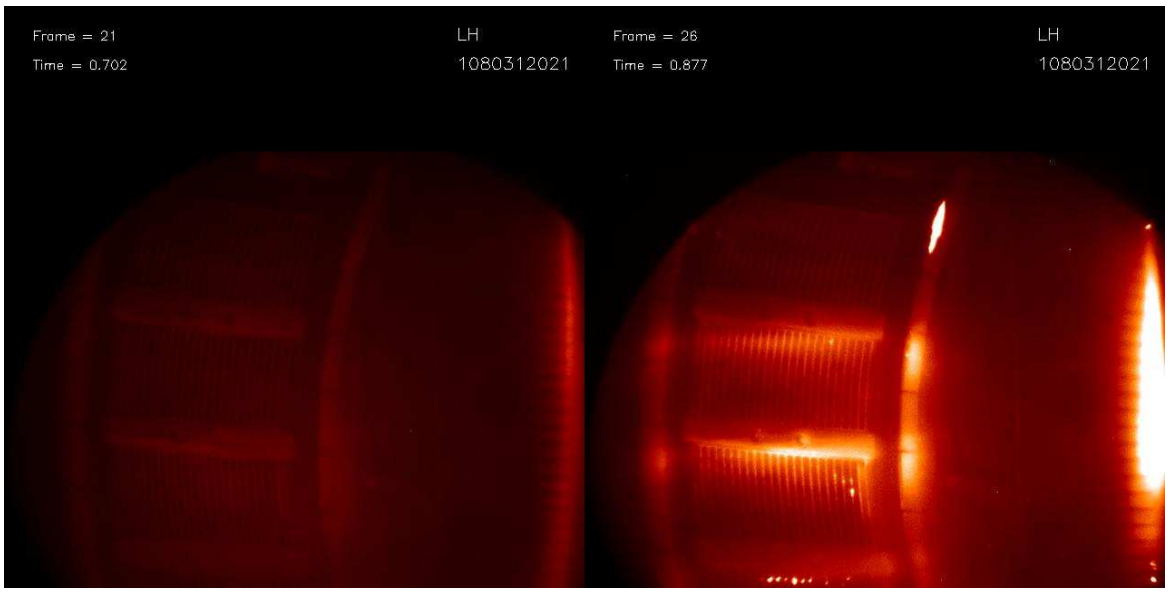

Figure 4-2: Comparison of visible plasma emission as captured by the LH video camera before high power LH (left) and during the high power LH (right). The bright lines across the launcher face are seen to be distinct from and titled at an angle with respect to the horizontal spacer bars. Both images are scaled identically. Shot number = 1080312021.

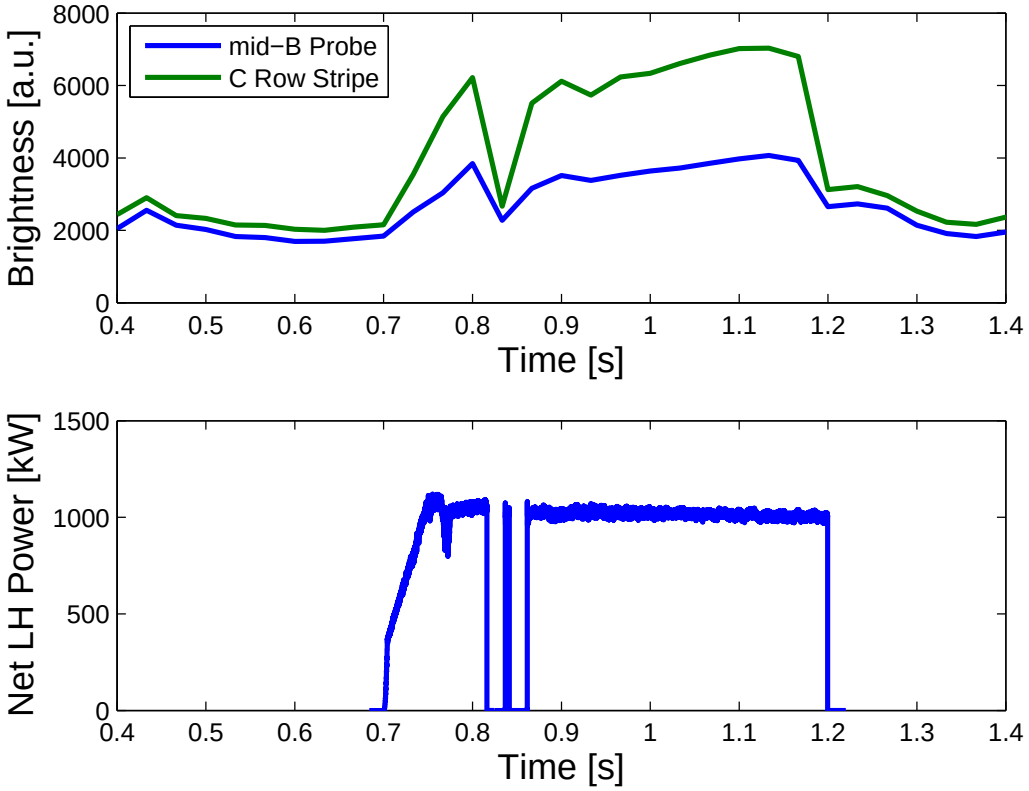

Figure 4-3: Time history of visible emission on the LH launcher for the mid-B Langmuir probe and the stripe across the C waveguide row. Shot number = 1080312020.

of deuterium in the plasma and can be used to estimate the line integrated plasma density along a line of sight through the SOL. Since the bright bands do not extend beyond the edge of the LH limiters on the left and right sides, the area of enhanced emission can be localized to a region toroidally bounded by the limiters and radially bounded between the location of the LH limiters and the LH launcher. By examining the relative change in brightness of the D_α emission at a position where the change in plasma density is known, we can extrapolate to other positions where the change in brightness is known but density measurements are unavailable. A convenient location to use as a baseline for this extrapolation is the Langmuir probe mounted on the B-side midplane of the LH launcher since it has a nearly identical viewing angle as the bright bands across the launcher but does not directly intersect the bright bands. Table 4.1 shows the change in brightness on the mid-B Langmuir probe as well as its change in density. The change in brightness for the bright stripe across the C waveguide row and its extrapolated change in density are also shown. Figure 4-4 shows the measured density at the mid-B probe and the estimated density in front of the C-row of waveguides as a function of net LH power. The measured changes in brightness (measured by the LH camera) and density on the mid-B Langmuir probe show that the increase in brightness correlates well with the increase in measured probe density. Changes in D_α brightness near the C waveguide row of $400 - 700\%$ are seen at the 1.0 MW net power level. This increase in D_α brightness corresponds to a density of $4 - 10 \times 10^{18}$ m^{-3} along the bright stripes. An increase in T_e measured by the LH Langmuir probes is observed with the increase in density. The electron temperature increases from ~ 10 to ~ 20 eV during LHCD, with the largest increases in temperature coming at the highest LH power levels.

Similar visible emission was observed on ASDEX during high power LHCD [54]. The emission was attributed to the formation of a vortex [59] caused by localized heating of the electrons in front of the LH launcher. The changes in density associated with the light on ASDEX were not assessed, although the edge temperature was

Table 4.1: Changes in D_α brightness and electron density on the LH launcher at high power.

Shot Number 1080226006	Power Level [kW] 1000	$\overline{n}_e$ [m^{-3}] 8.0×10^{19}
mid-B brightness [%] 205	mid-B n_e [m^{-3}] $1.57 \times 10^{18} \rightarrow 2.96 \times 10^{18}$	mid-B n_e [%] 188
C-row brightness [%] 403	C-row est. n_e [m^{-3}] $1.57 \times 10^{18} \rightarrow 5.82 \times 10^{18}$	mid-B T_e [eV] $10 \rightarrow 20$
Shot Number 1080312021	Power Level [kW] 1000	$\overline{n}_e$ [m^{-3}] 6×10^{19}
mid-B brightness [%] 390	mid-B n_e [m^{-3}] $1.49 \times 10^{18} \rightarrow 4.6 \times 10^{18}$	mid-B n_e [%] 308
C-row brightness [%] 731	C-row est. n_e [m^{-3}] $1.49 \times 10^{18} \rightarrow 8.6 \times 10^{18}$	mid-B T_e [eV] $7 \rightarrow 26$
Shot Number 1080312020	Power Level [kW] 1000	$\overline{n}_e$ [m^{-3}] 5.5×10^{19}
mid-B brightness [%] 235	mid-B n_e [m^{-3}] $1.18 \times 10^{18} \rightarrow 2.58 \times 10^{18}$	mid-B n_e [%] 219
C-row brightness [%] 435	C-row est. n_e [m^{-3}] $1.18 \times 10^{18} \rightarrow 3.85 \times 10^{18}$	mid-B T_e [eV] $7 \rightarrow 18$
Shot Number 1080402023	Power Level [kW] 800	$\overline{n}_e$ [m^{-3}] 7×10^{19}
mid-B brightness [%] 162	mid-B n_e [m^{-3}] $1.61 \times 10^{18} \rightarrow 2.65 \times 10^{18}$	mid-B n_e [%] 164
C-row brightness [%] 205	C-row est. n_e [m^{-3}] $1.61 \times 10^{18} \rightarrow 3.34 \times 10^{18}$	mid-B T_e [eV] $11 \rightarrow 16$
Shot Number 1080402026	Power Level [kW] 800	$\overline{n}_e$ [m^{-3}] 7.5×10^{19}
mid-B brightness [%] 214	mid-B n_e [m^{-3}] $1.73 \times 10^{18} \rightarrow 4.52 \times 10^{18}$	mid-B n_e [%] 261
C-row brightness [%] 320	C-row est. n_e [m^{-3}] $1.73 \times 10^{18} \rightarrow 6.75 \times 10^{18}$	mid-B T_e [eV] $11 \rightarrow 19$
Shot Number 1080402008	Power Level [kW] 500	$\overline{n}_e$ [m^{-3}] 7.5×10^{19}
mid-B brightness [%] 133	mid-B n_e [m^{-3}] $1.75 \times 10^{18} \rightarrow 2.27 \times 10^{18}$	mid-B n_e [%] 129
C-row brightness [%] 166	C-row est. n_e [m^{-3}] $1.75 \times 10^{18} \rightarrow 2.83 \times 10^{18}$	mid-B T_e [eV] $11 \rightarrow 15$

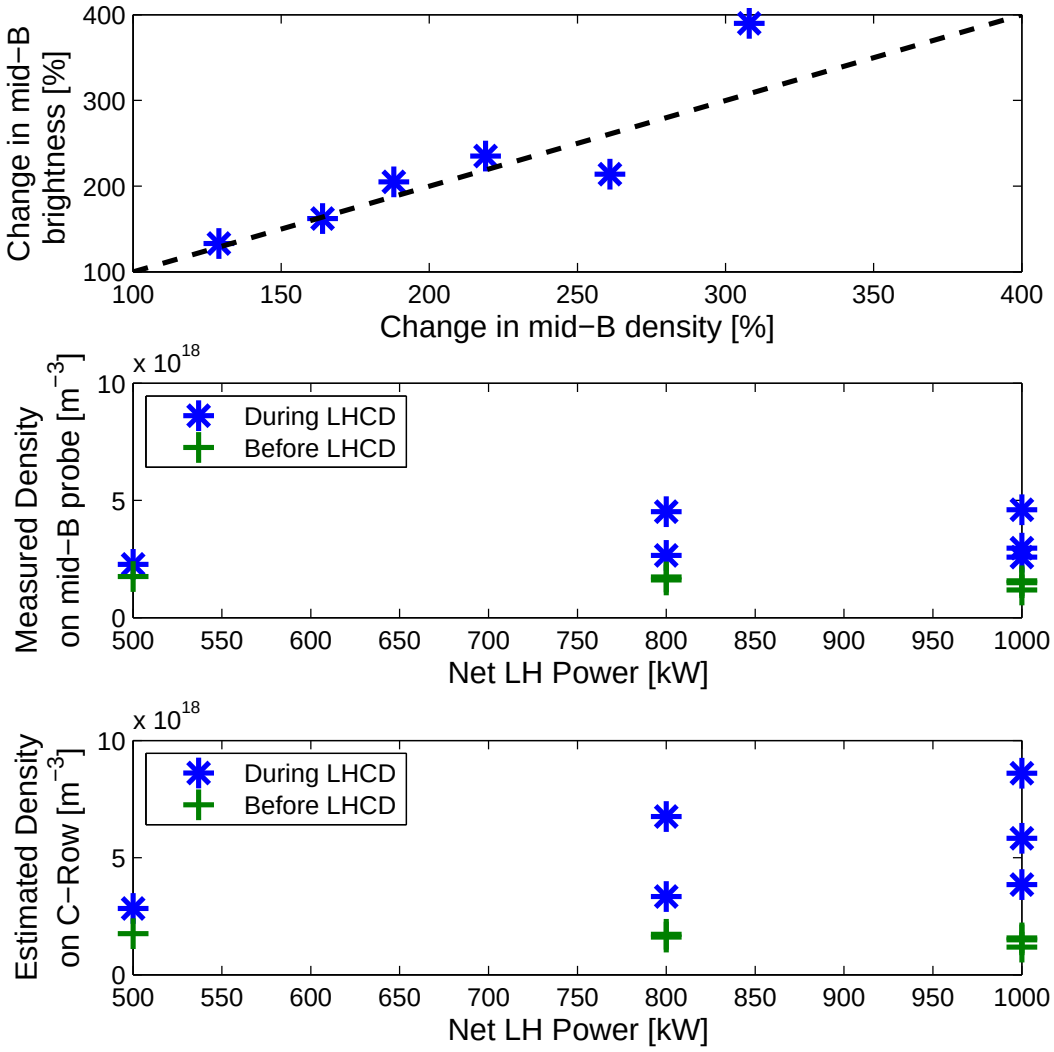

Figure 4-4: Change in brightness in the vicinity of the mid-B LH Langmuir probe as a function of change in density measured by the mid-B LH Langmuir probe. The dashed line indicates a 1:1 correspondence between change in brightness and change in density. (top) Density measured on the mid-B probe as a function of net LH power. (middle) Estimated density in front of the C-row of the LH launcher as a function of net LH power. (bottom)

estimated to increase by a factor of 1.5. An increase in visible emission was also reported during high power LHCD on JT60-U [60]. A corresponding increase in the density in front of the launcher, up to a factor of 10, was measured by Langmuir probes in front of the antenna. The heat flux on the LH launcher also increased as a result of the density enhancement. The peak heat flux measured was 1×10^5 W/m^2.

4.1.2 High Power Coupling

Non-linear coupling at high power, discussed in Section 3.2.3, suggests that the presence of high power LH waves modifies the edge density profile. Since the edge density measurement is an average over the 0.0015 m length of the Langmuir probe tips, multiple density profiles can exist for the same measured density. Furthermore, the bands of emission seen on the LH and WIDE2 cameras do not intersect the LH Langmuir probes located between the waveguide rows, but instead traverse across the middle of the waveguides. A change in density on the flux tubes where the bright bands are located will not result in a corresponding increase in the density measured by the Langmuir probes.

When compared with the smoothness of the low power coupling data in Figure 3-7, the large scatter of the data in Figure 3-13 indicates that either the edge density profiles are modified by the high power LH waves or an unknown non-linear phenomenon is changing the coupling behavior. If we assume that the coupling remains linear, then the coupling reflection coefficient, $\Gamma^2 \sim 20-30\%$ for $n_{||} = 1.55$, measured during high power operation at $n_{probe} = 4 \times 10^{19}$ m^{-3} corresponds to a density in front of the LH launcher waveguides $\geq 1 \times 10^{19}$ m^{-3} according to the models described in Section 3.2.2. This is similar in magnitude to the density estimated from the change in brightness described above.

4.2 Damage to the LH Launcher

Figure 4-5 shows the D row waveguide array of the Lower Hybrid launcher following the FY2008 run campaign. The septa between adjacent waveguides have melted, and in many cases liquid metal has flowed down the septum and hardened, thereby creating a "hill and valley" like profile along the length of the septum. These peaks protrude into the plasma farther than the undamaged section of the launcher, therefore receiving a higher heat flux and re-melting more readily.

The pattern of melt damage is angled from the center left to top right of the row, roughly parallel to the magnetic field and in the same location as the bright emission shown in Figures 4-1 and 4-2. As with the visible emission, the damage is most prominent on the C row, with less severe but still significant damage on the B and D rows. The A row shows the least melt damage compared with the other three rows.

The minimum power required to melt the waveguide septa in a fixed period of time can be estimated by solving the heat equation

$$\frac{\partial T}{\partial t} = k\nabla^2 T \tag{4.1}$$

where

$$k = \frac{\kappa}{c_p \rho}$$

and κ is the thermal conductivity of the material, c_p is the heat capacity, and ρ is the density. In keeping with the geometry of the coupler introduced in Section 3.1, we shall consider the plasma/coupler interface to be at $x = 0$, with the septum having a width of 0.0015 m in the z direction, and no variation in the y direction. If we assume uniform heating across the face of the coupler in the x direction and ignore radiative heat loss, we can reduce Equation 4.1 to the following one dimensional

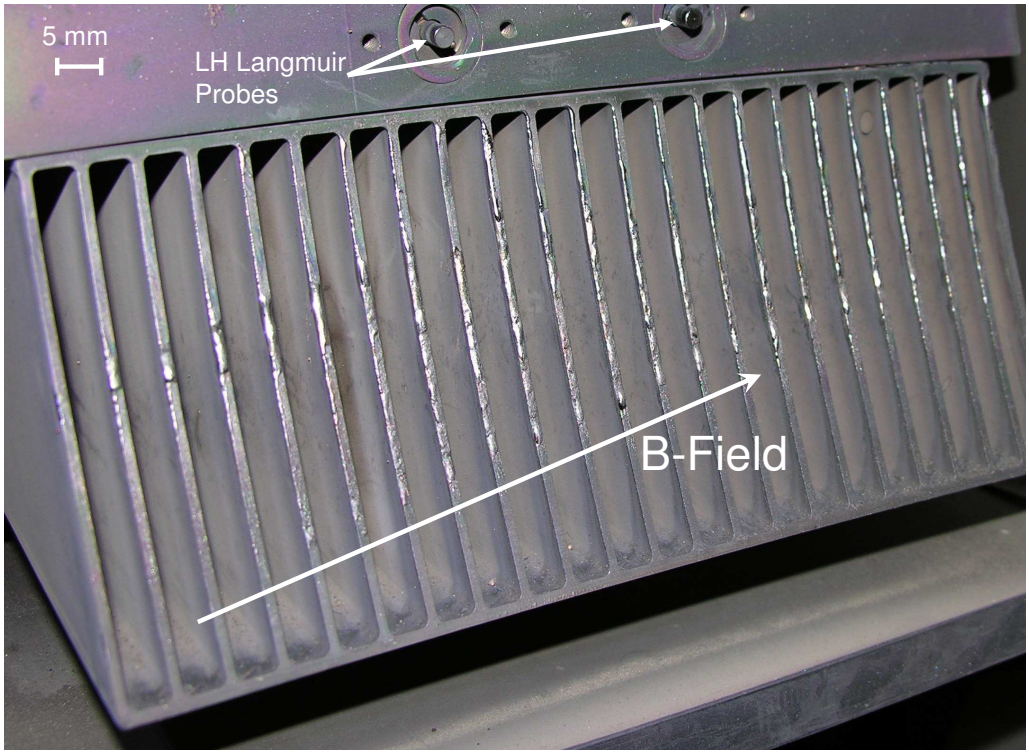

Figure 4-5: Melting of D row waveguide septa following FY2008 run campaign.

partial differential equation

$$\frac{\partial T}{\partial t} = kT'' \tag{4.2}$$

where the prime denotes a derivative with respect to x. We can solve the one dimensional heat equation by first setting the initial condition

$$T(0, x) = C \tag{4.3}$$

and the boundary conditions

$$\frac{\partial}{\partial x} T(t, 0) = \frac{q}{\kappa} \tag{4.4a}$$

$$T(t, \infty) = C \tag{4.4b}$$

where C is the initial temperature of the coupler in Kelvin and q is the power density incident on the coupler face in W/m^2.

Equation 4.2 can be solved numerically to determine the heat flux necessary to melt the waveguide septa in 0.5 s. The physical properties of the 304L stainless steel used to fabricate the coupler are $\kappa = 16.3$ W/(m K), $c_p = 500$ J/(kg K), and $\rho = 8030$ kg/m^3, which gives $k = 4.06 \times 10^{-6}$ m^2/s. With an initial condition of $C = 300$ K, the heat flux q needed to increase the temperature at $x = 0$ to the melting point of the stainless steel (1700 K) in half a second is 1.42×10^7 W/m^2. Figure 4-6 shows the evolution of temperature as a function of time and space for these parameters. It can be seen that the heat only diffuses ~ 1 mm during the course of the 0.5 s LH pulse. Because the heat diffuses such a short distance in 0.5 s, this treatment of the heat equation is applicable not only to the case where the septum is heated from the plasma facing surface, but also for the case where the heat is applied along the broad wall of the septum.

If the heat flux of 1.42×10^7 W/m^2 is evenly distributed across all 92 waveguide septa, this corresponds to a total incident heating power of 116 kW across the front of the launcher, or $\sim$10% of the net LH power during a high power discharge. Given

that the damage covers approximately half of the launcher structure, a total heating power of ∼50 kW is required to produce the observed damage.

4.2.1 Enhanced Parallel Heat Flux due to Plasma Density and Temperature Increase

One possible cause for the damage observed on the LH antenna is an increase in parallel heat flux from the plasma to the antenna during LHCD. This may be due to an increase in plasma temperature and/or density observed during high power LHCD experiments, which will naturally increase the heat flux to the launcher from the plasma.

Since plasma conduction along field lines is many orders of magnitude greater than across the field, even for grazing angles of incidence the parallel heat flux dominates over the perpendicular heat flux. The parallel heat flux is [53]

$$q_{||} = \gamma n_i c_s k_B T_i \tag{4.5}$$

where $\gamma \approx 10$ [61], n_i is the ion density, $c_s = \sqrt{k_B T_i / m_i}$ is the ion sound speed, k_B is the Boltzmann constant, m_i is the ion mass, and T_i is the ion temperature. For a poloidal flux surface shape which is not tangent to the shape of the LH launcher, the magnetic field lines will intersect the launcher surface at a finite angle. Multiplying the parallel heat flux by the dot product of the magnetic field line with the surface normal of the septum gives the incident heat flux on the face of the launcher

$$q_{laucher} = q_{||} \hat{b} \cdot \hat{n} = q_{||} \sin(\theta_p) \sin(\theta_f) \tag{4.6}$$

where θ_p is the pitch angle of the magnetic field at the launcher and θ_f is the angle created by the tangent to the flux surface and the tangent to the launcher in the poloidal plane. Assuming typical values for both angles of 10°, a parallel heat flux

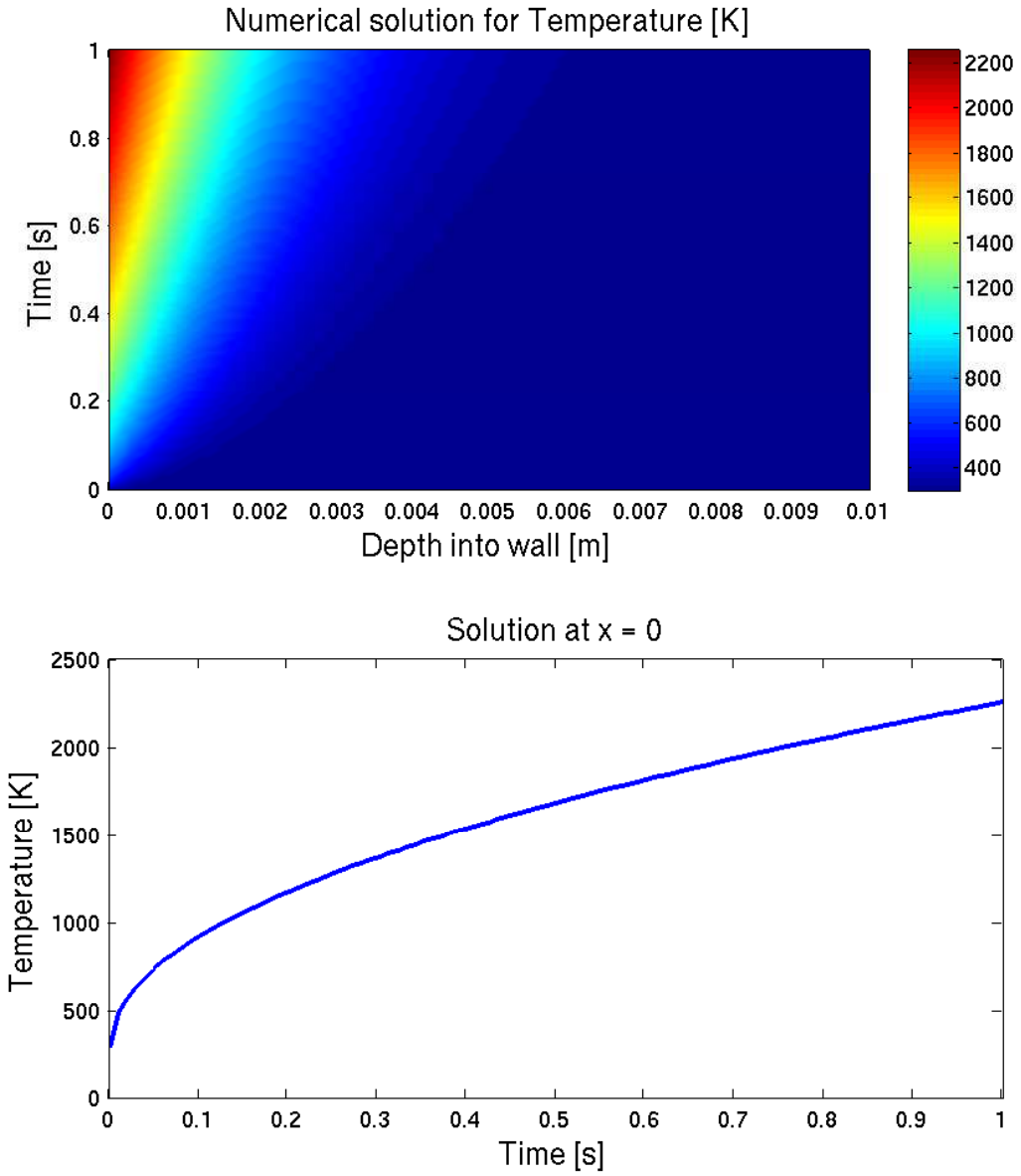

Figure 4-6: Solution of the 1D heat equation for the coupler geometry. The temperature at the plasma facing surface ($x = 0$) reaches the melting point of 304L stainless steel (1700 K) at 0.5 s for a heat flux of 1.4018×10^7 W/m^2.

of $\sim 5 \times 10^8$ W/m^2 would be required to deliver the necessary power to melt the launcher face in 0.5 s. Heat fluxes of this magnitude are not possible away from the separatrix.

Since there is some finite difference between the toroidal curvature of the LH launcher and the magnetic field, there will also be a narrow leading edge on the side of each septum. In this case, the field line angle of incidence is approximately 80° with respect to the leading edge and the required parallel heat flux is reduced to 1.4×10^7 W/m^2. A close inspection of the launcher melting damage shows an asymmetry in the damage location on each septum. For septa in the A and B rows, the melting is most pronounced on the right side of each septum when looking from the plasma toward the launcher, while on the C and D rows the melting is most pronounced on the left side of each septum. This asymmetry is consistent with the bulk of the heating taking place on the leading edge formed where each septum emerges from the shadow created by the adjacent septum. Since the pitch of the magnetic field is such that field lines connect from the lower left to the upper right of the launcher, a flux surface with a smaller radius of curvature than the LH launcher (as is the case in C-Mod) will create leading edges on the left side below the tangent point, and on the right side above the tangent point. Figure 4-7 shows the difference in curvature radius between the plasma shape and the LH launcher. Figure 4-8 shows a top-down view of the geometry of the leading edges. The asymmetry is most pronounced on the A and D rows as those rows are least tangent to the flux surface shape. The curvature mismatch between the LH launcher and the flux surfaces also creates a leading edge on the horizontal surfaces at the bottom of the A/B row waveguides, and at the top of the C/D row waveguides. Substantial melt damage can be seen along the bottom edge of the B row and top edge of the C row waveguides where the field lines intersect the launcher structure on a leading edge.

Substituting typical values measured by the LH Langmuir probes of $n_e = 1 \times 10^{18}$ m^{-3} and $T_e = 10$ eV into Equation 4.5 gives a value of 5×10^5 W/m^2 for $q_{||}$.

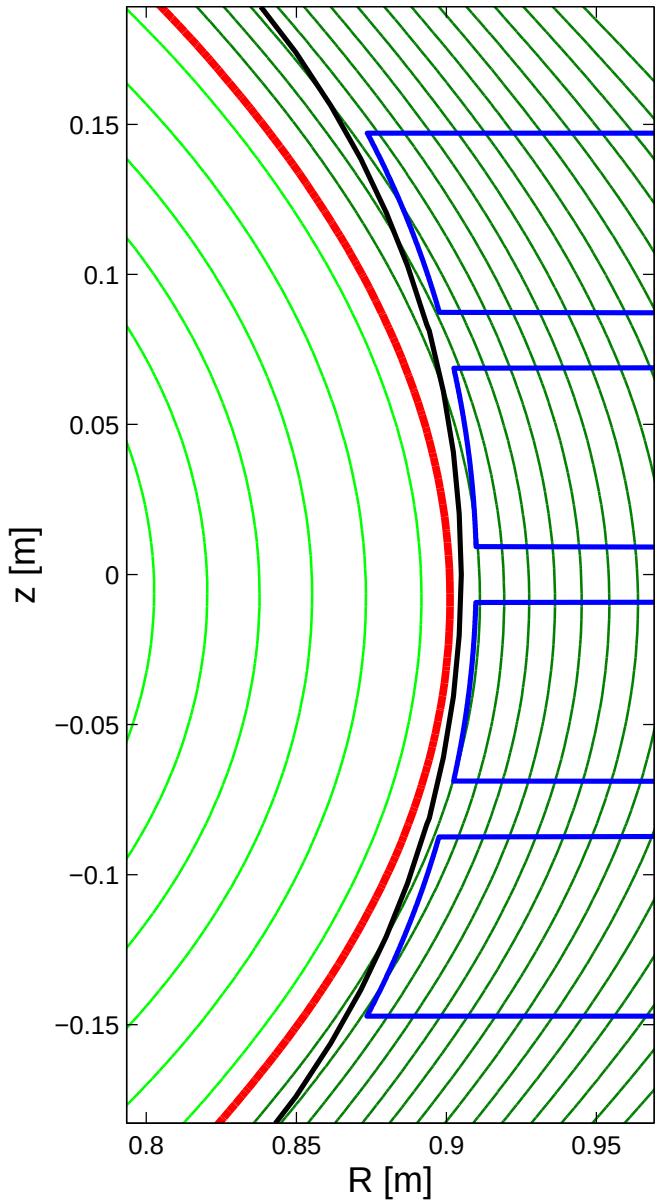

Figure 4-7: Poloidal cross-section showing the shape mismatch between plasma flux surfaces and LH launcher. Flux surfaces are shown in green with the separatrix in red. The black curve is the main limiter shape and the blue lines are the four rows of the LH launcher. The plasma current and toroidal magnetic field are both out of the page.

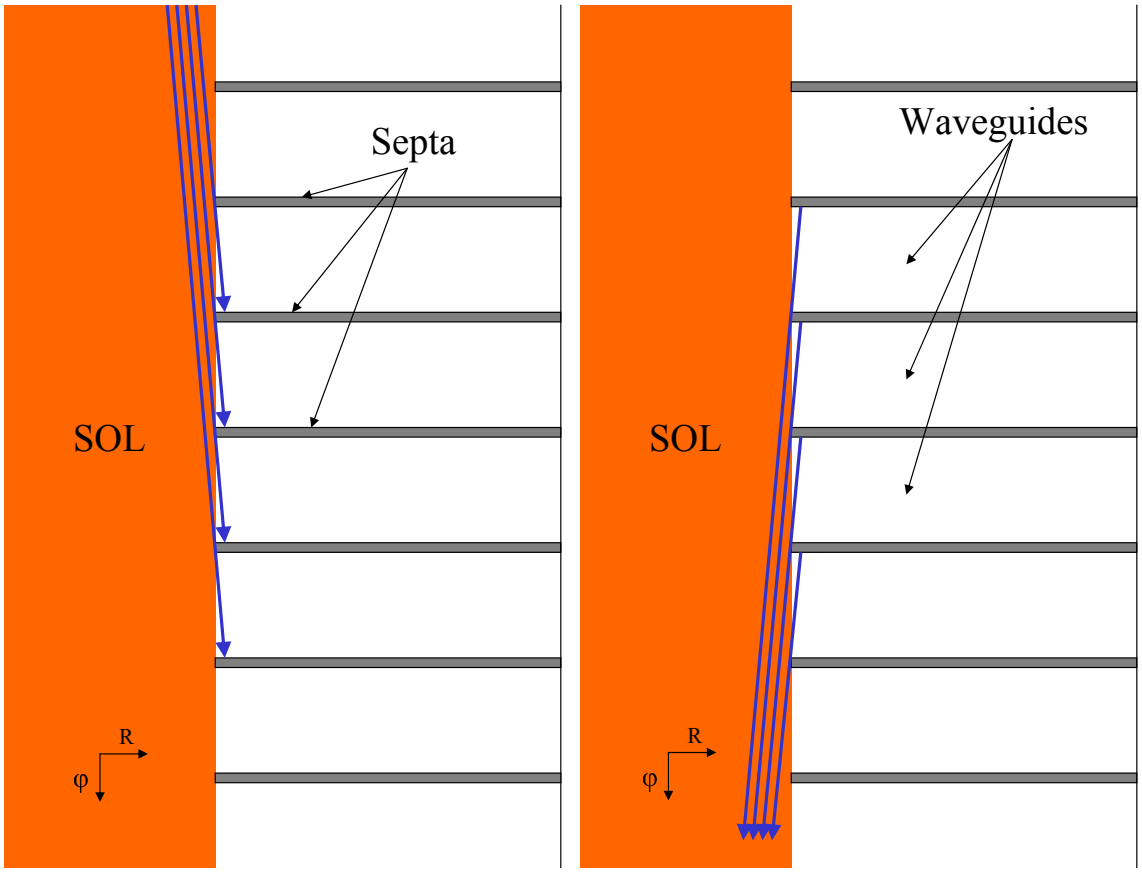

Figure 4-8: Top-down view of the formation of leading edges on the LH launcher septa. The blue arrows indicate the direction of the magnetic field. Misalignment between the shape of the coupler and the flux surfaces in the poloidal plane (see Figure 4-7) creates narrow leading edges on the sides of the waveguide septa. Leading edges are formed on opposite sides of the septa for C/D rows (left panel) and A/B rows (right panel). The plasma current and toroidal magnetic field are both in the ϕ direction.

At this density and temperature, the heat flux is not sufficient to melt the launcher face in 0.5 s even with normal incidence of the field lines. The necessary heat flux to melt the launcher in 0.5 s with grazing incidence of field lines on the face of the launcher can be obtained by increasing the temperature to 100 eV and the density to 1×10^{20} m^{-3} as shown by the dotted black line in Figure 4-9. For the leading edge case with nearly normal incidence, the necessary density and temperature are reduced to approximately 1×10^{19} m^{-3} and 20 eV. The dashed line in Figure 4-9 shows the contour of $q_{||} = 1.4 \times 10^7$ W/m^2. This density and temperature is at the upper end of the range recorded by the LH Langmuir probes. Due to the localization of visible emission described in Section 4.1.1, it is reasonable to conclude that the plasma density and temperature along these bands exceeds the measurements from the Langmuir probes and meets the conditions necessary to melt the launcher septa in 0.5 s.

4.2.2 Collisional Damping of LH Waves

By adding an imaginary component to the electron mass in the cold plasma dispersion relation, $m_{coll} = m_e(1 - i(\nu_0 + \nu_{ei})/\omega)$, it is possible to estimate the power lost by the wave due to elastic collisions in the plasma. The electron-neutral collision frequency is [6]

$$\nu_0 = n_0 \sigma_s \sqrt{k_B T_e / m_e} \tag{4.7}$$

where n_0 is the neutral density, $\sigma_s \sim 5 \times 10^{-19}$ m^2 is the electron neutral cross section, and $\sqrt{k_B T_e / m_e}$ is the thermal velocity of the electrons. The edge neutral density can be calculated using the ideal gas law

$$n_0 = \frac{P_0}{k_B T} \tag{4.8}$$

where P_0 is the neutral pressure, measured to be ~ 0.01 Pa on the LFS midplane of C-Mod at G-port, and $k_B T$ is the neutral temperature measured in J. This gives a

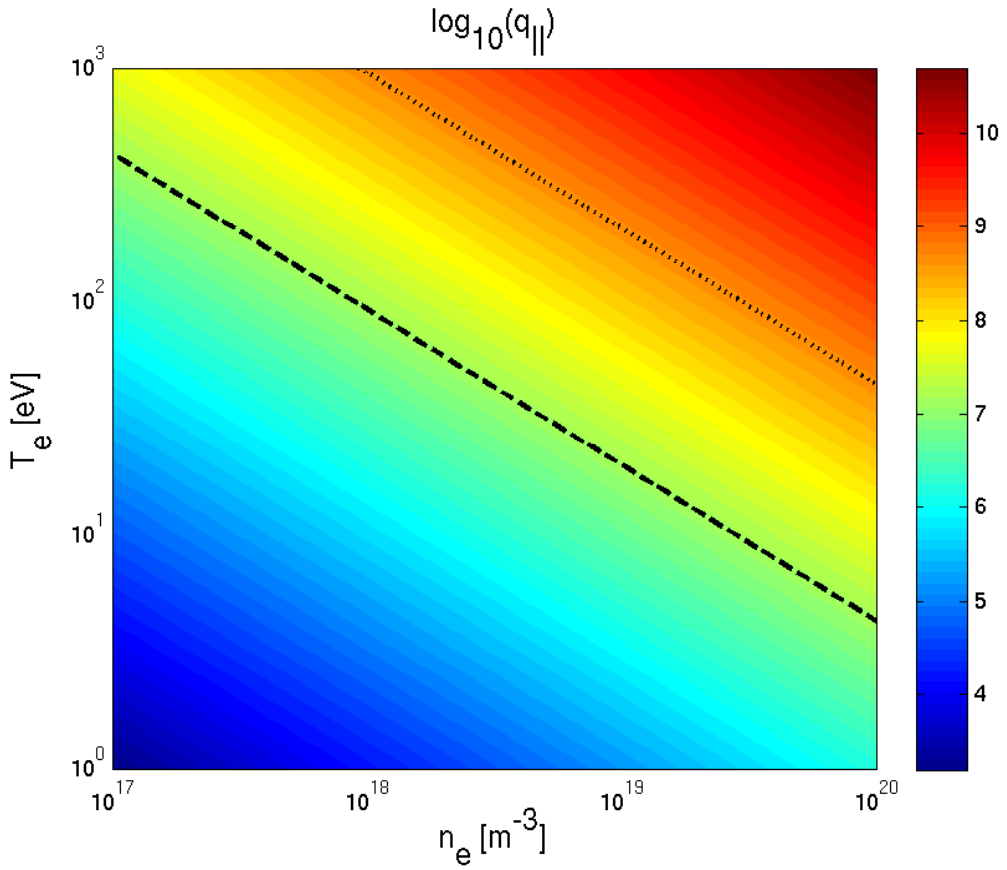

Figure 4-9: Parallel heat flux as a function of n_e and T_e. The color bar corresponds to $\log_{10}(q_{||})$. The dotted line represents a parallel heat flux of 4.6×10^8 W/m^2, at which point the surface of the coupler will reach the melting point in 0.5 s with grazing incidence of the magnetic field. The dashed line represents a parallel heat flux of 1.4×10^7 W/m^2, at which point the surface of the coupler will reach the melting point in 0.5 s on leading edges with nearly normal incidence of the magnetic field.

neutral density of $\sim 3 \times 10^{18}$ m^{-3}. The electron-neutral collision frequency is then $\sim 2 \times 10^6$ Hz for $T_e = 20$ eV. The electron-ion collision frequency is [1]

$$\nu_{ei} = 1.33 \times 10^5 \frac{n_{20}}{T_k^{3/2}} \tag{4.9}$$

where n_{20} is the electron density in units of 10^{20} m^{-3} and T_k is the electron temperature in keV. The electron-ion collision frequency is $\sim 5 \times 10^6$ Hz for $n_e = 1 \times 10^{19}$ m^{-3} and $T_e = 20$ eV. Combining electron-ion and electron-neutral collisions results in $k_{\perp i} = 0.13$ m^{-1} for $n_e = 1 \times 10^{19}$ m^{-3}, $P_0 = 0.01$ Pa, and $T_e = 20$eV. For a wave propagating through a region of plasma 1.5 mm thick in the radial direction (the radial distance between the LH limiters and the launcher) ~ 400 W of power is absorbed for $k_{\perp i} = 0.13$ m^{-1}. Decreasing the temperature from 20 eV to 10 eV increases the contribution of electron-ion collisions and reduces the contribution from electron-neutral collisions assuming that the electron and neutral densities remain constant. The net result is an increase in $k_{\perp i}$ to 0.28 m^{-1} corresponding to ~ 800 W of dissipated power.

The power lost due to electron-neutral collisions could increase if the neutral density is augmented by outgassing from the waveguide walls during high power operation. The neutral density used in this assessment is based on the neutral pressure measurement at the G-port midplane. A local source of neutrals at the LH launcher can be inferred from the frequently observed break in slope of the line averaged density at the onset of high power LHCD operation in L-mode on C-Mod.

4.2.3 Acceleration of Electrons in the Antenna Near Field by High $n_{||}$ Modes

The acceleration of electrons in the near field of multijunction type lower hybrid antennas has been reported across numerous experiments [62, 63, 64]. These fast electrons have been credited with generating intense localized heating on limiter and divertor surfaces as well as LH antennas. The study of these electrons begins with

solving the equation of motion for an electron in an electric field parallel to a magnetic field

$$\frac{\partial^2 z}{\partial t^2} = \frac{q}{m_e} E_z(z,t) \tag{4.10}$$

where z is the direction parallel to the DC magnetic field, q is the electron charge, m_e is the electron mass, and $E_z(z,t)$ is the component of the wave electric field parallel to the DC magnetic field.

For the TE_{10} waveguide mode, the peak transverse electric field on the midplane of the waveguide is [65]

$$E_z = \sqrt{\frac{4\omega\mu_0 P}{\beta ab}} \tag{4.11}$$

where $\beta = \sqrt{k_0^2 - k_c^2}$, $k_c = \pi/a$, and P is the power transmitted in the waveguide. In this geometry, a is the long dimension of the waveguide cross section and b is the narrow dimension, where b is aligned in the z direction. Using the parameters for the C-Mod grill, this results in an electric field on the waveguide midplane of 249 kV/m for 1MW of forward power divided evenly among 88 identical waveguides with dimensions of 0.060×0.0055 m.

The acceleration of electrons in the SOL by LH waves has been treated theoretically by Fuchs [66] and Goniche [67], and verified by particle-in-cell analysis by Rantamäki [68, 69]. If we consider the case of a thermal population of electrons in the presence of an electric field of the form

$$E_{||}(z) = \int_{-\infty}^{\infty} F(n_{||}) \exp(ik_{||}z) dk_{||} \tag{4.12}$$

there will be some small population of electrons with a parallel velocity resonant with each value of $k_{||}$. For a waveguide launching structure with periodicity $w + \delta$, where w is the waveguide width and δ is the septum width, the $n_{||}$ spectrum will have peaks spaced at intervals equal to

$$\Delta n_{||} = \frac{c}{f(w+\delta)} \tag{4.13}$$

Although there is a nonzero component of the spectrum between these peaks, the amplitude in the region between the dominant modes is very small as seen in Figure 4-10. To accelerate an electron with a parallel velocity resonant with $n_{||1}$ to interact with the next lower mode at $n_{||2} = n_{||1} - \Delta n_{||}$, the width of the resonance regions between adjacent modes must overlap [66]. This condition will be met if the increase in velocity of the particle due to interaction with the mode at $n_{||1}$ is greater than the spacing between the phase velocity of the two modes

$$\Delta v_{||} = c\Delta n_{||}/n_{||1}n_{||2} \tag{4.14}$$

Solving Equation 4.10 for the change in parallel velocity, $\Delta v_{||}$, gives

$$\Delta v_{||} = \frac{qE_{||}}{m_e\omega} \tag{4.15}$$

Combining Equations 4.14 and 4.15 gives a lower bound on $n_{||}$ for the transfer of an electron from a higher (slower) mode to a lower (faster) mode [67]

$$|n_{||}| \geq \sqrt{\frac{2\pi m_e c^2}{qE_{||}(w+\delta)}} \tag{4.16}$$

For an electric field of 250 kV/m with the geometry of the C-Mod antenna, this gives a minimum $n_{||}$ of 42.8. The parallel phase velocity of a LH wave with $n_{||} = 42.8$ is approximately 3 times the thermal velocity of a 20 eV electron distribution, which was shown in Section 1.5.3 to be the condition necessary for strong Landau damping of LH waves.

Since there is no direct measurement of the antenna spectrum in C-Mod, the launched $n_{||}$ spectrum must be calculated based on coupling theory. Only 0.2% of the power launched by the C-Mod antenna is contained in the region $100 > |n_{||}| \geq 42.8$ based onthe spectrum calculated by the GRILL code, corresponding to a total of $\sim$ 2 kW for a 1.0 MW LHCD pulse. Variation in the strength of the electric field

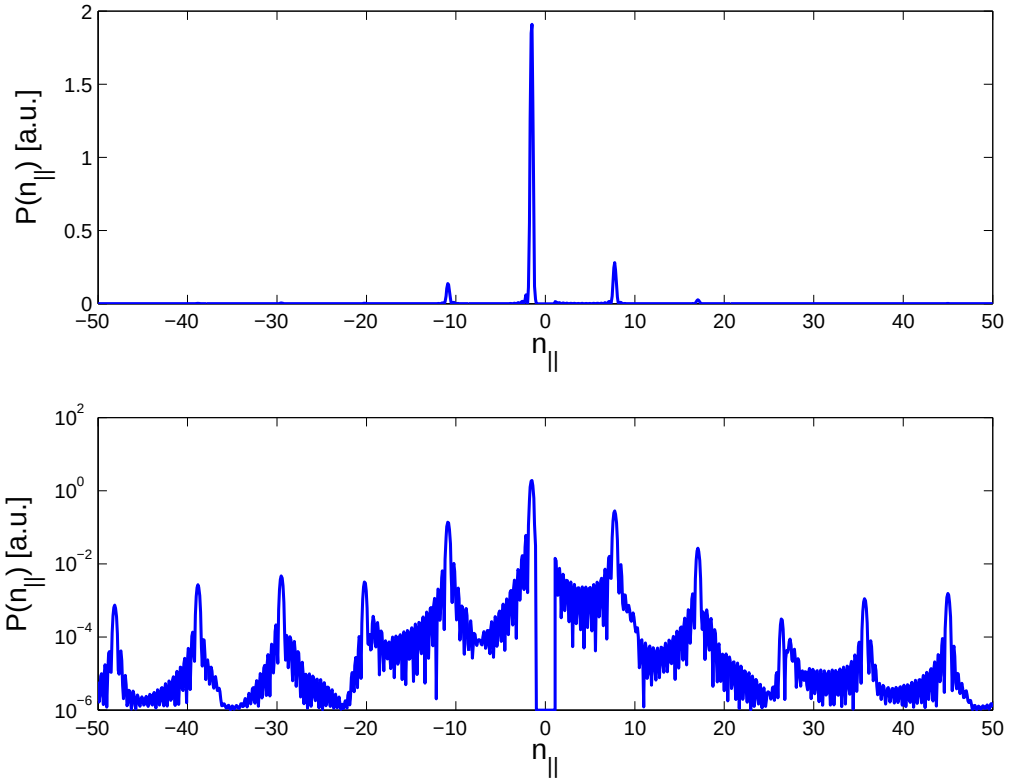

Figure 4-10: Power spectrum of launched $n_{||}$ including high harmonics up to $n_{||} = 50$ as calculated by the Grill code using the TE_{10}, TM_{11}, and TM_{12} waveguide modes. High $n_{||}$ components resonate with slower edge electrons.

in front of each waveguide of a non-infinite grill decreases the minimum $n_{||}$ necessary for resonance overlap by a factor of two [67], which increases the available power to $\sim$ 5 kW. This is significantly larger than the estimate for power lost to collisional damping in the previous section, but it is still an order of magnitude less than the power necessary to explain the damage to the launcher. Measurements of parasitic edge absorption from TdeV indicate that up to 10% of the incident LH power can be absorbed in the edge at high LHCD power and high edge density. It should be noted that the high $n_{||}$ part of the TdeV antenna spectrum is estimated to contain significantly more power than the C-Mod antenna spectrum.

4.3 ICRF Damage

In addition to the effects on coupling described in Section 3.2.4, interactions between the LHCD launcher on C-port and the D-port ICRF antenna have caused damage to the LH launcher. During operation of the D-port antenna with the LH launcher tangent to or slightly in the shadow of the LH limiters, injections were observed on the LH camera view. Injections were not caused by operation of the J- or E-port antennas. Figure 4-11 shows a typical injection from the LH antenna caused by the D-port ICRF antenna. Bolometry measurements revealed Be and Cu in the plasma immediately following these events. The location of the injection source in conjunction with the elemental analysis showed the source to be a piece of BeCu finger stock sandwiched between the C row of the LH grill and the stainless steel spacer bar in the middle of the launcher. This finger stock was installed to maintain a good RF contact between the grill and the spacer, and therefore prevent an electromagnetic resonance inside the cavity formed between the spacer and the grill. Inspection following the run campaign revealed that the finger stock had moved, possibly due to eddy current forces during a disruption, and was slightly proud of both the C row grill and the spacer bar. A similar analysis to that of Section 4.2 for the BeCu ($k = 5.6\times10^{-5}$ m^2/s, $T_{melt} = 1250$ K) shows that the heat flux necessary to increase the temperature of the BeCu to its melting point in 0.2 s (the nominal delay between the turn-on of the D-port antenna and the injection from the LH launcher) is 5.2×10^7 W/m^2. Similar localized heating has been observed during combined LHCD/ICRF operation on Tore Supra [70]. The heat load on the LH launcher from the ICRF was estimated to be $\sim 1 \times 10^6$ W/m^2 for this case.

4.4 Conclusions

Inspection of the LH launcher following its removal from the tokamak revealed melt damage localized on diagonal bands passing near the center of each waveguide row,

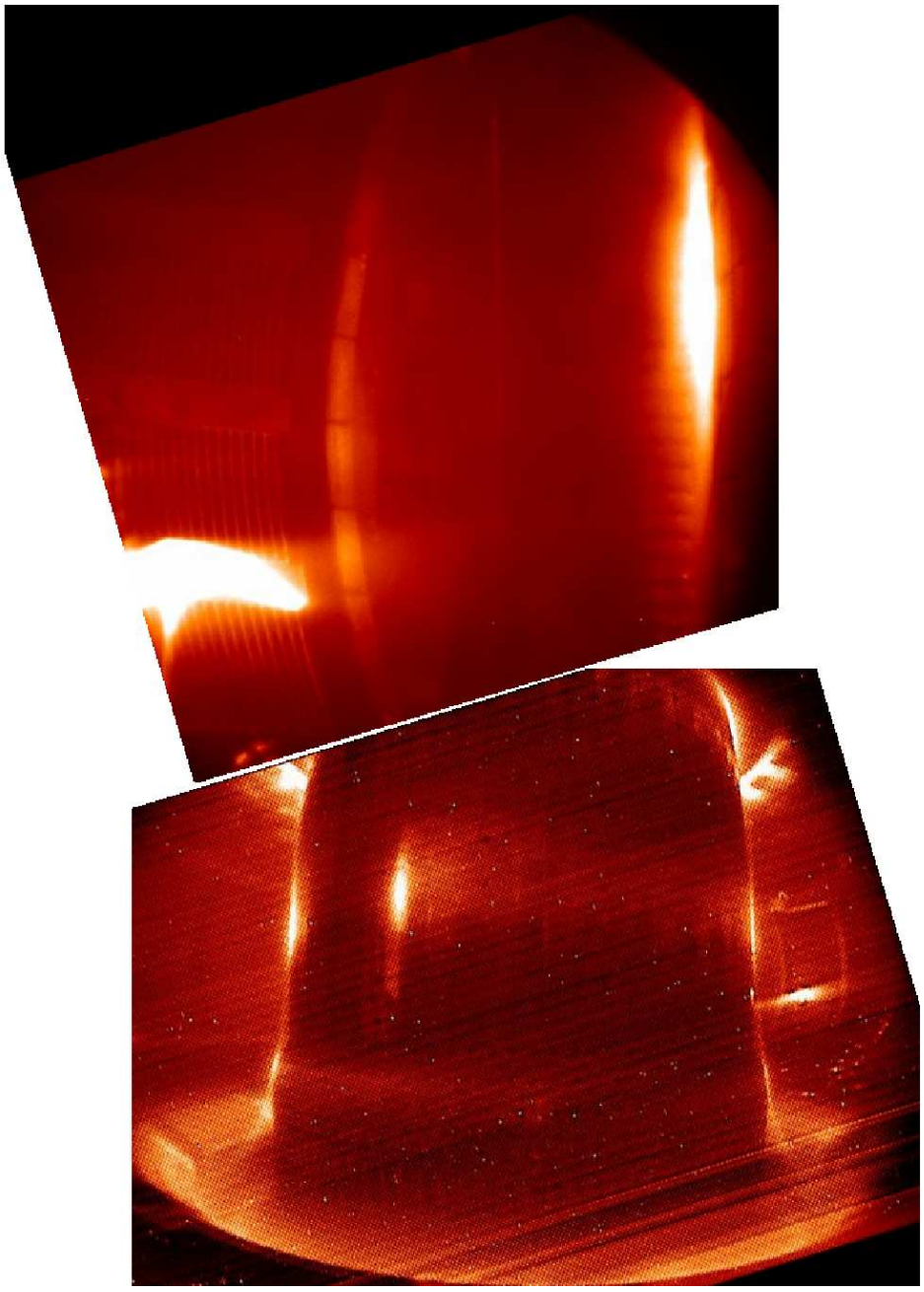

Figure 4-11: Injection from LH launcher caused by D-port ICRF antenna just prior to a disruption. The injection is visible in the lower left side of the top image (from LH camera) and the middle right side of the bottom image (from WIDE2 camera).

which is the same location as bright bands of visible light seen on video cameras during high power LH operation. An analysis of thermal diffusion in the launcher face during a 0.5 s LH pulse shows that an increase in plasma density and temperature to 1×10^{19} m^{-3} and 20 eV will generate sufficient heat flux on leading edges to cause melt damage. These values are reasonable estimates of the temperature and density in the diagonal bands of visible emission. A careful inspection of the melting pattern on the waveguide septa reveals that leading edges are created along the sides of the septa due to a shape mismatch between the plasma and the coupler.

An analysis of the power required to sustain the temperature and density observed in the bright bands is inconsistent with absorption of LH waves through collisions or Landau damping of high $n_{||}$ modes. At least one order of magnitude more power is absorbed in the launcher region than can be accounted for by these means.

The injections from the LH launcher caused by high power ICRF from a toroidally adjacent antenna again highlight the need to avoid having ICRF and LH antennas in close proximity along magnetic field lines. Beyond the risk of disruptions caused by injections from the ICRF/LH antenna interaction, ICRF antennas which are strongly connected along magnetic field lines pose a risk to the survivability of the LH antenna as well as the coupling problems associated with the D-port antenna described in Chapter 3.

Chapter 5

Absorption of Lower Hybrid Waves at High Density

5.1 Experimental Results

The accessibility criterion derived in Section 1.5 has traditionally been thought to be the limiting factor for the penetration of Lower Hybrid waves to the core of a tokamak plasma at high density. This is a simplified view based on the geometrical optics approximation in which waves freely propagate until they encounter a cutoff, are absorbed, or undergo a mode conversion process.

Recent results on Alcator C-Mod indicate that LH waves are not absorbed in the core of the plasma as would be expected based on the accessibility criterion. Several interesting phenomena indicate that the waves are not depositing power in the core at densities above $\bar{n}_e \sim 1 \times 10^{20}$ m^{-3}. These phenomena include reduced core bremsstrahlung and non-thermal ECE emission, and the presence of 4.6 GHz wave fields and plasma currents in the Scrape-Off-Layer. These observations suggest a lack of nonthermal electrons, and thus current drive, inside the separatrix.

The accessibility profile for a 5.4 T, 800 kA L-mode plasma with a line averaged density of 1.4×10^{20} m^{-3} is shown in Figure 5-1. According to the accessibility

criterion, any wave for which $n_{||}$ is locally greater than $n_{||,crit}$ everywhere in the plasma will be able to penetrate to the core of the plasma, provided that the wave is not fully absorbed in the edge region first. According to the principles of ray tracing in an axisymmetric toroidal geometry, the toroidal mode number of the wave is conserved everywhere in the plasma. The relationship between toroidal mode number, N_ϕ, and the toroidal component of the refractive index, n_ϕ, is

$$n_\phi = \frac{N_\phi}{R} \times \frac{c}{\omega} \tag{5.1}$$

Thus, assuming that $\hat{b} \cdot \hat{\phi} \approx 1$ and $n_\theta \ll n_\phi$, we can approximate $n_{||}$ as having a $1/R$ dependance as shown in Figure 5-1. If we assume that $n_e = n_e(\psi)$ and the minimum B, and thus the maximum value of $n_{||,crit}$, for a given density profile occurs on the midplane of the low field side in a tokamak, a wave will satisfy the accessibility criterion at all points in the plasma if the local value of $n_{||}$ is greater than the critical value on the midplane. It is important to note that the discussion of wave accessibility so far ignores possible modifications to $n_{||}$ that can occur owing to the variation of the poloidal mode number in toroidal geometry. This effect is taken into account in the simulations that are discussed later in this chapter.

5.1.1 Hard X-Ray Bremsstrahlung

The Hard X-Ray (HXR) diagnostic on C-Mod, described in Section 2.2.1, is used both for localizing the HXR emission, and for comparing the relative magnitude of the X-ray count rate. Since the thermalization rate of the fast electrons due to collisions is proportional to plasma density, it follows that, for a fixed source of fast electrons in an otherwise uniform plasma, the fast electron population should be inversely proportional to plasma density. The count rate can be taken as a proxy for the density of the fast electron tail generated by LHCD. This scaling is confirmed by simulations which will be discussed later in the chapter. Figure 5-2 shows that

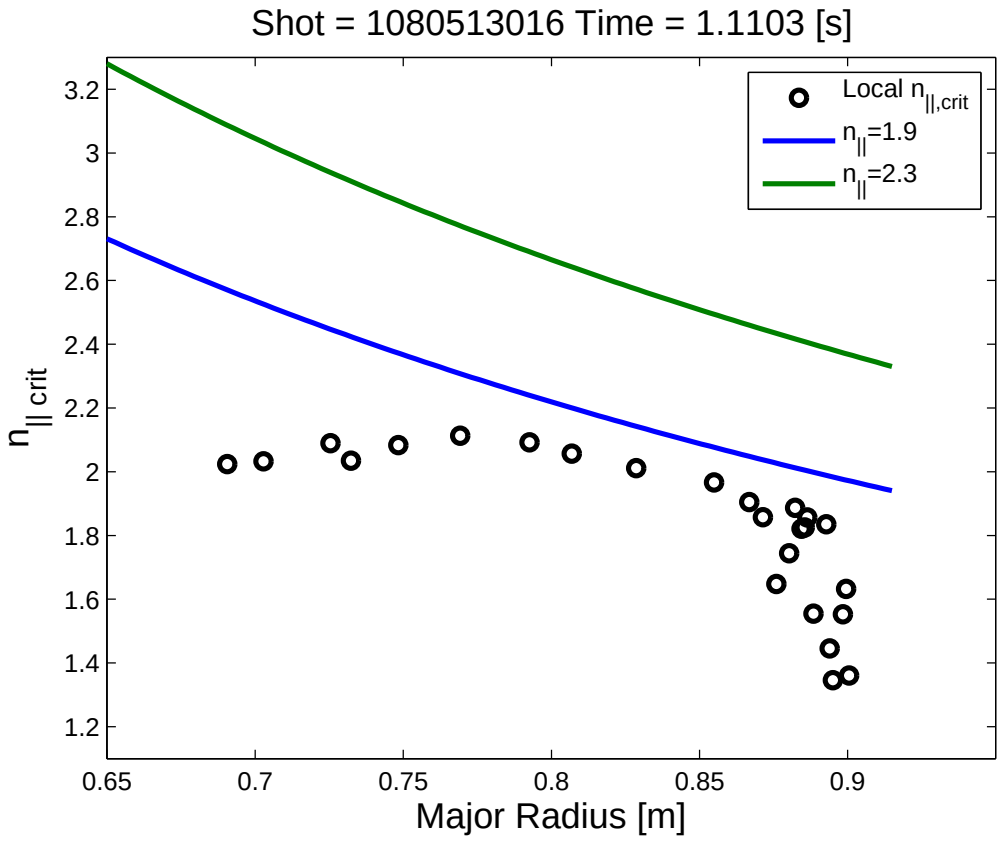

Figure 5-1: Locally accessible $n_{||}$ versus major radius on the midplane in a high density L-mode discharge ($\bar{n}_e = 1.4 \times 10^{20}$ m^{-3}). If the value of $n_{||}$ is above the black data points, then the wave is accessible. The two curves represent the toroidally upshifted value of $n_{||}$ for launched values of 1.94 (75°) and 2.33 (90°). The LH launcher is located at $R = 0.915$ m.

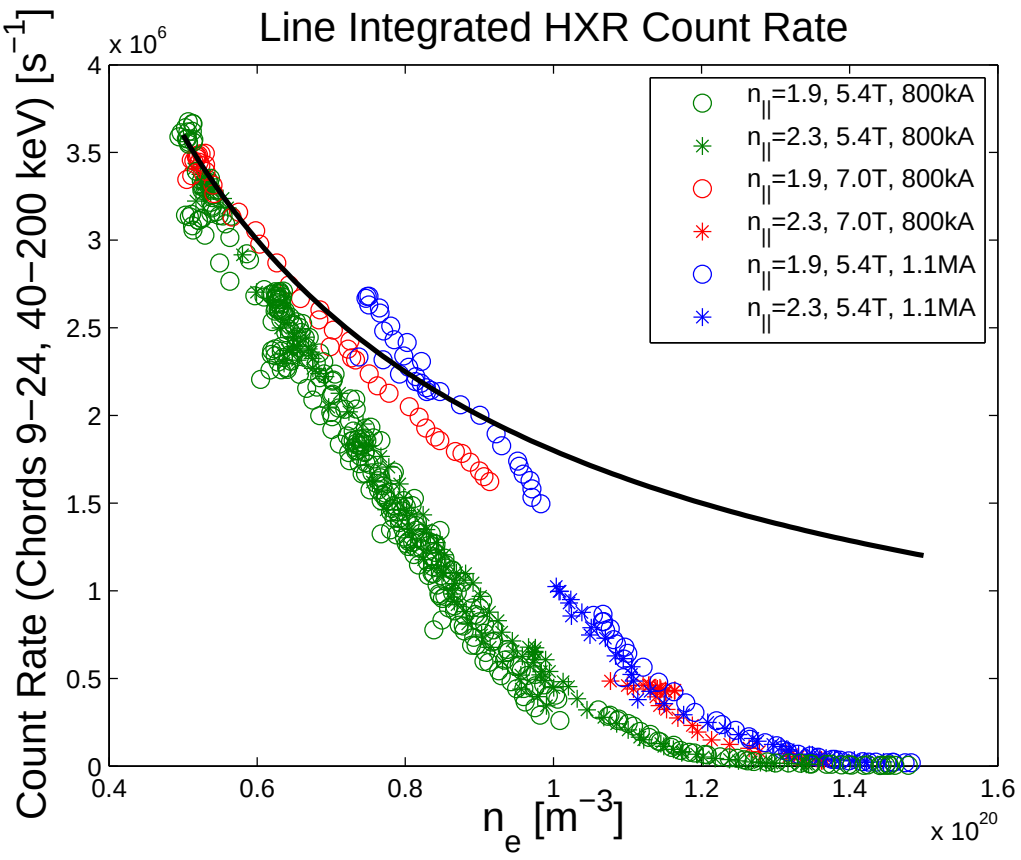

Figure 5-2: Line integrated X-ray emission on the central chords versus line averaged density. Data are plotted on a linear scale for X-rays between 40 and 200 keV. The black curve represents a $1/n_e$ falloff. The count rates in this figure are normalized to the square root of net LH power.

the experimental HXR count rates fall much steeper than the expected $1/n_e$ [71]. This is particularly true for the 5.4 T, 800 kA case, which deviates from the $1/n_e$ curve starting near $\bar{n}_e \sim 6 \times 10^{19}$ m^{-3}. The data at higher magnetic field and plasma current drop more slowly as density rises, but are still two orders of magnitude lower than the $1/n_e$ prediction at $\bar{n}_e = 1.5 \times 10^{20}$ m^{-3}.

The count rates shown in Figures 5-2 and 5-3 have been normalized to the magnitude of the wave electric field (square root of net LH power). The data represent a range of net LH power from 550 to 900 kW. For comparison, the count rate shown

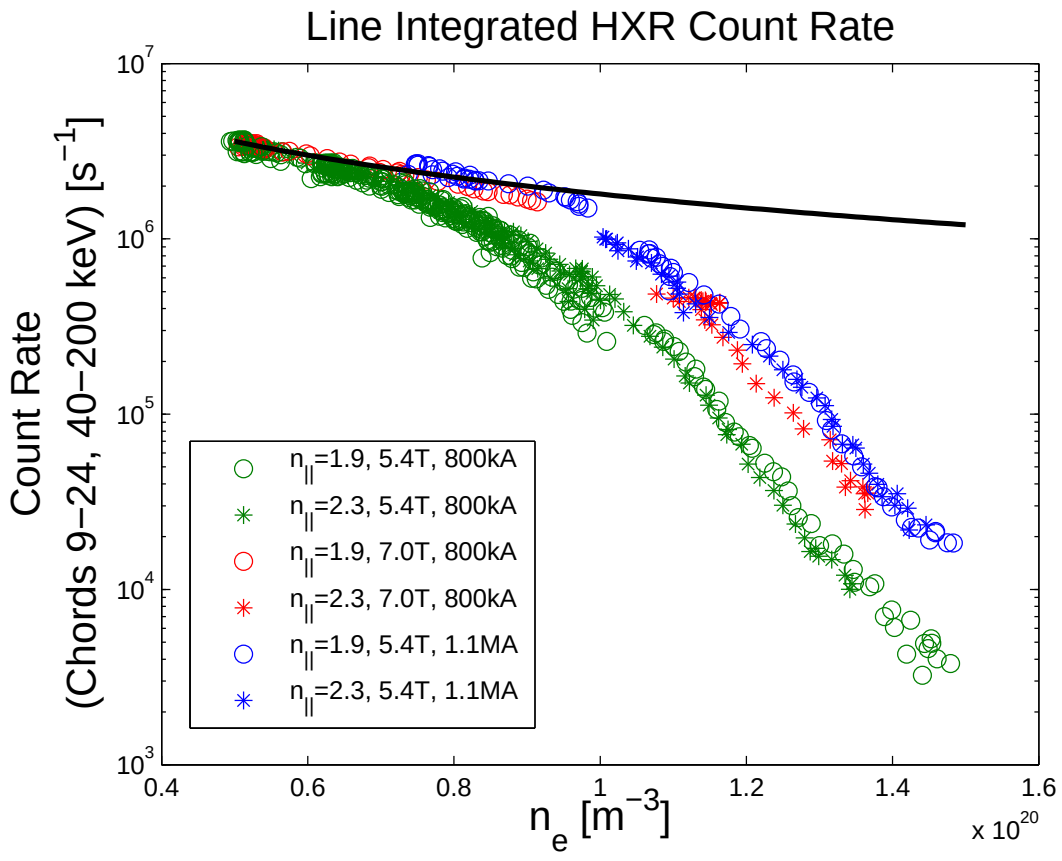

Figure 5-3: Line integrated X-ray emission on the central chords versus line averaged density. Data are plotted on a semi-logarithmic scale for X-rays between 40 and 200 keV. The black curve represents a $1/n_e$ falloff. The count rates in this figure are normalized to the square root of net LH power.

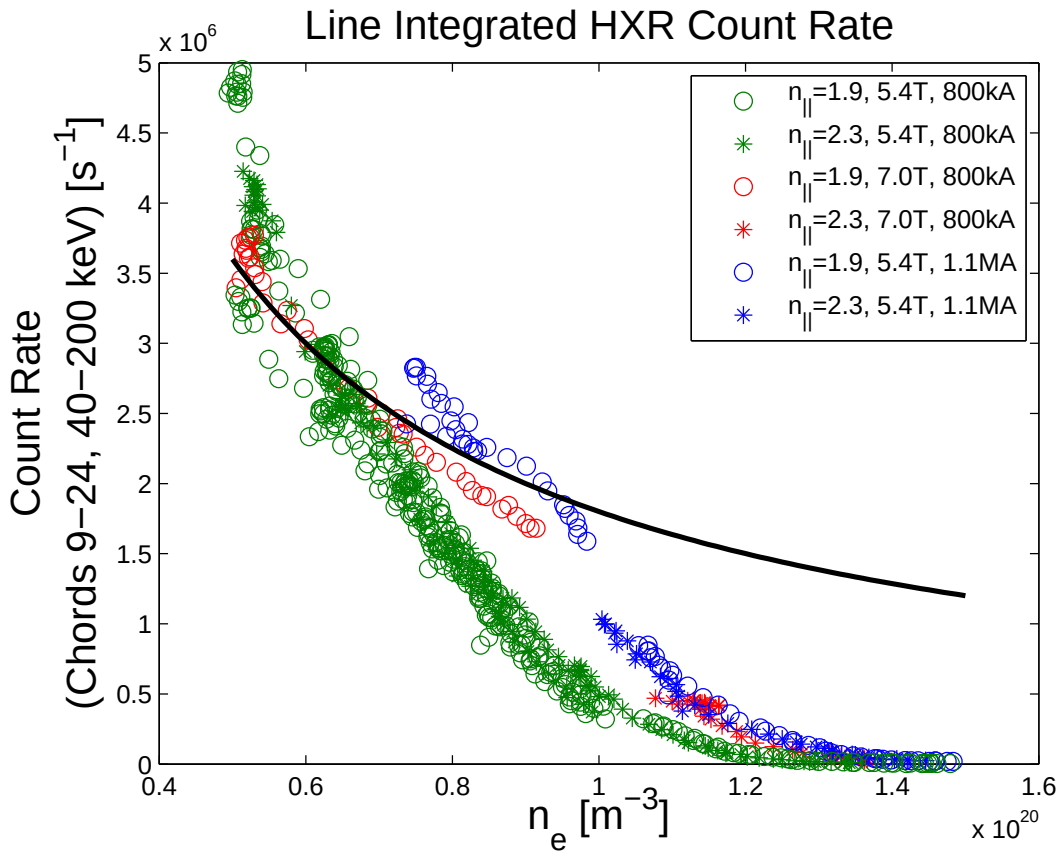

Figure 5-4: Line integrated X-ray emission on the central chords versus line averaged density. Data are plotted on a linear scale for X-rays between 40 and 200 keV. The black curve represents a $1/n_e$ falloff. The count rates in this figure are normalized to the net LH power.

in Figure 5-4 has been normalized to the net LH power, and Figure 5-5 has no normalization. The square root of power scaling leads to the tightest grouping of the experimental data.

Although a violation of the accessibility criterion above 1×10^{20} m^{-3} would appear to explain the results of Figure 5-3, there are several points which contradict the accessibility criterion explanation. First, the data taken at $n_{||} = 2.33$ (represented by asterisks) and the data taken at $n_{||} = 1.94$ (represented by circles) do not show a significant difference in count rate as the density changes. If the cause of the count

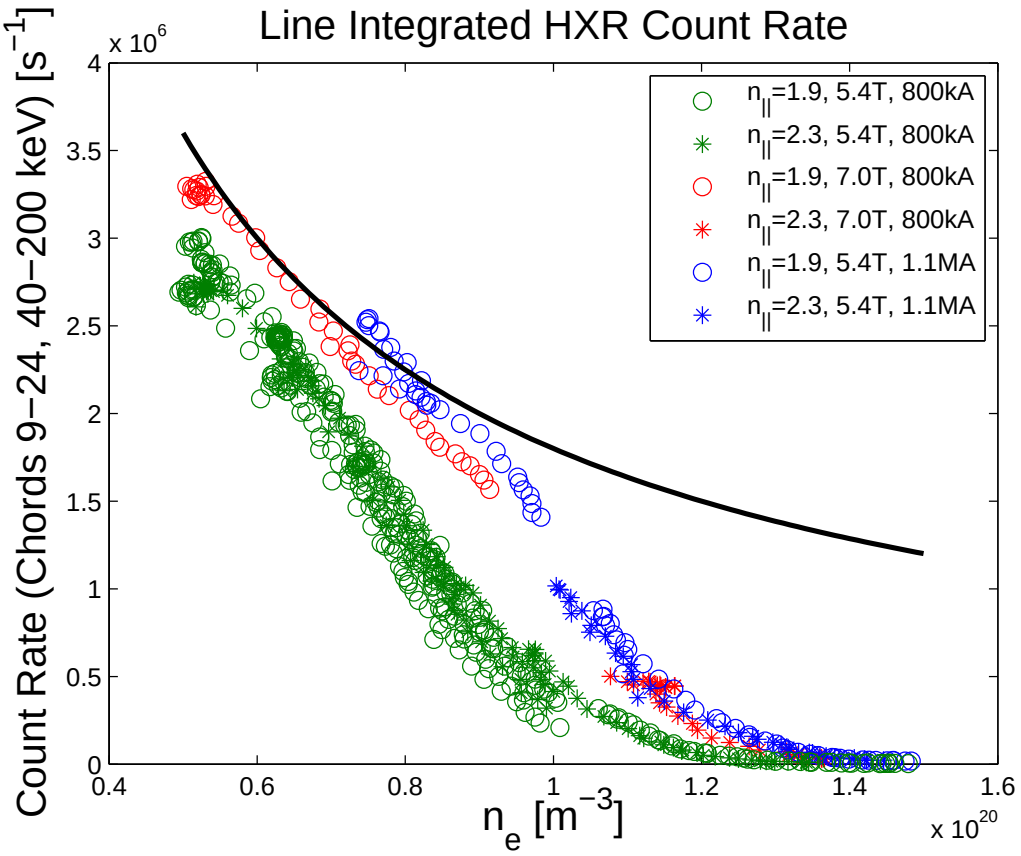

Figure 5-5: Line integrated X-ray emission on the central chords versus line averaged density. Data are plotted on a linear scale for X-rays between 40 and 200 keV. The black curve represents a $1/n_e$ falloff. The count rates in this figure are not normalized.

rate reduction were related to the accessibility criterion, one would expect the lower value of $n_{||}$ to be affected more severely and at a lower density than the higher value of $n_{||}$. The two sets of data are nearly coincident across a range of density, magnetic field, and plasma current. In addition, the midplane accessibility condition plotted in Figure 5-1 shows that the accessibility criterion is satisfied at both $n_{||}$ of 1.94 and 2.33, even for the highest density shown in Figure 5-3 at the lowest magnetic field. Figure 5-6 shows the bremsstrahlung emissivity as a function of $n_{||crit} - n_{||launch}$, with $n_{||crit}$ evaluated based on the line averaged density and on axis magnetic field. According to results from FTU [72], accessibility should only be an issue for $n_{||crit} - n_{||launch} > 0.05$ when calculated in this manner.

The so-called "density limit" observed on Alcator C has been attributed to parametric decay instabilities (PDI) as $\omega \rightarrow 2\omega_{LH}$ [73, 74, 75, 76]. LHCD efficiencies proportional to $1/\bar{n}_e$ with strong non-thermal ECE and HXR emission were observed up to $\bar{n}_e = 10^{20}$ m^{-3} [24]. The bremsstrahlung data from C-Mod show a precipitous drop in emission below $\omega/\omega_{LH} \sim 3.75$, as can be seen from Figure 5-7. All of the data from C-Mod occur at values of ω/ω_{LH} in excess of 3, for which there should be no significant parametric decay according to earlier results. The discrepancies between the data at 5.4 T and 7.0 T show that although the experimental bremsstrahlung emission scales as a function of ω/ω_{LH} at a given value of magnetic field, a comparison between different values of magnetic field at a fixed density do not agree with the ω/ω_{LH} scaling. An increase in magnetic field will increase the value of ω_{LH}, but the data show an increase in HXR emission at a fixed density for the higher field. The discrepancy seen in Figure 5-7 between the 5.4 T and 7.0 T data shows that bremsstrahlung emission is a function of density, not ω/ω_{LH}. This proves that ω/ω_{LH} is not the critical parameter for the density limit observed on C-Mod.

The "PDI Level" was recorded for several of the discharges shown in Figure 5-7 by measuring the microwave frequency spectrum picked up by the LH Langmuir probes. Figure 5-8 shows a typical spectrum for a discharge at 800 kA, 5.4 T, and

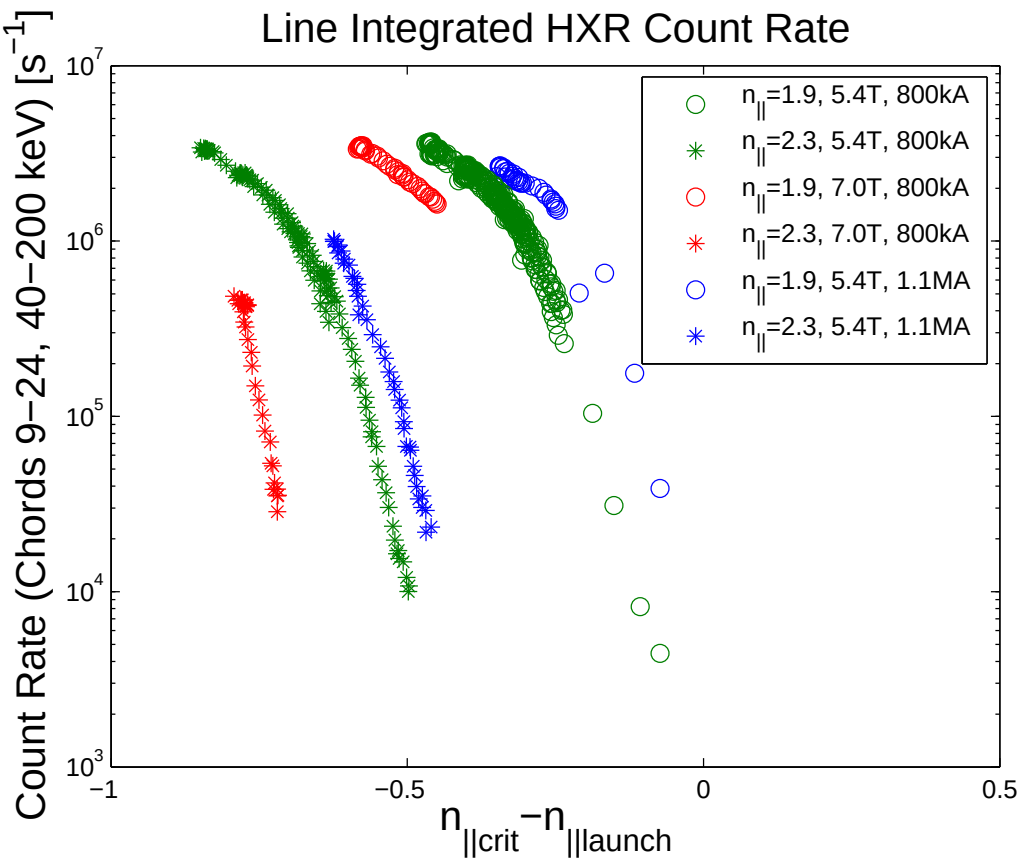

Figure 5-6: Fast electron bremsstrahlung emission as a function of $n_{||crit} - n_{||launch}$. The value of $n_{||crit}$ is calculated using line averaged density and on-axis magnetic field. Values of $n_{||crit} - n_{||launch} > 0.05$ show accessibility limitations on FTU.

1.35×10^{20} m^{-3}. The PDI Level is shown schematically as the height on the pump wave minus the height of the strongest sideband. The scaling of the PDI Level as a function of line averaged density and ω/ω_{LH} is shown in Figure 5-9. Even though the PDI level is observed to rise with line averaged density, at the highest densities (and consequently lowest values of ω/ω_{LH}) the strongest sideband is below -20 dB relative to the pump, corresponding to less than 1% of the total power contained in the sideband. Interpretation of the PDI level is somewhat problematic since the measurement location in this instance is in close proximity to the LH launcher. The relative magnitude of the downshifted sideband may be higher away from the launcher. PDI levels as high as -10 dB relative to the pump wave have been observed on C-Mod [49], although not in these discharges.

Recent results from the FTU LHCD experiment [77] indicate that Parametric Decay can contribute to a loss of LHCD efficiency under conditions of high density and low temperature in the SOL. The PDI signature in the FTU experiment is seen through broadening of the pump wave as opposed to the discrete downshifted harmonics of the ion cyclotron frequency seen in Figure 5-8. Figure 5-10 shows the width of the pump wave at several values relative to the peak of the spectrum. At -3 and -10 dB relative to the peak, the spectral width shows no clear increase as a function of line averaged density. However, a slight increase in pump width can be seen in the data lower relative to the peak. At -20 dB the pump width increases from $\sim 4 \times 10^6$ to $\sim 5 \times 10^6$ Hz, while at the -30 dB level the pump width increases from $\sim 5 \times 10^6$ to $\sim 8 \times 10^6$ Hz.

5.1.2 Wave Fields in Scrape-Off-Layer

For detecting the presence of LH waves in the SOL, one electrode from a reciprocating Mach probe was connected through a 4.6 GHz bandpass filter to a rectifier diode, the output of which was subsequently digitized. The reciprocating probe is located 11 cm above the midplane on A-port in a location that is not magnetically connected to

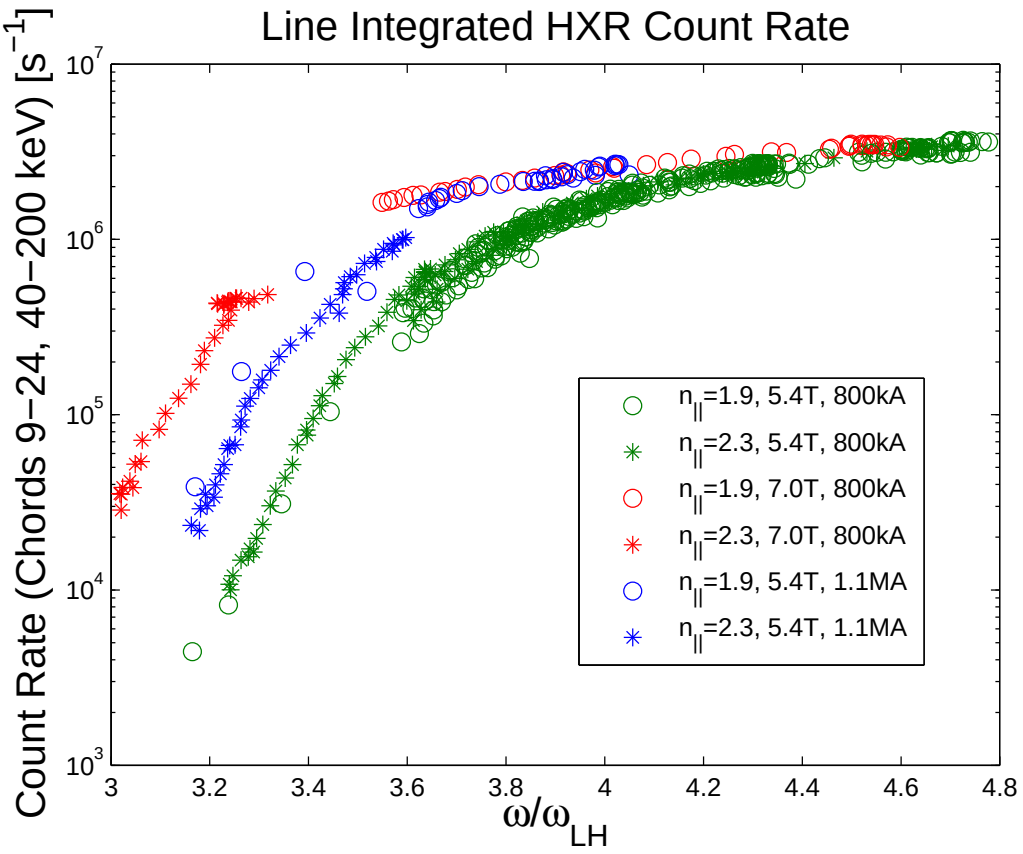

Figure 5-7: Fast electron bremsstrahlung as a function of ω/ω_{LH} at $B_T = 5.4$ and 7.0 T. ω_{LH} is computed using line averaged electron density and on axis magnetic field.

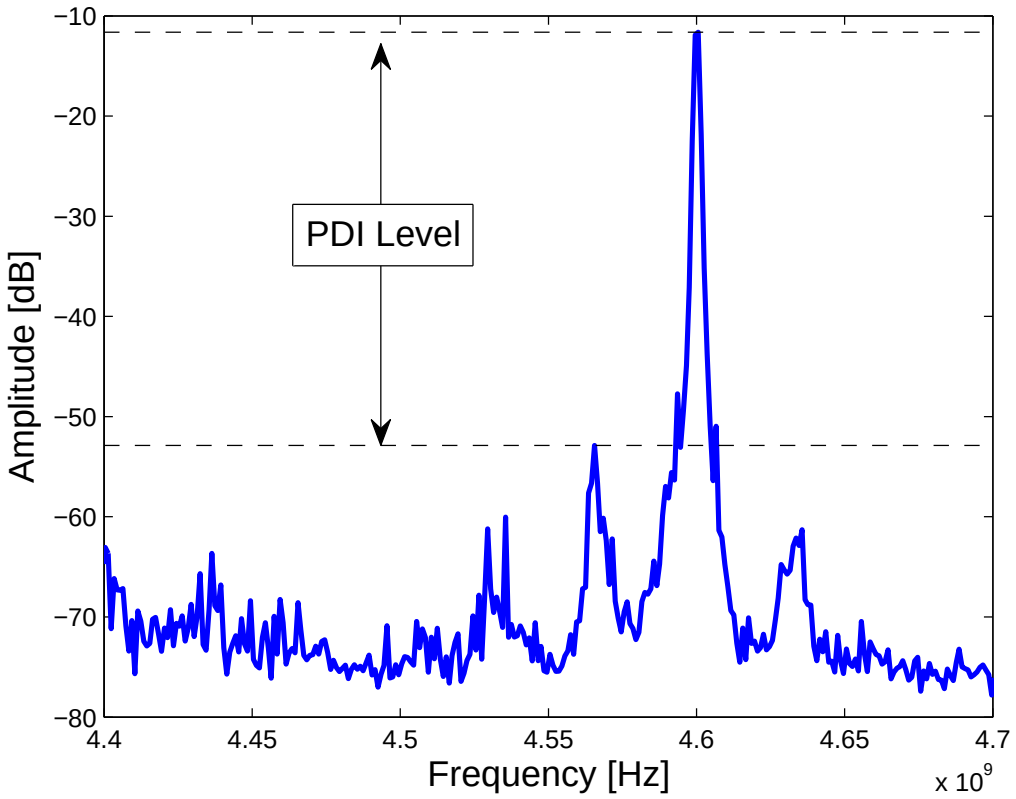

Figure 5-8: Frequency spectrum showing weak Parametric Decay Instability for a shot at 800 kA, 5.4 T, and 1.35×10^{20} m^{-3}. Method for defining the "PDI Level" is shown.

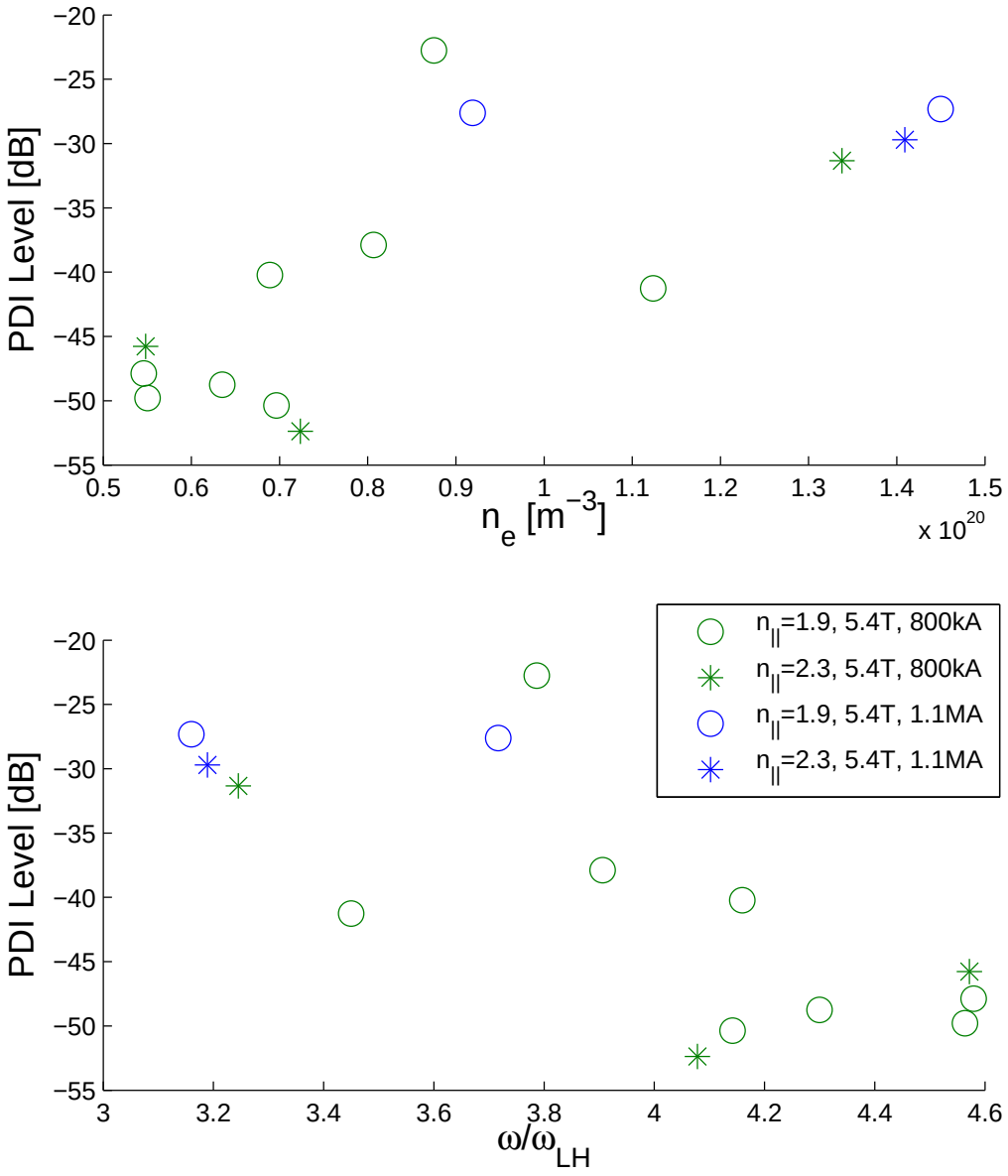

Figure 5-9: PDI Level as a function of density (top) and ω/ω_{LH} (bottom) for the discharges shown in Figure 5-7. Data for 7.0 T discharges are not available.

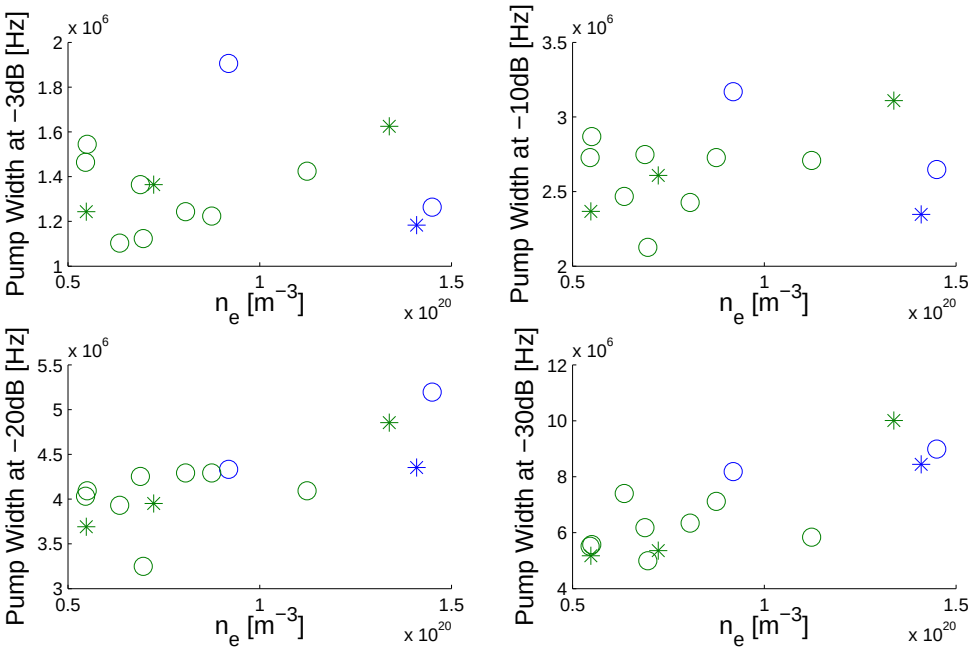

Figure 5-10: Pump wave width as a function of line averaged density for the discharges shown in Figure 5-7. Colors and symbols correspond to the same conditions as in Figure 5-7. Data for 7.0 T discharges are not available.

the LH antenna at C-port. (See Figure 5-11.)

Figure 5-12 shows a single in/out sweep of the reciprocating probe. The RF fields are localized near $\rho = 0.045$ m with a width of ± 0.015 m. Here, ρ is the distance from the separatrix on the midplane with positive values residing in the SOL. Although the width of the high field region appears larger on the second pass, this is because the out stroke of the probe occurs at a lower velocity than the in stroke. The location and width are consistent for both the in and out stroke of the probe. A single stroke in and out of the plasma occurs over the course of 80 ms. Since the resonance cones leaving the LH antenna roughly follow the field lines, with $v_{g\perp} \ll v_{g||}$, the reciprocating probe should not intersect waves leaving the antenna. This suggests that the wave fields observed in the SOL are due to waves which are not directly absorbed on the first pass through the plasma.

Data on the SOL wave fields is only available at one value of magnetic field and current, and mostly at densities above 1×10^{20} m^{-3}. Figure 5-13 shows the amplitude of the wave field peak relative to the background level as a function of line averaged density. Interestingly, the intensity of the peaks decreases strongly as density increases; however, the peaks are more pronounced at higher densities. This may be due to the fact that as the density increases, absorption in the SOL may also increase. If wave absorption in the confined plasma is weak, the plasma will act somewhat like a cavity resonator, and as the edge region of the cavity becomes more lossy, the field amplitude in the cavity will decrease.

5.1.3 Scrape-Off-Layer Currents

The flush-mounted Langmuir probes mounted in the upper and lower divertor regions of C-Mod are typically operated in a swept configuration. As the potential difference between the probe and the vacuum vessel wall passes through zero, the "ground current" collected by the probe, I_{gnd}, can be measured. This current is equal to the free flowing current into the wall parallel to the magnetic field. Figure 5-14 shows

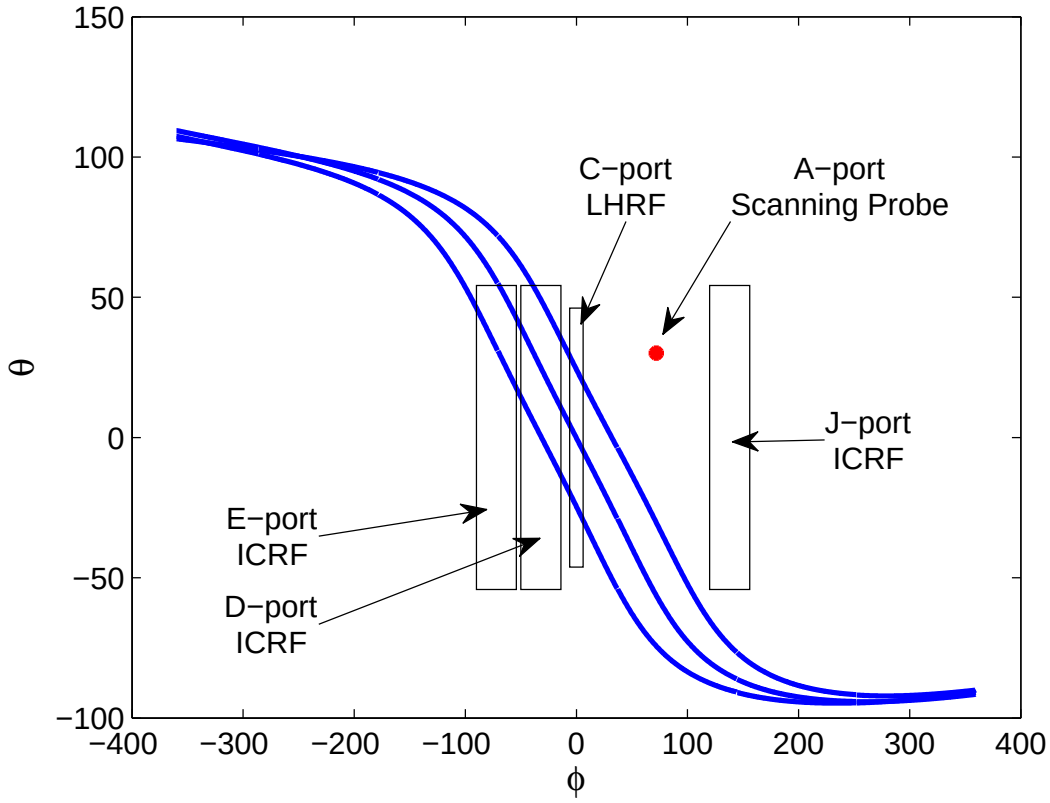

Figure 5-11: Field line map showing location of A-port Scanning Probe (ASP) for a 5.4 T, 800 kA discharge. The ASP does not connect magnetically to the LH launcher at C-port.

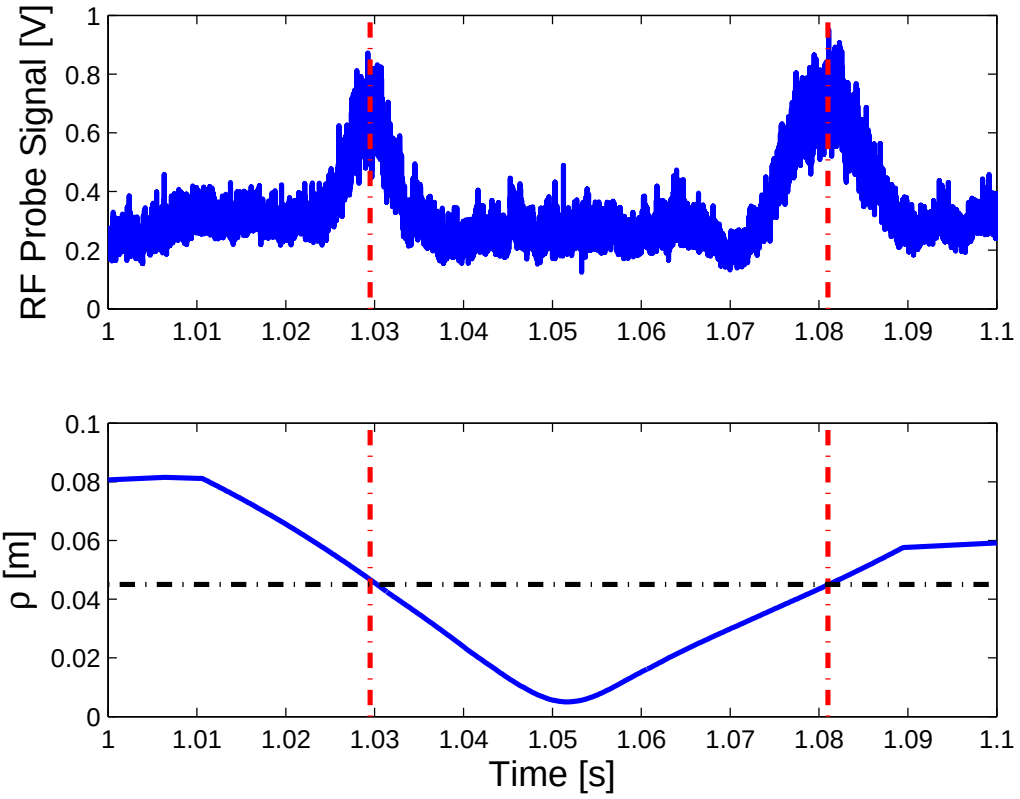

Figure 5-12: 4.6 GHz wave fields in the SOL picked up by the A-port reciprocating Langmuir probe. The North West electrode of the pyramidal probe is connected through a 4.6 GHz bandpass filter to an RF diode detector. The launcher was positioned at $\rho = 0.025$ m for this discharge, while the cutoff layer is located at $\rho \sim 0.06$ m. Shot number = 1070824011.

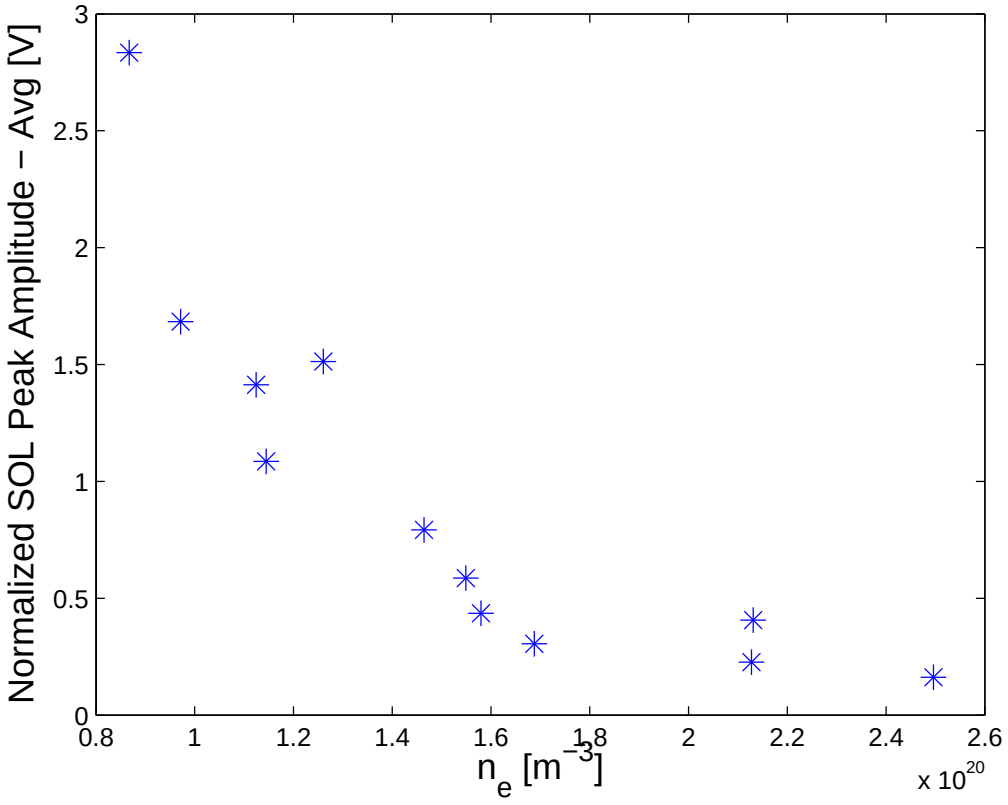

Figure 5-13: 4.6 GHz wave fields in the SOL picked up by the A-port reciprocating Langmuir probe as a function of line averaged electron density. Amplitude is normalized to net LH power / 400 kW. All data points are at 5.4 T and 1.0 MA.

the location of I_{gnd} on the $I-V$ characteristics of two probes during a high power LHCD pulse. The convention taken here is that a positive current will be measured if the probe is collecting ions. Since the geometry of the probe (see Figure 5-15) is known, the parallel current density measured by the probe is

$$J_{||} = \frac{I_{gnd}}{A_{\perp}} \approx \frac{I_{gnd}}{\sin(\theta)\pi r_{probe}^2} \tag{5.2}$$

where θ is the angle of incidence of the field line and r_{probe} is the radius of the probe electrode. Figure 5-16 shows the location of the C-Mod divertor Langmuir probes.

In normal operation, the $J_{||}$ measured by the divertor probes is less than $\sim 1 \times 10^5$ A/m^2 and of similar magnitude on all of the probes. During high power LH operation in USN at line averaged densities above $\sim 1 \times 10^{20}$ m^{-3} the magnitude of $J_{||}$ measured by some probes increases dramatically. Figure 5-17 shows the ground currents for probes on the inner and outer side of the lower divertor in a lower null discharge. The two probes, which lie on approximately the same flux surface, see ground currents which are nearly the same in magnitude and opposite in polarity. The polarity difference between the inner and outer divertors indicates that the current flowing between the two probes is leaving the outer divertor, traveling up and around the top of the plasma, and returning to the vacuum vessel wall on the inner divertor. When projected in the toroidal direction, this corresponds to the same direction as the current in the confined plasma, I_p, if we assume that the SOL current is traveling parallel to the magnetic field.

Figure 5-18 shows the SOL current observed in a high density upper null discharge. In the upper null configuration, the current is observed to leave the upper inner divertor and flow towards the upper outer divertor. Again, this is the same direction as I_p. Figure 5-19 shows the direction of the SOL currents as projected on to the poloidal cross section for upper and lower null configurations. Figure 5-18 also gives some indication of the scaling of the SOL current with density. As $\bar{n}_e$ increases from 1.0×10^{20} to 1.5×10^{20} m^{-3}, the ground current on the probe rises from near zero to 0.3

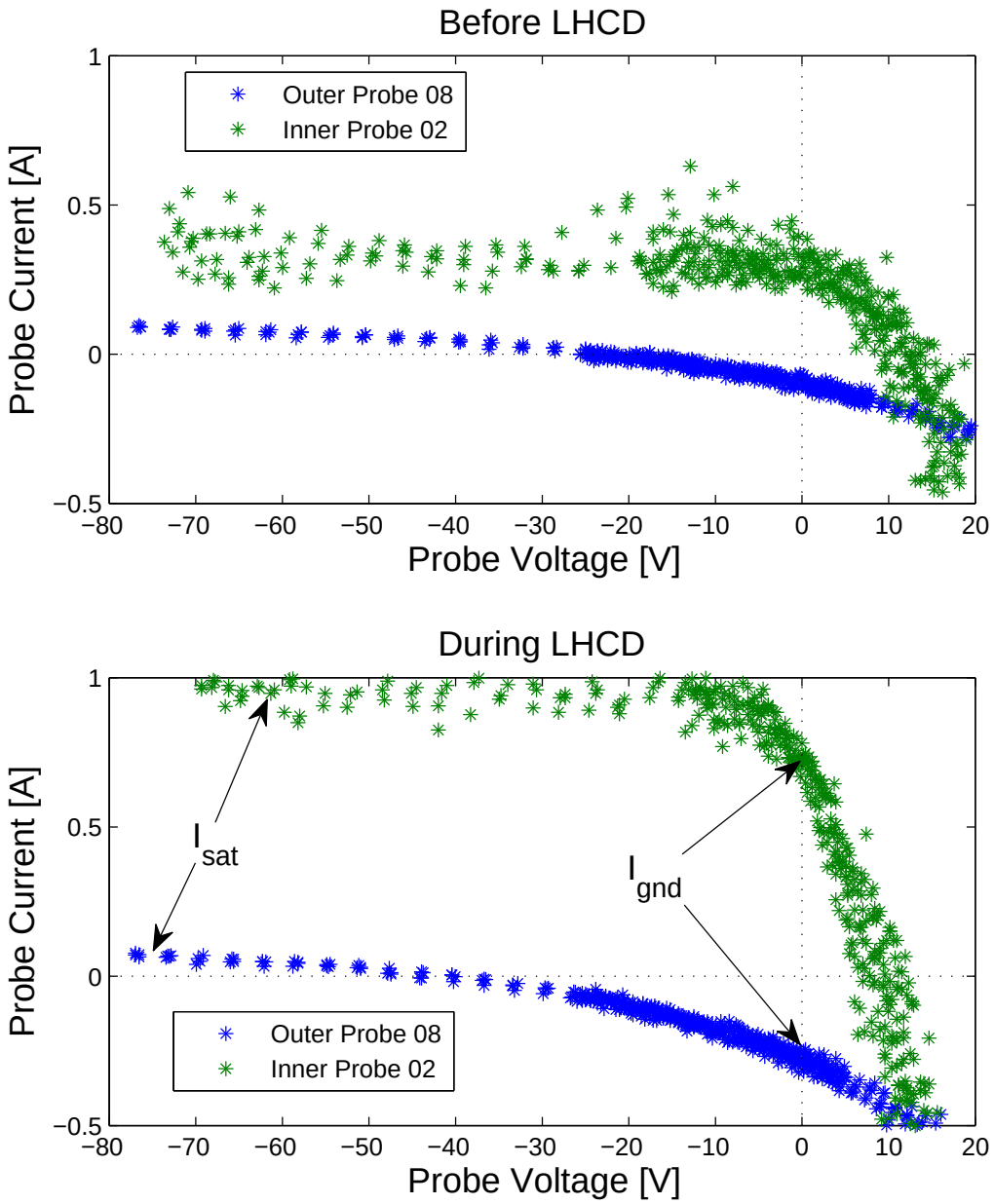

Figure 5-14: $I-V$ characteristic for Langmuir probes mounted in the inner and outer lower divertors before and during high power LHCD. The ground current, I_{gnd}, and the ion saturation current, I_{sat} are shown. Both probes are located at $\rho = 0.008$ m. Shot number = 1080402031.

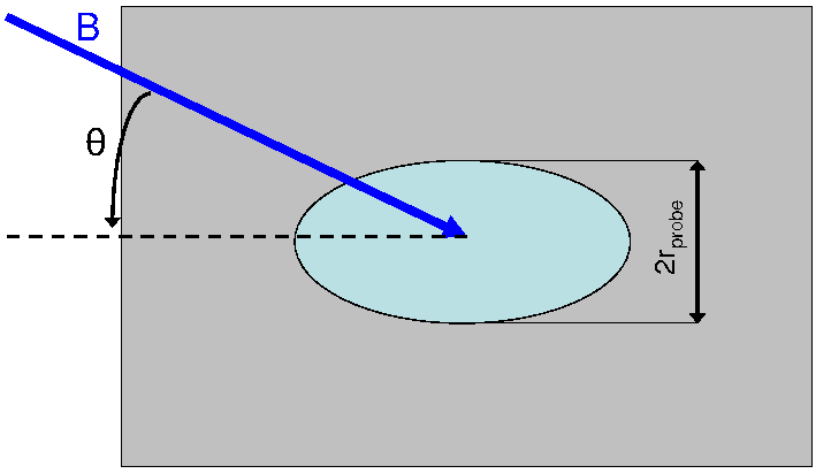

Figure 5-15: Geometry of the divertor Langmuir probes. The probes are mounted nearly flush to the surface of the divertor tile. The magnetic field intersects the circular probe face (light blue) at an angle, θ.

A. Figure 5-20 shows the change in the SOL current density for the USN discharges in Figure 5-3. The SOL currents can be seen to suddenly increase in magnitude at $\bar{n}_e \sim 1.0 \times 10^{20}$ m^{-3}, the same density at which fast electron bremsstrahlung disappears from the central HXR chords. Enhanced SOL currents during high power LHCD have been observed in LSN as low as $\bar{n}_e = 7 \times 10^{19}$ m^{-3}. Modulation of the SOL current during LHCD is also present in discharges with a launched $n_{||}$ in the counter-current drive direction. The SOL current in these discharges is also in the direction of I_p in LSN despite a change in the sign of $n_{||}$.

Figure 5-21 shows the values of I_{sat} and I_{gnd} for probes on the inner and outer divertor surfaces in a lower single null discharge. On the ion collecting end of the flux tube (which in LSN is the inner divertor) there is a substantial increase in the ion saturation current, I_{sat}, during LHCD. Interestingly, there is no corresponding change in I_{sat} at the electron collecting end of the flux tube (which in LSN is the outer divertor). On the end of the field line which collects ions, $|I_{gnd}|$ cannot exceed

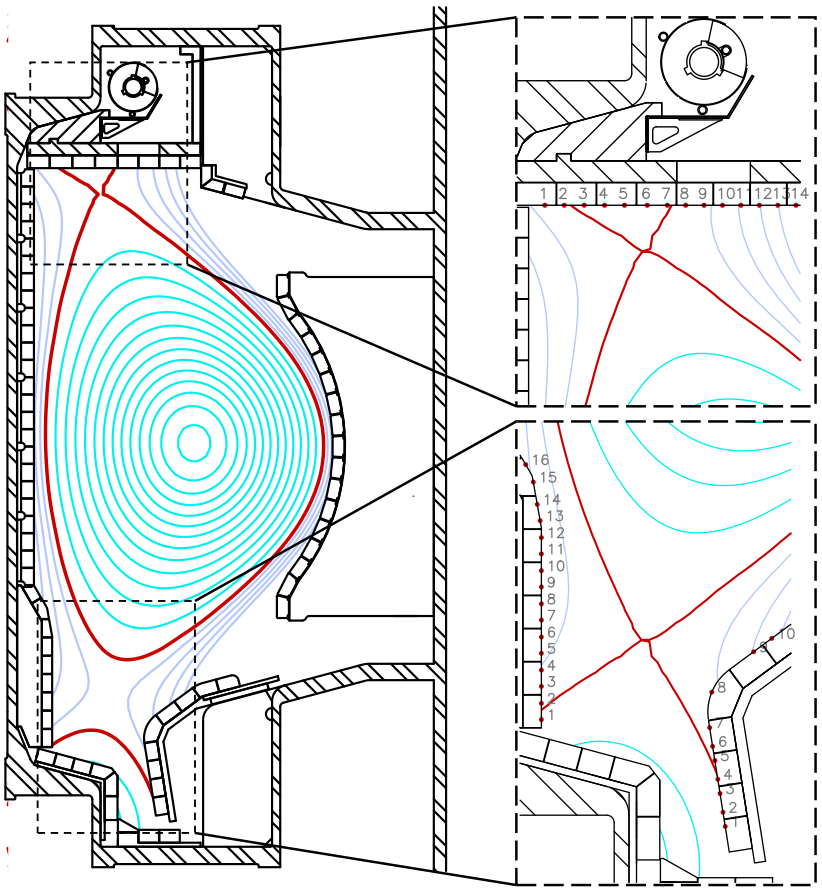

Figure 5-16: Location of Langmuir probes mounted in the upper and lower divertors.

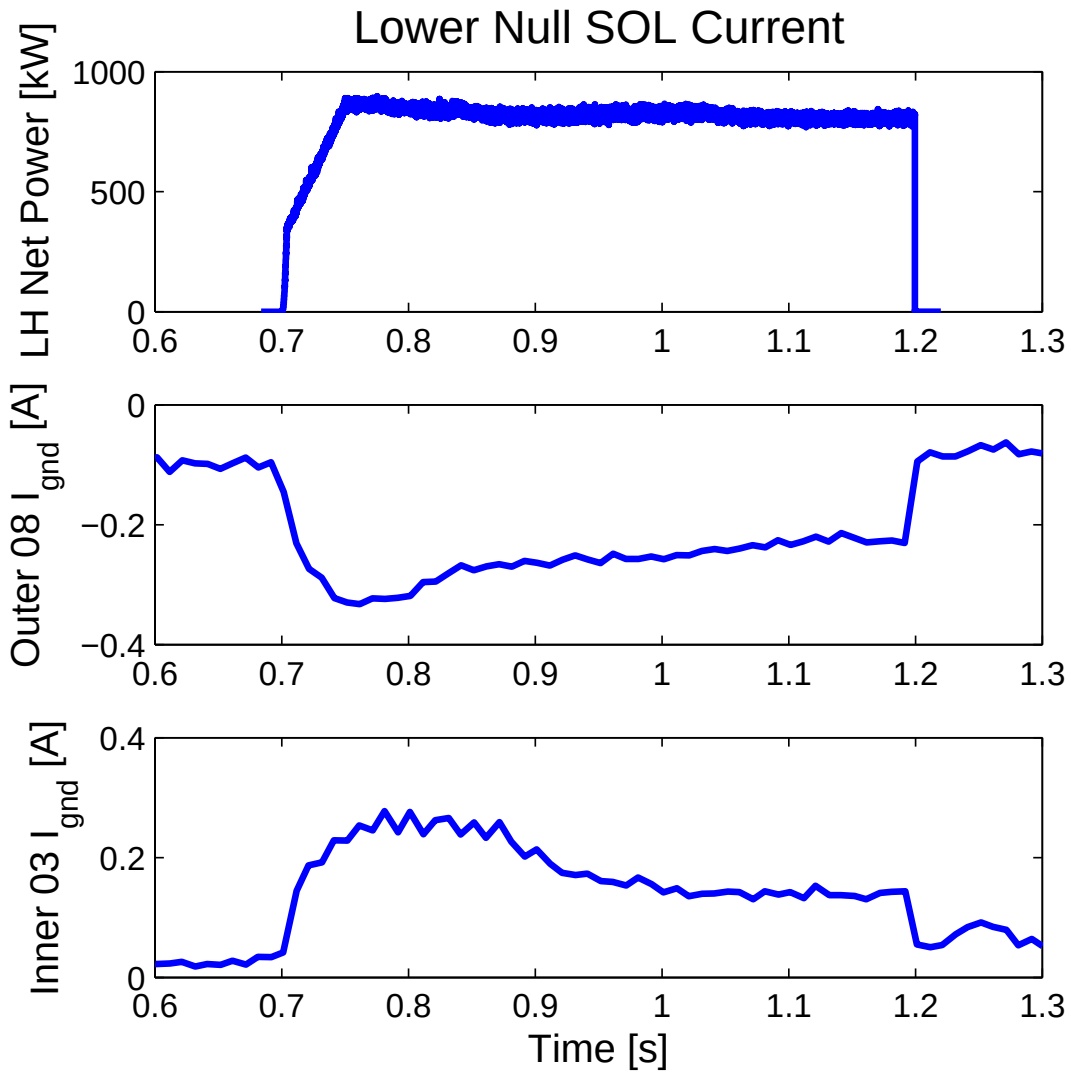

Figure 5-17: Waveform of SOL currents observed during LHCD experiments in Lower Single Null. Equal and opposite I_{gnd} currents are observed on the inner and outer divertor probes. The SOL current is flowing in the same toroidal direction as the main plasma current. For this discharge $\rho_{launch} = 0.015$ m and $\rho_{probe} = 0.008$ m with $\bar{n}_e = 7 \times 10^{19}$ m^{-3}. Shot number = 1080402031.

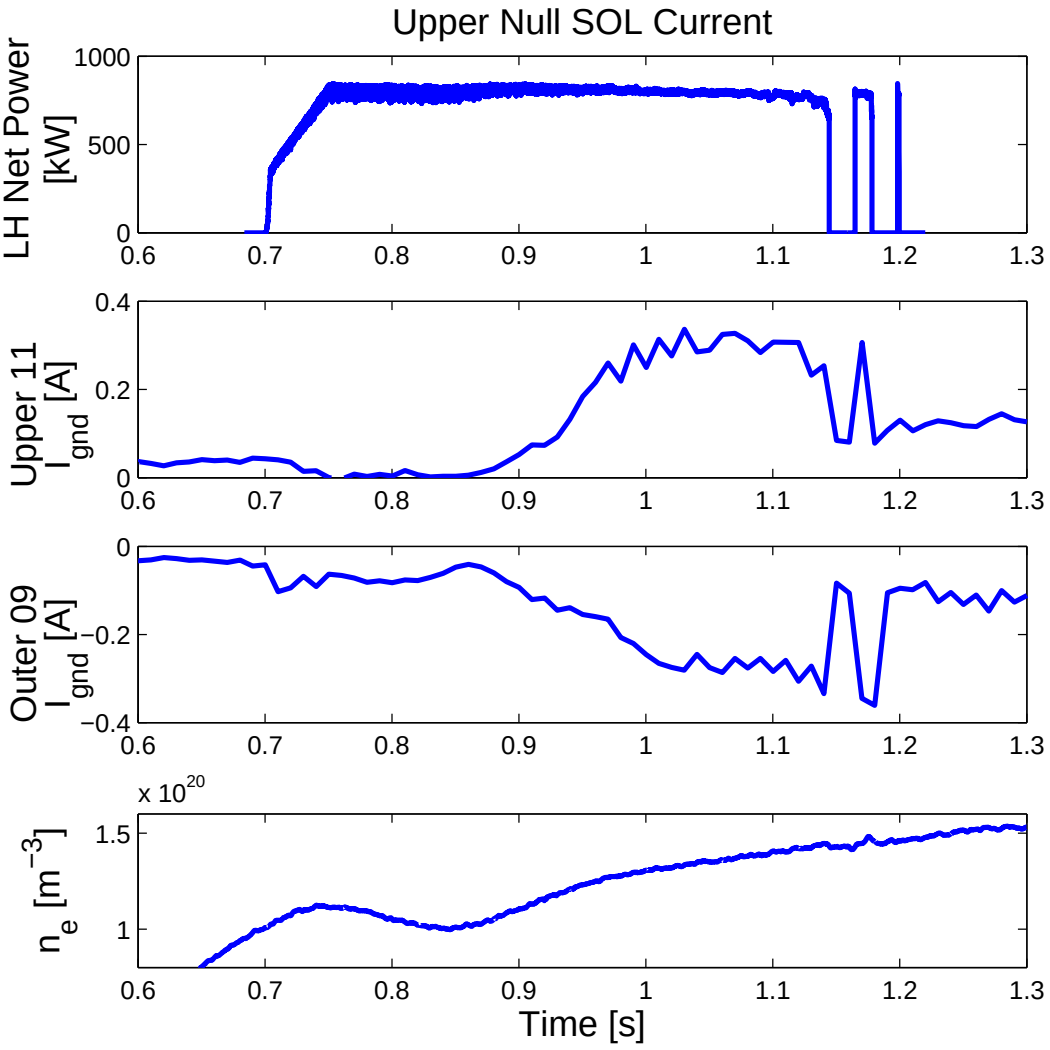

Figure 5-18: Waveform of SOL currents observed during LHCD experiments at high density in Upper Single Null. The SOL currents connect between probe 11 in the upper divertor and probe 9 in the lower outer divertor for this discharge. (See probe locations in Figure 5-16.) The I_{gnd} signal on upper divertor probe 11 increases from nearly 0 A to over 0.3 A as line averaged density rises above 1.2×10^{20} m^{-3}. The current is well modulated with net LH power as shown by the trips after 1.1 s. Due to the shape of the plasma, the electron collecting end of the current path does not intersect a Langmuir probe. For this discharge $\rho_{launch} = 0.025$ m and $\rho_{probe} = 0.015$ m. Shot number = 1080513019.

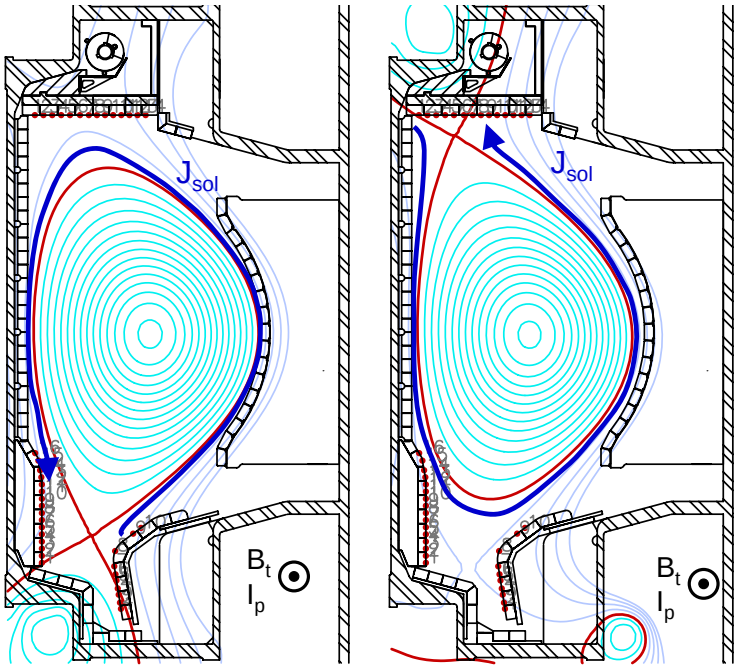

Figure 5-19: Direction of the SOL currents projected on the poloidal cross section for USN and LSN. In both configurations the SOL current is observed to flow in the same toroidal direction as the current on closed flux surfaces.

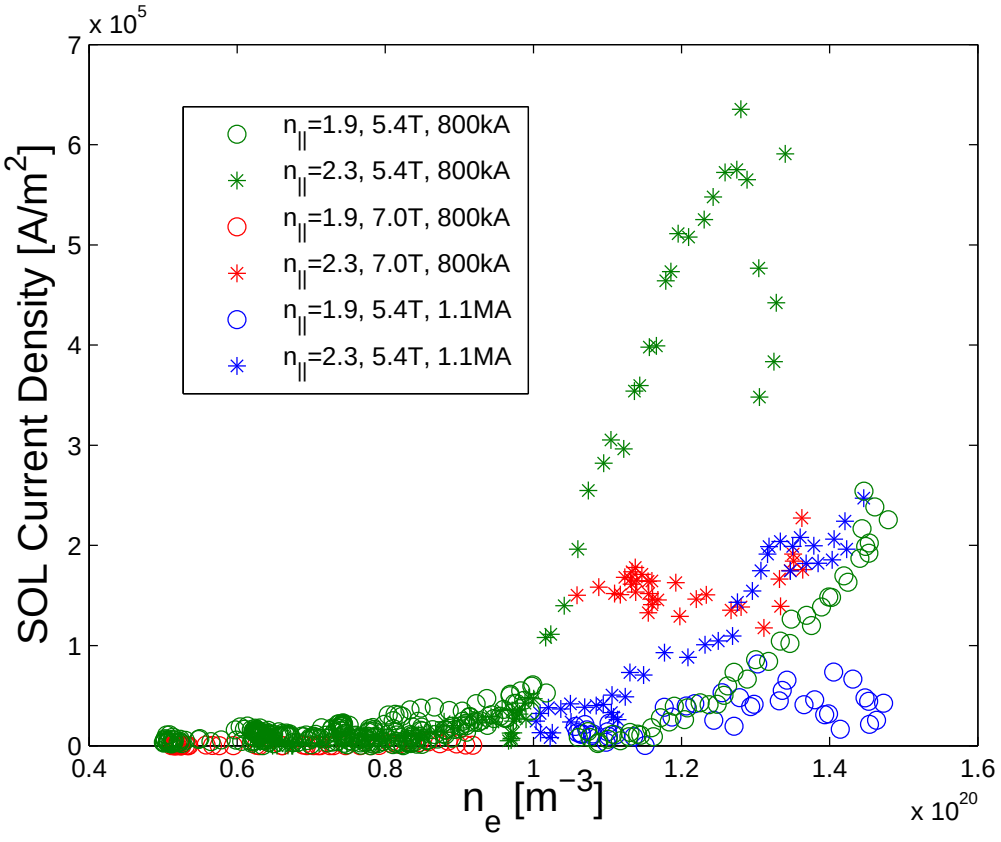

Figure 5-20: Peak SOL current density as a function of line averaged density in USN L-mode discharges, as measured by the outer upper divertor Langmuir probes. Data at $n_{||} = 2.3$ show significantly more current than data at $n_{||} = 1.9$. SOL currents are strongest for smaller values of magnetic field, and plasma current.

$|I_{sat}|$, and the ratio I_{gnd}/I_{sat} is near 0.8 with and without LHCD. On the end of the field line collecting electrons, $|I_{gnd}|$ would be limited by the electron saturation current. However, the electron saturation current is many times larger than $|I_{sat}|$. This means that $|I_{gnd}|$ may easily exceed $|I_{sat}|$ on the electron collecting end of the field line.

If the SOL current were carried by non-thermal electrons generated by LHCD via Landau damping, then the currents should change directions with $n_{||}$, but the counter-current drive data shows that the direction of the SOL current does not change with the sign of $n_{||}$. When combined with the fact that the ratio of I_{sat} to I_{gnd} is near 0.8 on the ion collecting end of the flux tube before and during LHCD, this suggests that the current is not directly driven by the LH waves. Rather, the increase in the SOL current appears to be due to an increase in density, and thus I_{sat}, at the ion collecting end of the field line. The increase in I_{sat} then allows the SOL current (which cannot exceed I_{sat} at the ion collecting end of the flux tube) to increase as well. The driving mechanism of the SOL current is consistent with a thermoelectric current [53, 78] flowing from the hotter, less dense electron collecting divertor to the colder, denser ion collecting divertor. The temperature and density asymmetry on the ion and electron collecting divertors can be inferred from the shapes of the $I-V$ curves in Figure 5-14.

An increase in plasma density at the inner divertor could be caused by a source of density localized to the outer mid-plane. In the established view of SOL flows in a diverted tokamak, ballooning transport pushes particles out of the plasma at the outer mid-plane. These particles are exhausted through the SOL to the active X-point [79]. If a source of plasma density is localized to the outer mid-plane region of the SOL, this should result in an increase in density at the inner divertor, regardless of whether the density is coming from inside the separatrix or from an external source (i.e. the LH launcher region).

Collisionally damped Lower Hybrid waves have been observed to drive current on

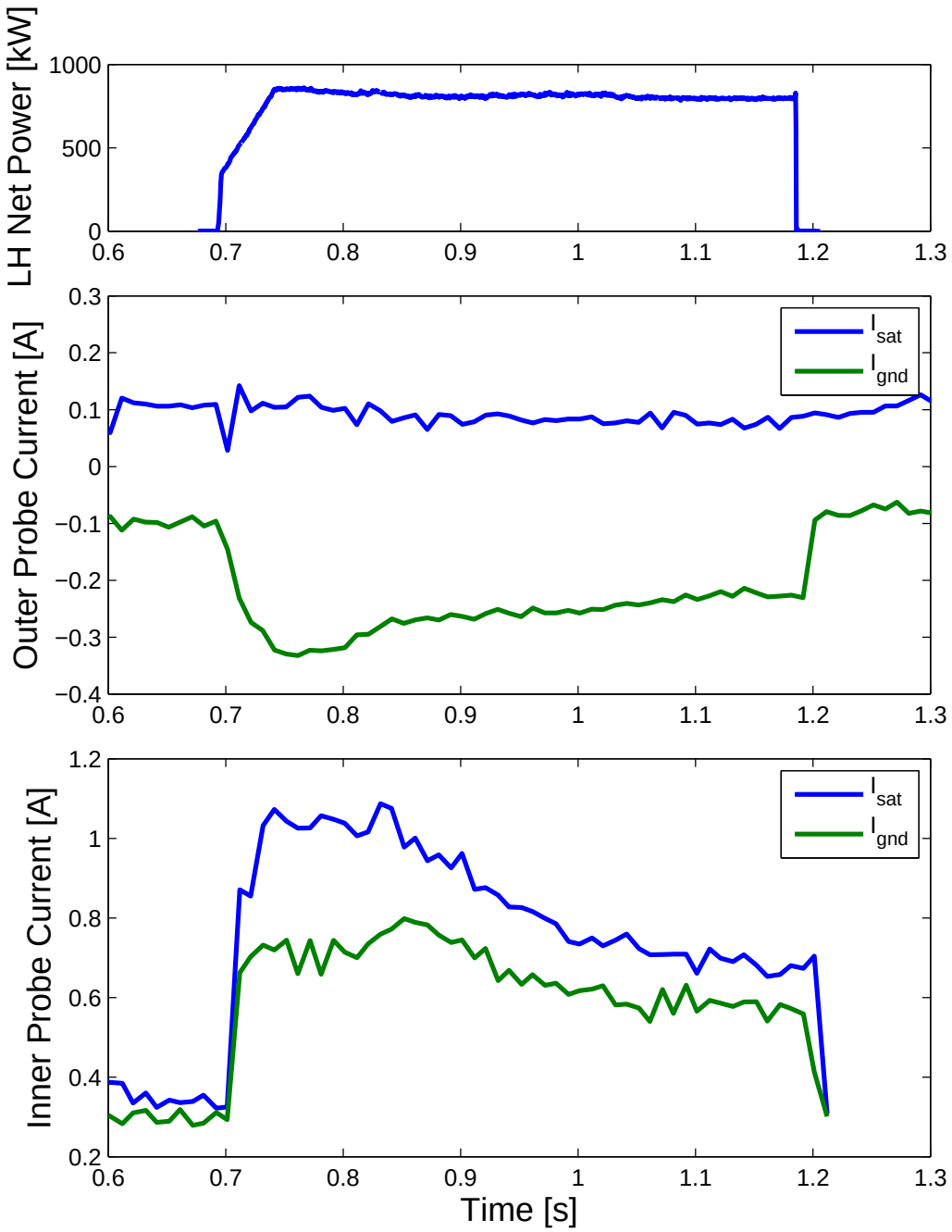

Figure 5-21: Ratio of I_{gnd} to I_{sat} on divertor probes in LSN configuration. I_{gnd} on the inner divertor is near the limit set by I_{sat}, while on the outer divertor I_{gnd} exceeds I_{sat}. Shot number = 1080402031.

open field lines in the linear H-1 device with $k_{||}v_t/\omega \ll 1$ [80]. The time averaged parallel current density driven in this case is

$$\langle j_{||} \rangle = -4.6 \times 10^{-11} \frac{q}{m_e} \frac{1}{L} \int_0^L \frac{\omega_{pe}^2(z) k_{||} |E_{||}(z)|^2}{\omega^3} dz \tag{5.3}$$

where $\langle \ldots \rangle$ represents the time average over a wave period, L is the distance from the antenna to the end of the magnetic field line, $E_{||}(z)$ is the component of the wave electric field parallel to the magnetic field, and z is the distance traveled along the field line. An upper limit on the driven current can be obtained by assuming that $E_{||}(z)$ is a constant. This assumption reduces the integral to

$$\langle j_{||} \rangle = -4.5978 \times 10^{-11} \frac{q}{m_e} \frac{\omega_{pe}^2}{\omega^3} k_{||} |E_{||}|^2 \tag{5.4}$$

The wave electric fields in the SOL of C-Mod are calculated to be ~ 10 kV/m. At a density of 1×10^{19} m^{-3}, a parallel current density of 236 kA/m^2 arises. Increasing the electric field by a factor of 10 increases the current density to 2.36×10^4 kA/m^2. Given that this upper limit on the driven current is still an order of magnitude lower than the observed current, this result is not a sufficient explanation for the observed currents. This suggests that the SOL current is a consequence of the density increase at the divertor on the ion collecting end of the field line, not the cause of the density increase at the divertor.

The resistivity of the plasma is given by the following formula [6]

$$\eta = \frac{\sqrt{2}}{12\pi^{3/2}} \frac{e^2 m_e^{1/2}}{\epsilon_0^2 T_e^{3/2}} \ln \Lambda = 6.5 \times 10^{-8}\, T_k^{-3/2} \tag{5.5}$$

where T_k is the electron temperature in keV and η is the resistivity of the plasma in Ωm. Taking a typical temperature for the region of the SOL where the currents are observed of 10 eV, this corresponds to a resistivity of 6.5×10^{-5} Ωm. If the DC toroidal electric field were solely responsible for the currents observed, the current

density should be equal to $E/\eta \sim 4$ kA/m^2. This is a factor of 100 less than the current densities observed at high density.

We can use Joule's Law

$$P = \eta J^2 \tag{5.6}$$

to estimate the power dissipated per unit volume in the SOL. For a SOL current density of 500 kA/m^2 and a plasma temperature of 10 eV, this gives a value of 1.625×10^7 W/m^3. If we take the current to be evenly distributed in a 1 cm thick annulus surrounding the separatrix, this results in a dissipated resistive power of approximately 850 kW, similar to the total injected LH power in these discharges. The total current in the SOL during LHCD is $\sim$ 20 kA, again assuming that the current is evenly distributed in a 1 cm thick annulus surrounding the separatrix.

5.2 Simulation of Wave Behavior

The GENRAY/CQL3D code package described in Chapter 1.6 includes a fast electron bremsstrahlung x-ray synthetic diagnostic that can be directly compared with the experimental results in Section 5.1.1. Figure 5-22 shows the measured and simulated bremsstrahlung emission for a range of plasma parameters. The simulations use experimental profiles of plasma density, temperature, and Z_{eff} from the same discharges plotted in the experimental HXR data. The simulated emission at values of $\bar{n}_e$ between 5×10^{19} and 1×10^{20} m^{-3} is higher than the experimental data by a factor of $\sim$5, while at 1.5×10^{20} m^{-3} the discrepancy is 2-3 orders of magnitude. However, the simulated emissivity is in qualitative agreement with the $1/n_e$ estimate. As with the experimental data, the simulations predict nearly identical emissivity for $n_{||}$ values of 1.9 and 2.3.

Figure 5-23 shows the simulated ray trajectories for a 5.4 T, 800 kA plasma at $\bar{n}_e = 1.4 \times 10^{20}$ m^{-3}. A close examination of the simulated ray trajectories in high density ($\bar{n}_e \geq 1 \times 10^{20}$ m^{-3}) shots shows that many of the rays are trapped in the

edge region of the plasma immediately after launch. At first glance this appears to be a simple accessibility problem; however, the traditional accessibility picture of ray reflection at the slow/fast wave mode-conversion point is not substantiated by the simulated ray behavior.

Figure 5-24 focuses on a single "trapped" ray from Figure 5-23. The accessibility criterion is violated when the discriminant of the dispersion relation reaches zero. However, in this case, the discriminant is at or near a local maximum at the radial turning point. Therefore, the radial reflection is not caused by mode conversion from the slow wave to the fast wave. In fact, the only location where the discriminant approaches zero is when the ray reflects off the cutoff layer at the very edge of the plasma. In these simulations an artificial cutoff layer is created by setting the density at the separatrix below the cutoff density of 2.6×10^{17} m^{-3}. The edge plasma density is set below the cutoff to avoid specular reflection of rays by a perfectly conducting surface located at the separatrix. Avoiding specular reflection is necessary since wavenumber shifts due to specular reflection are not the same as shifts caused by reflection at a cutoff. Reflections from a cutoff are the more likely cause of inward reflections near the edge of the plasma. This creates a very narrow region in which the rays are trapped between reflections at the cutoff layer and refraction caused by the change in dielectric constant.

In a toroidal geometry, this radial reflection can also be caused by refraction of the ray as it propagates in a dielectric medium with curved surfaces. In a slab geometry with a constant magnetic field, a ray will refract such that its direction becomes more parallel to the magnetic field as it moves into a region of higher density, however the ray will never reflect. The radial reflection illustrated in Figure 5-24 is actually due to refraction of the ray in a toroidal geometry, not from a violation of the accessibility criterion. At the same time as a ray becomes tangent to a flux surface, the flux surface curves away from the ray, thus creating a reflection. Although the radial component of the wavenumber passes through zero, the poloidal component of the wavenumber

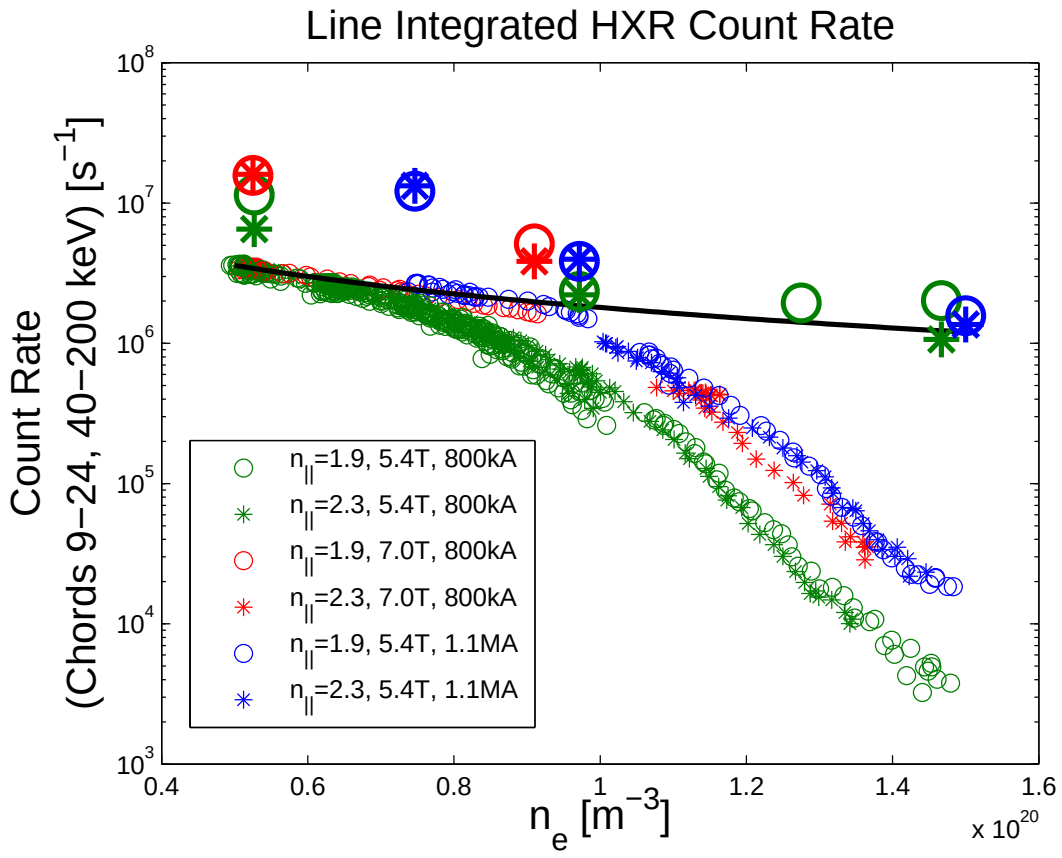

Figure 5-22: Simulated and measured HXR emission as a function of line averaged density. The output of the synthetic diagnostic is shown with large symbols, while the experimental data are shown with small symbols.

remains finite through the reflection. Figure 5-25 contains the same information as the two right panels of Figure 5-24 but for a slab geometry. It is clear in this case that the ray propagates into the plasma until the discriminant of the dispersion relation vanishes, at which point a mode conversion to the Fast Wave occurs and the ray returns back to the edge of the plasma.

The GENRAY code counts the number of radial reflections from the separatrix for each ray as it propagates through the plasma. In the standard GENRAY model, the separatrix is modeled as a perfectly conducting surface. By varying the parameter $irefl m$ in the namelist file of the code, it is possible to stop a ray after a specified

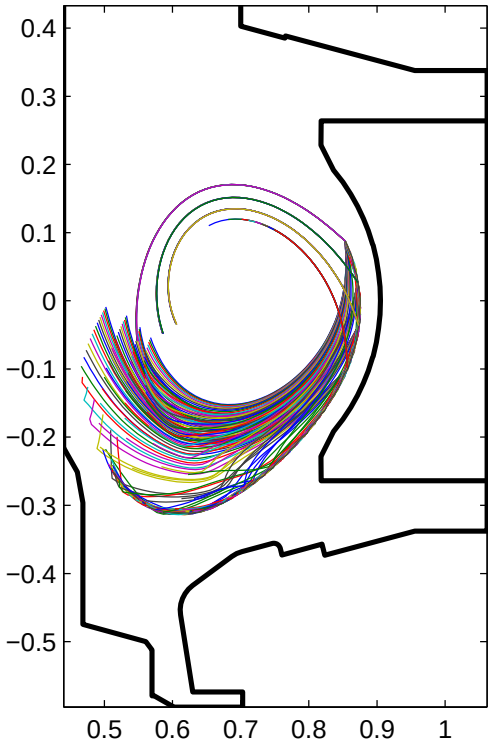

Figure 5-23: GENRAY simulation showing rays trapped near the edge of the plasma. The highest $n_{||}$ rays penetrate to near the core of the plasma, but the lower $n_{||}$ rays stay close to the edge.

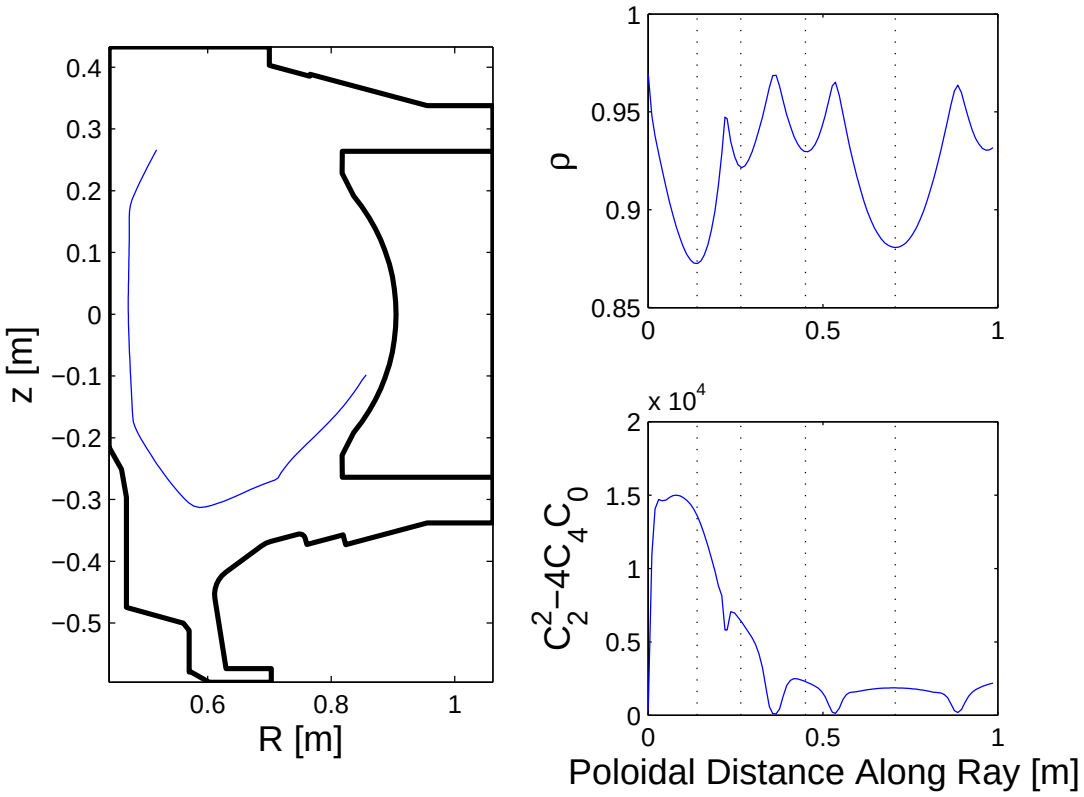

Figure 5-24: Accessibility criterion of "trapped" rays from GENRAY. The accessibility criterion is violated if the discriminant of the cold plasma dispersion relation reaches zero. For this ray, the discriminant is at a local maximum each time the ray reaches its maximum penetration into the plasma, indicating that the accessibility criterion is satisfied. The discriminant does approach zero as the ray reflects from the density cutoff at the edge of the plasma.

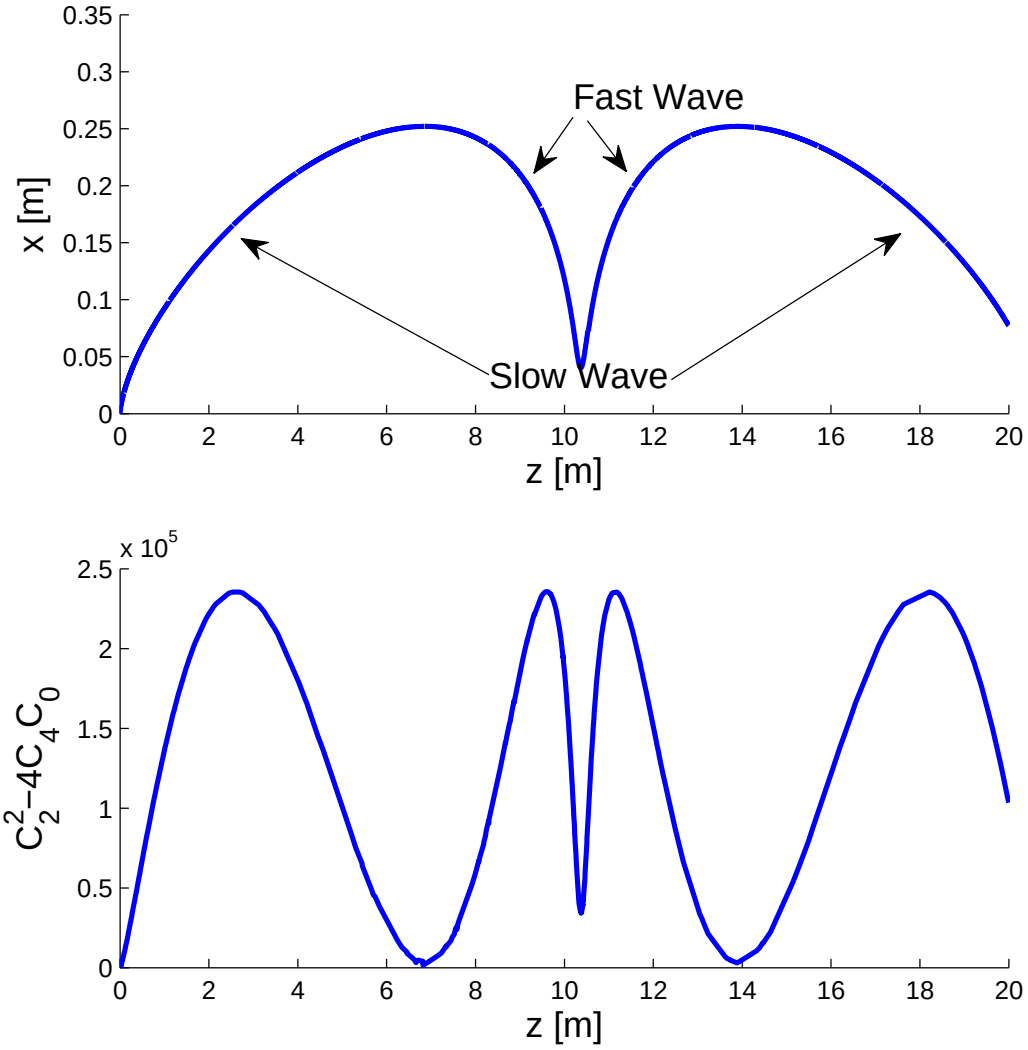

Figure 5-25: Ray path in a slab plasma with B_0 in the $\hat{z}$ direction and ∇n in the $\hat{x}$ direction. Simulation parameters are $n_{||} = 1.9$, $B_0 = 5.0$ T, $n_{edge} = 3 \times 10^{17}$ m^{-3} and $\frac{dn}{dx} = 5 \times 10^{20}$ m^{-4}. The ray mode converts between the slow and fast wave at $x = 0.25$ m ($n_e = 1.25 \times 10^{20}$ m^{-3}) where the accessibility criterion is violated (discriminant of the dispersion relation reaches zero).

number of reflections off the wall. Figure 5-26 shows the results of a scan with 19, 1, and 0 reflections from the wall. By decreasing from 19 allowed reflections, for which all off the power in every ray is absorbed, to 1 allowed reflection, the simulated HXR emission decreases by nearly an order of magnitude at high density. This is a substantial improvement in agreement, but still an overestimate of the experimental data by a factor of ∼50 at $\bar{n}_e = 1.5 \times 10^{20}$ m^{-3}. Reducing the number of reflections to zero, such that any ray will be immediately stopped after it makes contact with the separatrix, decreases the simulated HXR emission by an additional 4 orders of magnitude at 1.5×10^{20} m^{-3} and more than two orders of magnitude at 5×10^{19} m^{-3}. This shows that single-pass damping is weak even at the low density end of the scan, and we must properly account for what happens to the rays as they reflect from, or are absorbed at, the edge of the plasma. For the synthetic diagnostic HXR emissivity to agree fully with the experimental data, some amount of reflection from the cutoff must be taken into account, but there also must be some loss mechanism at the edge.

5.2.1 Scrape-Off-Layer Model for GENRAY

A close examination of the ray trajectories in Figures 5-23 and 5-24 shows that a more careful treatment of the pedestal and SOL regions is necessary to accurately represent the wave behavior in the edge region. Artificially setting the edge density below cutoff creates a narrow region between the low density cutoff layer and the high density refracting layer. The subtle shifting of the wave number has a substantial impact on current drive efficiency and will not be properly accounted for without accurately representing the plasma in this critical region. To account for this, a primitive SOL model has been added to GENRAY. The SOL model is poloidally symmetric and has an exponential decay based on the shortest distance from a given point to the last closed flux surface. Magnetic fields in the SOL are imported directly from an EFIT equilibrium. Figure 5-27 illustrates the SOL model profile used in GENRAY. The SOL is only included in the GENRAY code and is not a part of CQL3D. Consequently,

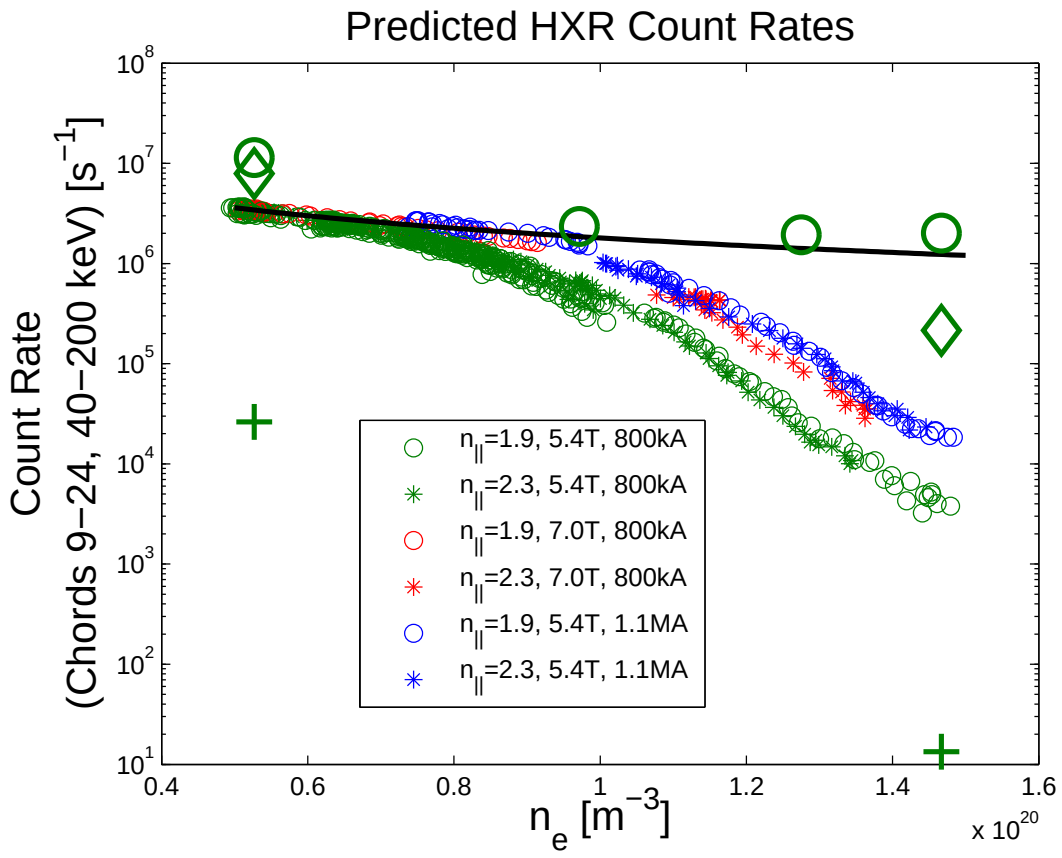

Figure 5-26: Simulated HXR emission as a function of density for the maximum number of radial reflections set to 19 (circles), 1 (diamonds), and 0 (crosses).

quasi-linear wave absorption is not calculated in the SOL, and the radiation from fast electrons born in the SOL is not included in the synthetic diagnostic. The symmetric SOL model added to GENRAY includes collisional damping effects. At the low temperatures encountered in the SOL, collisional damping can be comparable to or exceed Landau damping for low $n_{||}$ waves; however, information regarding the collisional absorption of the rays in the SOL is not included in the quasilinear diffusion coefficient used in CQL3D. The effects of collisional damping in the SOL will be discussed further in Section 5.2.3.

The ray trajectories for low and high density cases at 5.4 T and 800 kA with a density scrape off length, σ_{ne}, of 0.1 m are shown in Figure 5-28 and 5-29, respectively. The black lines, representing the vacuum vessel wall and limiters, are overlaid for reference but not included in the simulation. The ray trajectories in the low density case are nearly unchanged when compared to simulations at the same density without a SOL. In the high density case with the SOL present, the "trapped" rays are seen to propagate in the SOL region in such a way that many intersect either the limiter or the divertor. It should be noted that a uniform scrape off length of 0.1 m is reasonable in the divertor regions but unrealistic for the inner and outer walls of C-Mod. Figure 5-30 compares two GENRAY/CQL3D runs with and without the SOL model. The runs including the SOL, represented by the large crosses, show no difference in X-ray count rate at $\bar{n}_e = 5 \times 10^{19}$ m^{-3}. At 1.5×10^{20} m^{-3} there is a difference of 2-5 in count rate. This clearly does not fully account for the discrepancy between the simulated and experimental data points at high density, although it is a significant step in the right direction.

A two dimensional SOL profile, for which the density scale length, σ_n, is a function of poloidal angle, has also been implemented in GENRAY. Figure 5-31 shows a comparison between GENRAY/CQL3D with no SOL model and with the 2-D SOL model. As compared with the 1D SOL model, the 2-D model shows better agreement with the experimental data at 800 kA. The agreement is worse at 1.1 MA with

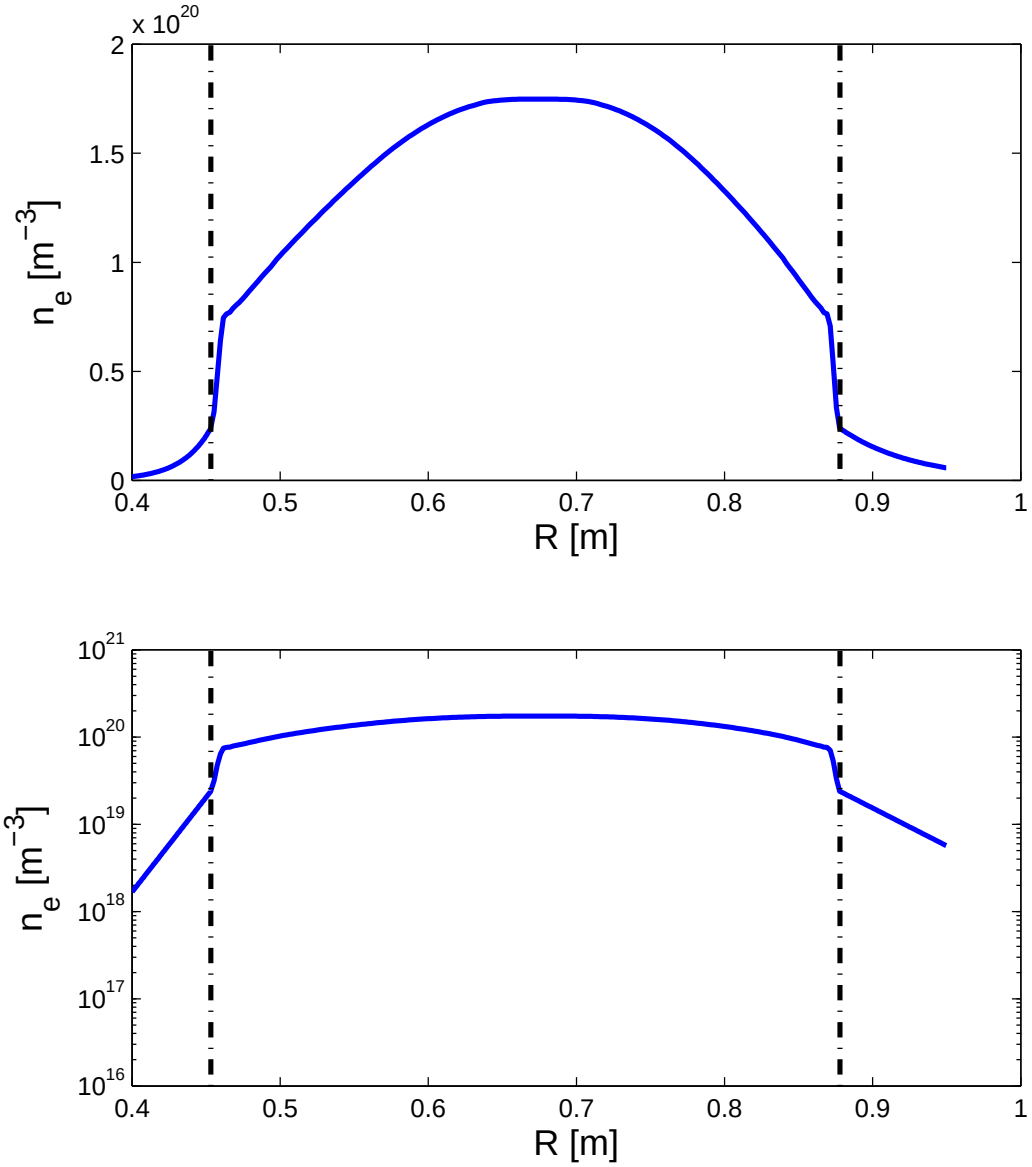

Figure 5-27: Mid-plane density profile with SOL model, plotted on linear and logarithmic scales. The e-folding length on the low field side for this case is 0.05 m, while on the high field side it is 0.02 m. Vertical dashed lines represent the separatrix location on the HFS and LFS.

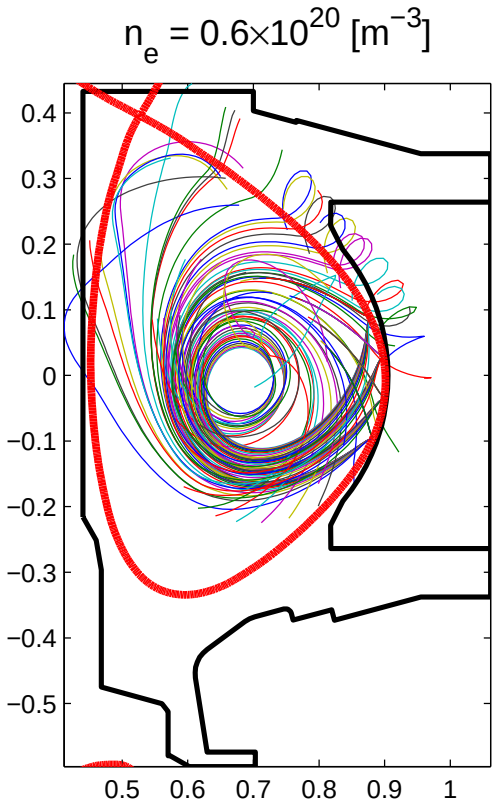

Figure 5-28: GENRAY simulation showing rays in the SOL at $\bar{n}_e = 0.6 \times 10^{20}$ m^{-3}. The SOL model in this simulation is poloidally symmetric with a density decay length of 0.1 m, and a temperature decay length of 0.01 m. The vacuum vessel walls and limiters shown in black are superimposed for reference and are not included in the simulation. The separatrix location is shown in red.

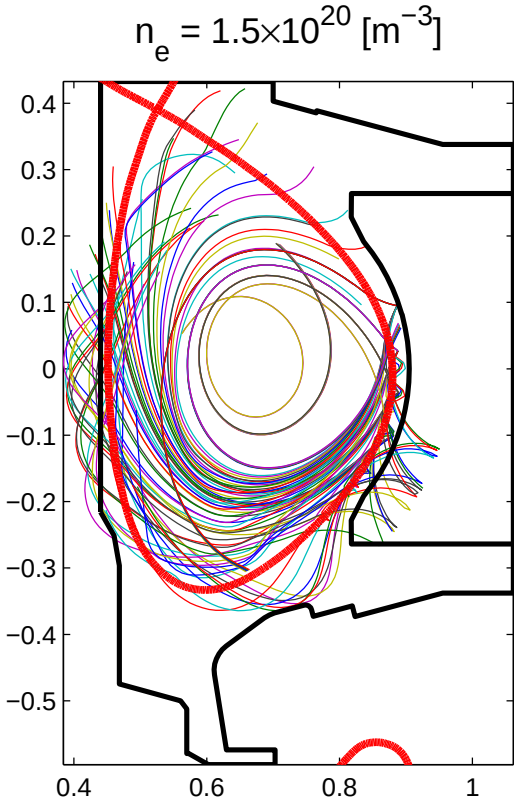

Figure 5-29: GENRAY simulation showing rays in the SOL at $\bar{n}_e = 1.5 \times 10^{20}$ m^{-3}. The SOL model in this simulation is poloidally symmetric with a density decay length of 0.1 m, and a temperature decay length of 0.01 m. The vacuum vessel walls and limiters shown in black are superimposed for reference and are not included in the simulation. The separatrix location is shown in red.

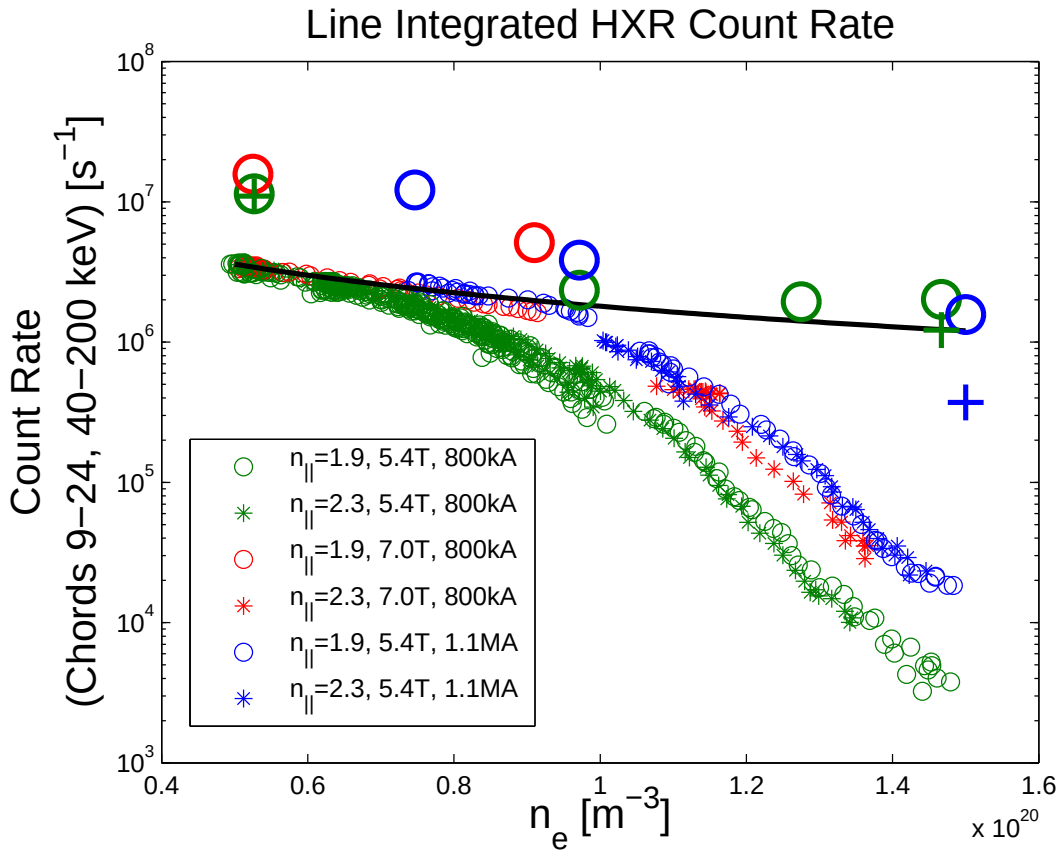

Figure 5-30: Comparison of fast electron bremsstrahlung emission predicted by GENRAY/CQL3D code package with and without simple SOL included in GENRAY. Large circles do not include the SOL, while large crosses do include the SOL. CQL3D does not include the SOL for either set of simulations.

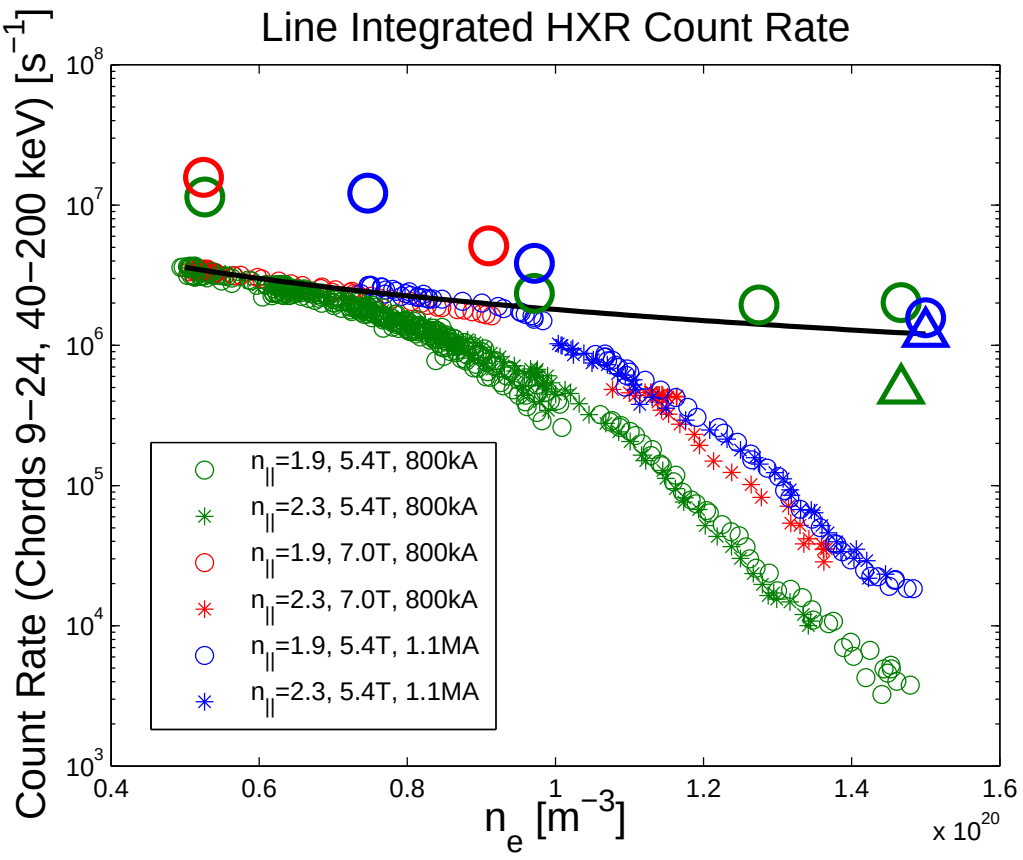

Figure 5-31: Comparison of fast electron bremsstrahlung emission predicted by GENRAY/CQL3D code package with and without a 2-dimensional SOL model included in GENRAY. Large circles do not include the SOL, while large triangles include the 2-D SOL. CQL3D does not include the SOL for either set of simulations.

the 2-D SOL. The 2-D SOL model also includes the C-Mod vacuum vessel geometry and reflects rays that intersect the metallic surfaces of the vessel. Figure 5-32 shows the ray trajectories for a high density ($\bar{n}_e = 1.5 \times 10^{20}$) discharge with the 2-D SOL model. Although shifts of $k_{||}$ that occur in the SOL reduce the predicted x-ray emissivity, the experimental data are still several orders of magnitude below that predicted by CQL3D. Therefore, there must be an additional mechanism or mechanisms responsible for the discrepancy.

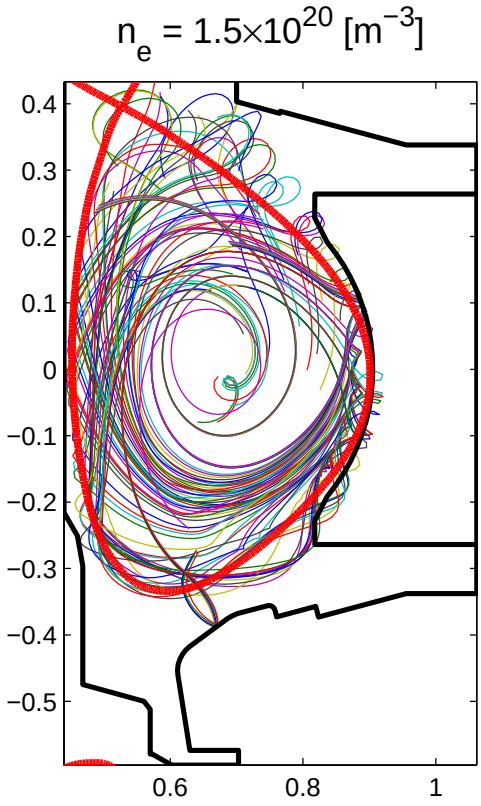

Figure 5-32: Ray trajectories including a 2-D SOL model and reflections from the vacuum vessel. The separatrix location is shown in red. $\sigma_T(\theta)$ is estimated on the basis of flux expansion.

5.2.2 Density Fluctuation Scattering

Scattering from density fluctuations can cause substantial shifts in the wavenumber of lower hybrid waves [81]. GENRAY has the capability to parametrize the fluctuations in terms of their radial location, intensity, and toroidal/poloidal mode numbers.

$$n(\rho, \theta, \phi) = n(\rho)(1 + \delta n_0 \beta(\rho, \theta, \phi)) \tag{5.7}$$

where

$$\beta(\rho, \theta, \phi) = \beta_\rho \beta_\theta \beta_\phi \tag{5.8a}$$

$$\beta_\rho = 0.5(1 + \frac{2}{\pi} \frac{\rho - \rho_0}{1 - \rho_0} \arctan(\frac{\rho - \rho_0}{\sigma_n^2})) \tag{5.8b}$$

$$\beta_\theta = 0.5(1 + \cos(N_\theta \theta)) \tag{5.8c}$$

$$\beta_\phi = \cos(N_\phi \phi) \tag{5.8d}$$

Here, ρ_0 is the minimum radius at which the fluctuations are present, δn_0 is a scaling factor for the amplitude of the fluctuations, σ_n is the radial width of the density fluctuations, N_ϕ is the toroidal mode number of the fluctuations, and N_θ is the poloidal mode number of the fluctuations. Figure 5-33 shows the radial profile of the density fluctuations.

When the density fluctuations are present in a model that has no SOL, the effect on the predicted HXR emissivity is small. (See Figure 5-34.) When the effects of the density fluctuations are combined with the SOL model, however, there can be a dramatic reduction in X-Ray emissivity. Figure 5-35 shows a reduction in emissivity of greater than 2 orders of magnitude, agreeing closely with the experimental data. The values for N_θ and N_ϕ are based on measurements from the Gas Puff Imaging (GPI) system, which show that the perpendicular wavelength of the density fluctuations in the SOL is ~ 2 cm. The perpendicular wavelength can be converted to poloidal mode

number

$$N_\theta = \frac{2\pi a \cos(\xi)}{\lambda_\perp} \tag{5.9}$$

and toroidal mode number

$$N_\phi = \frac{2\pi R_0 \sin(\xi)}{\lambda_\perp} \tag{5.10}$$

where a is the minor radius of the plasma, R_0 is the major radius of the plasma, and ξ is the angle between $\hat{b}$ and $\hat{\phi}$. The fluctuation parameters for both the 5.4 T, 800 kA case and the 5.4 T, 1.1 MA case are identical: $N_\theta = 68$, $N_\phi = 48$, and $r/a = 0.999$.

Figures 5-35 and 5-36 show the sensitivity of the x-ray emissivity to the amplitude and mode number of these fluctuations, respectively. Measurements of the fluctuations with the Gas Puff Imaging (GPI) diagnostic on C-Mod show that the amplitude of the fluctuations is in the range of ???% with perpendicular mode numbers of ???. Since measurements of the mode number and amplitude of the density fluctuations in C-Mod have error bars larger than the range of values shown in these figures, it is difficult to quantitatively determine exactly how much the fluctuation scattering contributes to the lack of x-ray emissivity.

5.2.3 Collisional Absorption in the SOL

The simulations previously discussed do not include any contribution of damping in the SOL calculated by GENRAY. The collisional absorption of the LH waves can be strong in regions of high density and low temperature ($T_e <\sim 10$ eV) as shown in Figure 5-37. At temperatures above ~ 10 eV the damping is small even at high density. The values of $\Im(k_\perp)$ shown in Figure 5-37 is calculated by substituting the electron mass, m_e, with $m_e(1 + i\nu_{ei}/\omega)$ in the cold plasma dispersion relation, where ν_{ei} is the electron-ion collision frequency.

By including the effect of power absorbed in the SOL due to collisional damping, the x-ray emissivity at high density is reduced significantly [82]. (See Figure 5-38.)

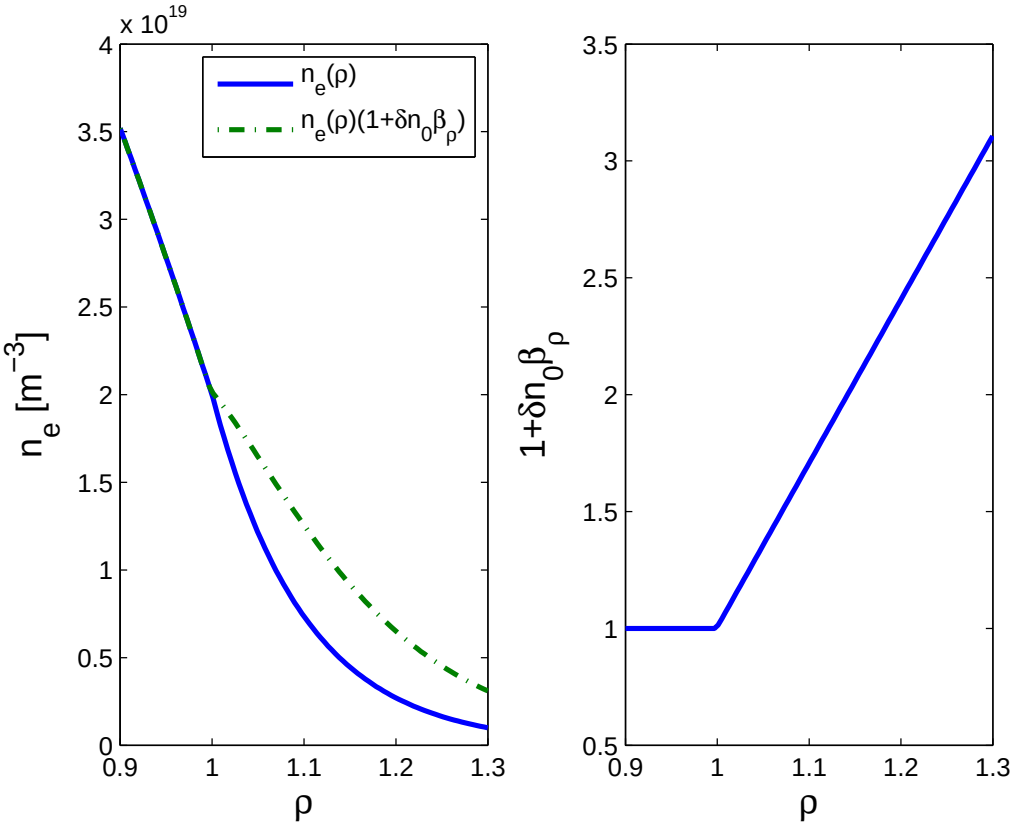

Figure 5-33: Radial profile of density fluctuations in the SOL. $\delta n_0 = 0.007$, $\sigma_n = 0.01$, and $\rho_0 = 0.999$.

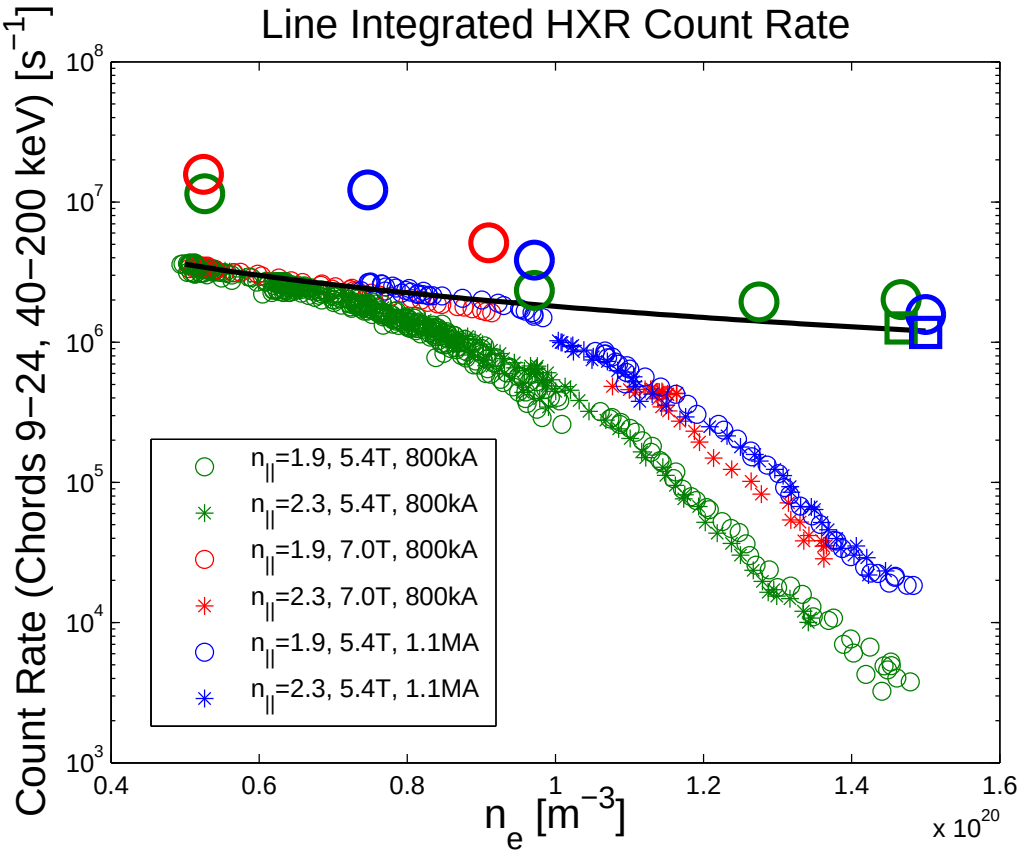

Figure 5-34: Simulated X-Ray emission including the effect of scattering from density fluctuations inside the separatrix with no SOL included in the model. Large squares indicate emission with density fluctuations while large circles indicate emission without density fluctuations.

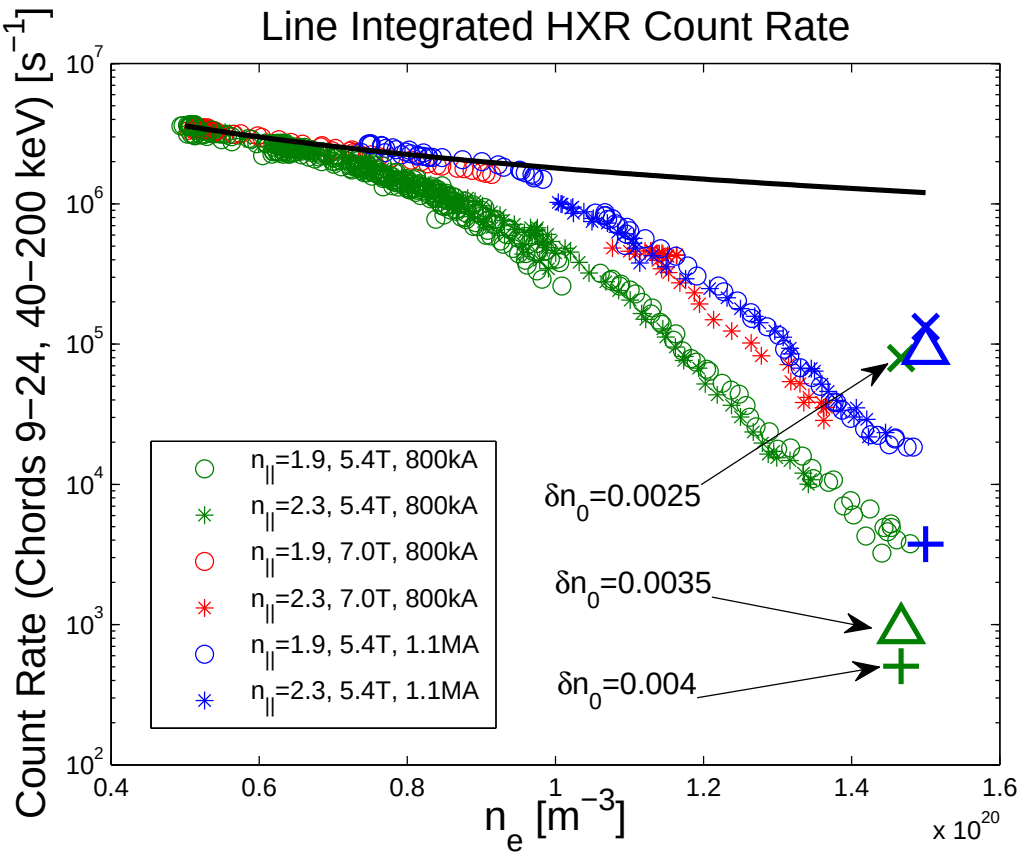

Figure 5-35: Simulated X-Ray emission including the effect of scattering from density fluctuations near the separatrix and a 2-D SOL model. Large symbols indicate emission with $\rho_0 = 0.999$, $\sigma_n = 0.01$, $N_\theta = 68$ and $N_\phi = 48$. A range of δn_0 from 0.0025 to 0.004 is shown.

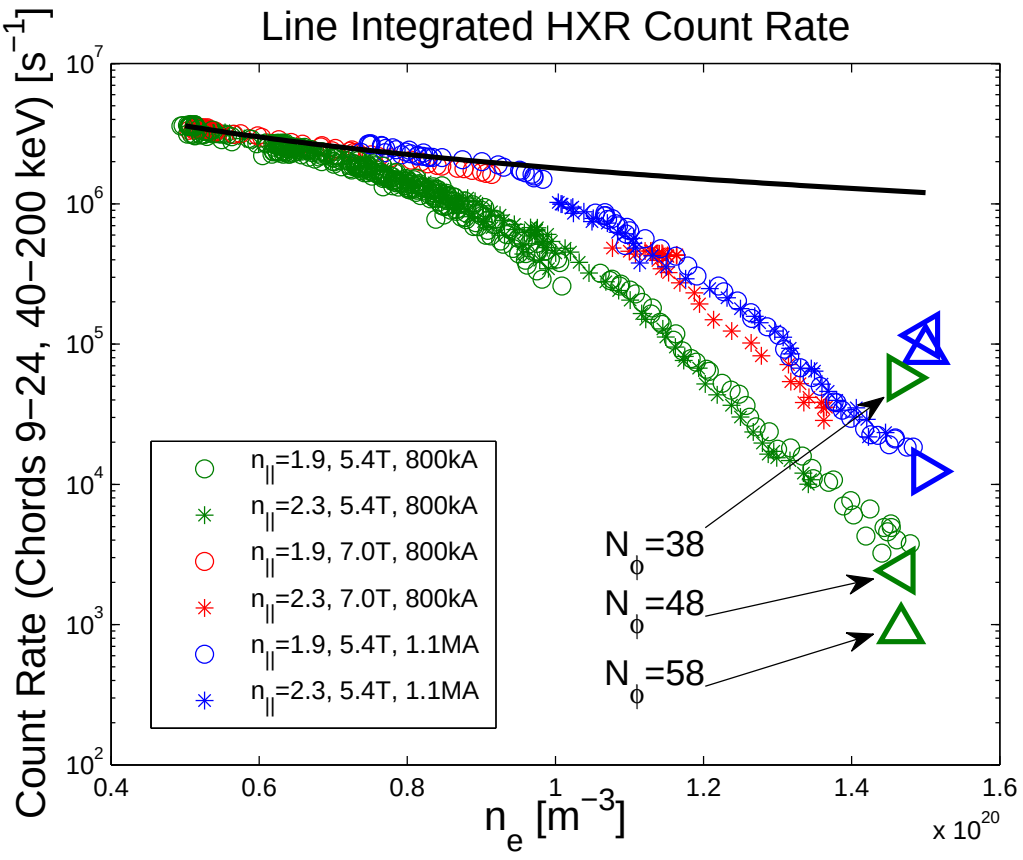

Figure 5-36: Simulated X-Ray emission including the effect of scattering from density fluctuations near the separatrix and a 2-D SOL model. Large symbols indicate emission with $\rho_0 = 0.999$, $\sigma_n = 0.01$, $N_\theta = 68$ and $\delta n_0 = 0.0035$. A range of N_ϕ from 38 to 58 is shown.

The agreement between experimental data and predictions from CQL3D is improved across the entire density range, although the agreement is most improved at 1.5×10^{20} m^{-3} where the discrepancy was reduced from a factor of $\sim 100 - 1000$ to a factor of $\sim 3 - 30$.

It should be noted that the SOL parameters are identical for all of the simulation data points in Figure 5-38. The temperature in the SOL decays exponentially with an e-folding length, σ_T, of 0.005 m until the temperature reaches a minimum of 5 eV. These values are consistent with measurements of the SOL temperature profiles typically observed in C-Mod L-mode discharges. The density e-folding length varies between 0.1 m in the divertor regions and 0.02 m on the midplane. Again, these values are typical for L-mode discharges.

Collisional absorption in the SOL is sensitive to the specifics of both the temperature and density profiles. Since the absorption peaks in areas of low temperature and high density, such as divertor regions, the exact path of the ray will determine the level of damping in the SOL. At a fixed density, the experimental x-ray emissivity is consistently weaker for the 5.4 T, 800 kA discharges with $\bar{n}_e$ above $\sim 8 \times 10^{20}$ m^{-3}; however, the simulation data does not show this same trend. This may be due to the sensitivity of the SOL absorption to the temperature and density profiles. Results from Alcator C [24] show an increase in current drive efficiency at higher magnetic field. The increase in efficiency was attributed to an increase in electron temperature at higher field. There may be small differences in the SOL profiles as a function of plasma current and magnetic field, although in the discharges considered there are no profile measurements in the SOL. Still, the strong downward trend in x-ray emission as density increases suggests that a damping mechanism in the SOL that is roughly proportional to n_e and inversely proportional to T_e may be largely responsible for the absence of fast electrons in the plasma.

Collisional absorption in the edge of the tokamak was suggested as a possible explanation for the density limit observed on PLT [83]. In PLT, single-pass damping

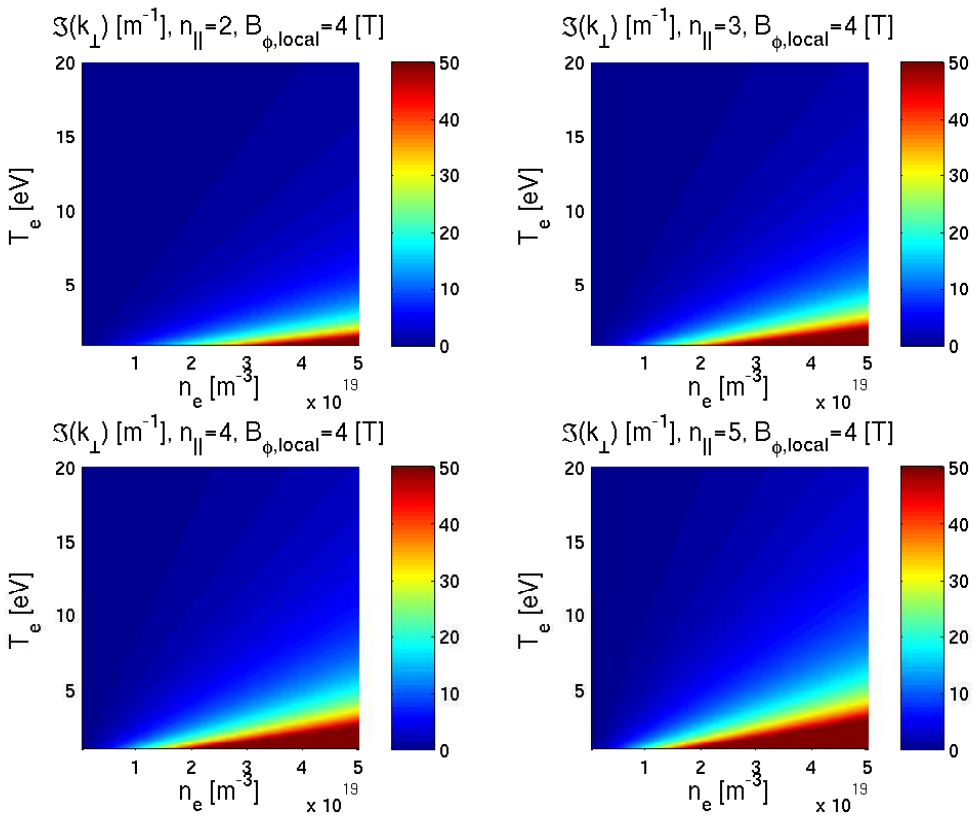

Figure 5-37: Imaginary component of $k_\perp$ due to collisions at 4.0 T.

at high density was observed to be low, and an arbitrary increase of edge collisional absorption of a factor of 5-7 in the computational modeling correctly reproduced the experimental density limit. A more careful analysis of the results from PLT and Alcator C revealed that PDI was in fact the cause of the density limit for those experiments, whereas in C-Mod PDI has been eliminated as a possible cause. Although the mechanism of edge collisional absorption was incorrectly applied for those experiments, the prediction that collisional edge absorption could be important proved to be correct for C-Mod.

Although collisional absorption does not by itself lead to a net driven current in the plasma, it is possible that the SOL currents discussed in Section 5.1.3 may be due to asymmetric heating in the SOL. If the waves leaving the LH launcher deposit their

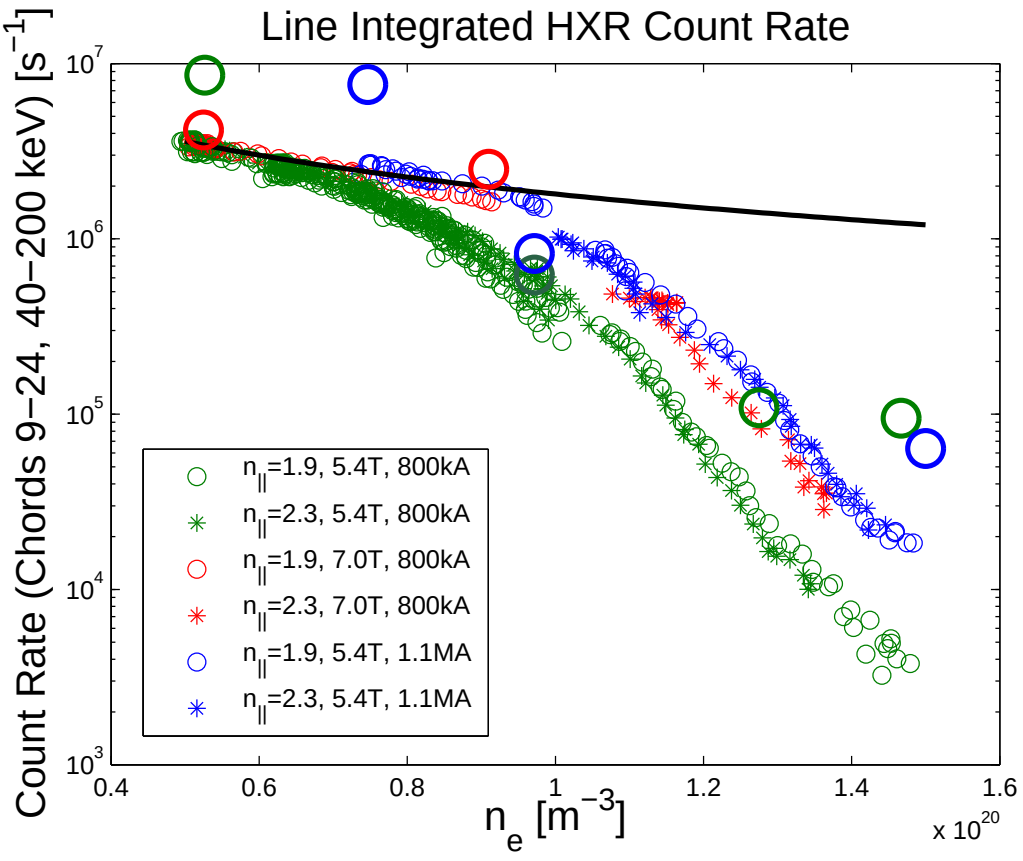

Figure 5-38: Comparison of fast electron bremsstrahlung emission predicted by GENRAY/CQL3D code package with a 2-dimensional SOL model in GENRAY including the effects of collisional damping in the SOL. The large symbols represent simulations while the small symbols are experimental data.

energy preferentially in one direction along the field lines, this can cause a parallel thermal gradient, which in turn can drive a current along the open field lines [53]. There is some inconsistency in this explanation. If a thermal gradient is responsible for driving the currents in the SOL, then the region of plasma where the waves are absorbed through collisional damping would heat up. As can be seen from Figure 5-37, the collisional damping rate falls sharply as plasma temperature rises. Furthermore, measurements of T_e in the divertors do not show a change in temperature on either end of the field line during the application of LHCD.

This same reasoning suggests that it may be possible to "burn through" the observed density limit. If sufficient energy is deposited in the SOL, the temperature will rise and the collisional damping rate will fall, thereby increasing the amount of power absorbed on closed flux surfaces. This self-regulating mechanism could provide a means to ameliorate the density limit phenomenon, although if this is possible the critical power level is above 900 kW on C-Mod.

Another possible solution to the problem of LH wave absorption in the SOL may be to increase the temperature inside the separatrix such that waves with poor penetration to the core plasma are still absorbed before refracting back into the SOL. If the single-pass absorption is high for all rays, then the loss in the SOL will be significantly reduced. Alternatively, dramatically increasing $n_{||}$ while keeping the plasma temperature constant will increase single-pass absorption at the cost of overall current drive efficiency.

5.2.4 Full Wave SOL Solution

The treatment of the Lower Hybrid wave developed in Section 3.1 can also be used to investigate the propagation of LH waves through the SOL and pedestal regions, although relevant expressions for $\epsilon_\perp$ and $\epsilon_\times$ at densities much greater than the cutoff

density must be included. The function $n(x)$ from Equation 3.7 can be taken to be

$$n(x) = n_0 \exp(x/\sigma) + \frac{n_{ped} - n_0}{2}(1 + \tanh(\pi\lambda(x - \Delta))) \tag{5.11}$$

where n_0 is the density at the antenna, σ is the density scale length in the SOL, n_{ped} is the density at the top of the pedestal, Δ is the location of the pedestal, and λ is the inverse of the pedestal width. Equation 5.11 provides a reasonable approximation of the density profile near the separatrix of a tokamak. Figure 5-39 shows the edge density profile for $n_0 = 2.0 \times 10^{17}$ m^{-3}, $n_{ped} = 1.5 \times 10^{20}$ m^{-3}, $\sigma = 0.01$ m, $\lambda = 1000$ m^{-1}, and $\Delta = 0.035$ m.

By superimposing the solutions for the electric field for a spectrum of $k_{||}$, it is possible to reconstruct the electric field structure in the vicinity of the LH antenna. Figures 5-40, 5-41, and 5-42 show the field structure for spectra peaked at $n_{||} =$ 1.55, 2.33, and 3.1, respectively. The waves propagate towards the pedestal of a low density H-mode described by a tanh density profile. The resonance cones are observed to refract increasingly parallel to the magnetic field in the vicinity of the pedestal. Furthermore, partial reflection of waves off of the density pedestal produces a wave traveling in the z direction outside the density pedestal, bounded by the wall and the pedestal itself.

In the geometrical optics approximation used in ray tracing, only full transmission or reflection at a dielectric interface is allowed. Partial reflection is not treated, and therefore ray tracing will not accurately reproduce the behavior of waves encountering a steep dielectric gradient. This problem exists both for rays crossing from the launcher into the confined plasma and also for rays making multiple passes through the plasma. The Poynting vector is defined as

$$\vec{S} = \vec{E} \times \vec{H}^* \tag{5.12}$$

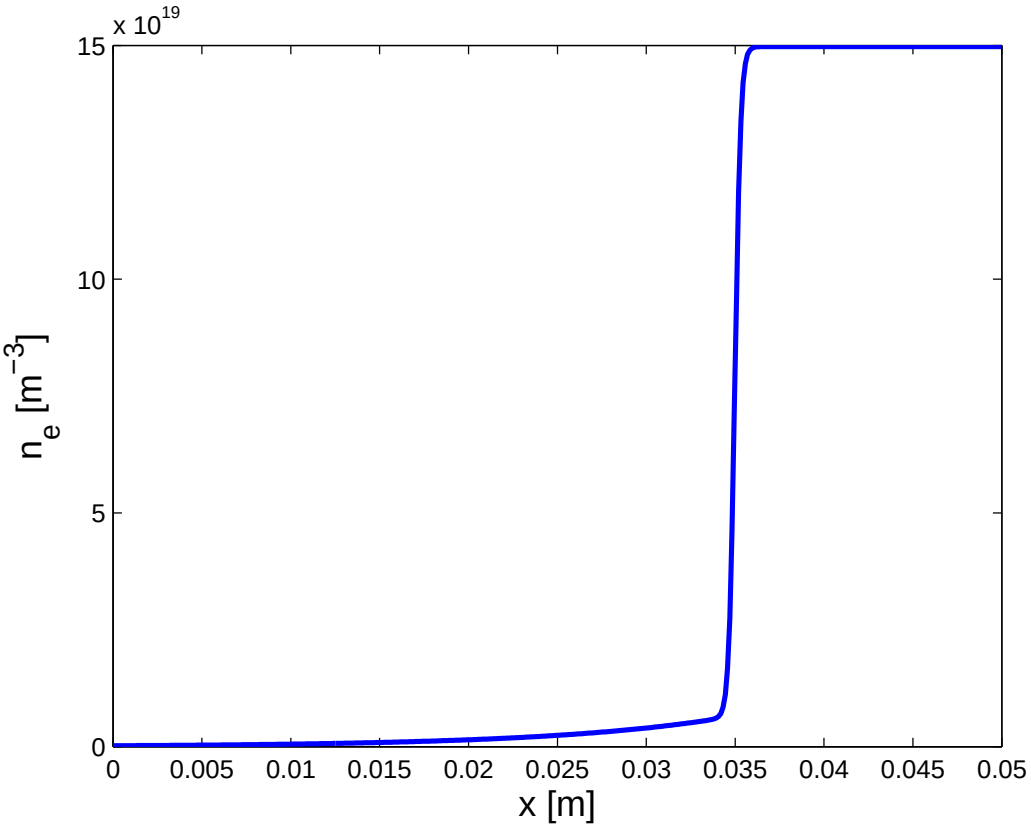

Figure 5-39: Hyperbolic tangent density profile used for simulations in Figures 5-40, 5-41, and 5-42. This density profile is defined in Equation 5.11 with $n_0 = 2.0 \times 10^{17}$ m^{-3}, $n_{ped} = 1.5 \times 10^{20}$ m^{-3}, $\sigma = 0.01$ m, $\lambda = 1000$ m^{-1}, and $\Delta = 0.035$ m.

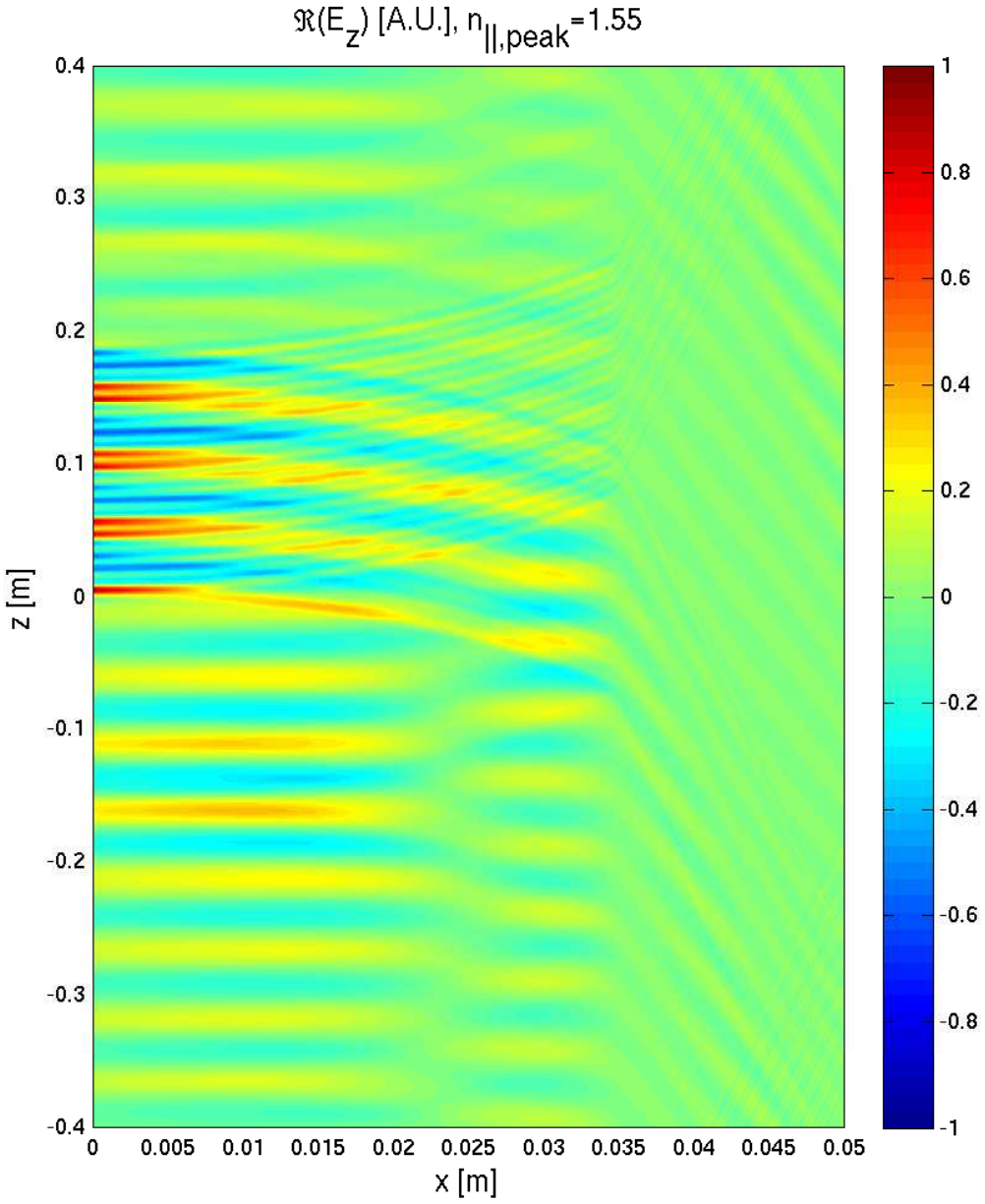

Figure 5-40: One dimensional full wave simulation showing penetration of Lower Hybrid waves through a tanh density pedestal located at 0.035 m with $n_{||} = 1.55$. The density at the pedestal foot is $n_e = 5 \times 10^{18}$ m^{-3} and the density at the pedestal top is $n_e = 1 \times 10^{20}$ m^{-3}.

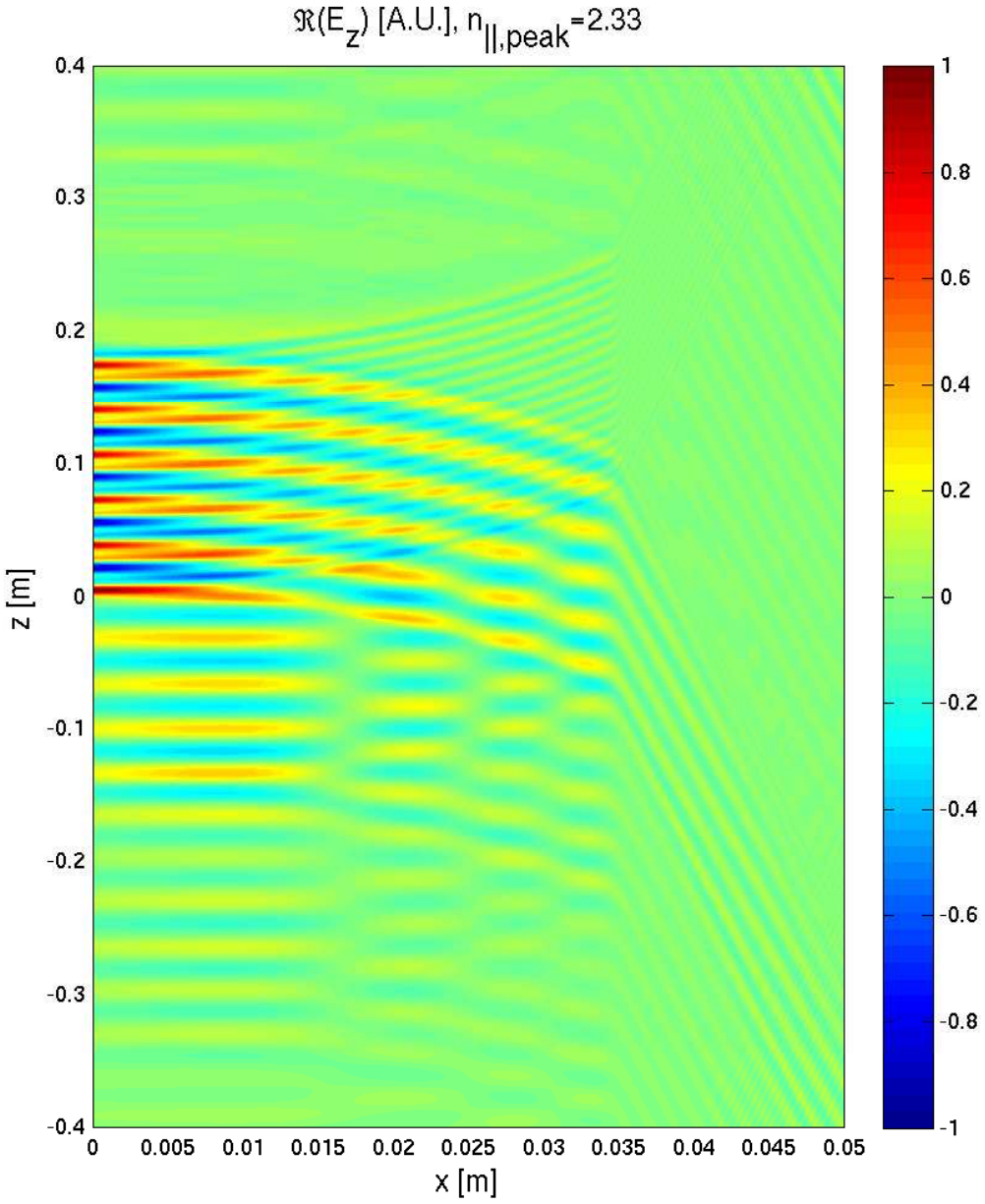

Figure 5-41: One dimensional full wave simulation showing penetration of Lower Hybrid waves through a tanh density pedestal located at 0.035 m with $n_{||} = 2.33$. The density at the pedestal foot is $n_e = 5 \times 10^{18}$ m^{-3} and the density at the pedestal top is $n_e = 1 \times 10^{20}$ m^{-3}.

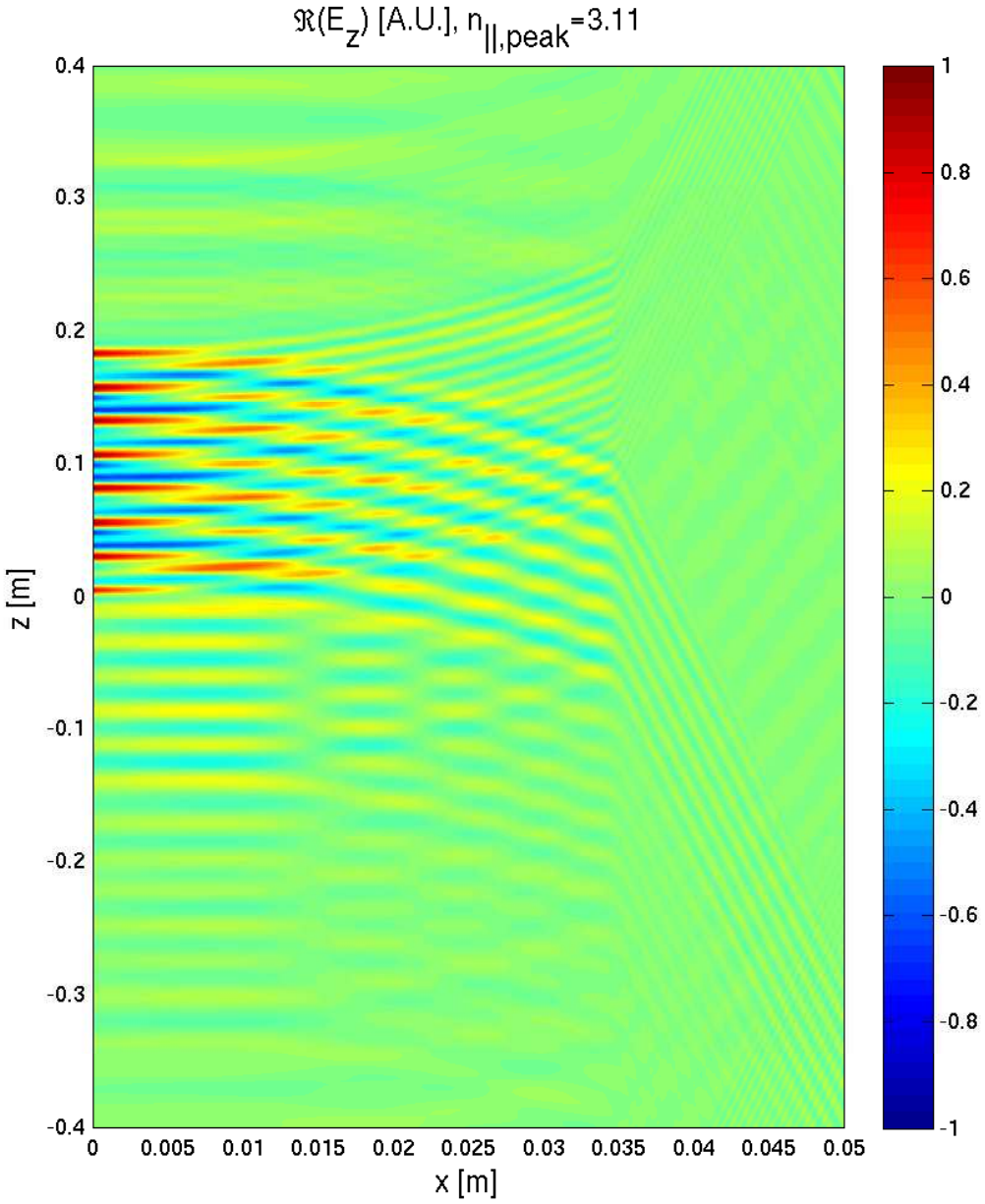

Figure 5-42: One dimensional full wave simulation showing penetration of Lower Hybrid waves through a tanh density pedestal located at 0.035 m with $n_{||} = 3.1$. The density at the pedestal foot is $n_e = 5 \times 10^{18}$ m^{-3} and the density at the pedestal top is $n_e = 1 \times 10^{20}$ m^{-3}.

where we have previously solved for $\vec{E}$ as

$$\vec{E} = E_x\hat{x} + E_z\hat{z} \tag{5.13}$$

$\vec{H}$ can be determined by applying Ampere's Law to Equation 5.13, which results in

$$\vec{H} = \frac{ik_{||}E_x - E'_z}{i\omega\mu_0}\hat{y} \tag{5.14}$$

By combining Equations 5.12, 5.13, and 5.14, the Poynting vector can be expressed as

$$\vec{S} = -E_z H_y^*\hat{x} + E_x H_y^*\hat{z} \tag{5.15}$$

Figures 5-43 and 5-44 show both the electric field and the Poynting vector for $n_{||}$ values of 1.94 and 2.33. The black boxes in the figures represent a closed integration path for determining the Poynting flux. Since there is no variation in the y direction, integrating along the path in the xz-plane gives the Poynting flux per unit length in the y direction. The vertices of these boxes are chosen such that the "single pass" resonance cones leave the box through the right hand side, while the "multiple pass" resonance cones leave through the top and bottom of the box. The Poynting flux is then normalized so that the incident power on the left hand side of the box is 1 in arbitrary units. The power leaving through the right hand side is 0.78 for Figure 5-43 and 0.83 for Figure 5-44. The $\sim 20\%$ of the power that does not leave through the right hand side of the box escapes through the top and bottom in the wave that is confined in the SOL. This discrepancy of $\sim 20\%$ is especially significant in cases for which the rays undergo multiple transitions through the SOL prior to fully damping. (See Figure 5-24.)

Figure 5-45 shows the percentage of power transmitted through the pedestal in the primary resonance cone as a function of pedestal width ($\lambda_{\tanh}$) and height (n_{ped}). The parameter scan shows that the transmission of power to the core plasma is hampered

by a taller, narrower pedestal such as would be found in an H-mode discharge. Even for relatively low, wide pedestals, nearly 5% of the incident power is lost from the primary resonance cone due to partial reflection off the pedestal. Since many rays transit through the pedestal several times before they are absorbed in the plasma, even relatively small partial reflection may result in a substantial fraction of the power remaining in the SOL.

5.3 Implications for LHCD in H-mode on Alcator C-Mod

In general, H-mode discharges have considerably higher line averaged densities than L-modes. On C-Mod, H-modes with $\overline{n}_e < 1.5 \times 10^{20}$ are extremely difficult to obtain, and the highest peformance H-modes have $\overline{n}_e > 2.0 \times 10^{20}$. Given that the density of these discharges is well above the L-mode density limit for LHCD, the scaling of the LHCD density limit in H-mode is of considerable interest for the future of C-Mod.

When LHCD is applied to relatively low density, $\bar{n}_e < 2 \times 10^{20}$ m^{-3}, low Z_{eff} H-mode plasmas on C-Mod, substantial changes occur in the plasma despite the fact that the density is above the limit described previously in this chapter. During the application of high power LHCD, the density profile is observed to relax, with a decrease in density at the top of the pedestal and an increase in density at the foot. The temperature profile also changes, although in a different manner than the density profile. The temperature increases at the top of the pedestal but remains nearly constant at the pedestal foot. These complementary changes in the temperature and density result in a nearly unchanged pedestal pressure profile. The pressure at $r/a < 0.6$ increases by 10-15%. The temperature, density, and pressure profiles for an H-mode discharge before (0.95 s) and during (1.25 s) LHCD are shown in Figure 5-46.

Figure 5-47 shows the changes to the H-mode pedestal with LHCD. The changes

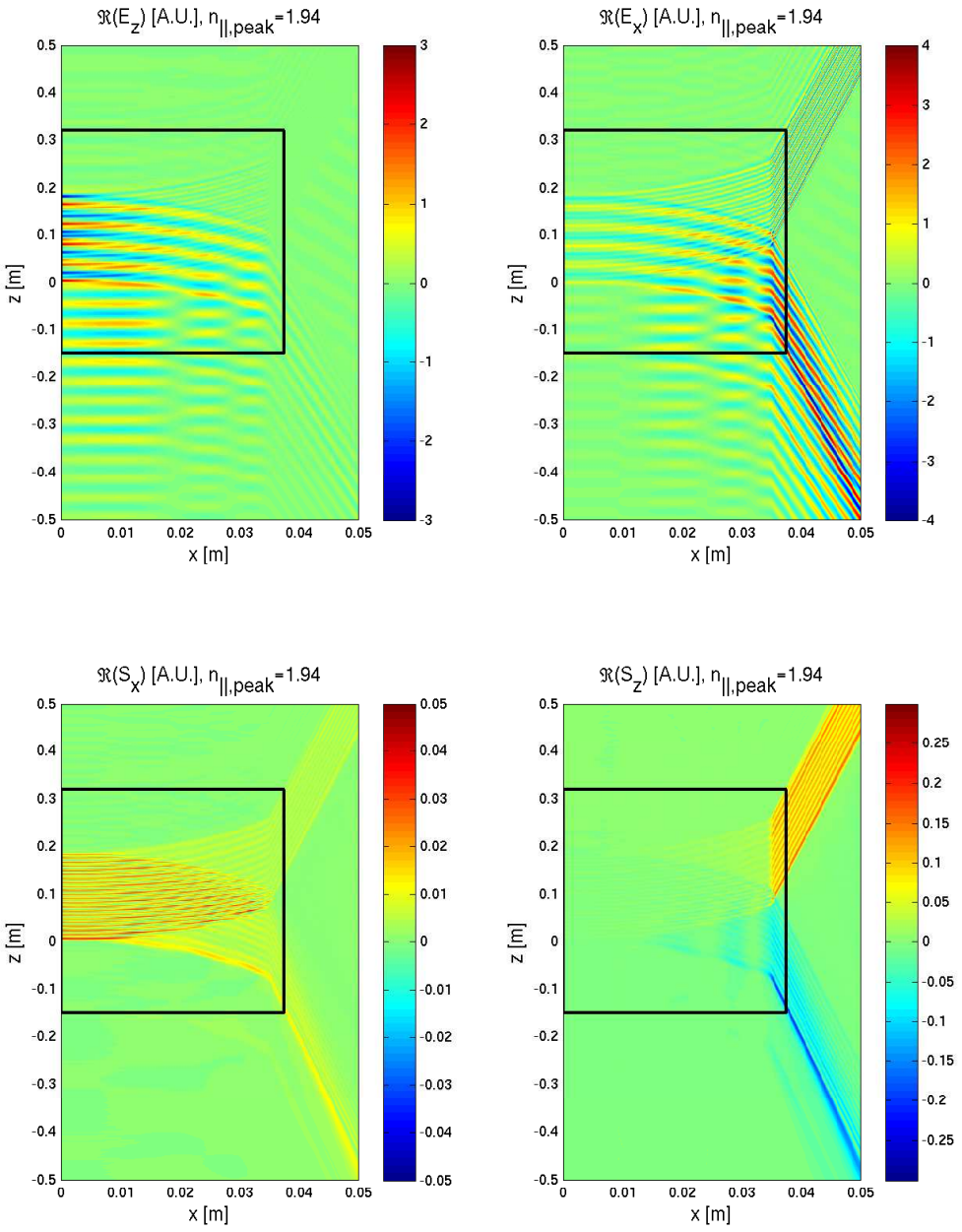

Figure 5-43: One dimensional full wave simulation showing penetration of Lower Hybrid waves through a tanh density pedestal located at 0.035 m with $n_{||,peak} = 1.94$. The density at the pedestal foot is $n_e = 5 \times 10^{18}$ m^{-3} and the density at the pedestal top is $n_e = 1 \times 10^{20}$ m^{-3}. The transmission coefficient from the left side of the box to the right side of the box is 78%.

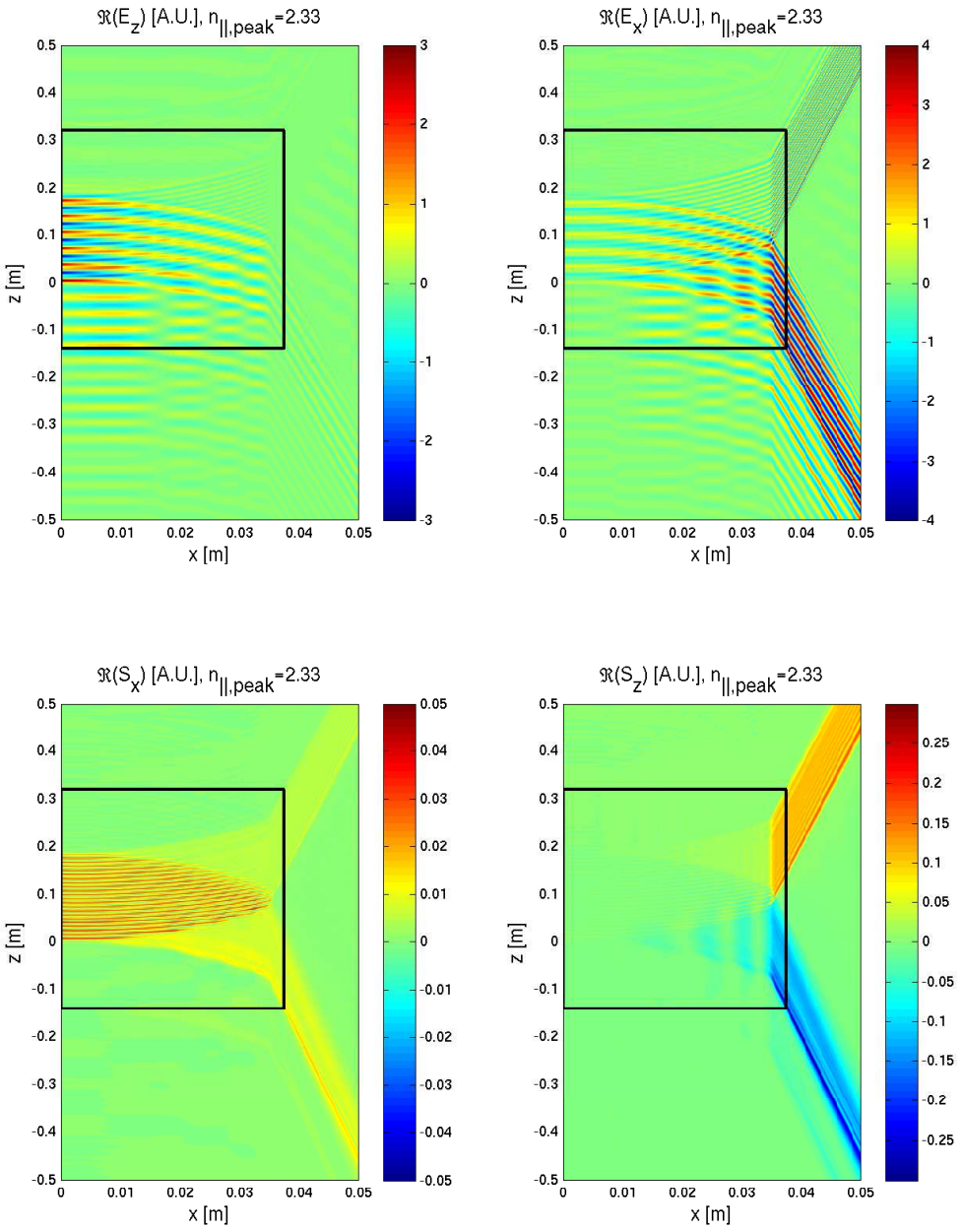

Figure 5-44: One dimensional full wave simulation showing penetration of Lower Hybrid waves through a tanh density pedestal located at 0.035 m with $n_{||,peak} = 2.33$. The density at the pedestal foot is $n_e = 5 \times 10^{18}$ m^{-3} and the density at the pedestal top is $n_e = 1 \times 10^{20}$ m^{-3}. The transmission coefficient from the left size of the box to the right side of the box is 83%.

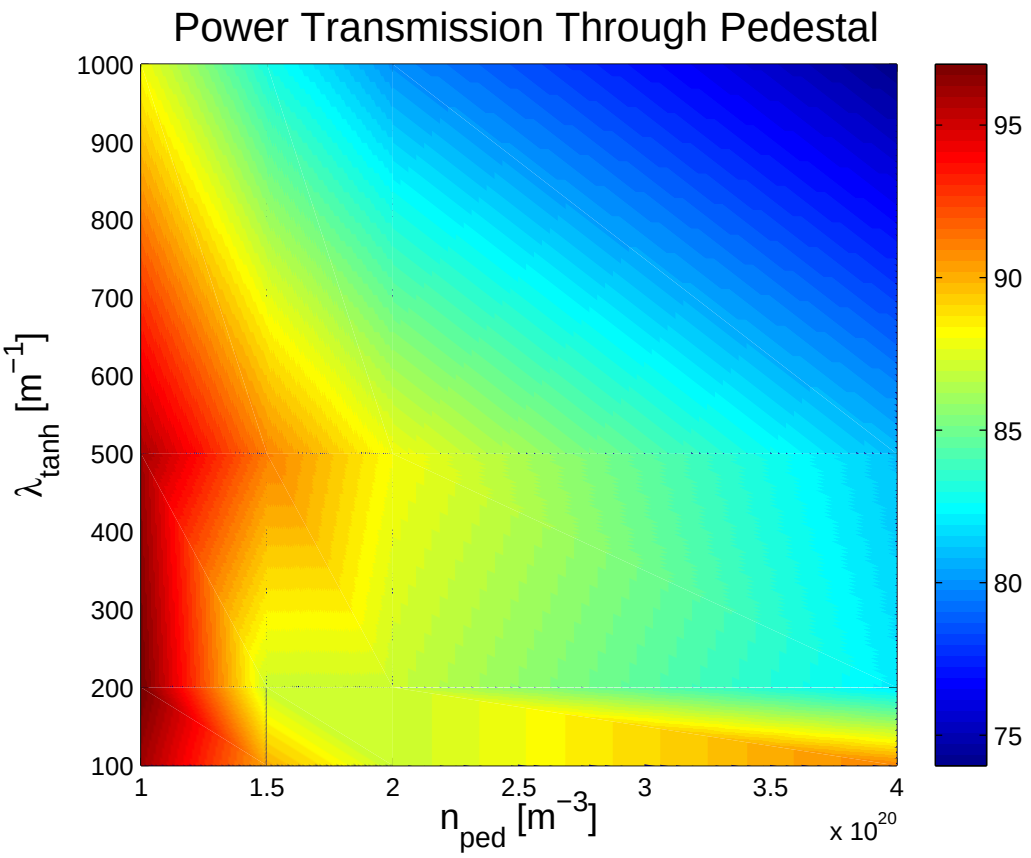

Figure 5-45: Transmission of Lower Hybrid waves through a tanh density pedestal located at 0.035 m with $n_{||,peak} = 2.33$. The density at the pedestal foot is $n_e = 5 \times 10^{18}$ m^{-3}. The power transmission coefficient, $(1 - \Gamma^2)$, for the primary resonance cone is plotted as a function of $\lambda_{\tanh}$ and n_{ped}.

to the pedestal are a function of P_{NET}, which is the total heating power (ICRF, LHCD, and ohmic) minus the radiated power. Since the radiated power increases with Z_{eff}, this effect has only been seen in clean discharges immediately following a thorough boronization. Although the P_{NET} is the sum of all heating power, it should be noted that this phenomenon has not been observed without a combination of both ICRF and LHCD. Figure 5-48 shows the changes in several key plasma parameters during an H-mode discharge that has a strong modification to the pedestal. Both the core and line averaged density decrease during the application of LHCD, but the core temperature increases. Radiation measured by the 2π bolometer also decreases when the LHCD is turned on. Although the HXR camera shows a considerable background count rate during the ICRF only portion of the H-mode, a clear increase can be seen during LHCD.

The change to the density pedestal has the effect of increasing density in the SOL, which allows for the LH waves to propagate further into the SOL. As the distance to the separatrix increases, the electron temperature decreases, allowing for stronger collisional absorption. At the same time, partial reflections from the impedance mismatch at the pedestal (see Section 5.2.4) are reduced due to the decrease in the density gradient in the pedestal. The lower density also causes refraction to be less severe. The net effect of these competing trends is not immediately apparent, and must be addressed through examining the experimental data and comparing with models of the H-mode discharge in its unperturbed state (immediately prior to the application of LHCD) and in its perturbed state.

Figure 5-49 shows the HXR emission during several H-mode discharges modified by $\sim$ 900 kW of LHCD. The black points represent the H-mode discharges, all of which had an $n_{||}$ of 2.33 at the launcher. The bremsstrahlung emission during these discharges was significantly higher than for the high density L-modes at comparable line averaged density, however it should be noted that the background level prior to the application of LHCD was high due to the ICRF. Even after subtracting the

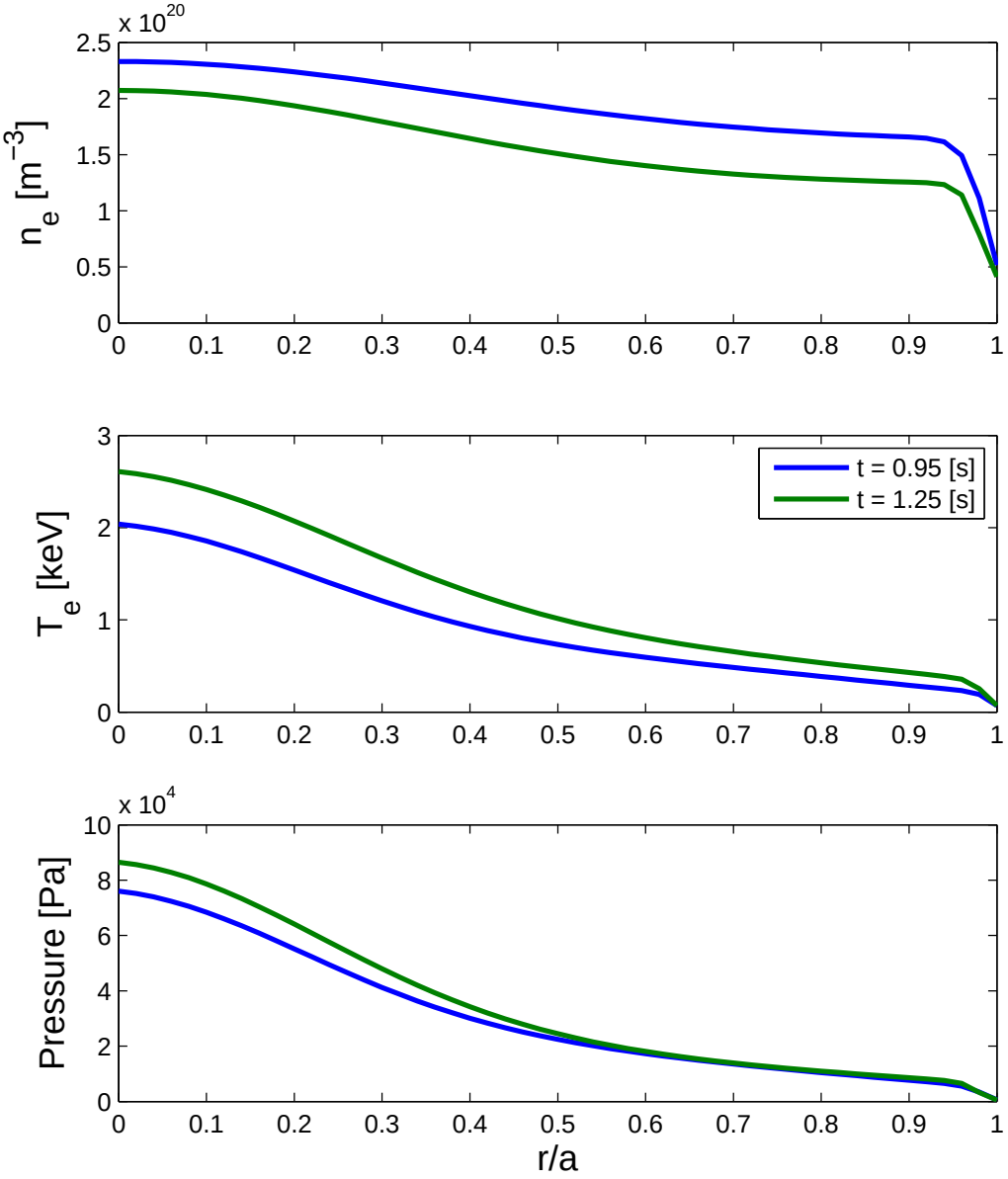

Figure 5-46: Changes in H-mode density, temperature, and pressure profiles with the application of LHCD. LHCD is applied from 1.1 to 1.4 s in this discharge. Complimentary changes in T_e and n_e profiles result in a nearly unchanged pedestal pressure at $r/a > 0.6$, although the core pressure rises noticeably during LHCD. Shot number = 1080306013.

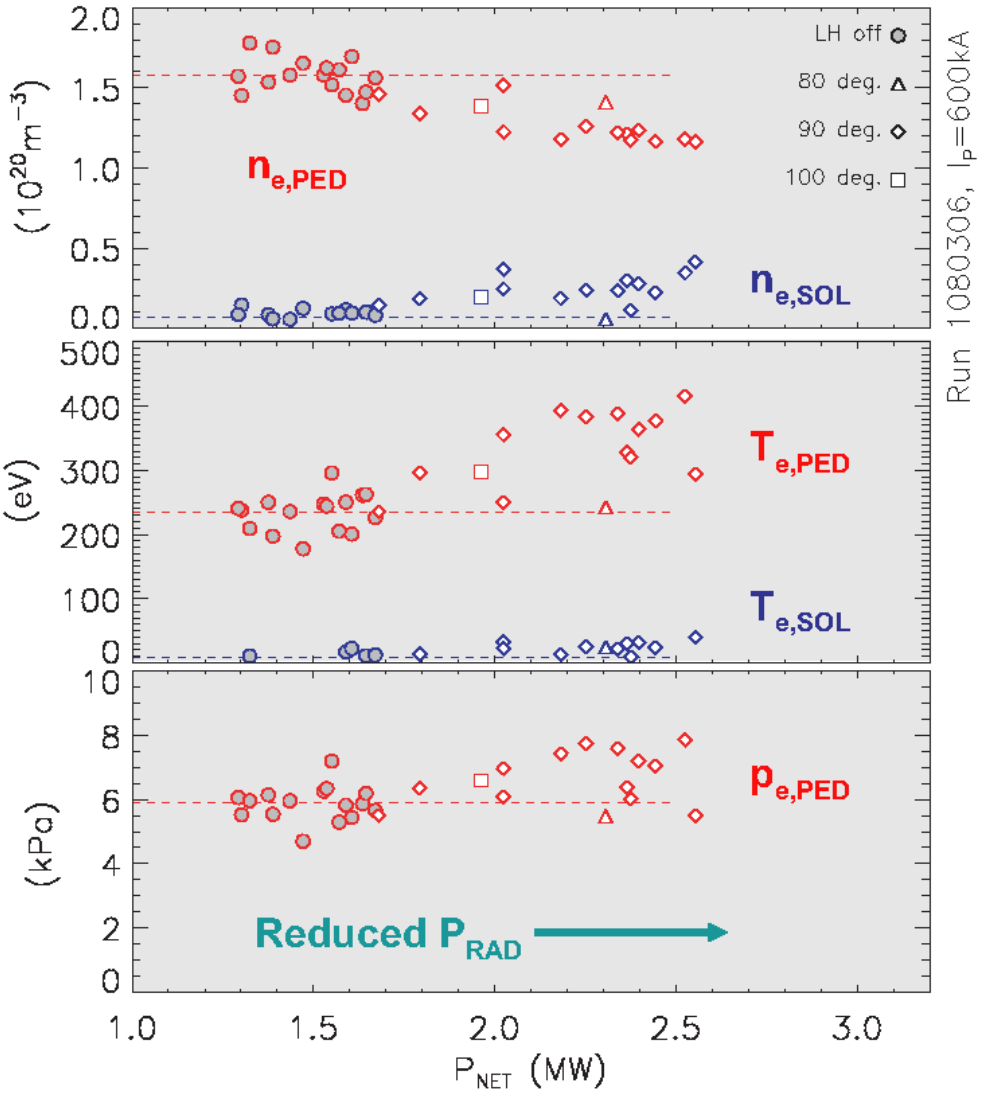

Figure 5-47: Changes in H-mode pedestal parameters with application of LHCD. P_{NET} is the total heating power (ICRF, LHCD, ohmic) minus the radiated power. (Figure courtesy of J.W. Hughes.)

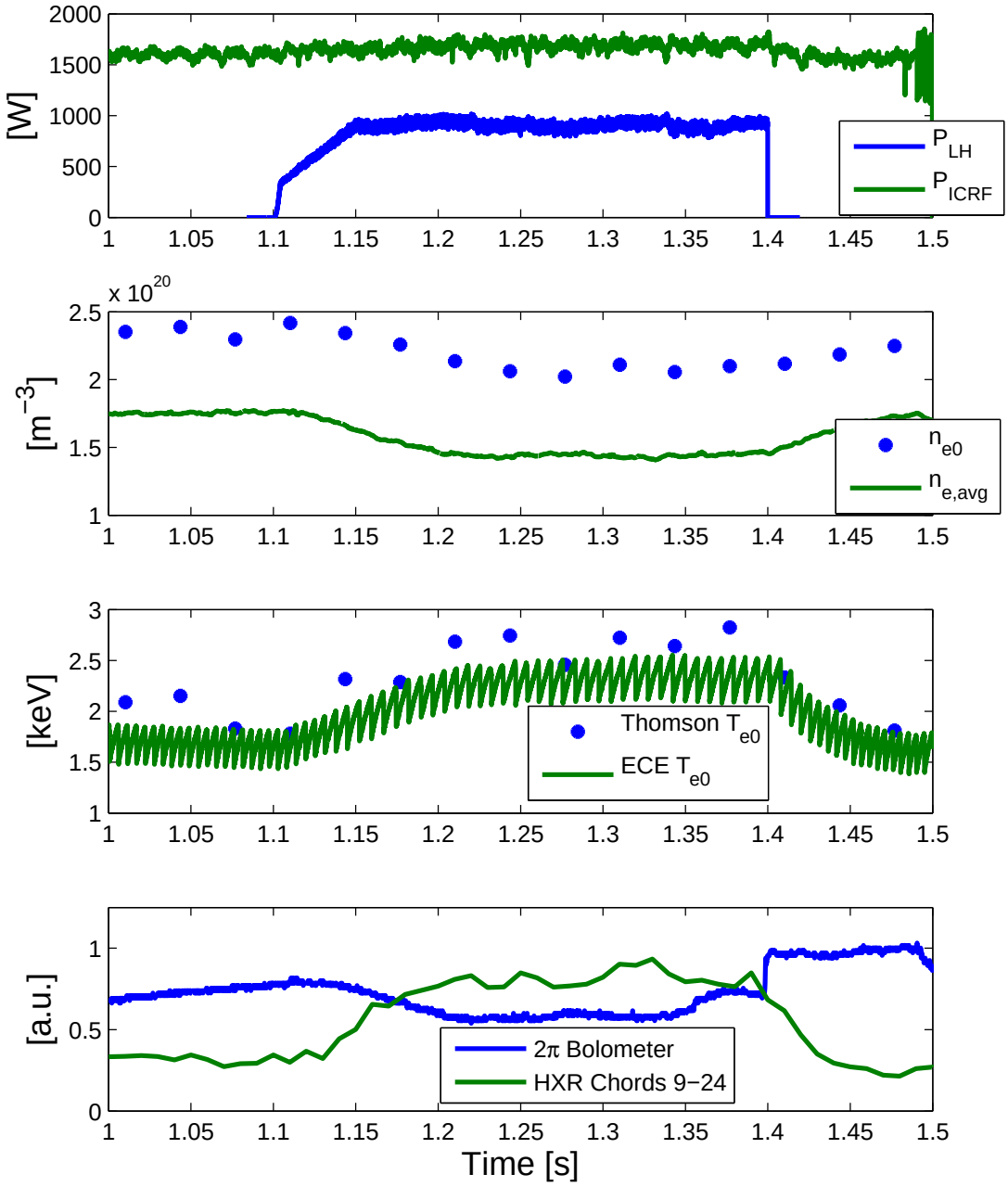

Figure 5-48: Low density H-mode with LH induced pedestal modification. Temperature and HXR emission increase during the application of LHCD while density decreases along with radiated power. Shot number = 1080306013.

background, as shown in Figure 5-50, the bremsstrahlung emission in H-mode is higher than even the 1.1 MA L-mode data at comparable densities.

The current drive for this discharge can be estimated based on the loop voltage because the plasma remains in steady state for a sufficient time for the current to redistribute. To estimate the amount of current driven, it is necessary to consider not just the relative change in loop voltage, $V_l(t_1)/V_l(t_2)$, but also the change in resistivity due to temperature.

$$\frac{\eta(t_2)}{\eta(t_1)} = \left(\frac{T(t_1)}{T(t_2)}\right)^{\frac{3}{2}} \tag{5.16}$$

The loop voltage changes from -1.05 V before 1.1 s to a steady -0.6 V between 1.2 and 1.4 s for a relative change of 0.57. The core temperature measured by Thomson Scattering increases from 2 keV to 2.75 keV, corresponding to a relative change in η of 0.62. This shows that change in V_l can be attributed almost entirely to the increase in plasma temperature, not due to direct current driven by the LH waves. Although this analysis shows that little or no current is directly driven by LHCD in this discharge, the changes in the plasma discussed above prove that LHCD applied to H-modes can have a substantial positive effect even above the observed density limit for L-modes.

Figure 5-51 shows the ray trajectories calculated by GENRAY both before (left panel) and after (right panel) the density profile is modified by the application of LHCD. A subtle difference in the penetration of the rays into the core plasma can be seen, with the modified profile showing that more rays penetrate into the core plasma. However, it is clear in both cases that many rays do not penetrate directly to the core. This of course does not take into account the propagation of the waves through the SOL, which must be included to accurately represent the experiment.

When the SOL is included in the model, the ray trajectories can be observed to dwell considerably outside the separatrix both before and after the profiles are modified by LHCD. Figure 5-52 shows the ray trajectories under the same conditions as in Figure 5-51 but with the SOL included. As with the high density L-mode

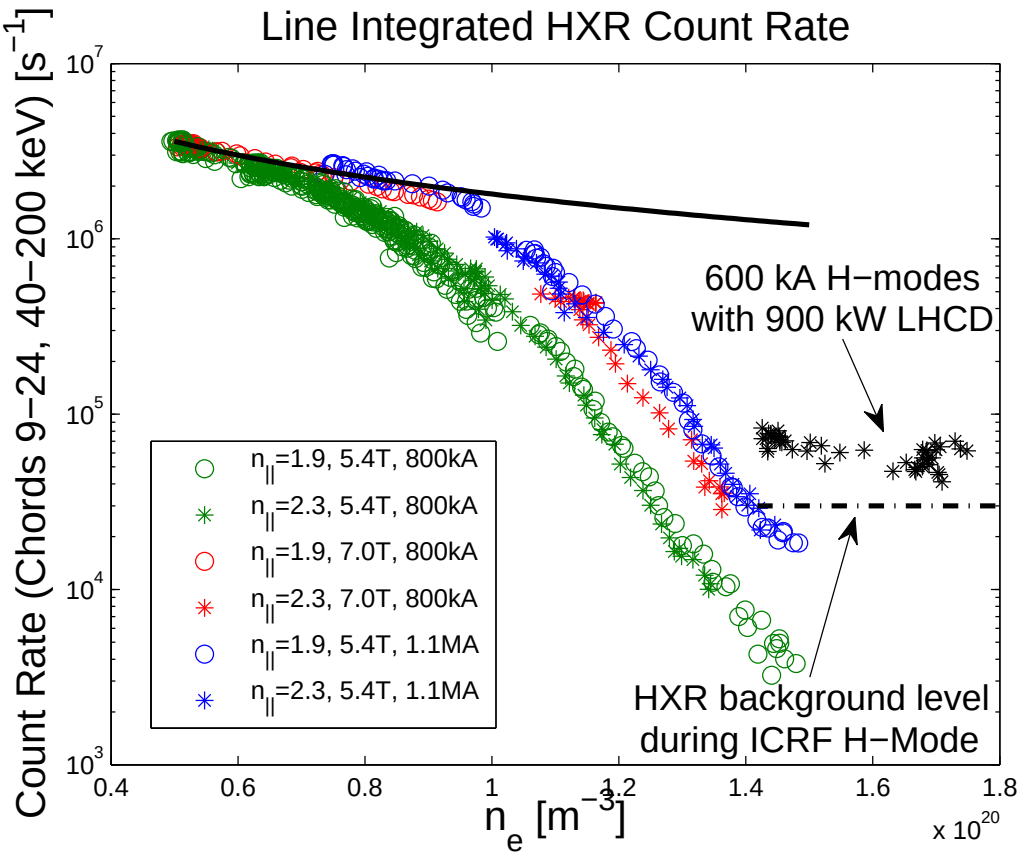

Figure 5-49: HXR emission as a function of line averaged density during H-mode. The H-mode discharges (black data points) show higher bremsstrahlung emission than the high density L-mode discharges (colored points). The dashed line shows the pre-LHCD HXR background level due to ICRF.

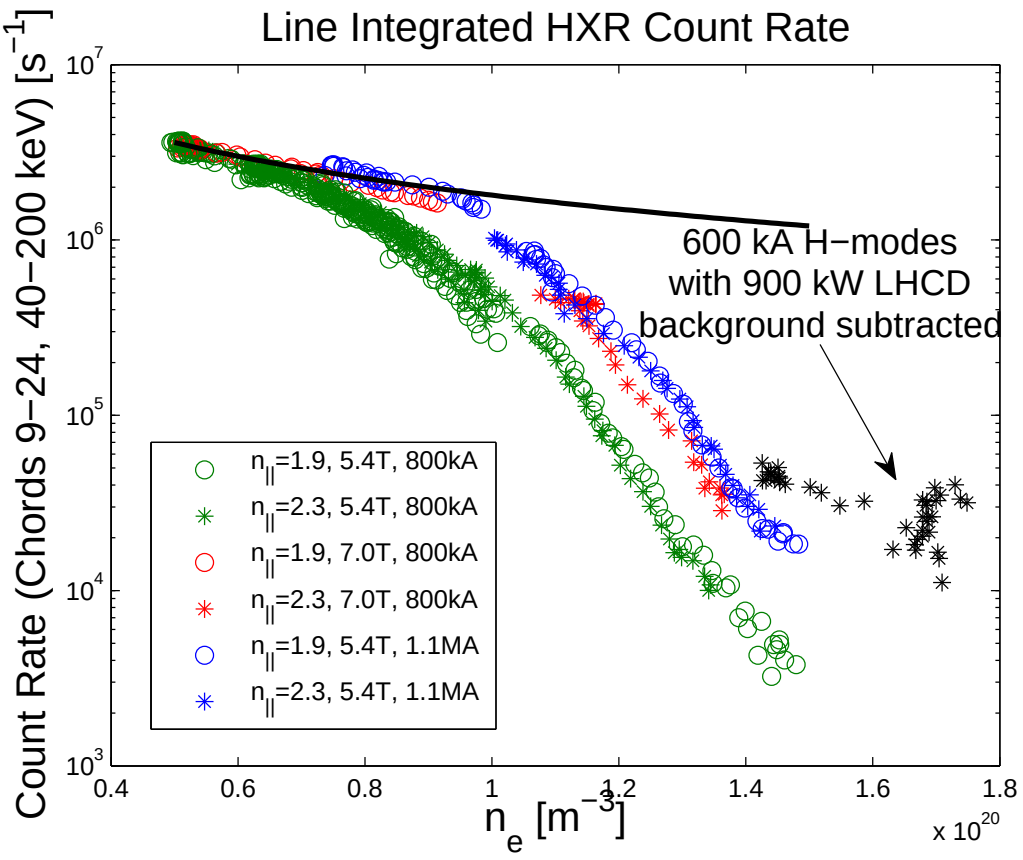

Figure 5-50: HXR emission as a function of line averaged density during H-mode. The background due to ICRF has been subtracted from these data points. The H-mode discharges (black data points) show higher bremsstrahlung emission than the high density L-mode discharges (colored points).

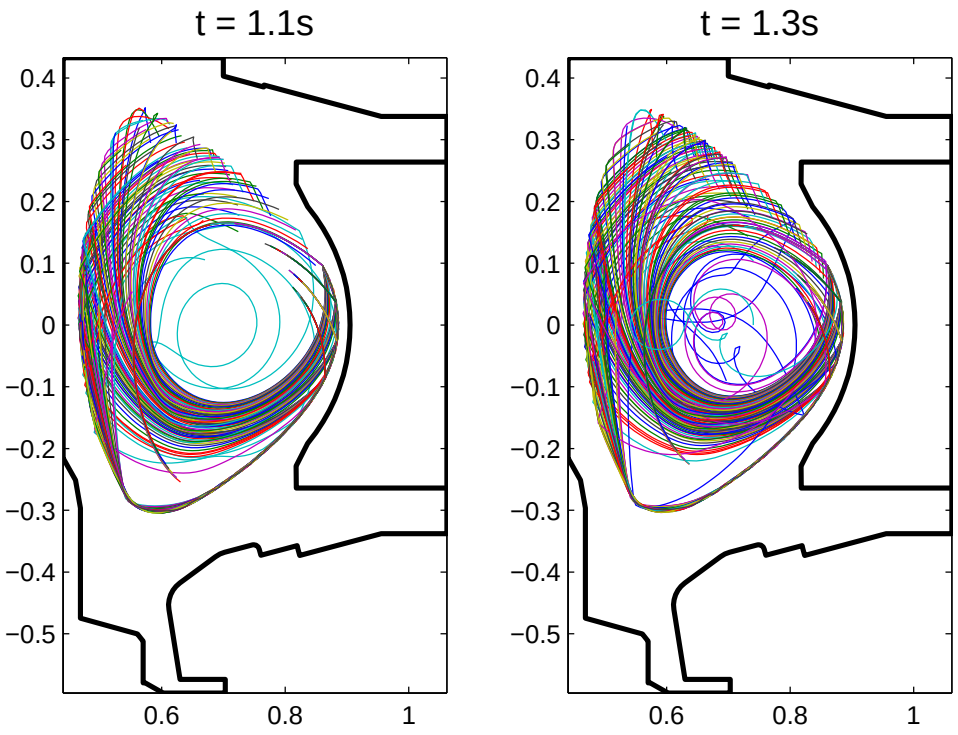

Figure 5-51: Ray trajectories in a low density H-mode with no SOL model. The left panel shows the ray trajectories in the baseline H-mode, while the right panel shows the ray trajectories in the H-mode as modified by the application of 900 kW of LHCD.

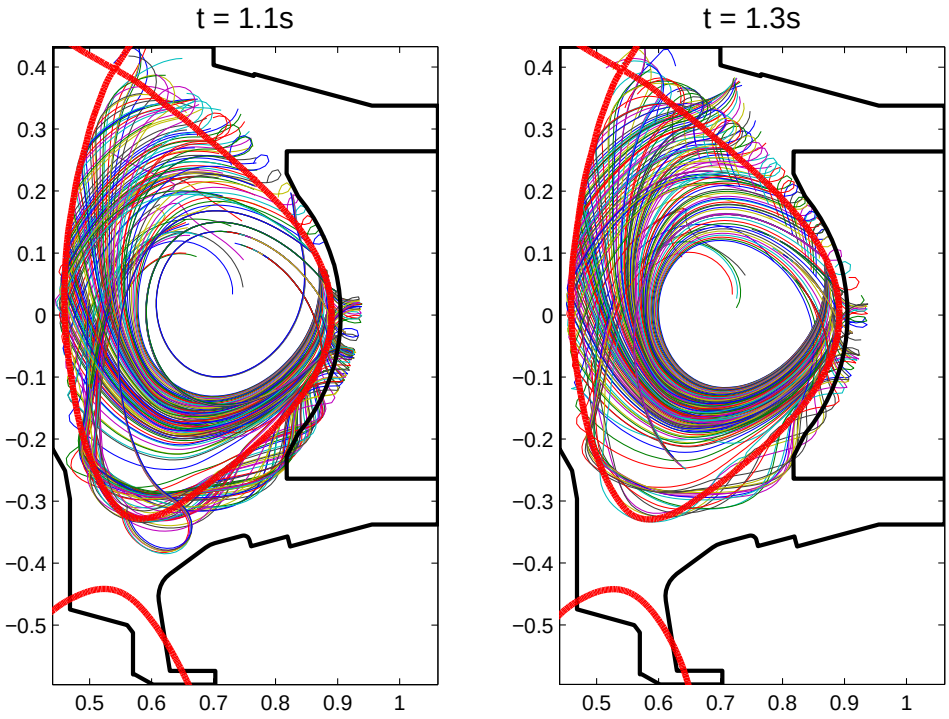

Figure 5-52: Ray trajectories in a low density H-mode with SOL model. The left panel shows the ray trajectories in the unperturbed H-mode, while the right panel shows the ray trajectories in the H-mode as modified by the application of 900 kW of LHCD.

discharges, many rays are observed to dwell considerably in the SOL, and even rays that are not trapped outside the separatrix do not penetrate far into the core plasma.

The discrepancy between experimental data and the predictions from CQL3D is smaller for H-mode than for L-mode, even with no SOL model or collisional damping included in GENRAY, as seen in Figure 5-53. Figure 5-54 shows the results of simulations with a 2-D SOL model including collisions compared with the experimental results. As with the L-mode discharges, including both the SOL and collisional damping improves agreement between the experiment and the simulations considerably.

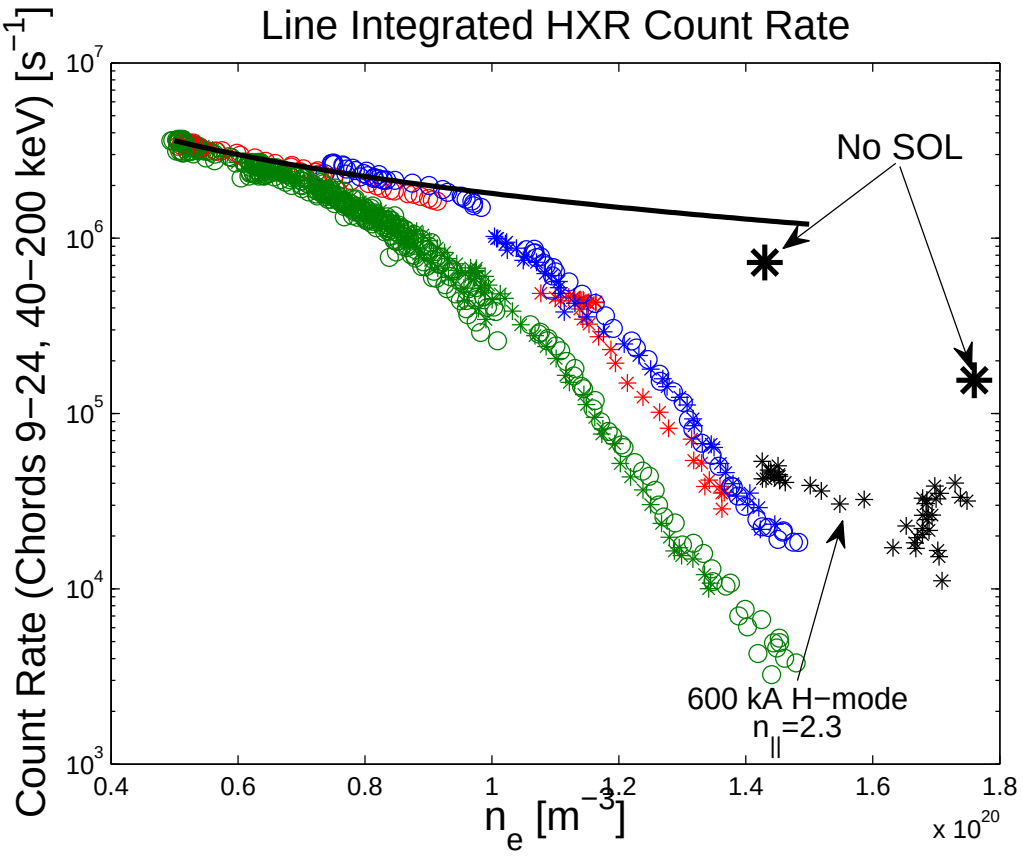

Figure 5-53: HXR emission as a function of line averaged density during H-mode. Small black data points show experimental data in H-mode, while large black data points represent simulated emission from GENRAY/CQL3D with no SOL model.

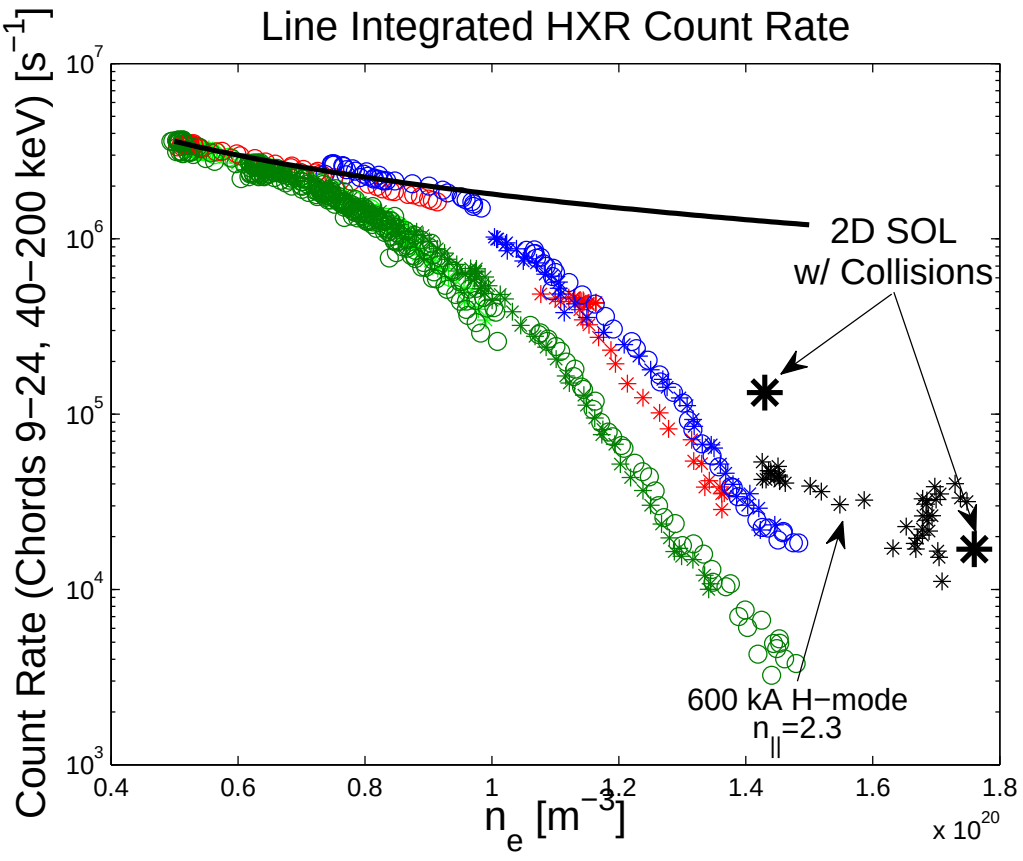

Figure 5-54: HXR emission as a function of line averaged density during H-mode. Small black data points show experimental data in H-mode, while large black data points represent simulated emission from GENRAY/CQL3D with 2-D SOL model including collisional absorption.

5.3.1 Conclusions

Experimental observations of bremsstrahlung emission and non-thermal ECE show that the fast electron population in L-mode plasmas is significantly reduced at line averaged densities above 1×10^{20} m^{-3}. Electric currents measured in the SOL rise sharply at approximately the same density. Taken together, this suggests that the LH waves are depositing their energy outside the separatrix. "Density limits" for effective LHCD have been observed on previous experiments, although the expected limit on C-Mod is significantly higher than the observed limit.

Explanations for the previously observed density limits, such as PDI and accessibility criterion violation, disagree with the phenomenology of the C-Mod limit. The sudden drop in fast electrons at high density are not predicted by conventional ray tracing/Fokker-Planck models. By adding the effects of collisional absorption in the SOL to these models the agreement with experiment at high density is significantly improved. Based on interpretation of the modeling results, the loss of fast electrons at high density is caused by a confluence of several effects. The high density prevents waves from penetrating deep into the hottest part of the plasma and also lowers the overall temperature of the plasma. This further reduces single pass absorption, which is weak even at low density for $n_{||} \leq 2.33$. When combined with an edge loss mechanism the weak damping inside the separatrix allows the power to be absorbed outside the separatrix. The result can be mitigated by either reducing the edge loss mechanism or increasing core damping. The increased temperature of H-mode plasmas strengthens core absorption although no experimental means of eliminating the edge losses has been identified short of operating at lower density.

The disconnect between the edge coupling problem treated by coupling codes such as GRILL, and the core propagation/absorption problem treated by ray tracing/Fokker-Planck codes such as GENRAY/CQL3D, must be bridged and the two problems treated together. Recent advances in full wave simulations with codes such as TORIC-LH [84, 85] and COMSOL [86, 87] allow proper treatment of both the edge problem

(including penetration through the pedestal) and core propagation/absorption in a seamless manner. It is imperative to consider not only the power leaving the antenna, but the power actually absorbed on closed flux surfaces when simulating tokamak plasmas.

Chapter 6

Conclusions and Future Work

6.1 Conclusions

The goal of the LHCD system on the Alcator C-Mod tokamak is to investigate current profile control under plasma conditions relevant to future devices such as ITER and DEMO. This thesis addresses the behavior of LH waves in the edge and SOL of a compact, high field, high density, diverted tokamak. In this thesis we have identified and analyzed conditions in C-Mod under which the absorption of power in the SOL can increase antenna reflection coefficients, cause damage to the launcher, and dramatically reduce current drive in the core plasma. In particular, the critical density associated with reduced current drive in the core plasma is somewhat unique in that it occurs at a value significantly lower than what would have been expected based on prior LHCD experiments. These interactions between lower hybrid waves and the SOL plasma can have a substantial impact on the operational effectiveness of a LHCD system.

A coupling model (the GRILL code) has been used with a variety of edge density profiles and compared to low power experimental coupling results. For each type of density profile considered, there exists at least one free parameter that can be varied to obtain good agreement between the theory and experiment. In the absence

of accurate density profile measurements that would completely constrain these free parameters, it is not possible to determine which profile type is most similar to the experimental profile. Therefore, the model itself cannot be fully tested. However, the "fixed edge density with variable density gradient" model, which has only one free parameter (versus multiple free parameters for the other models) gives good agreement with experimental results above $n_{probe} = 4 \times 10^{17}$ m^{-3} (see Figure 3-8). However, this model requires a negative density gradient for measured edge densities below 4×10^{17} m^{-3}, and consequently its validity in that regime is questionable.

Reflection coefficients are observed to rise during LHCD operation at high power (see Figure 3-13) and during ion cyclotron resonance heating (ICRH), although without density profile measurements it is not possible to determine if these effects are due to a modification of the edge conditions or an as yet undetermined process. Attempts to improve wave coupling with localized gas puffing at the LH launcher were inconclusive despite a significant increase in local edge density due to the puffing. It would be necessary to make a localized measurement of the density profile on field lines which pass directly in front of the LH launcher grills to improve the understanding of coupling physics under these conditions, but this is not possible with the present design.

Damage to the front of the LHCD launcher sustained during the 2008 run campaign, changes in D_α emission during LHCD, and measurements from the LH Langmuir probes suggest that the plasma edge is modified by the presence of high power LH waves. Figures 4-2 and 4-4 show the changes in plasma density in front of the LH launcher as measured by changes in D_α brightness. Increases in density of up to nearly 1×10^{19} m^{-3} during high LH power are estimated along the bright stripes, while the Langmuir probes measure an increase in temperature to 20 eV. A careful inspection of the melting pattern on the waveguide septa reveals that leading edges are created along the sides of the septa due to a shape mismatch between the magnetic flux surfaces and the coupler. The melt damage was confined to areas that exhibited

increased D_α emission during operation at high power. An analysis of the heat flux required to cause this melting during a 0.5 s LH pulse is consistent with a plasma density and temperature of 1×10^{19} m^{-3} and 20 eV in the vicinity of the damaged areas. These densities and temperatures agree with estimates based on the increase in D_α light combined with LH Langmuir probe measurements. The non-linear coupling of LH waves at high power is also consistent with such a density increase. Analysis of the power required to sustain the temperature and density in the bright bands is inconsistent with absorption of LH waves through collisions or Landau damping of high $n_{||}$ modes and must be further investigated.

Injections from the LH launcher caused by high power ICRH from a toroidally adjacent antenna highlight the need to avoid having ICRH and LH antennas in close proximity along magnetic field lines. Besides the risk of disruptions caused by injections from the ICRH/LH antenna interaction, the ICRH antennas that are strongly connected along magnetic field lines pose a risk to the survivability of the LH antenna itself.

Through experiments conducted during the 2008 run campaign, it was discovered that, for line averaged densities in excess of 10^{20} m^{-3}, the fast electron bremsstrahlung emissivity (and thus the population of fast electrons carrying the non-inductive current) was 2–3 orders of magnitude lower than is predicted by simple estimates based on the $1/\bar{n}_e$ scaling of current drive efficiency. Also, ray tracing/Fokker-Planck solvers do not agree with the experimental data above this experimental "density limit." Figure 5-22 shows that the experimental data diverges from the synthetic diagnostic above 10^{20} m^{-3}. This density limit is observed at a significantly lower density than was expected based on previous results from other experiments for which accessibility or parametric decay instabilities set the LHCD density limit. The scaling of the density limit with magnetic field and $n_{||}$ also eliminates these phenomena as possible explanations for the C-Mod results.

Parallel electric currents in the SOL are observed during high power LHCD at high

density. The direction of the SOL currents, shown in Figure 5-19 for lower- and upper-single-null configurations, is the same as the plasma current inside the separatrix. The polarity of the SOL current is also in the direction of I_p when the launched $n_{||}$ is in the counter-current drive direction. Equal and opposite SOL currents are measured on the inner and outer divertors, with the circuit completed through the vacuum vessel wall. The magnitude of the SOL current increases rapidly across the same range of densities for which the core X-ray emission drops, i.e. $\bar{n}_e > 1 \times 10^{20}$ m^{-3} (see Figures 5-22 and 5-20). The increase in SOL current is well correlated with an increase in ion saturation current, I_{sat}, and thus plasma density, at the ion collecting end of the field line. A modification of density in the SOL of this magnitude indicates strong absorption of the LH waves outside the separatrix.

The core bremsstrahlung and SOL current observations suggest that power absorption is shifting from inside the separatrix into the SOL as density increases. By including a SOL with collisional absorption in the ray tracing model, agreement between modeling and experimental results is dramatically improved at high density . Figure 5-38 shows a comparison between the experimental data and the model including absorption in the SOL. A slight improvement of agreement between the synthetic diagnostic and experimental data is seen at low density as well. Thus, the observed density limit on C-Mod appears to be a consequence of poor wave penetration and weak single pass absorption inside the separatrix combined with a loss mechanism in the SOL phenomenologically similar to collisional damping.

This interpretation of underlying mechanisms of the density limit suggest that the limit can be overcome by either increasing the strength of LH wave absorption inside the separatrix or by reducing the strength of absorption in the SOL. When LHCD is applied to a relatively low density H-mode, the bremsstrahlung emissivity is increased significantly relative to L-mode discharges of the same line averaged density, although still below the $1/\bar{n}_e$ scaling (see Figure 5-54). Although only a small amount of current is driven by LHCD in these H-modes, there are significant changes to the

temperature and density profiles induced by the application of LHCD. This shows that LHCD can be a useful tool for profile control even above the empirical density limit.

The work carried out in this thesis highlights the importance of treating the edge core propagation/absorption problems simultaneously. The disconnect between edge coupling, treated by coupling codes such as GRILL, and core propagation/absorption, treated by traditional ray tracing/Fokker-Planck codes such as GENRAY/CQL3D, must be bridged and the two problems treated together. Recent advances in full wave simulations with codes such as TORIC-LH and COMSOL allow proper treatment of both edge coupling (including penetration through the pedestal) and core propagation/absorption in a seamless manner. It is imperative to consider not only the power leaving the antenna, but the power actually absorbed on closed flux surfaces when simulating tokamak plasmas in the low single pass absorption regime.

6.2 Future Work

Studies of LH wave coupling and current drive efficiency at high density would benefit both from additional run time and diagnostic upgrades. The second- and third-generation LH2 and LH3 antenna systems will reduce losses in the transmission system and provide more power to the plasma for current drive studies.

An X-mode reflectometer system will be attached to the LH2 antenna for measurement of the edge density profile. This should be a significant benefit to the understanding of LH wave coupling since simulation models can be run using actual density profiles measured in front of the grill. This may remove ambiguities regarding the coupling of LH waves at high power and in the presence of ICRF. The density profile measurements obtained with the reflectometer can be used in conjunction with the recently developed three-dimensional finite element full wave solver [87] to accurately model the coupling of LH waves in a realistic geometry including curvature of

the grill and excitation of the fast wave.

The research plan for further exploration of the density limit should build upon experiments conducted on C-Mod during 2008. These experiments used fast electron bremsstrahlung and electron cyclotron emission as proxies for the non-thermal part of the electron distribution function. In order to scan a large parameter space in a small number of discharges, the plasma density was intentionally ramped over the range of $\overline{n}_e = 0.5 - 1.5 \times 10^{20}$ m^{-3}. This makes it very difficult to determine a quantitative measure of the current driven in the plasma since the density was changing on a timescale short compared to the current redistribution time. Repeating these experiments with steady density and temperature profiles would require considerably more experimental time but would allow for measurements of the driven current in addition to X-rays generated by non-thermal electrons.

The proposed experiments would make use of current profile diagnostics to directly measure the current profile as a function of plasma density, toroidal magnetic field, plasma current, plasma temperature, parallel refractive index of the wave, and plasma topology. Both the Motional-Stark-Effect (MSE) and Faraday Rotation Polarimeter systems are receiving significant upgrades for the 2010 run campaigns which should allow for more sensitive measurements of the plasma current profile.

In addition to determining the driven current by means of current profile measurements, the total driven current can also be obtained by allowing the plasma current to relax, over the course of several hundred milliseconds, to a steady state under conditions of zero loop voltage. This will allow a simple measurement (via Rogowski coils) of the plasma current with no need to subtract the ohmic component, thereby giving a clearer indication of the current drive efficiency for a set of plasma conditions.

Observations of SOL currents during LHCD at high density, along with the presence of localized RF wave fields in the outer SOL, suggest that at high density the LHCD power not absorbed by the core is deposited near the edge or outside the plasma. Current data on the SOL RF wave fields exists for only a few shots where

a horizontal reciprocating Langmuir probe on the low field side of the tokamak was connected through a bandpass filter to a rectifier diode. A better diagnosis of the SOL RF wave fields using both vertical and horizontal scanning Langmuir probes on both the low field and high field sides should be conducted along with the current drive efficiency measurements.

In previous experiments there has been no measurement of the presence of LH waves in the core plasma. Above the density limit there are indications that the fast electron population disappears although it is not known if the waves penetrate into the core plasma. An upgrade to the 50 GHz O-mode reflectometer [88] should make it possible to detect 4.6 GHz oscillations in the location of the cutoff layer ($\sim 3 \times 10^{19}$ m^{-3}). The phase contrast imaging system [89] is scheduled to receive an upgrade which would allow for heterodyne detection of LH waves in the core plasma.

Appendix A

Launcher Calibrations

Launching the desired $n_{||}$ spectrum requires that the correct phase difference be maintained between adjacent columns of the launcher. The calculation of the $n_{||}$ spectrum for a grill type waveguide is addressed in Section 1.5.2. The C-Mod LH system is divided into two sections for calibration. The first section includes all components in the system from the low power master oscillator through to the intermediate directional couplers (IDC). A switch immediately after the IDCs allows for this section of the system to be connected to either a dummy load (for testing purposes) or the rest of the launcher (for plasma operations). This section of the system is calibrated at a range of power levels and phasings to determine lookup tables used in open loop operation. Operation in closed loop is possible although this functionality has not been used to date.

The section of the launcher from the IDCs through to the vacuum windows is calibrated seperately. A low power thru-phase launcher calibration was performed on 07/02/2008 following the FY2008 run campaign. Table A.1 shows the data from this phase calibration. Phase measurements were performed with a two port vector network analyzer. Port 1 was connected to the input of the Jungle Gym with a SMA to WR187 adapter, and port 2 was connected to a specially designed magnetic field probe. The vacuum windows were used as a phase reference plane for the probe.

When conducting the measurement with the 2 port analyzer, the seven unused ports of the nine port network were terminated with specially designed wedge loads made with an absorbing ferrite material. This calibration technique provides for a quick (single day), reliable way to measure the through phase of all 88 waveguides in the launcher, although measuring the amplitude through the system requires a more involved measurement. The stainless steel grills must be carefully removed from the front of the launcher and replaced by adapter plates. A SMA to WR187 adapter is attached to a transformer, which is in turn attached to the adapter plate. The transformer must be realigned and re-torqued for each waveguide, and a new gasket between the adapter and transformer must be fashioned for each waveguide as well. Additionally, four new RF gaskets are required when reattaching the grills to the launcher after the calibration is complete.

Table A.2 contains a comparison between the through-phase measured in October of 2007 and the through-phase measured in July of 2008. The difference is normalized assuming that the through-phase of waveguide 2A did not change between the two measurements. The 2007 measurement was conducted with the manual phase shifters set to zero, while the 2008 measurement was conducted with the fixed phase shims set to create a 90° difference between adjacent columns. A histogram of the change in phase between the two calibrations when the phase shifter offset is removed is shown in Figure A-1. The shift of the mean seen in the histogram suggests that the mesurement of the waveguide used as a zero reference, 2A, has in fact shifted in phase by approximately 4.8°. The RMS phase error after zeroing the mean (shifting by +4.8°) is 5.5°. Phase errors of this magnitude will not affect the launched $n_{||}$ spectrum. Figure A-2 shows the $n_{||}$ spectrum for a "perfect" launcher with no phase errors compared with the spectra of the four rows of the C-Mod launcher. For the C-Mod launcher spectra the difference between the 2007 and 2008 calibrations is used as the error in phasing. The amplitude error used in Figure A-2 is based on the 11/06/2005 full calibration.

Table A.1: Thru-phase launcher calibration performed on 07/02/2008.

	1	2	3	4	5	6	7	8	9	10	11	12
A		63.5	-125.6	155	-101	155	-14.6	-119	92.8	9.2	172	81.8
B		-40.6	125.1	55.1	157	77.9	-131	138	-7.9	-97	71.7	-20.5
C		-38.2	144	54.7	153	77.8	-132	148	-8	-92.2	83.2	-15.5
D		54.6	-128.2	155	-114	164.1	-32.7	-117	76.7	0	160.1	78

	13	14	15	16	17	18	19	20	21	22	23	24
A	-163	114	-81.3	-175	37.6	-58	133.33	34.9	161	70.1	-99.3	
B	96.6	15.9	171	83.5	-63.2	-137	25.2	-60.5	65.1	-18.6	162	
C	102	15.3	-172	97.4	-42.1	-153	29.6	-66	55.1	-24.13	180	
D	-160	117	-81.5	-172	63.2	-43.9	126	51.6	153	68.93	-89.1	

Table A.2: Difference in thru-phase calibration from 10/26/2007 to 07/02/2008.

	1	2	3	4	5	6	7	8	9	10	11	12
A		0	264.2	-6.2	260.4	-7	-102.7	-11.3	-88.2	-6.2	-86.5	-5.1
B		-4.6	-95	-10.4	-94.2	-11.1	261.8	-15.4	-82.6	-9.9	-87.1	-4.4
C		-8.6	-96.6	-7.4	-94.2	-11.5	265.3	-7.1	-76.9	-8.1	-93.5	-7.4
D		-7.7	264	-6.4	262.2	-4.7	-96.1	-2.9	-80	-5.1	-79.8	-1.9

	13	14	15	16	17	18	19	20	21	22	23	24
A	280.2	-2.5	-93.6	-2.2	-2.4	94.2	-5.73	81.7	-4.6	75.4	-3.3	
B	-76.5	-5.8	-80.3	1.8	-1.8	79.6	-2.9	73.3	-4.3	64.2	-6.4	
C	-77.9	-4.8	260.5	-7.2	-3.6	99.2	-7.7	82	-1.6	60.43	-18.3	
D	280.2	-3.1	-87.6	-5.9	-17.2	92.2	-9.1	79.2	-8.1	70.07	-10.6	

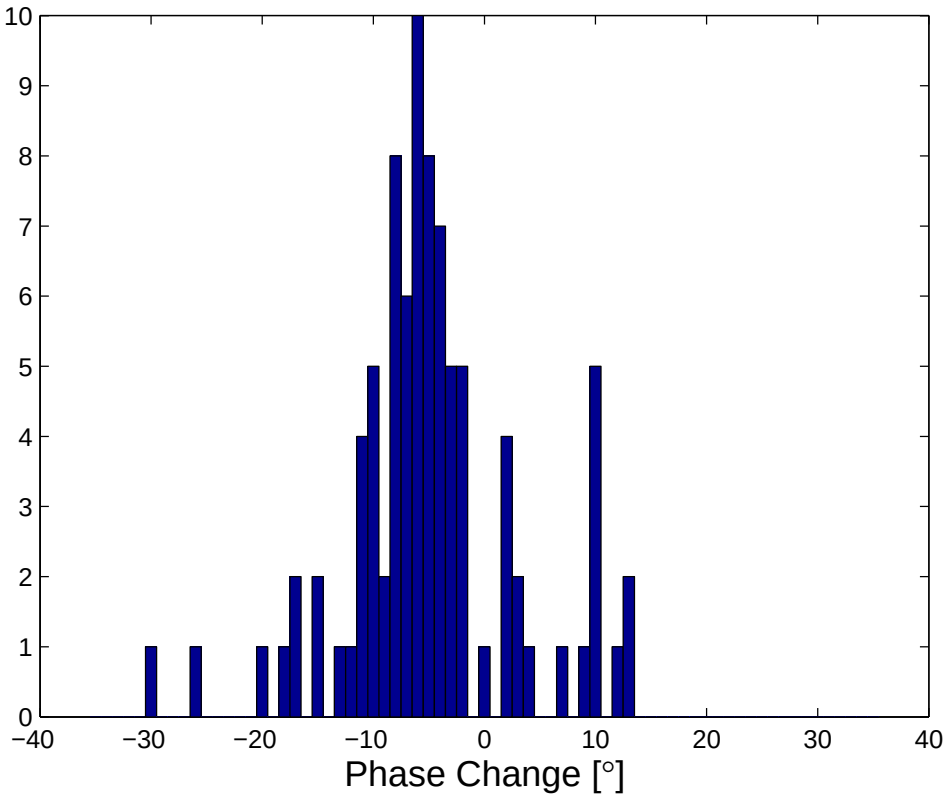

Figure A-1: Histogram of phase difference between calibrations . The 90° phase shift on every other column has been removed from the errors shown in Table A.2. Mean phase error is −4.8°. RMS phase error is 7.7°. RMS phase error after zeroing the mean (shifting by +4.8°) is 5.5°.

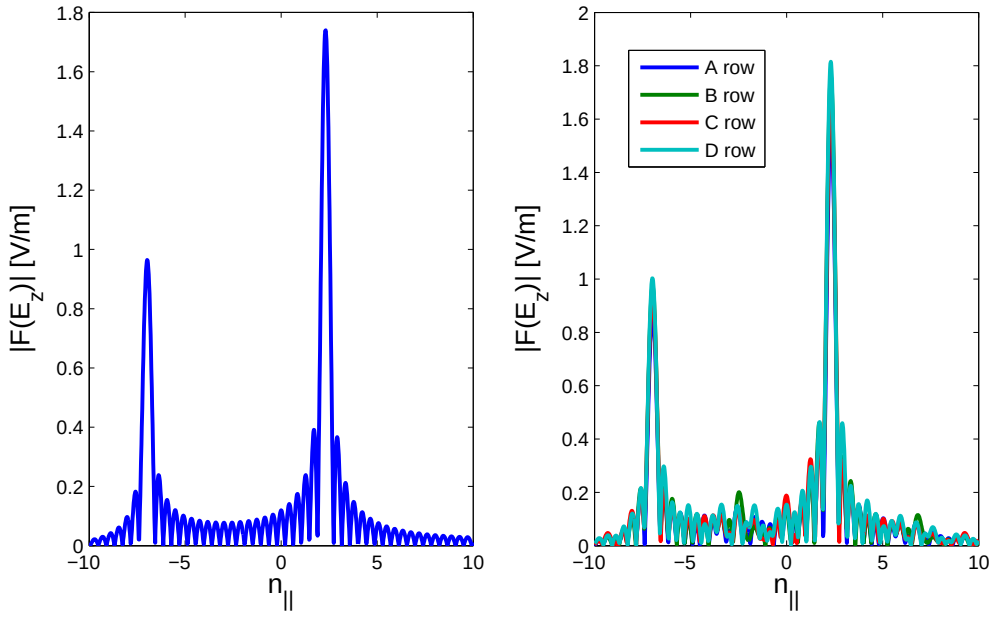

Figure A-2: Change in $n_{||}$ spectrum due to error in waveguide phasing and amplitude. A "perfect" launcher (left) produces a spectrum similar to that of the four rows of the C-Mod launcher with imperfect phasing and amplitude (right).

Appendix B

Analysis Tools

Several useful interactive tools have been developed to assist in the analysis of C-Mod LHCD data. Brief descriptions of what these tools are used for, along with how to use them, are included here for reference.

B.1 LH Post Shot Processing

Raw voltage data from the various directional couplers and IQ detectors described in Section 2.1.2 is stored in the LH tree of the C-Mod MDS+ data system. After the shot, this data is converted from raw voltage signals to power measurements based on the individual calibration points for each directional coupler. The mathematical conversion from raw voltage to power level is performed live each time a directional coupler measurement is retrieved. The computational power necessary to perform this conversion is trivial, and the storage space required is cut in half by not storing two essentially equivalent signals.

Following each C-Mod shot for which the LH tree is turned on, the LH post-processing routine is automatically launched via a shell script, lhpost6.sh, which is stored in /usr/local/cmod/codes/lh/analysis. lhpost6.sh exports the current C-Mod shot number to MATLAB, where the lhpost6.m data processing script retrieves the

directional coupler signals from the LH tree. The various signals are then transformed into measurements of net LH power, reflection coefficient, and segment averages of waveguide phase, amplitude, and reflection coefficient. Measurements from directional couplers located in the Jungle Gym assembly far from the grill are corrected for losses in the waveguide splitting network according to the following formulas

$$P_n^f = \alpha_n P_n^{f\ raw} \tag{B.1a}$$

$$P_n^r = \frac{1}{\alpha_n} P_n^{r\ raw} \tag{B.1b}$$

where α_n is the power transmission coefficient between the directional coupler and the waveguide aperture for the n^{th} waveguide. The corrected forward and reflected power signals are used in the calculation of net power and reflection coefficient.

The LH post processing can also be run in an interactive manner for a specific discharge. Sometimes this is necessary if the data system hangs following a shot, or to reprocess old shots if, for instance, post-run campaign calibrations indicate that the losses or phase shifts have changed. To run the post processing routine, open a new terminal at a C-Mod workstation and type the following commands:

```
cd /home/wallaceg/matlab/lhgui
matlab -nosplash -nodesktop
lhpost6(shotnum)
```

where *shotnum* is the number of the C-Mod shot that will be processed. LH post processing can also be initiated by hitting the "LH Post" button on the LH Analysis GUI described in the following section.

B.2 LH Analysis GUI

The LH Analysis GUI is an interactive utility which allows the user to view data from previous C-Mod shots for which the LH system was active. Data is organized

by segment, with the phase and amplitude of each klystron displayed during the selected segment. The $n_{||}$ spectrum for each segment is also displayed for each row of the LH launcher. By default the selected segment is 1. Changing the segment is accomplished by typing the desired segment in the "Segment Plotting" box and clicking the "Plot Segment" button. The LH Analysis GUI was created by John Liptac with subsequent improvements and corrections by Atma Kanojia and Greg Wallace.

To run the LH Analysis GUI, open a new terminal on a C-Mod workstation and type the following commands:

```
cd /home/wallaceg/matlab/lh
matlab -nosplash -nodesktop -r lhanalysis
```

B.3 Accessibility GUI

The Accessibility GUI is a tool for determining the critical value of $n_{||}$ necessary to satisfy the accessibility criterion for a specific shot. This tool uses the experimental magnetic field and electron density profiles to calculate the value of $n_{||crit}$ along the midplane of the tokamak as a function of major radius.

To run the Accessibility GUI, open a new terminal on a C-Mod workstation and type the following commands:

```
cd /home/wallaceg/matlab/ncritgui
matlab -nosplash -nodesktop -r ncrit_gui
```

At this point, a GUI will appear with two data entry boxes. Replace the text in the upper box with the desired shot number, then replace the text in the lower box with the desired time in the discharge (in seconds), then click the "Load Shot" button. A dialog box should appear indicating if the shot has been loaded successfully. After loading the shot, click the "Load Time" button. A plot of $n_{||crit}$ as a function of major

radius will appear in the formerly blank plot on the right side of the GUI. Other time points in the same shot can be plotted by changing the time and clicking "Load Time" again. If it is necessary to save the plot, click on the "Save Plot" button. An identical plot will appear in a new window. Go to File>Save As and the figure can be saved in several formats including .jpg, .pdf, .eps, and .tiff. Figure 5-1 was created with this tool.

B.4 Field Line Mapping

This function uses data from an EFIT reconstruction to trace out paths along a field line. The toroidal, vertical, and radial components of the field are calculated at each point in the plasma, and then a field line is traced for a given initial position. The field line is then plotted in $\phi - \theta$ space which shows the poloidal and toroidal mapping of the field line on a given flux surface. Figures 3-15 and 5-11 were created with this tool. To run the field line mapping utility, open a new terminal on a C-Mod workstation and type the following commands:

```
cd /home/wallaceg/matlab/map_field_lines
matlab -nosplash -nodesktop -r fieldlines
```

The initial conditions for the field lines drawn, along with the shot number and time at which the EFIT reconstruction is evaluated, can be changed manually in the fieldlines.m file.

Bibliography

[1] J.P. Freidberg. *Plasma Physics and Fusion Energy*. Cambridge University Press, 2007.

[2] L.E. Dorman. International Energy Outlook 2009. Technical report, Energy Information Administration, U.S. Department of Energy, Washington, DC, May 2009.

[3] K.S. Krane. *Introductory Nuclear Physics*. John Wiley & Sons, Inc., 1988.

[4] J.D. Lawson. Some Criteria for a Useful Thermonuclear Reactor. Technical report, Atomic Energy Research Establishment, 1955.

[5] J D Lawson. Some criteria for a power producing thermonuclear reactor. *Proceedings of the Physical Society. Section B*, 70(1):6–10, 1957.

[6] J.D. Huba. NRL Plasma Formulary. Technical report, Naval Research Laboratory, 2004.

[7] N. J. Fisch. Theory of current drive in plasmas. *Reviews of Modern Physics*, 59:175–234, January 1987.

[8] A. G. Peeters. The bootstrap current and its consequences. *Plasma Physics and Controlled Fusion*, 42:B231–B242, December 2000.

[9] V. E. Golant. Plasma Penetration near the Lower Hybrid Frequency. *Soviet Physics Technical Physics*, 16:1980, June 1972.

[10] F. Troyon and F.W. Perkins. Lower hybrid heating in a large tokamak. *Proceedings of the 2^{nd} Topical Conference on RF Plasma Heating*, Paper B4, June 1974.

[11] P.T. Bonoli. Linear Theory of Lower Hybrid Heating. *Plasma Science, IEEE Transactions on*, 12(2):95–107, June 1984.

[12] N. J. Fisch and A. H. Boozer. Creating an Asymmetric Plasma Resistivity with Waves. *Physical Review Letters*, 45(9):720–722, Sep 1980.

[13] A. P. Smirnov and R.W. Harvey. *Bulletin of the American Physical Society*, 40:1837, 1995.

[14] L.D. Landau and L.M. Lifshitz. *The Classical Theory of Fields*, volume 2. Pergamon Press, New York, 1974.

[15] S. Weinberg. Eikonal Method in Magnetohydrodynamics. *Physical Review*, 126:1899–1909, June 1962.

[16] R.W. Harvey and M.G. McCoy. The CQL3D Fokker-Planck Code. Technical report, General Atomics, 1992.

[17] R. W. Harvey and M. McCoy. The CQL3D Fokker-Planck Code. *Proceedings of the IAEA Technical Committee Meeting on Simulation and Modeling of Thermonuclear Plasmas*, pages 489–526, 1992.

[18] C. F. Kennel and F. Engelmann. Velocity Space Diffusion from Weak Plasma Turbulence in a Magnetic Field. *Physics of Fluids*, 9(12):2377–2388, 1966.

[19] A.A. Vedenov. Theory of a Weakly Turbulent Plasma. *Reviews of Plasma Physics*, 3:229, 1967.

[20] C.F.F. Karney and N.J. Fisch. Numerical studies of current generation by radio-frequency traveling waves. *Physics of Fluids*, 22(9):1817–1824, 1979.

[21] I. H. Hutchinson, R. Boivin, F. Bombarda, P. Bonoli, S. Fairfax, C. Fiore, J. Goetz, S. Golovato, R. Granetz, M. Greenwald, S. Horne, A. Hubbard, J. Irby, B. LaBombard, B. Lipschultz, E. Marmar, G. McCracken, M. Porkolab, J. Rice, J. Snipes, Y. Takase, J. Terry, S. Wolfe, C. Christensen, D. Garnier, M. Graf, T. Hsu, T. Luke, M. May, A. Niemczewski, G. Tinios, J. Schachter, and J. Urbahn. First results from Alcator C-MOD. *Physics of Plasmas*, 1(5):1511–1518, 1994.

[22] P. T. Bonoli, R. Parker, S. J. Wukitch, Y. Lin, M. Porkolab, J. C. Wright, E. Edlund, T. Graves, L. Lin, J. Liptac, A. Parisot, A. E. Schmidt, V. Tang, W. Beck, R. Childs, M. Grimes, D. Gwinn, D. Johnson, J. Irby, A. Kanojia, P. Koert, S. Marazita, E. Marmar, D. Terry, R. Vieira, G. Wallace, J. Zaks, S. Bernabei, C. Brunkhorse, R. Ellis, E. Fredd, N. Greenough, J. Hosea, C. C. Kung, G. D. Loesser, J. Rushinski, G. Schilling, C. K. Phillips, J. R. Wilson, R. W. Harvey, C. L. Fiore, R. Granetz, M. Greenwald, A. E. Hubbard, I. H. Hutchinson, B. LaBombard, B. Lipschultz, J. Rice, J. A. Snipes, J. Terry, S. M. Wolfe, and the Alcator C-Mod Team. Wave-Particle Studies in the Ion Cyclotron and Lower Hybrid Ranges of Frequencies in Alcator C-Mod. *Fusion Science and Technology*, 51(3):401–436, April 2007.

[23] S. Bernabei, J. Hosea, C. Kung, G. Loesser, J. Rushinski, J. Wilson, R. Parker, and M. Porkolab. Design of a Compact Lower Hybrid Coupler for Alcator C-Mod. *Fusion Science and Technology*, 43:145–152, March 2003.

[24] M. Porkolab, J. J. Schuss, B. Lloyd, Y. Takase, S. Texter, P. Bonoli, C. Fiore, R. Gandy, D. Gwinn, B. Lipschultz, E. Marmar, D. Pappas, R. Parker, and P. Pribyl. Observation of Lower-Hybrid Current Drive at High Densities in the Alcator *C* Tokamak. *Physical Review Letters*, 53(5):450–453, Jul 1984.

[25] M. Grimes, D. Gwinn, R. Parker, D. Terry, and J. Alex. The Alcator C-Mod lower hybrid current drive experiment transmitter and power system. *Proceedings of the 19th Symposium on Fusion Engineering*, pages 16–19, 2002.

[26] X. Litaudon, G. Berger-by, P. Bibet, J. P. Bizarro, J. J. Capitain, J. Carrasco, M. Goniche, G. T. Hoang, K. Kupfer, R. Magne, D. Moreau, Y. Peysson, J.-M. Rax, G. Rey, D. Rigaud, and G. Tonon. Lower hybrid wave coupling in TORE SUPRA through multijunction launchers. *Nuclear Fusion*, 32:1883–1898, November 1992.

[27] M. Pain, H. Brinkschulte, G. Bosia, M. Brusati, J.A. Dobbing, A. Ekedahl, M. Gammelin, C. Gormezano, C. Idelon, J. Jacquinot, G. Jessop, A. Kaye, M. Lenholm, J. Plancoulaine, P. Schild, A. Sibley, T. Wade, C. Walker, R. Walton, and G. Wilson. The 15 MW microwave generator and launcher of the lower hybrid current drive experiment on JET. *Proceedings of the IEEE Thirteenth Symposium on Fusion Engineering, 1989*, pages 1083–1088 vol.2, Oct 1989.

[28] A. S. Kaye. Progress in ICRH and lower hybrid launcher development. *Plasma Physics and Controlled Fusion*, 35(SA):A71–A90, 1993.

[29] Y. Ikeda, M. Seki, T. Imai, K. Ushigusa, S. Takahashi, M. Sawahata, K. Suganuma, and A. Takasa. A new LHRF multijunction launcher with oversized waveguides for JT-60U. *Proceedings of the 14th IEEE/NPSS Symposium on Fusion Engineering, 1991*, pages 122–125 vol.1, Sep-3 Oct 1991.

[30] D. Gwinn. Notes on Lower Hybrid Launcher 1 RF Losses. Technical report, MIT Plasma Science and Fusion Center, 2005.

[31] N.P. Basse, A. Dominguez, E.M. Edlund, C.L. Fiore, R.S. Granetz, A.E. Hubbard, J.W. Hughes, I.H. Hutchinson, J.H. Irby, B. LaBombard, L. Lin, Y. Lin, B. Lipschultz, J.E. Liptac, E.S. Marmar, D.A. Mossessian, R.R. Parker, M. Porkolab, J.E. Rice, J.A. Snipes, V. Tang, J.L. Terry, S.M. Wolfe, S.J. Wukitch, and K. Zhurovich. Diagnostic Systems on Alcator C-Mod. *Fusion Science and Technology*, 51(3):476–507, Apr 2007.

[32] J. Liptac, R. Parker, V. Tang, Y. Peysson, and J. Decker. Hard x-ray diagnostic for lower hybrid experiments on Alcator C-Mod. *Review of Scientific Instruments*, 77(10):103504, 2006.

[33] J.E. Liptac. *Lower Hybrid Modeling and Experiments on Alcator C-Mod*. PhD thesis, Massachusetts Institute of Technology, 2006.

[34] Y. Peysson and Tore Supra Team. High power lower hybrid current drive experiments in the Tore Supra tokamak. *Nuclear Fusion*, 41:1703–1713, November 2001.

[35] F. Kazarian, E. Bertrand, L. Delpech, C. Goletto, M. Prou, J. Achard, G. Berger By, F. Bouquey, R. Magne, A. Beunas, C. Bellemere, R. Marchesin, B. Beaumont, and C. Darbos. Progress in the high power CW klystron development for Tore Supra. *Fusion Engineering and Design*, 84(2-6):1006 – 1009, 2009. Proceeding of the 25$^{\text{th}}$ Symposium on Fusion Technology - (SOFT-25).

[36] A. Ekedahl, G. Granucci, J. Mailloux, Y. Baranov, S. K. Erents, E. Joffrin, X. Litaudon, A. Loarte, P. J. Lomas, D. C. McDonald, V. Petrzilka, K. Rantamäki, F. G. Rimini, C. Silva, M. Stamp, A. A. Tuccillo, and J. EFDA Contributors. Long distance coupling of lower hybrid waves in JET plasmas with edge and core transport barriers. *Nuclear Fusion*, 45:351–359, May 2005.

[37] M. Aquilini, L. Baldi, P. Bibet, R. Bozzi, A. Bruschi, R. Cesario, S. Cirant, C. Ferro, F. Gandini, S. Di Giovenale, G. Granucci, T. Fortunato, G. Maddaluno, F. De Marco, G. Maffia, A. Marra, V. Mellera, F. Mirizzi, V. Muzzini, A. Nardone, A. Orsini, M. Papalini, P. Papitto, V. Percolini-Ridolfini, P. Petrolini, S. Petrosino, S. Podda, G.L. Ravera, G.B. Righetti, M. Roccon, F. Santini, M. Sassi, A. Simonetto, C. Sozzi, N. Spinicchia, A.A. Tuccillo, and P. Zampelli. The Heating and Current Drive Systems of the FTU. *Fusion Science Technology*, 45(3):459–482, May 2004.

[38] V. Pericoli Ridolfini, P. Bibet, F. Mirizzi, M. L. Apicella, E. Barbato, P. Buratti, G. Calabrò, A. Cardinali, G. Granucci, L. Panaccione, S. Podda, C. Sozzi, and A. A. Tuccillo. LHCD and coupling experiments with an ITER-like PAM launcher on the FTU tokamak. *Nuclear Fusion*, 45:1085–1093, September 2005.

[39] Y. Ikeda, O. Naito, M. Seki, T. Kondoh, S. Ide, K. Anno, H. Fukuda, Y. Ikeda, T. Kitai, K. Kiyono, M. Sawahta, S. Shinozaki, K. Suganuma, N. Suzuki, and K. Ushigusa. Simple multijunction launcher with oversized waveguides for lower hybrid current drive on JT-60U. *Fusion Engineering and Design*, 24(3):287–298, June 1994.

[40] Masami Seki, Shinichi Moriyama, Shin ichi Shinozaki, Kouichi Hasegawa, Shinichi Hiranai, Kenji Yokokura, Mitsugu Shimono, Masayuki Terakado, and

Tsuneyuki Fujii. Performance of the LH antenna with carbon grill in JT-60U. *Fusion Engineering and Design*, 74(1-4):273 – 277, 2005. Proceedings of the 23rd Symposium of Fusion Technology - SOFT 23.

[41] S. F. Knowlton and M. Porkolab. Lower Hybrid Wave Launching and Antenna Design. *Nuclear Fusion*, 29(9):1544–1583, 1989.

[42] P. Lallia. *Proceedings of the 2nd Topical Conference on Radio Frequency Plasma Heating*, 1974.

[43] M. Brambilla. Slow-wave launching at the lower hybrid frequency using a phased waveguide array. *Nuclear Fusion*, 16:47–54, February 1976.

[44] M. Abramowitz and I. Stegun. *Handbook of Mathematical Functions*. Dover Publications, 1972.

[45] J. Stevens, M. Ono, R. Horton, and J. R. Wilson. Edge density profile effects for lower hybrid waveguide coupling. *Nuclear Fusion*, 21:1259–1264, October 1981.

[46] M. Brambilla. Waveguide Launching of Lower Hybrid Waves. *Nuclear Fusion*, 19(10):1343–1357, 1979.

[47] G. Wallace, P. Koert, R. Parker, D. Terry, and S. J. Wukitch. Microstrip Directional Coupler Design For A Reduced Height Waveguide. *RADIO FREQUENCY POWER IN PLASMAS: 16th Topical Conference on Radio Frequency Power in Plasmas*, 787:331–336, September 2005.

[48] P. Koert, G. Wallace, R. Parker, D. R. Terry, and S. J. Wukitch. New microstrip Directional Coupler Design for Side of Waveguide in Lower Hybrid Current Drive System on Alcator C-Mod. *Fusion Engineering 2005, Twenty-First IEEE/NPS Symposium on*, pages 1–3, Sept. 2005.

[49] G. Wallace, P. Bonoli, A. Parisot, R. Parker, A. Schmidt, J. R. Wilson, and the Alcator C-Mod Team. Lower Hybrid Coupling Experiments on Alcator C-Mod. *Proceedings of the 17th Topical Conference on Radio Frequency Power in Plasmas*, 933(1):277–280, 2007.

[50] G. M. Wallace, P. T. Bonoli, A. E. Hubbard, Y. Lin, R. R. Parker, A. E. Schmidt, C. E. Kessel, and J. R. Wilson. Lower Hybrid Coupling Experiments on Alcator C-Mod. *APS Meeting Abstracts*, page 8069, November 2007.

[51] C. Lau, Y. Lin, G. Wallace, S. Wukitch, G. Hanson, and J. Wilgen. SOL reflectometer for Alcator C-Mod. *APS Meeting Abstracts*, page 6097, November 2008.

[52] G. R. Hanson, J. B. Wilgen, C. Lau, Y. Lin, G. M. Wallace, and S. J. Wukitch. Scrape-off layer reflectometer for Alcator C-Mod. *Proceedings of the 17th Topical Conference on High-Temperature Plasma Diagnostics*, 79(10):10F114, 2008.

[53] P.C. Stangeby. *The plasma boundary of magnetic fusion devices*. Institute of Physics Publishing, 1999.

[54] V.A. Petržilka, F. Leuterer, F.-X. Söldner, L. Giannone, and R. Schubert. Non-linear Coupling of the Lower Hybrid Grill in ASDEX. *Nuclear Fusion*, 31(9):1758–1767, 1991.

[55] A. Ekedahl, L. Colas, M.-L. Mayoral, B. Beaumont, P. Bibet, S. Brémond, F. Kazarian, J. Mailloux, J.-M. Noterdaeme, and Efda-Jet Contributors. Density Convection near Radiating ICRF Antennas and its Effect on the Coupling of Lower Hybrid Waves. *Radio Frequency Power in Plasmas: Proceedings of the 15th Topical Conference*, 694:259–262, December 2003.

[56] F. Leuterer, F. Soldner, M. Brambilla, M. Munich, F. Monaco, M. Zouhar, R. Bartiromo, A. Tuccillo, S. Bernabei, and C. Forest. Coupling of the 2 $\times$ 24 waveguide grill for lower hybrid waves in ASDEX. *Plasma Physics and Controlled Fusion*, 33:169–180, March 1991.

[57] D. Jablonski. *Local gas injection as a scrape-off layer diagnostic on the Alcator C-Mod tokamak*. PhD thesis, Massachusetts Institute of Technology, 1996.

[58] K. K. Kirov, J. Mailloux, A. Ekedahl, and LHCD team JET EFDA Contributors. Impurity Radiation From The LHCD Launcher During Operation In JET And Investigation Of Launcher Damage. *RADIO FREQUENCY POWER IN PLASMAS: 16th Topical Conference on Radio Frequency Power in Plasmas*, 787(1):315–318, 2005.

[59] R. W. Motley. Vortex formation during radio frequency heating of plasma. *Physics of Fluids*, 23(10):2050–2060, 1980.

[60] O. Naito, Y. Ikeda, M. Seki, S. Ide, T. Kondoh, and K. Ushigusa. Launcher heat load on high power LHCD experiments in JT-60U. *Journal of Nuclear Materials*, 220-222:425 – 428, 1995. Plasma-Surface Interactions in Controlled Fusion Devices.

[61] J. Marki, R. A. Pitts, T. Eich, A. Herrmann, J. Horacek, F. Sanchez, and G. Veres. Sheath heat transmission factors on TCV. *Journal of Nuclear Materials*, 363:382–388, June 2007.

[62] J. Mailloux, Y. Demers, V. Fuchs, M. Goniche, P. Jacquet, C. Boucher, A. Ct, C. Ct, J. Gunn, B. Terreault, P. Bibet, P. Froissard, D. Guilhem, J. H. Harris,

G. Rey, and M. Tareb. Strong toroidal asymmetries in power deposition on divertor and first wall components during LHCD on TdeV and Tore Supra. *Journal of Nuclear Materials*, 241-243:745 – 749, 1997.

[63] I. Pugno, J. J. Cordier, Ph. Ghendrih, M. Goniche, A. Grosman, J. P. Gunn, J. Mailloux, and S. Person. Localized heat flux due to lower hybrid wave coupling in the Ergodic Divertor configuration on Tore Supra. *Journal of Nuclear Materials*, 266-269:280 – 284, 1999.

[64] K M Rantamäki, V Petrzilka, P Andrew, I Coffey, A Ekedahl, K Erents, V Fuchs, M Goniche, G Granucci, E Joffrin, S J Karttunen, P Lomas, J Mailloux, M Mantsinen, M-L Mayoral, D C McDonald, J-M Noterdaeme, V Parail, A A Tuccillo, F Zacek, and Contributors to the EFDA-JET Workprogramme. Bright spots generated by lower hybrid waves on JET. *Plasma Physics and Controlled Fusion*, 47(7):1101–1108, 2005.

[65] D.M. Pozar. *Microwave Engineering*. John Wiley & Sons, Inc., 1998.

[66] V. Fuchs, M. Goniche, Y. Demers, P. Jacquet, and J. Mailloux. Acceleration of electrons in the vicinity of a lower hybrid waveguide array. *Physics of Plasmas*, 3(11):4023–4035, 1996.

[67] M. Goniche, D. Guilhem, P. Bibet, P. Froissard, X. Litaudon, G. Rey, J. Mailloux, Y. Demers, V. Fuchs, P. Jacquet, J. H. Harris, and J. T. Hogan. Enhanced heat flux in the scrape-off layer due to electrons accelerated in the near field of lower hybrid grills. *Nuclear Fusion*, 38:919–937, June 1998.

[68] K. M. Rantamäki, T. J. H. Pättikangas, S. J. Karttunen, X. Litaudon, D. Moreau, P. Bibet, and A. Ekedahl. Particle-in-cell simulation of parasitic absorption of lower hybrid power in edge plasmas of tokamaks. *Plasma Physics and Controlled Fusion*, 41:1125–1133, September 1999.

[69] K. M. Rantamäki, T. J. H. Pättikangas, S. J. Karttunen, P. Bibet, X. Litaudon, and D. Moreau. Estimation of heat loads on the wall structures in parasitic absorption of lower hybrid power. *Nuclear Fusion*, 40:1477–1490, August 2000.

[70] C. Portafaix, P. Bibet, J.H. Belo, A. Bou, M. Chantant, L. Delpech, A. Ekedahl, J.P. Gaston, and M. Goniche. Thermal behavior of the LHCD launchers in Tore Supra. *Fusion Engineering and Design*, 82(5-14):658 – 661, 2007. Proceedings of the 24$^{\text{th}}$ Symposium on Fusion Technology - SOFT-24.

[71] G. M. Wallace, R. R. Parker, P. T. Bonoli, A. E. Schmidt, D. G. Whyte, J. R. Wilson, and S. J. Wukitch. Interaction of Lower Hybrid Waves with the Scrape Off Layer. *APS Meeting Abstracts*, November 2008.

[72] V. Pericoli-Ridolfini, E. Barbato, S. Cirant, H. Kroegler, L. Panaccione, S. Podda, F. Alladio, B. Angelini, M. L. Apicella, G. Apruzzese, L. Bertalot, A. Bertocchi, M. Borra, G. Bracco, A. Bruschi, G. Buceti, P. Buratti, A. Cardinali, C. Centioli, R. Cesario, S. Ciattaglia, V. Cocilovo, F. Crisanti, R. De Angelis, F. De Marco, B. Esposito, and D. Frigione. High Plasma Density Lower-Hybrid Current Drive in the FTU Tokamak. *Physical Review Letters*, 82(1):93–96, Jan 1999.

[73] M. Porkolab. Parametric instabilities due to lower-hybrid radio frequency heating of tokamak plasmas. *Physics of Fluids*, 20(12):2058–2075, 1977.

[74] M. Porkolab, S. Bernabei, W. M. Hooke, R. W. Motley, and T. Nagashima. Observation of parametric instabilities in lower-hybrid radio-frequency heating of Tokamaks. *Physical Review Letters*, 38:230–233, January 1977.

[75] W. Hooke. Review of experiments on current drive in Tokamaks by means of RF waves. *Plasma Physics and Controlled Fusion*, 26(1A):133–144, 1984.

[76] Y. Takase, M. Porkolab, J. J. Schuss, R. L. Watterson, C. L. Fiore, R. E. Slusher, and C. M. Surko. Observation of parametric instabilities in the lower-hybrid range of frequencies in the high-density tokamak. *Physics of Fluids*, 28(3):983–994, 1985.

[77] R. Cesario, A. Cardinali, and C. Castaldo. Lower Hybrid Current Drive at ITER-relevant high plasma densities. *RADIO FREQUENCY POWER IN PLASMAS: 18th Topical Conference on Radio Frequency Power in Plasmas*, 2009.

[78] B. Labombard, J. A. Goetz, I. Hutchinson, D. Jablonski, J. Kesner, C. Kurz, B. Lipschultz, G. M. McCracken, A. Niemczewski, J. Terry, A. Allen, R. L. Boivin, F. Bombarda, P. Bonoli, C. Christensen, C. Fiore, D. Garnier, S. Golovato, R. Granetz, M. Greenwald, S. Horne, A. Hubbard, J. Irby, D. Lo, D. Lumma, E. Marmar, M. May, A. Mazurenko, R. Nachtrieb, H. Ohkawa, P. O'Shea, M. Porkolab, J. Reardon, J. Rice, J. Rost, J. Schachter, J. Snipes, J. Sorci, P. Stek, Y. Takase, Y. Wang, R. Watterson, J. Weaver, B. Welch, and S. Wolfe. Experimental investigation of transport phenomena in the scrape-off layer and divertor. *Journal of Nuclear Materials*, 241-243:149 – 166, 1997.

[79] B. LaBombard, J. E. Rice, A. E. Hubbard, J. W. Hughes, M. Greenwald, J. Irby, Y. Lin, B. Lipschultz, E. S. Marmar, C. S. Pitcher, N. Smick, S. M. Wolfe, S. J. Wukitch, and the Alcator Group. Transport-driven Scrape-Off-Layer flows and the boundary conditions imposed at the magnetic separatrix in a tokamak plasma. *Nuclear Fusion*, 44:1047–1066, October 2004.

[80] R. McWilliams, E. J. Valeo, R. W. Motley, W. M. Hooke, and L. Olson. Steady-State Currents Driven by Collisionally Damped Lower-Hybrid Waves. *Physical Review Letters*, 44(4):245–248, Jan 1980.

[81] Paul T. Bonoli and Edward Ott. Accessibility and Energy Depositon of Lower-Hybrid Waves in a Tokamak with Density Fluctuations. *Physical Review Letters*, 46(6):424–427, Feb 1981.

[82] G.M. Wallace, R.R. Parker, P.T. Bonoli, R.W. Harvey, A.E. Schmidt, A.P. Smirnov, D.G. Whyte, J.R. Wilson, J.C. Wright, and S.J. Wukitch. Observations of Lower Hybrid Wave Absorption in the Scrape Off Layer of a Diverted Tokamak. *RADIO FREQUENCY POWER IN PLASMAS: 18th Topical Conference on Radio Frequency Power in Plasmas*, 2009.

[83] P.T. Bonoli, R.C. Englade, and M. Porkolab. A Computational Model for Lower-Hybrid Current Drive. *Proceedings of the Fifth Topical Conference on Radio Frequency Plasma Heating*, pages 72–75, 1983.

[84] J. C. Wright, P. T. Bonoli, A. E. Schmidt, C. K. Phillips, E. J. Valeo, R. W. Harvey, and M. A. Brambilla. An assessment of full wave effects on the propagation and absorption of lower hybrid waves. *Physics of Plasmas*, 16(7):072502, 2009.

[85] J.C. Wright, MIT-PSFC, and RF-SciDAC Team. Full wave simulations of lower hybrid wave propagation in tokamaks. *RADIO FREQUENCY POWER IN PLASMAS: 18th Topical Conference on Radio Frequency Power in Plasmas*, 2009.

[86] O. Meneghini, S. Shiraiwa, and R. Parker. Full wave simulation of lower hybrid waves in maxwellian plasma based on the finite element method. *Physics of Plasmas*, 16(9):090701, 2009.

[87] S. Shiraiwa, O. Meneghini, R. Parker, G. Wallace, and J. Wilson. Plasma wave simulation based on versatile FEM solver on Alcator C-Mod. *RADIO FREQUENCY POWER IN PLASMAS: 18th Topical Conference on Radio Frequency Power in Plasmas*, 2009.

[88] A. Dominguez, P. Bonoli, E. Marmar, R. Parker, S. Shiraiwa, and G. Wallace. Proposal for the Study of LH Wave Propagation Using Reflectometry on Alcator C-Mod. *APS Meeting Abstracts*, page 6079, November 2008.

[89] L. Lin, E. M. Edlund, M. Porkolab, Y. Lin, and S. J. Wukitch. Vertical localization of phase contrast imaging diagnostic in Alcator C-Mod. *Review of Scientific Instruments*, 77(10):918, 2006.